CARDIFF UNIVERSITY

Damage Detection of Rotating Machinery

by
Aaron Cockerill

A thesis submitted in partial fulfilment for
the degree of Doctor of Philosophy

Mechanics, Materials and Advanced Manufacturing Engineering
School of Engineering

2017

Abstract

Acoustic emission (AE) is an emerging technique for the condition monitoring of rotating machinery components, including both rolling element bearings and gears. Due to the high frequency range over which AE is sensitive to, AE potentially offers advantages for detection of incipient damage at an early stage of failure when compared to traditional techniques such as vibration. This thesis first investigates the effects of increased speed and load on the generation of AE within cylindrical roller bearings, and determines similarities and differences between AE and vibrational data. A traditional AE sensor was used in conjunction with a Dual Function Sensor (DFS) capable of recording both low frequency AE and vibration. It was shown that increasing speed has the greatest influence on the AE signals produced whereas the effect of load was limited. Order analysis of both AE and vibrational data also demonstrated that characteristic bearing defect frequencies are visible in the AE spectrum but not in the vibrational spectrum. Bearings with seeded defects upon the outer raceway were investigated under a fixed speed and it was found that load increased the energy within the signal frequency spectrum as the damaged increased. Two bearing life tests were also conducted, one accelerated to 12 hours and the second extended to over 2800 hours however as damage detection only occurred after significant damage had developed, it is concluded that AE of seeded defects indicate a false sensitivity. Both life tests were able to demonstrate that signal levels increase as damage propagates over the bearing raceway however it was not possible to determine any advantage of using AE over vibration. AE sensors were also applied to test rigs of increased complexity, including the monitoring a wind turbine planet bearing and a helical gear pair. AE was able to detect cracking of the shaft surface within the wind turbine bearing test rig which was mistaken for being an inner raceway failure, highlighting the difficulty in damage location. A tooth failure occurred during the testing of the helical gear pair however AE was not able to detect growing damage, instead only increasing in amplitude after the tooth had sheared off, similar to the detection from vibrational signals.

Declaration of Authorship

This work has not been submitted in substance for any other degree or award at this or any other university or place of learning, nor is being submitted concurrently in candidature for any degree or other award.

Signed ……………………………………………… (candidate) Date………………………………

STATEMENT 1

This thesis is being submitted in partial fulfilment of the requirements for the degree of PhD.

Signed ……………………………………………… (candidate) Date………………………………

STATEMENT 2

This thesis is the result of my own independent work / investigation, except where otherwise stated. Other sources are acknowledged by explicit references. The views expressed are my own.

Signed ……………………………………………… (candidate) Date………………………………

STATEMENT 3

I hereby give consent for my thesis, if accepted, to be available for photocopying and for inter-library loan, and for the title and summary to be made available to outside organisations.

Signed ……………………………………………… (candidate) Date………………………………

STATEMENT 4

I hereby give consent for my thesis, if accepted, to be available for photocopying and for inter-library loans after expiry of a bar on access previously approved by the Academic Standards and Quality Committee.

Signed ……………………………………………… (candidate) Date………………………………

This thesis is dedicated to all of the people that have made it possible for me to get this far.

Acknowledgements

Firstly, I would like to acknowledge the funding provided by Mistras Group and EPSRC who made it possible for this PhD to be carried out in the first place. Also, my gratitude is extended to all of the support staff working within Cardiff University who work behind the scenes, manufacturing test rigs, wiring them up and making the research possible. I also wish to thank the team at Newcastle University Gear Design Unit for allowing me to use their test rigs and sharing their extensive knowledge and experience with me.

My sincere appreciation is also extended to my supervisors Rhys, Al and Karen for making this journey possible, supporting and encouraging me through all of the rough patches.

During my time at the university I have made a number of friends but none have made me laugh more than those in the CUSP lab and the Tribology Office. You have demonstrated to me that life has not got to be too serious and really showing that if you enjoy doing what you do, you'll never work a day in your life. I look forward to visiting you all in the future for Nerf gun fights and whatever else is introduced to the lab.

It goes without saying that my family, however chaotic and unconventional it may be, is the foundation of my success so far. They made me believe that undertaking a PhD was possible and, although I am restricted to only 100 words or less when discussing my PhD, they have always demonstrated an interest in my subject offering me unconditional support, encouragement, love and faith alongside an endless supply of warm meals and hot coffee on the tiresome nights.

I would finally like to thank my partner Nikita, the relationship with whom started in the first week of my PhD. I know the undertaking of this thesis has been difficult for the two of us but you have been there for me through all of the highs and the lows, and are always able to put a smile on my face no matter how frustrated or tired I may be. Although the 8 chapters contained within this PhD are now being put to rest, I look forward to starting the next chapter of my life with you as we continue to build and grow our relationship together.

Thank you all!

Contents

List of Figures

List of Tables

List of Abbreviations

ACMS	-	Autonomous Condition Monitoring System
AE	-	Acoustic Emission
ALE	-	Adaptive Line Enhancer
BPFI	-	Ball Pass Frequency of the Inner Race
BPFO	-	Ball Pass Frequency of the Outer Race
BSF	-	Ball Spin Frequency
CAE	-	Computer Aided Engineering
DFS	-	Dual Function Sensor
DLC	-	Diamond Like Carbon
EDM	-	Electric Discharge Machining
EHL	-	Elastohydrodynamic Lubrication
FFT	-	Fast Fourier Transform
FTF	-	Fundamental Train Frequency
HFNBRI's	-	High Frequency Natural Bearing Resonance Frequencies
HFRT	-	High Frequency Resonance Technique
HN	-	Hsu-Nielson
NDT	-	Non-Destructive Testing
PAC	-	Physical Acoustics
PLB	-	Pencil Lead Breaks
RMS	-	Root Mean Squared
RPM	-	Revolutions per Minute

SCADA - Supervisory Control and Data Acquisition

SNR - Signal to Noise Ratio

STRMS - Short Time RMS

VI - Virtual Instrument

WEC White Etching Crack

Nomenclature

Symbol	**Description**	**SI Unit**
a	Acceleration	m/s^2
a_1	Modification factor for cleanliness	-
a_{skf}	SKF modification factor	-
b	Semi-contact width	m
B	Ball or Roller Diameter	m
b_{face}	Facewidth	m
C	Basic Dynamic Load Rating	N
C_0	Static Load Rating	N
d	Inner Race Diameter	m
d_a	Tip diameter	m
d_b	Base Diameter	m
d_f	Root Diameter	m
d_p	Pitch Diameter	m
d_{ref}	Reference Diameter	m
E'	Relative Modulus of Elasticity	N/m^2
F	Force	N
F_p	Pinion Speed	Hz
F_s	Shaft Speed	Hz
F_w	Wheel Speed	Hz
h	Nominal Tooth Depth	m
h_{min}	Minimum Fluid Film Thickness	m
K_n	Load Deflection Factor	-
L	Roller Length	m
L_{10}	L10 Life of a bearing	million revs
m	Mass	kg
m_n	Normal Module	mm
n	Accelerated exponent	-
N	Number of Rollers	-

P	Equivalent Bearing Load	N
P_d	Diametrical Clearance	m
p_m	Average Contact Pressure	MPa
P_u	Fatigue Load Rating	N
Q	Total Load	N
R	Relative Radius of Curvature	m
RPM	Revolutions per Minute	rpm
R_q	RMS Surface Roughness	m
t	Current time sample	-
T	Total number of time samples	-
$\bar{u}$	Mean Speed	m/s
w'	Load Per Unit Length	N/m
x_p	Profile Shift Coefficient	-
x_t	Signal amplitude at time, t	Volts
Z	Number of Teeth	-
α	Viscosity/pressure coefficient	-
α_n	Pressure Angle	Degrees
δ	Deflection	m
ε	Radial Deflection	m
η	Oil viscosity under pressure	cSt
η_0	Oil viscosity at atmospheric pressure	cSt
θ	Contact Angle	Degrees
λ	Lambda Ratio	-
ν	Poisson Ratio	-
ρ_f	Minimum root fillet radius	mm
ϕ	Roller Angle	Degrees

1 Introduction

1.1 Introduction

Rotating machinery is a broad term used to cover the mechanical systems that are increasingly used and heavily relied upon within modern society. All dominant industry sectors, including aerospace, automotive and power generation, require their assets or products to perform efficiently and reliably, especially when the failure of such machinery could result in the loss of human life. Operators therefore continue to adopt advanced pro-active maintenance strategies, rather than undertaking costly reactive maintenance (García Márquez *et al.,* 2012).

This thesis focuses predominantly on the health monitoring of rolling element bearings although there is also acknowledgement towards geared systems. Early condition monitoring techniques focussed heavily on the vibrational response of a mechanical system, relying on the increase in amplitude of the bearing defect frequencies, i.e. the fundamental frequencies at which the various bearing components interact with each other, as damage propagated along the rollers and raceways (Howard, 1994). In recent years, research has investigated the application of Acoustic Emission (AE) to bearing condition monitoring. Whereas traditional vibration transducers are typically sensitive between 0-50kHz, AE sensors operate over a far wider frequency range typically between 20kHz and 1MHz. As a result, AE sensors have the ability to detect the transient elastic surface waves associated with the strain energy released during the plastic deformation of materials, by crack initiation and propagation, by frictional sources and throughout the wear process (Hase *et al.,* 2012).

Initial AE analysis of rolling element bearings demonstrated an increased sensitivity to increases in the bearing defect frequencies commonly used in vibrational data analysis (Hawman & Galinaitis, 1988). Although the bearing defect frequencies commonly exist below 1kHz, the frequency content of each ‘burst’, created as a roller passes over a defect, has been seen to exceed 100kHz enabling its detection through AE. When combined with the fact that AE operates in a frequency band outside of the typical mechanical noise frequency range, it is thought that AE will have a much greater sensitivity to incipient bearing defects when compared to vibration due to its enhanced signal to noise ratio.

Over recent years, AE has been applied to wind turbines for the purpose of monitoring and detecting damage within the wind turbine blades, rather than being employed to monitor the condition of the rotating machinery such as the bearings and gears (García Márquez et al. 2012). The application of AE to rotating machinery within the aerospace industry however, is rapidly developing with AE sensors being introduced to integrate with the Health Usage and Monitoring Systems (HUMS) currently applied to helicopters (Finlayson et al. 2001; Elasha et al. 2015)

1.2 Aims of the Study

There is a large debate within the literature as to whether AE is a viable technique for companies and organisations to use when monitoring the condition of rotating machinery. Whilst significant research has been conducted to demonstrate the advantages of AE over vibration, the majority of the existing research has focussed on seeded/artificial defects as opposed to natural damage propagation. This thesis aims to demonstrate the benefits of using AE as a condition monitoring technique with specific application to rotating machinery. Only one series of tests carried out within this thesis is performed on a simplified test rig, designed for the sole purpose of detecting AE signals from rolling element bearings. The other two studies monitor the condition of rotating machinery on third party test rigs, and therefore, are more akin to the application of AE to rotating machinery in service. The surrounding literature only briefly discusses the effects of both speed and load and therefore a significant part of this study aims to determine the characteristic signals emitted from healthy bearings, as well as investigating the effect of the lubrication regime.

Both seeded defects and accelerated life tests are conducted to demonstrate the sensitivity of AE as well as determining how the AE signal changes with the introduction of damage and discontinuities. Third party test rigs were also instrumented to determine how rig complexity, as well as a difference in source mechanism, affects the characteristics observed in the AE signals. The rotational speed of the components investigated within this study vary between 400 and 6000rpm. As well as traditional AE, a combined AE/Vibration sensor was also applied to some of the test rigs in order to, where possible, draw comparisons between AE and vibration, discussing the similarities and differences between the two techniques as well as observing which technique is more sensitive to damage initiation.

1.2.1 *Objectives*

This thesis aims to expand on the research topic of bearing and gear condition monitoring by:

- Investigate the generation and characteristics of AE from a variety of test rigs, each incorporating different elements of rotating machinery.
- Demonstrate the sensitivity of AE as a technique overall, determining the effect of applied load and speed, repeatability and reliability on set up procedure as well as the response of AE to a variety of defects.
- Establish a significant data base from which further analysis work can be carried out on in future analysis.

1.3 *Novelty Statement*

This research presents novelty in the following areas. The work herein:

- Contributes to the discussion of how speed and load contribute to the generation of AE and increases the knowledge surrounding the effect of the Lambda ratio on the AE signal, through extensive testing and characterisation of a healthy bearing.
- Demonstrates how the frequency analysis of AE wavestreams can be used in the analysis of bearing and gear defects, aiding in the detection of damage growth.
- Demonstrates that with the increasing complexity of test rigs introduces a number of challenges and obstacles that may affect the application of AE to wider industries.
- Demonstrates the sensitivity of AE overall with the ability of detecting roller slap in a large full complement bearing.
- Draws comparisons between both vibration and AE data.

1.4 Published Outcomes

1.4.1 Journal Papers

Cockerill, A., Clarke, A., Pullin, R., Bradshaw, T., Cole, P. and Holford, K.M., 2016. **Determination of rolling element bearing condition via acoustic emission**. *Proceedings of the Institution of Mechanical Engineers, Part J: Journal of Engineering Tribology*

Cockerill, A., Holford, K.M., Bradshaw, T., Cole, P., Pullin, R and Clarke, A., 2015. **Use of high frequency analysis of acoustic emission signals to determine rolling element bearing condition**. *Journal of Physics. Conference Series 628.*

1.4.2 Conference Presentations

Cockerill, A., Clarke, A., Pullin, R., Holford, K.M., Bradshaw, T. and Cole, P., 2015. **Acoustic emission as an aid to understanding raceway damage in rolling element bearings** [Abstract]. Presented at: 42nd Leeds-Lyon Symposium on Tribology, Lyon, France, 7-9 September 2015.

Cockerill, A., Holford, K.M, Bradshaw, T., Cole, P., Pullin, R. and Clarke, A., 2015. **Use of high frequency analysis of acoustic emission signals to determine rolling element bearing condition.** Presented at International Conference on Damage Assessment of Structures, Ghent, Belgium, 24-26 August 2015.

Cockerill, A., Clarke, A., Holford, K. M., Bradshaw, T., Cole, P. and Pullin, R., 2014. **Damage assessment of rolling element bearings using acoustic emission**. Presented at: 16th International Workshop on Experimental Mechanics, Cambridge, UK, 7 - 11 July 2014.

1.5 Thesis Structure

Chapter 2 discusses the current literature surrounding the condition monitoring of rotating machinery. An overview is given of the mechanical components considered within the thesis, the damage mechanisms which lead to their failure and how existing condition monitoring techniques have been employed previously by other authors, before discussing the benefits of AE for damage detection.

Chapter 3 focusses on detailing the experimental apparatus used in subsequent chapters and then concludes with the derivation of equations used to determine the loads and tribological conditions of the mechanical components investigated.

Chapter 4 forms the foundations for understanding how AE can be used to detect damage in rolling element bearings operating at speeds up to 6000rpm. A healthy bearing characterisation is conducted to establish a baseline to which seeded defects and accelerated life tests are compared.

Chapters 5 and 6 both apply the technique of AE to test rigs which are of increased size and complexity when compared to the test rig used in Chapter 4. The purpose of this is to demonstrate the difficulty in moving from small, specifically designed test rigs to test rigs which are more akin to ‘real-world’ applications.

Chapter 7 provides discussion of the thesis as a whole, before bringing together the main conclusions of the thesis as well as providing recommendations for future research in the subject area.

The references and supporting appendix can be found in Chapters 8 and 9 respectively.

2 Literature Review

2.1 Chapter Overview

This chapter reviews the literature relevant to this thesis. First, the importance of condition monitoring within modern society is discussed and then the various methods of condition monitoring are reviewed with the focus on vibration and AE. Following this, the reader will be introduced to the fundamentals of the two key components of rotating machinery, i.e., gears and rolling element bearings, including a brief history of their development as well as common applications where knowledge regarding their condition is deemed as critical. The chapter will go on to discuss the current state of the art of condition monitoring techniques used to detect damage within such bearings and new techniques currently undergoing development.

2.2 Purpose of condition monitoring

As more research and development is conducted, the mechanical machinery of the modern world continues to evolve in terms of its complexity and application. With increasing complexity comes increased cost, both in terms of capital and operating costs, further driving the need for research into component longevity. With that said, the knowledge surrounding metallurgy, material properties and the way two bodies in contact interact with each other, is constantly growing and enabling improved life and performance for mechanical systems. Engineers have the ability to hand-pick the properties and characteristics of different materials, increasing the use of surface coatings and hardness treatments and hence leading to stronger or more durable materials and surfaces. In order to further improve the design of components, Computer Aided Engineering (CAE) is commonly used to simulate how a component reacts to a number of different operating conditions. As well as enabling engineers to optimise the design of their components to increase their resistance to external influences, it is also possible to calculate the theoretical lifespan of a component, reducing the likelihood of premature component failure.

However, as it is purely a simulation, the use of CAE is only valid when the modelled parameters are matched in real life and, even then, there is still an inherent randomness in the failure process, largely due to human error and manufacturing variability.
Figure 2-1, extracted from Tavner (2011) demonstrates that for onshore wind turbines, the most common type of failure is due to electrical components, although it can be seen that the downtime per failure is much larger for mechanical components such as the gearbox and drive train. Much of this is due to the availability of components, as well as the logistics involved to repair and replace them. For similar failure modes, the cost of offshore wind turbines is far greater than onshore wind turbines due to the inherent difficulty in effecting repairs or inspections (Nilsson & Bertling, 2007).

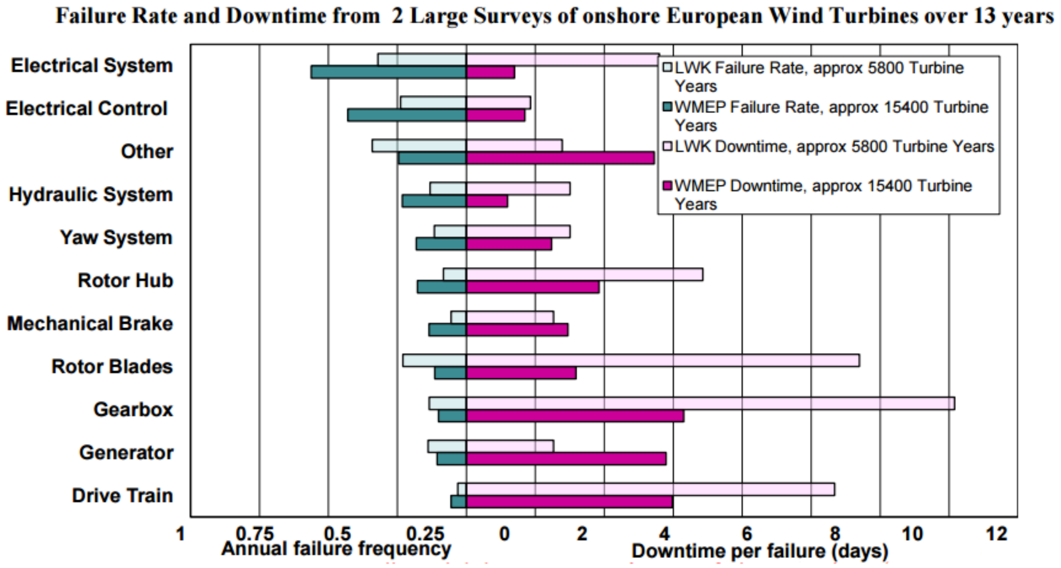

Figure 2-1 – Failure rate and downtime of wind turbines (Extracted from Tavner (2011))

To reduce the likelihood of sudden failures, many high value assets have a maintenance strategy set out in order to maximise the life of the asset (Wiggelinkhuizen *et al.,* 2008). As a society, this is something that we do regularly and somewhat autonomously with our own valued possessions, for example a family car. Table 2-1 describes the different maintenance strategies and demonstrates these strategies using to the example of a family car.

Table 2-1 - Maintenance Strategies

Preventative Maintenance	Corrective Maintenance
Calendar Based - Performed routinely to increase reliability regardless of component condition. - E.g. A family car has an annual service where the oil, oil filter and air filter are changed.	Planned Maintenance - A part which is known to have a known life cycle and is scheduled to be replaced in advance. - E.g. Cam belts need to be changed once a particular mileage has been reached.
Condition Based - Parameters are monitored over a long period of time and items are often changed when a predetermined threshold is reached. - E.g. The brake pads and tyres of a car are periodically monitored and once they reach the threshold, they do not fail catastrophically, but the performance of them is slightly reduced.	Unplanned Maintenance - Any component that fails prematurely and requires immediate attention. - E.g. Connecting rod failure within the engine.

A similar analogy can be translated to much more complex and costly machinery. The most critical assets are those which are inaccessible, such as off-shore wind turbines, or where a critical failure has the potential to endanger human life, for example helicopters and other forms of aircraft (Bashir *et al.,* 1999).

As a result, most industrial sectors adopt a scheduled maintenance routine comprised of both condition based and calendar based preventative maintenance. Carrying out these inspections on a regular basis allows for any damage or irregularities to be captured early, allowing for planned maintenance to be carried out in due course (García Márquez *et al.,* 2012). A vast majority of sectors, where planned maintenance is a necessary process to reduce potential unforeseen expense, are interested in the development of condition monitoring techniques as if they are able to accurately determine the condition of all components, the chance of catastrophic failure occurring before detection is greatly reduced. Also, knowledge of the condition of the machinery can be used to inform the timings of the calendar based maintenance, further reducing overheads.

2.3 Condition Monitoring Techniques

Modern machinery is often instrumented with a number of sensors and gauges and their values are constantly monitored and compared to known thresholds. For the example of a wind turbine, the system and environmental data recorded often includes, but is not limited to, ambient air and oil temperature, the rotational speed of individual parts, torque, power consumption/generation, wind speed etc. This information is often referred to as SCADA (Supervisory Control and Data Acquisition) data as it is recorded periodically to allow analysts to check the operating history if an error occurs.

As a particularly holistic form of condition monitoring, alarms caused by a parameter exceeding a threshold may be able to indicate an approximate source of damage but fails to distinguish which part is responsible as well as the severity of the damage. In order to determine this, other condition monitoring techniques are available, for example vibration and AE, as these methods record waveforms over a set period of time, which are then subject to further processing to allow the identification and potentially location of the defect.

2.3.1 Vibration

Vibration is measured using sensors commonly referred to as accelerometers which, as the name suggests, are used to measure the acceleration of a surface or body. In order to transfer mechanical motion into electrical energy most modern sensors contain a small mass, m, placed above a piezoelectric crystal, often a quartz or ceramic crystal lattice, that produces a small electrical charge when subjected to a force, F. This electrical charge is produced as the position of both positive and negative ions are altered, creating a build-up of charge, further illustrated in Figure 2-2, (Jeevagan *et al.,* 2014). When excited in the sensor's operating frequency range, the sensor output obeys Newton's law of motion (1),

$$F = ma \tag{1}$$

where, as the mass (*m)* is constant, the force applied (*F*) is proportional to the acceleration (*a*).

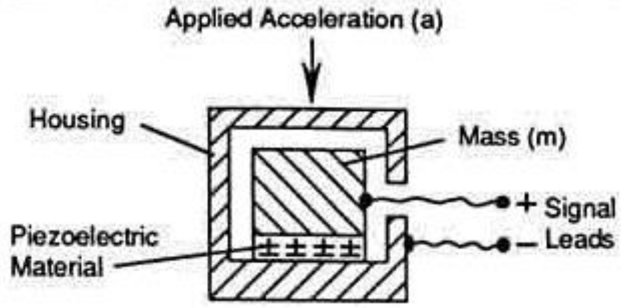

Figure 2-2 - Schematic of accelerometer construction (Jeevagan *et al.,* 2014)

Vibration sensors are typically sensitive between 0-10kHz and provide a flat amplitude response over this range. Their application is wide and varied, ranging from seismic activity monitoring to detecting imbalances in fans and motors. Not only do the sensors produce a higher output when subjected to a force, but they are also able to detect periodicity within signals through recording amplitude over a period of time. This periodicity can then be linked to characteristics of the mechanical system to locate the source of the damage or imperfection (Figure 2-3).

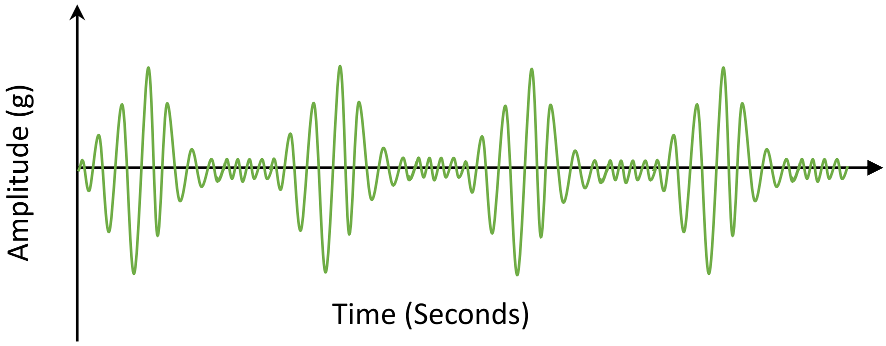

Figure 2-3 - Example vibration signal

2.3.2 Acoustic Emission

Similar to the vibration sensors, AE also utilises the properties of a piezoelectric crystal to convert mechanical motion into electrical energy. However, unlike an accelerometer, AE sensors do not contain a sprung mass and, as a result, are sensitive over a much higher frequency range, between 20kHz – 1MHz. Due to this, the AE sensors are able to detect the release of

> *"Transient elastic waves generated by the rapid release*
> *of energy from localised sources within a material"* - (ASTM E1313-17, 2017)

A localised source in this context refers to the boundary dislocations of the microstructure below the surface. The elastic wave generated travels along the surface of a material, exciting the piezoelectric crystal and converting kinematic energy into electrical energy. Mature applications of AE include the structural health monitoring of bridges, vessels and other static structures where an increase in AE activity is attributed to the plastic deformation of materials, crack initiation/propagation as well as other potential sources depending on application (Hase *et al.,* 2012).

When a pencil lead is broken (a typical method used to generate an AE source in a laboratory environment), a transient wave is emitted from the source. When broken on an infinately large elastic body, the transient wave is formed from two components that travel along the, a transverse (shear) wave and a longitudinal (compression) wave, commonly referred to as Rayleigh waves (Rindorf, 1981) (Figure 2-4). For AE sources carried out on a thin plate, the wave propagation increases in complexity as the AE wave now interacts with two surfaces, forming Plate or Lamb waves. Plate waves exist in two different modes, s_0 and a_0. The s_0 mode forms as a symmetrical wave and the a_0 mode forms as an asymmetrical wave (Figure 2-5). The two waves travel with different velocities, with the a_0 travelling faster than the s_0 wave (typically twice the velocity (Mistras Group Inc., 2011). As this research takes AE measurements from bearing housings, it is considered that only bulk waves will be produced in this research.

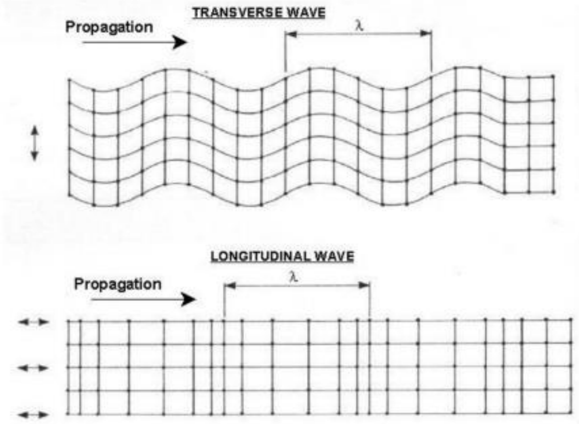

Figure 2-5 - Wave propagation modes in a large solid body (Rindorf, 1981)

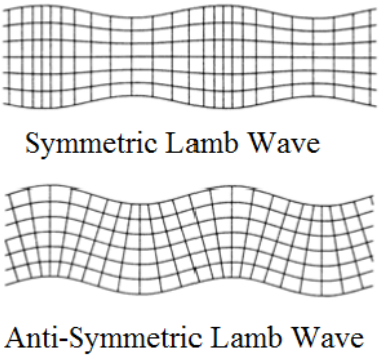

Figure 2-4 - Wave propagation in plates (Torkamani et al. 2014)

The difference in velocity, and hence difference in time of arrival at the sensor, can be seen in the raw waveform of a pencil lead break. Figure 2-6 is an example of an AE wavestream recorded when a pencil lead was broken close to the sensor. It can be seen that shortly after the first peak, a second transient wave with a much larger amplitude is recorded by the sensor. The time difference between the first and second arrival is fairly short, and it is possible within a waveform to detect reflections of the s_0 mode as it reflects from the edges of the material as well as any surface discontinuities such as holes.

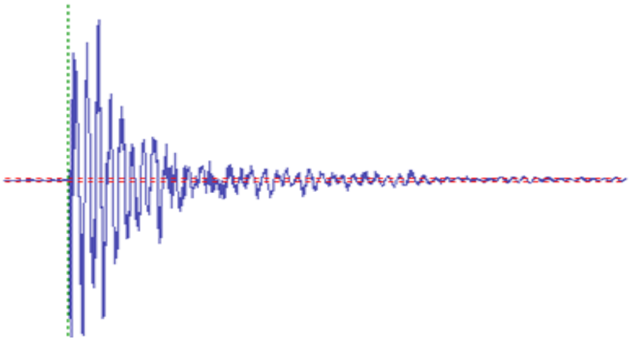

Figure 2-6 - Example AE wavestream

Traditional AE analysis methods use the raw signal features from an AE 'hit' to translate the severity of a defect to a user, directly correlating the increase in signal features with an increase in signal amplitude and length. A 'hit' is defined as "the detection and measurement of an AE signal on a channel" (Mistras Group Inc., 2011). To prevent excessive hits which may not relate to the damage itself, a threshold level is set at a predetermined level. Within the raw AE signal, the following signal features can be easily extracted: Peak Amplitude, Counts, Duration, Risetime and Energy. Figure 2-8 describes how each feature is defined. These signal features are currently the standard parameters used to monitor the condition of solid structures within industry. A user can easily understand the output values and it is clear to see that an increase in one or more parameter values over time indicates damage within an asset. However, the application of such techniques to rotating machinery, where signals from multiple sources may overlap and interfere, is more complex and is discussed in subsequent sections.

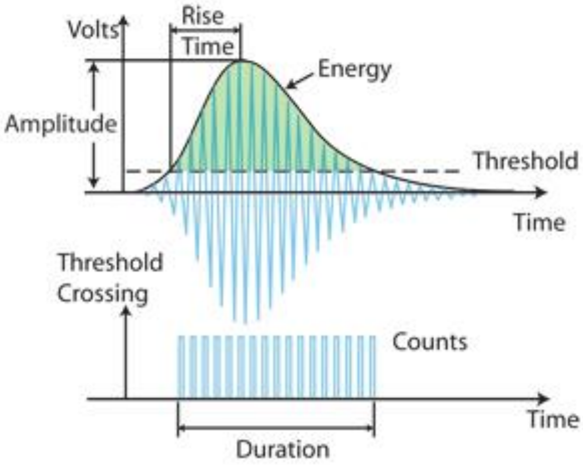

Figure 2-7 - Measurement of AE signal features - Extracted from Mistras Group Inc. (2011)

Rotating Machinery

Rotating machinery is a blanket term covering a wide variety of mechanical systems found within a number of industrial sectors. Although each machine differs in its overall design, there exist a number of common components fundamental to the facilitation of relative motion during the transmission of power and energy, namely gears and bearings.

2.3.3 Rolling Element Bearings

Bearings are available in a variety shapes and sizes and their fundamental design varies depending upon their application. Generally speaking, bearings are divided into two categories, rolling element bearings and plain bearings. Plain bearings are formed when two conformal bodies are used to move relative to each other, often with a sacrificial bush or liner between them. These bearings are often used in locations such as suspension rod ends, where it is difficult to provide lubrication. Other forms of plain bearing use either a hydrodynamically or hydrostatically-generated lubricant film to separate the rotating and fixed surfaces.

Rolling element bearings on the other hand are composed of an inner and outer raceway, separated by a number of rolling elements that are usually, but not always, constrained within a cage (Figure 2-8). If there is no cage present, commonly referred to as being ‘full complement’, the space gained allows for additional rollers to be added, increasing the load capacity of the bearing. The rolling elements themselves are varied in shape and are often either a ball or cylindrical/spherical rollers. The rolling element can also be arranged in single or double rows to accommodate larger radial loads as well as being tapered or angled to be able to accommodate any axial force/displacement.

Standard SKF bearings are manufactured from through-hardened carbon chromium steel (100Cr6) to the specifications of ISO 683-17 (2014). For some applications, the surface can be coated with Diamond Like Carbon (DLC) coatings in order to improve the wear and friction properties of the bearing, or ceramic materials may be used where high speeds or temperatures are likely to be encountered.

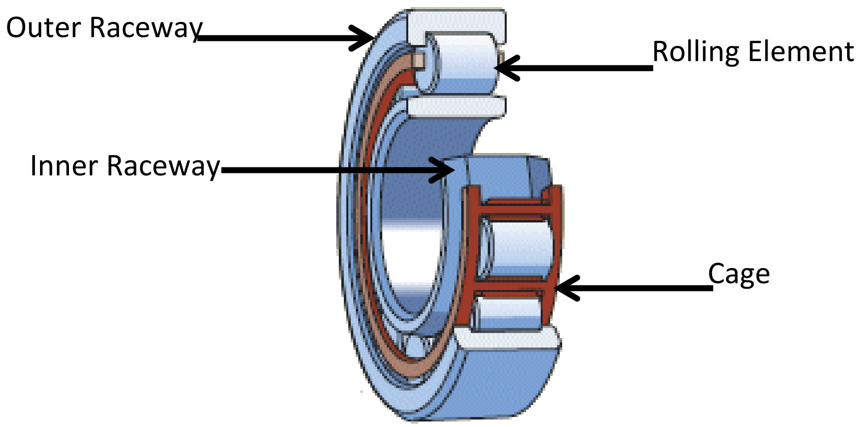

Figure 2-8 Single Row Roller Bearing (SKF, 2015)

2.3.4 Gears

Gears are often found within rotating machinery and as such, are an additional source within the signals produced at the bearing. Gears are used to facilitate the transmission of power and rotation from one shaft to another and are often paired together in ratios to increase/decrease both speed and torque depending on the application. As with bearings, gears come in a number of different designs and are capable of transmitting power between both parallel and perpendicular shafts. Common gear types, as pictured in Figure 2-9, include spur gears, helical gears, bevel gears and worm gears.

Figure 2-9 - Examples of gears; a) Spur Gear, b) Helical Gear, c) Bevel Gear and d) Worm Gear

2.4 Tribology of Bearings

Tribology, the study of friction, wear and lubrication, demonstrates that metallic surfaces are never truly smooth and are instead formed of a number of peaks (known as asperities) and adjacent valleys. Both gears and bearings rely on the relative rolling and/or sliding of two bodies in contact and, when these two bodies are in contact with a force applied, under realistic engineering loads, the asperities which make contact, initially plastically deform, and eventually fail or fracture due to the high stresses involved. Figure 2-10 illustrates the surface roughness of bearing raceway as measured by a Taylor Hobson Talysurf profilometer.

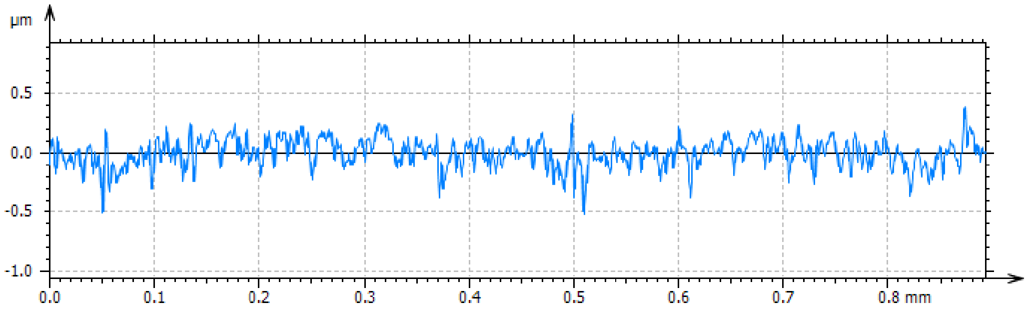

Figure 2-10 - Example of a surface roughness profile as measured by a Taylor Hobson profilometer

To combat excessive wear, lubrication is supplied, commonly in the form of an oil, which forms a film to help separate the two bodies in contact. The oil is drawn into the converging gap between the two bodies and becomes pressurised, forming a thin film (a few microns in thickness) to separate the surfaces. Due to the high contact pressures (1-2 GPa typically), the elastic deformation of the surfaces is significant and further assists in the generation of a viable oil film. This lubrication mechanism is therefore known as elastohydrodynamic lubrication (EHL). The thickness of this film between an idealised, smooth cylindrical roller and a raceway is calculated using the Dowson and Higginson formula, Equation (2),

$$h_{min} = \frac{\alpha^{0.6}(\eta\bar{u})^{0.7}(E')^{0.03}R^{0.43}}{(w')^{0.13}} \tag{2}$$

where α is the viscosity/pressure coefficient of the oil used, $\bar{u}$ is the mean speed of the two bodies within the contact, E' is the relative modulus of elasticity, R is the relative radius of contacting bodies and w' is the load per unit length. The oil viscosity, η, rises exponentially with pressure, and is given by Equation (3), where α is the viscosity/pressure coefficient of the lubricant as follows,

$$\eta = \eta_0 \exp(\alpha p) \tag{3}$$

The Lambda ratio, λ, the relationship between the minimum film thickness and composite surface roughness is calculated by Equation (4),

$$\lambda = \frac{h_{min}}{\sqrt{R_{q1}^2 + R_{q2}^2}} \tag{4}$$

where R_{q1} and R_{q2} are the RMS surface roughness values, R_q, of the two contacting bodies. (Further explanation and determination of the variables used to calculate the minimum film thickness are carried out in the derivation within Section 3.3).

As the value of the minimum film thickness increases, the two bodies are forced away from each other, reducing the asperity contact. Figure 2-11 illustrates the different lubrication regimes present for contacting bodies as well as the associated change in friction, illustrated by the Stribeck curve. For very low Lambda ratios where $\lambda < 1$, commonly referred to as boundary lubrication, there are a significant number of asperities in contact and the friction is very high, with no effective lubricant film able to separate the surfaces. As the fluid film thickness increases, $1 < \lambda < 3$, the lubrication regime is referred to as mixed lubrication and the amount of asperity contact, and hence friction, reduces significantly. Load is carried by both direct asperity contact and by a partial lubricant film. Full film EHL exists when $\lambda > 3$ and it is considered at this point that the fluid film thickness is significant enough to force the two bodies apart resulting in little/no asperity contact. The friction level increases however due to the shearing of the oil within the contact.

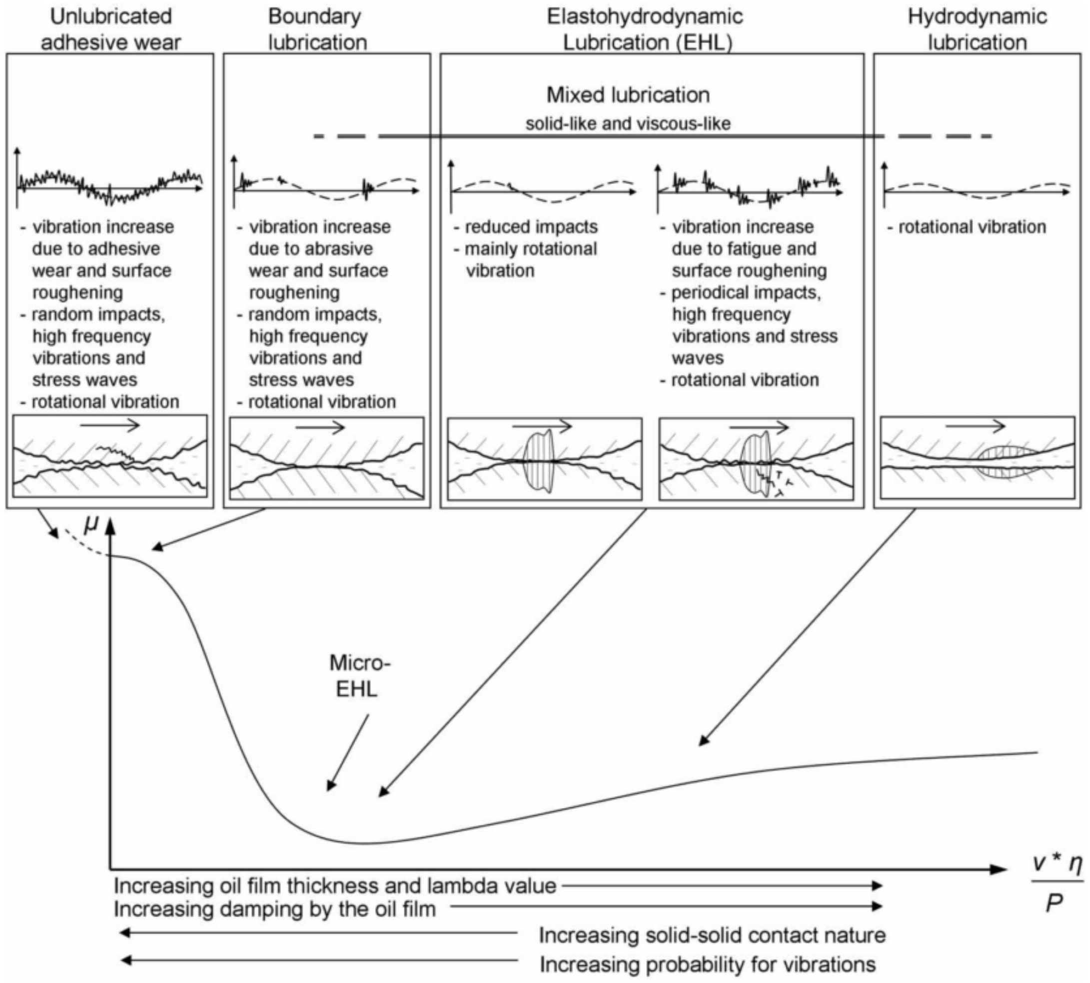

Figure 2-11 - Illustrations of the lubrication regimes present within lubricated contacts and the associated Stribeck Curve - (Halme & Andersson, 2010)

2.4.1 Rolling Contact Fatigue Failure

> *"Failures other than that caused by classical rolling-element fatigue are considered avoidable if the component is properly designed, handled, installed, and not overloaded"*
>
> *- Zaretsky et al. (1996)*

Failure by means of rolling contact fatigue originates through the cyclic loading and plastic deformation below the surface of a material as rollers pass over the raceway within the loaded zone. The plastic deformation occurs at a depth of typical of the maximum shear stress in a Hertzian contact, approximately 0.7 times the contact dimension below the surface. Rolling contact fatigue is characterised by an even distribution of flaking across the loaded region of the race with a conchoidal or ripple pattern (Figure 2-12) (Neale, 1995). Through repeated loading, boundary dislocations and subsurface cracks begin to form and as the cracks reach the surface, material becomes dislodged. This material, if not quickly flushed out with the lubrication, can be over-rolled increasing the stress concentrations at the raceway and hence accelerating the wear process.

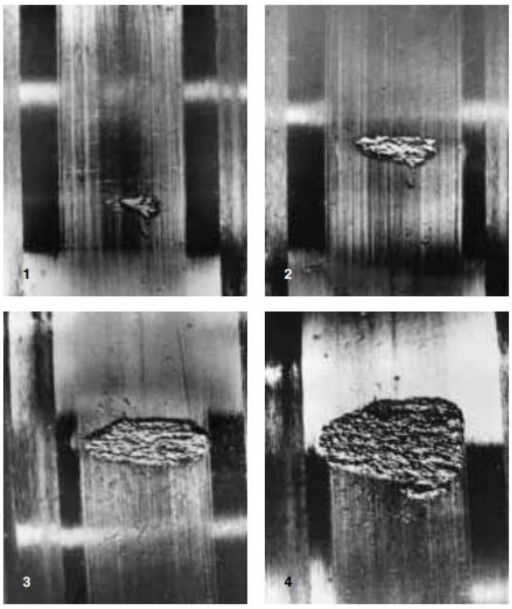

Figure 2-12 - Fatigue Flake Growth - (SKF, 1994)

Based on the statistical analysis of a large data set of natural bearing failures, the work of Lundberg & Palmgren (1947) was used to create ISO 281 (1990) a standard for calculating the dynamic load ratings and rating life of roller bearings. The simplest form of calculating bearing life is the L_{10} life, that is the number of cycles of a bearing rotation (in millions of revolutions) after which 10% of a bearing population would have failed. The L_{10} life is calculated by Equation (5),

$$L_{10} = \left(\frac{C}{P}\right)^n \tag{5}$$

where C is the basic dynamic load rating, P is the equivalent bearing load and n is an exponent with a value of n = 3 for ball bearings and n = 10/3 for roller bearings. Since

1947, there has been extensive research into the effects of lubrication cleanliness, external stresses and material properties and now a modified life modification factor, a_1, is available in ISO 281 (2007). SKF, a world leader in bearing construction, also have the confidence in their products to also provide their own modification factor, a_{skf}, which, like ISO 281 (2007), takes into the lubrication conditions but applies a greater safety factor based on their bearing properties (SKF, 2012a). Therefore, the most up to date life calculation for bearings is Equation (6),

$$L_{10} = a_1 \times a_{skf} \times \left(\frac{C}{P}\right)^n \tag{6}$$

2.4.2 Other Failure modes

Fitch (2003) states that although the L_{10} life determines the number of cycles which 90% of a bearing population will complete without failure, typically only 10% of bearings will reach their L_{10} life. This is mainly due to the conditions under which the bearing is operating and includes:

- Misalignment
- Overloading
- Oil starvation/debris
- Incorrect interferences between raceway and shaft/housing
- Excessive vibration
- Moisture

Figure 2-13 illustrates a selection of bearing failures that are commonly found in industry including flaking, roller cracking, failure of the cage and smearing of the raceway. The effects of inadequate lubrication can be seen in Figure 2-13 a and d. Figure 2-13 a demonstrates an axial crack along the length of the roller which may be caused due to overloading of the bearing or inclusions within the material itself. Some bearings, such as spherical roller bearings and ball bearings, are able to operate effectively in the presence of misalignment due to the conformity between the roller and the raceway. When a bearing is cylindrical roller bearing is subjected to excessive misalignment, the radial load capacity is severely reduced as the load becomes concentrated towards the end of the roller. As this reduces the contact area, the contact pressure increases significantly. White Etching Cracks (WEC) are generally only found in heavily loaded, slow operating bearings such as those found in wind turbine bearings (SKF 2017c). Caused by rolling contact fatigue, WEC appears as small cracks within the bearing microstructure and initiates damage due to manganese sulphide inclusions (Bruce et al. 2015). WEC have only recently been determined as the root cause of failure of a number of wind turbine bearings as the number of wind turbines commissioned worldwide has increased significantly in recent decades.

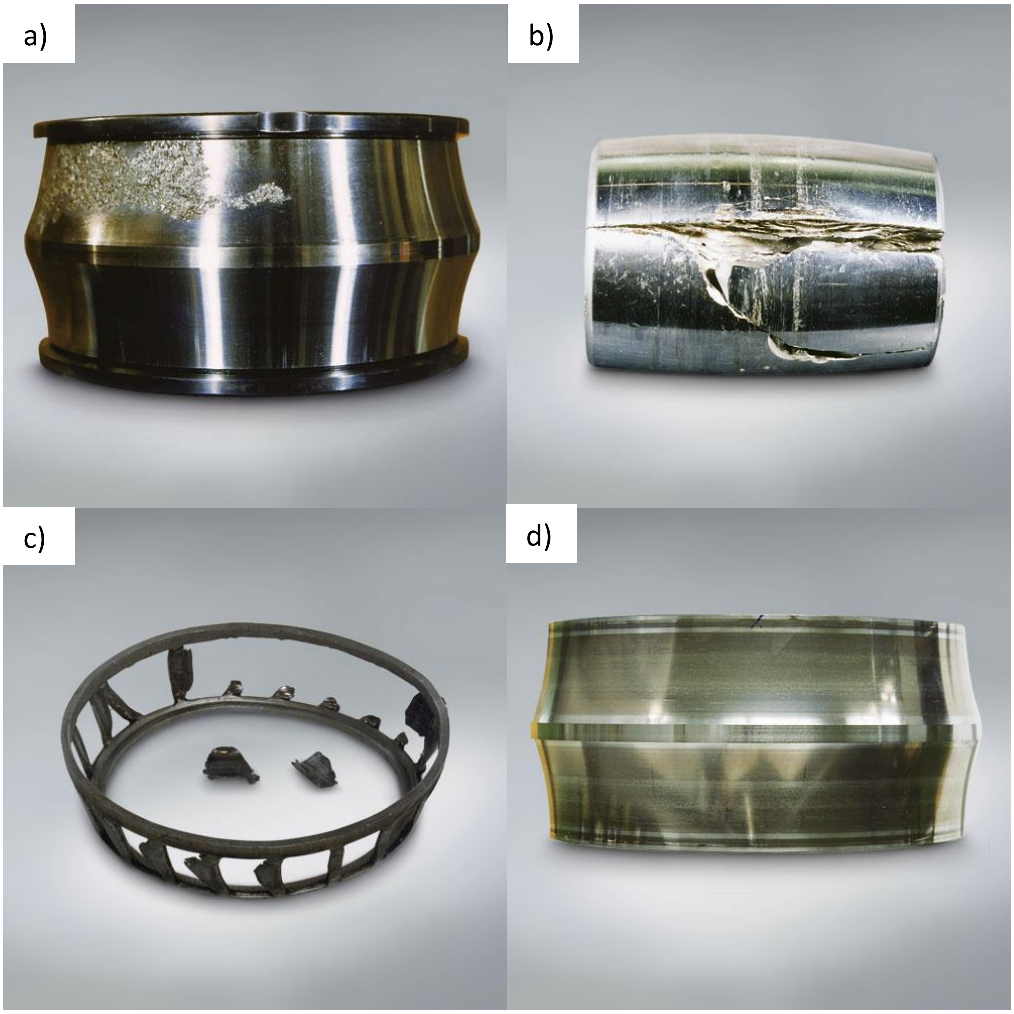

Figure 2-13 - Examples of bearing damage showing a) Flaking of the inner raceway due to poor lubrication, b) Axial cracking of a roller, c) Cage Pillar Failure and d) Smearing due to poor lubrication – Extracted from (NSK, 2009)

2.5 Condition Monitoring of Rotating Machinery

> *"If the forces, stresses and acceleration of bearing components could be measured directly, the task of monitoring the health of the bearing would be quite simple."*
>
> \- (Howard, 1994)

2.5.1 Vibration of Bearings

The use of vibration to detect failures of gears and bearings has owed its success to the ability to detect periodic characteristics related to damage location. For a roller bearing a series of equations, Equations (7)-(10), are available, describing the frequency of the rollers passing over particular points within the bearing (Figure 2-14). Graney & Starry (2012) define these frequencies as:

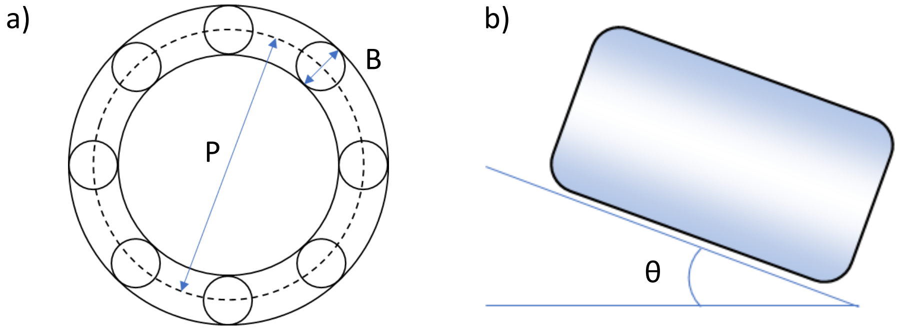

Figure 2-14 - a) Bearing Geometry and b) Angle of Rolling Element relative to raceway

$$BPFI = \frac{N}{2} \times F\left(1 + \frac{B}{P}cos\theta\right) \qquad (7)$$

$$BPFO = \frac{N}{2} \times F\left(1 - \frac{B}{P}cos\theta\right) \qquad (8)$$

$$FTF = \frac{F}{2}\left(1 - \frac{B}{P}cos\theta\right) \qquad (9)$$

$$BSF = \frac{P}{2B} \times F\left(1 - \left(\frac{B}{P}\right)^2 (cos\theta)^2\right) \qquad (10)$$

Where,

BPFI = Ball Pass Frequency Inner Raceway,
BPFO = Ball Pass Frequency Outer Raceway,
FTF = Fundamental Train Frequency,
BSF = Ball Spin Frequency,

B = Ball or Roller Diameter, mm,
P = Pitch Diameter, mm,
N = Number of Rolling Elements,
F = Shaft Speed, Hz,
Θ = Contact Angle, degrees.

Figure 2-15 is extracted from Halme and Andersson (2010) and provides a visual representation of how the characteristic defect signals are produced for a bearing where the inner raceway rotates and the outer raceway is held stationary. For inner race failures, the BPFI represents a roller passing over a defect located on the inner raceway. The amplitude of the vibration increases as the defect located on the inner raceway passes through the loaded region, followed by a decrease as it rotates out. A defect on a fixed outer raceway, where the region of maximum load remains constant, produces an equal amplitude pulse each time a roller passes over the defect, assuming that the defect size does not change. And finally, for a defect located on a rolling element, there are two pulses per revolution of the roller, one when it makes contact with the inner raceway and another when it contacts the outer raceway. Again, there are changes in the amplitude of pulses, with a large difference at the FTF as the damaged roller passes through the heavily loaded region, as well as a less significant change as the roller contacts the inner/outer raceway. This is because the outer raceway is generally closer to the sensor and hence the signal does not attenuate as quickly as the inner raceway.

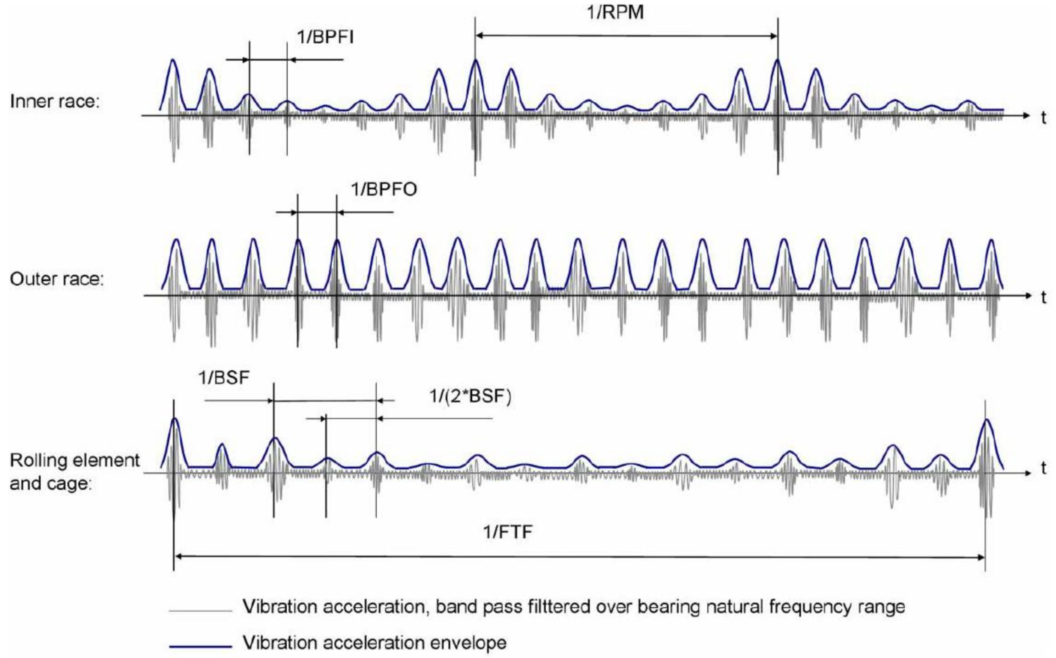

Figure 2-15 - Visualisation of vibrational response for different defect locations - Extracted from (Halme & Andersson, 2010)

2.5.2 Damage Detection Using Vibration

Damage detection using vibration can be relatively straightforward due to its periodic and repeatable nature. Even without sensors and processing equipment, it is possible to place a hand onto the housing of a mechanical system and feel the pulse produced by a defect, knowing naturally that as the vibration becomes more intense the damage is worsening. Accelerometers work in very much the same way and a number of commercially available handsets are available to record and characterise the frequencies and amplitudes of vibrations in mechanical systems (Monavar *et al.,* 2008). Extensive work into the detection of bearing damage through vibration has been carried out over the years and there is a significant body of published work detailing the key findings. Howard (1994) discusses the difficulties when using vibration in an industrial environment, providing a table detailing the difficulty in measuring a variety of machinery (Table 2-2). It is discussed that the difficulty arises when sensors are not able to be placed on top of the bearing housing or where there exist external sources of noise.

Table 2-2 - Degree of Difficulty of bearing fault detection as a function of machine class. (Reproduced from (Howard 1994))

Class of Machine	Degree of Difficulty for Bearing Fault Detection	Machine Type
Easiest	1	Fans, Electric Motors, Generators
Slightly Complicated	2	Compressors, Pumps
Complicated	4	Industrial Gearboxes
Difficult	5	Turbines including Gas Turbine Engines
More Difficult	7	Helicopter Transmissions
Most Difficult	10	Specialised Rotating Machinery with Extreme Noise Environments

The vibration from a single source is attenuated and modulated at every boundary it encounters, additionally changing with each material it encounters. Bearings, particularly those found in transmissions, are also prone to being affected by signals originating from other components (Howard, 1994).

In laboratory based environments where the levels of external noise are limited, and the tests conducted are accelerated and vigorous, authors have been able to successfully detect failures of the inner and outer raceway in addition to the rolling element.

Qiu *et al.* (2003) successfully used vibration to detect bearing damage for a number of life tests on a test rig capable of monitoring four double row tapered roller bearings concurrently. It was demonstrated that increases in the RMS amplitude were able to correctly identify damage due to the failures of the inner race, outer race and rolling element. Figure 2-16 illustrates this whilst also demonstrating the inconsistency of bearing life and failure location as Test 1:Bearing 3 and 4 resulted in an inner race and rolling element failure respectively and Test 3:Bearing 1 and Test 4:Bearing 3 resulted in outer race defects.

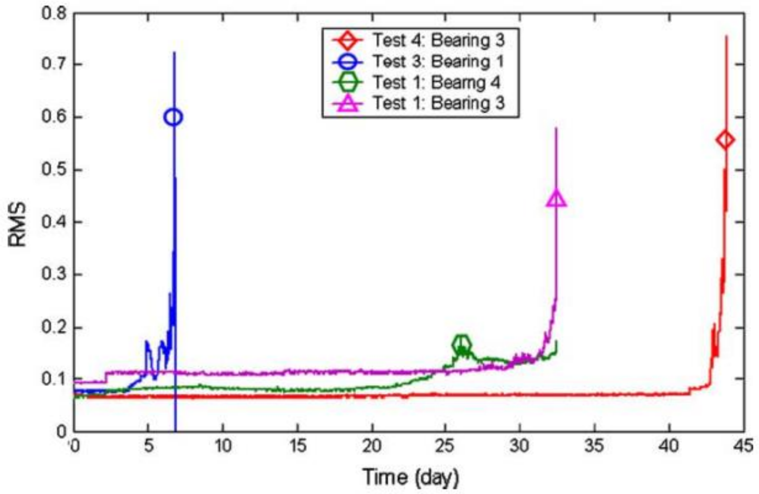

Figure 2-16 - Detection of bearing failures through RMS. Extracted from (Qiu *et al.* 2003)

The authors also demonstrate how a signal from a bearing with an incipient defect fails to clearly show the presence of any of the defect characteristic frequencies but then go on to use an adaptive filter to enhance their visibility, detecting the outer race frequency. Although successful, there was no discussion of the healthy bearing signals and, as a result, it is unknown whether the detection of the outer race frequency was due to the natural frequency as the rollers passed through the region of maximum load, or whether they correspond to surface damage.

Studies outside of the laboratory have also been published with similar success. Orhan *et al.* (2006) studied the vibration levels of a damaged centrifugal pump and fan motor. Both pieces of equipment were operational at the time of being tested and the authors were able to detect pitting of the outer raceway as well as the looseness of a ball bearing via spectral analysis.

Graney and Starry (2012) discuss that as the running surfaces of the bearing begin to deteriorate, the increased friction causes the bearing to skid. This skidding in turn excites the resonances of the bearing and the detection of these frequencies is referred to as the High Frequency Natural Bearing Resonance Indicators (HFNBRIs). These frequencies range from 3-50kHz and are excited through both shock and friction.

Vibration as a whole is highly beneficial as it allows for a relatively rapid, inexpensive means of determining the condition of a mechanical system. However, there are a number of disadvantages to using vibration as a condition monitoring tool.

Small defects on the raceways of large bearings, often operating at low speeds and under a high dynamic force, are unable to produce enough excitation energy in order to excite the bearing housing and hence the accelerometer (Kuboyama, 1986; Kim *et al.,* 2009). McFadden and Smith (1984) determined that although slow speed damage detection through the measurement of high frequency stress waves (AE) is capable, once a bearing exceeds certain speeds, the method becomes too sensitive and instead the bearing defect frequencies now become unwanted noise.

Another disadvantage of using vibrational measurements as a means of condition monitoring is that the damage has already developed onto the bearing surface. Due to the difficulty in extracting small defect signals due to excessive mechanical noise, the time between initial damage detection and bearing failure in industry can be quite short. Although it is possible to determine the bearing damage location via the bearing defect frequencies, it is not possible to detect the growth of subsurface cracks which eventually lead to surface defects. The ability to detect incipient damage allows the repair or replacement of machine components such as bearings before the damage has reached such a level that excessive vibration occurs which can potentially lead to damage being induced in other parts of the machine.

2.5.3 AE of Contacting Bodies

The search for a monitoring technique more sensitive to incipient failures leads to consideration of AE. However, the nature of the AE generated from tribological systems is complex and has been the subject of much research in the literature. When testing static structures, it is possible to link the burst type emission to microscopic subsurface plastic deformation as well as the growth of cracks propagating throughout the structure. The type of emission for rotating machinery however, depends largely on the type of contact under investigation, i.e., sliding and rolling contact.

2.5.3.1 Sliding and Rolling Contacts

The generation of AE from rolling or sliding contacts has been found to depend heavily on the conditions under which those contacts are operating. The contacts within this thesis are operating in the lubricated regime, where the Lambda ratio (the ratio of smooth surface EHL film thickness to composite surface roughness) is used to characterise the extent of surface interaction. As discussed in Section 2.5.1, for Lambda ratios below 1, the contact is generally taken to be operating under a predominantly boundary lubrication regime, where the load is carried by elastic and plastic dry contact of asperities. The contact conditions are such that it is not possible to generate a lubricant film, although tribofilms may exist on the surfaces. As the Lambda ratio increases, between 1 and 3, the regime changes to one of mixed lubrication, where the load is carried by both dry asperity contact and by a partial lubrication film. Where Lambda ratios are higher, the regime becomes elastohydrodynamic, with full lubricant films separating the surfaces and effects due to surface roughness features diminish.

Choudhury and Tandon (2000) concluded that, when testing a rolling element bearing, the increase in AE parameter amplitude with increased rotational speed was due to the increase in dynamic stresses. It has however been shown that for pure sliding contacts, interactions between the surface roughness features (asperities) is the underlying cause of continuous emission (Price *et al.,* 2005; Toutountzakis *et al.,* 2005; Tan and Mba, 2005; Ho and Randall, 2000; Boness *et al.,* 1990; Boness and McBride, 1991). Raja Hamzah and Mba (2009) determine that for a rolling/sliding contact operating under a low Lambda ratio, like those commonly witnessed in gear tooth interactions, AE is produced from the plastic deformation of asperities as they are constantly in contact. It is also demonstrated by Raja Hamzah and Mba (2009) that rolling contact, commonly found in rolling element bearings and at the pitch points of a gear tooth pair contact, is responsible for producing burst type emission at the gear mesh frequency. Comparisons between both spur and helical gears were drawn by Raja Hamzah and Mba (2009) and it was found that, due to the reduction in the amount of rolling contact, the AE produced by helical gears (Figure 2-17) contained less prominent burst-type emission at the gear mesh frequency when compared with the emission of a spur gear pair (Figure 2-18).

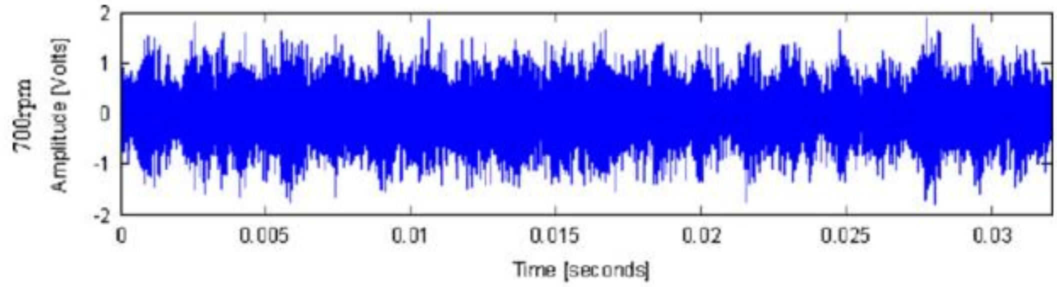

Figure 2-17 - AE produced by helical gears - Extracted from Raja Hamzah & Mba (2009)

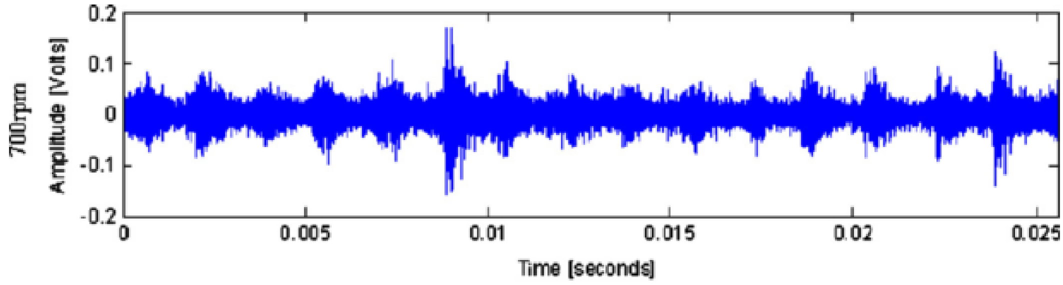

Figure 2-18 - AE produced by spur gears - Extracted from Raja Hamzah & Mba (2009)

Separate studies by Tan and Mba (2005), Novoa & Vicuna (2013) and Vicuña (2014) investigated the possibility of asperity contact causing AE by changing the operating speed, load, oil viscosity and temperature, and hence varying the minimum film thickness, of spur gears in contact. Both found that for low Lambda values, where the lubrication regime was known to be either boundary or mixed lubrication, the amplitude of AE RMS grew as the speed was increased. Although an increase in speed produces a larger oil film thickness, moving the surfaces apart reduces the interaction between surface features. It was concluded that the increased emission was due to the increase in asperity contact rate as the speed was increased. This may be because, although the speed was increased, the film thickness was unable to grow large enough to change the lubrication regime from boundary/mixed lubrication to full film lubrication. It is also discussed by Vicuña (2014) that if the gears are allowed to continue running for a prolonged period of time, the level of AE RMS begins to reduce in amplitude. This is thought to be due to the polishing/running-in effect that asperity contact has on the surfaces, causing the asperities to become smaller or less aggressive and hence reducing the number of contacts.

The AE source mechanism produced by the rolling/sliding contacts of gear teeth is also thought to be the cause of AE within rolling element bearings (Couturier and Mba, 2008). Again, for Lambda ratios lower than 3, it was demonstrated that the AE increases with increasing speed and load. The AE response of bearings operating under a larger Lambda value was not discussed but it was speculated in this study that because there would exist a much lower amount of asperity contact, there will be a reduction in the AE RMS due to asperity interaction once full film conditions are reached.

Both He *et al.* (2009) and Choudhury and Tandon (2000) demonstrate that although the amount of AE produced by a rolling element bearing is highly dependent on the shaft speed, the peak amplitude shows insignificant changes when the load is increased. Raharjo *et al.* (2011) found that for a self-aligning spherical journal bearing, a plain bearing with no rolling elements, the statistical parameters such as RMS, peak amplitude, crest factor and kurtosis increased in amplitude with increased load. This is thought to be due to the increased asperity contact, and hence increased friction, within the sliding contact.

2.5.3.2 AE due to Cracking

Much like the AE produced during the static testing of tensile coupons, research demonstrates that AE is detectable when static tests are carried out on gear teeth and roller bearings. Pullin *et al.* (2012) carried out a static fatigue test on a spur gear pair, cyclically loading a tooth pair between 0.35-2.5kN at 1Hz intervals. An AE sensor placed on the face of the gear was able to detect the AE propagation as the tooth crack grew. Analysis of the frequency spectrum demonstrated broad, low level excitation between 90 – 125kHz but as the crack grew larger, there existed a strong concentration of spectral energy between 110-120kHz. This provided a visual indication of severity and it was thought by the authors that this method may be able to be used in rotating applications to determine information regarding lubrication regimes as well as gear condition. It should be stated however that the frequency content of AE signals is in part a function of the characteristics of the sensor used, making comparisons of frequency content difficult between different researchers.

Lees *et al.* (2011) carried out a static compression test of a ball bearing in an attempt to isolate the AE generated from sub-surface cracking and the emission produced from continuous surface wear when the bearing is in operation. Computational analysis was used to determine the modal frequencies of the ball bearing. It was found that the sub-surface cracking of the ball bearing was amplified at the frequencies associated with the calculated modal frequencies of the rolling element. Although the causes of this were not discussed in detail in this work it was suggested that it occurs because of how the frequency of AE sources is determined. The instant a broadband AE source such as a pencil lead break or a fatigue crack occurs, the signal produced excites all frequencies equally. As the wave-front propagates, it excites the material through which it is travelling and as a result, quickly becomes modulated by the material's natural frequency (Figure 2-19).

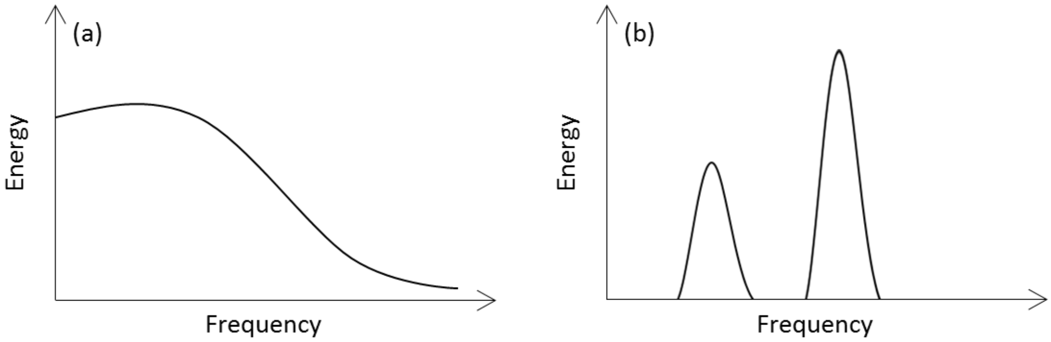

Figure 2-19 - Frequency content of signals (a) at the AE source and (b) away from the AE source

2.5.4 Detection of Damage Using AE

Much like vibration, it has been demonstrated in a number of studies that AE is capable of detecting increases in the characteristic defect frequencies caused when damage is present on a component, whether it be a gear or a bearing (Raja Hamzah & Mba, 2009; Eftekharnejad & Mba, 2009; Toutountzakis *et al.,* 2005; Halme & Andersson, 2010). It can also be seen that, although AE is the detection of high order frequencies, the periodic characteristic defect frequencies are produced by a number of high frequency bursts as the area of contact passes over the discontinuity upon the surface (Figure 2-20). In an attempt to better understand and hence characterise the effects of different damage types, researchers have conducted a number of controlled laboratory based experiments.

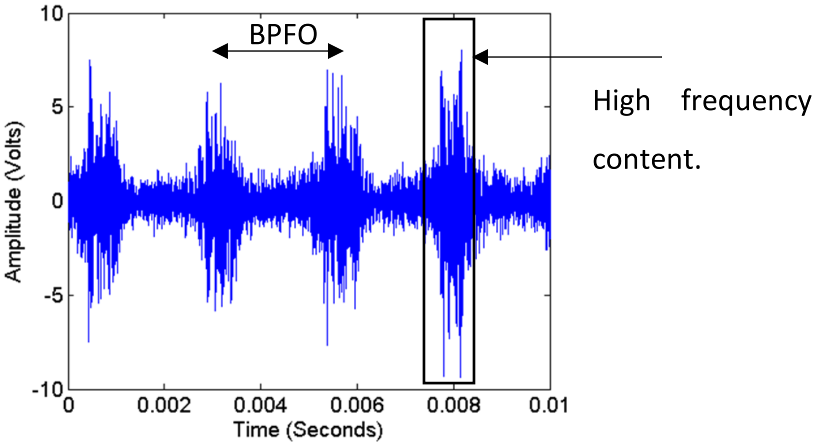

Figure 2-20 - Example of high frequency signal content

2.5.4.1 Seeded Defects

Most research into the detection of bearing defects relies on the data produced when artificial defects are seeded onto the running surface of a gear or bearing. Common methods of producing these defects include engraving and electric discharge machining (EDM). As the defects produced through these methods are superficial, they are not truly representative of natural defects but are able to provide data sets quickly for the application of damage detection techniques. Engraving, as it does not remove material, produces surface defects by forcing material up and out of the hole created thus causing large peaks of material around the circumference of the crater formed. EDM instead removes the excess material and forms a crater with no peaks around the circumference leaving it ‘smooth’. A real defect cannot be truly represented by either of these techniques, particularly given that seeded tests do not accurately capture the AE generated by the growth of naturally occurring defects, only that generated by the interaction of bearing elements with a stable defect.

Tan and Mba (2005) argue that by removing material away from the contact zone the number of asperities now in contact are reduced, and hence the potential for the source of AE is now diminished slightly. It is also discussed that the peaks around the crater of an engraved defect will increase the emission as the protrusions increase stress concentrations, but they expected the emission to return back to a normal level once these protrusions are flattened. Orhan *et al.* (2006), although studying the vibrational response, found that higher vibrational frequencies decreased as the roller bearing 'self-peened', temporarily healing itself.

Al-Ghamd and Mba (2006) compared the response of a 'smooth' surface discontinuity, an oil hole manufactured into the bearing, with a rough defect, a 0.85x0.85mm point defect engraved in the centre of the outer raceway with a 4µm peak height. Although not discussed in detail, and in contrary to the assumptions made by Tan and Mba (2005), the smooth defect produces more AE events when compared to when the bearing was run on the continuous raceway with no surface discontinuities. This is reflected slightly in the RMS plot where increases in RMS amplitude are witnessed. The point defect further increases the number of AE events and these are much more periodic when compared with the smooth defect. Al-Ghamd and Mba (2006) continue to conclude that material protruding above the average surface roughness is likely to cause AE events due to the plastic deformation during the over-rolling of material. It is not discussed however why AE still exists in the presence of a smooth defect although it is thought that it may be due to the relaxing and reloading of the material as it rolls over the hole. Similar responses have been witnessed by other authors when studying engraved defects located on the outer raceway of both ball and roller bearings (Miettinen & Pataniitty, 1999; Li & Li, 1995; Liu *et al.,* 2011; Al-Dossary *et al.,* 2009; Sandoval *et al.,* 2013). Some authors have also tried to produce a correlation between AE parameters and the size of a seeded defect (Al-Ghamd & Mba, 2006).

Choudhury and Tandon (2000) aimed to quantify the effect bearing size, applied load, shaft speed and defect size have on an AE signal. They investigated the number of counts registered over a 2-minute period for each of the changed variables. The bearings under investigation were SKF NJ Series single row cylindrical roller bearings with inner race bore sizes of 15, 20, 25, 30 and 35mm. The initial study focussed on counts to quantify the effect of defect size on the AE signal on both the inner race and the rolling element. A sharp increase of approximately 10,000 counts was seen for both defect locations as the defect width was increased from 0 - 0.5mm. After that, a plateau was observed as the defect increased in size. It is believed that this was due to the entire signal crossing the threshold line, thus the number of counts would not increase unless there was an increase in frequency.

A number of other authors have been able to successfully determine a trend between defect size and the statistical parameters (Badgujar & Patil, 2014; Sandoval *et al.,* 2013; Rao *et al.,* 2013). A distinct correlation between the defect width and statistical parameters including kurtosis, RMS, peak value and ring-down counts was successfully determined by Sandoval *et al.* (2013). All defects studied by Sandoval *et al.* (2013) were applied across the axial length of the bearing but the width was less than 1mm for both inner and outer raceway defects.

He *et al.* (2009) studied 3 and 5mm diameter defects spark eroded onto the outer race of a ball bearing. As well as using standard AE parameters, the frequency spectrum, Short-Time RMS (STRMS) and auto-correlation were used to extrapolate the characteristic defect frequencies also obtained from vibrational analysis as well as details of the frequency response of the sensor as a whole. Under zero load it was difficult to determine the characteristic defects which were detectable under 7kN of applied load. This could be due to looseness within the bearing, reducing the contact stress between the rolling element and the outer race.

Applying a defect across the width of a roller bearing will always increase the AE response as the running path of the whole roller will be affected, changing the loading distribution on other rollers. Similar effects occur when defects are created by EDM on ball bearings. The crater produced, although smooth, allows for the ball to sink into the hole created and it is unknown whether the AE is produced when the ball rolls in or as it is forced to roll out. Therefore, it is necessary to analyse the response of life tests to determine the true response of bearings in the presence of surface discontinuities.

2.5.4.2 Life Tests

Elforjani and Mba (2010) study the natural propagation of surface damage of a thrust ball bearing. The degradation of the bearing is accelerated by replacing one of the grooved raceways with a flat race, increasing the Hertzian contact stresses and hence producing significantly more sub-surface plastic deformation. The bearing ran for a total of 20 hours with wavestreams recorded every 2 hours. Due to the slow speed of the bearing, it was possible for the authors to determine the length of defect by looking at the duration of the AE bursts.

Earlier work by Elforjani and Mba (2009) investigated the bending fatigue failure of a drive shaft rotating at 72rpm. After running for 100 minutes, high amplitude transients began to occur in the raw wavestreams and this is thought to be the early detection of crack growth within the shaft. Further tests produced evidence of AE produced from a rubbing source and this was linked to the visual observation of the crack faces coming together. Unlike the signals witnessed in the testing of gears and bearings with seeded defects, the initial wavestreams demonstrate that the transient AE events occur randomly over the length of the recorded time series. The speed was only 1.2 revolutions per seconds and therefore periodicity between shaft revolutions could not be deduced as the time series was recorded for only a second.

Williams *et al.* (2001) carried out a number of accelerated life tests on both roller and ball bearings by loading each bearing type to 67% and 50% of their dynamic load rating respectively. Both vibration and AE condition monitoring techniques were employed, with significantly more emphasis placed on the use of vibration. This may have been to the hindrance of the AE work in this paper as both the vibration and AE were sampled at 30kHz. The author was using AE sensors with a resonant frequency of 150kHz so, due to Nyquist's theory, the maximum detectable was 15kHz. Regardless, it was found that a naturally propagated inner race defect was detectable through both AE and vibration although the accelerometers increased in RMS amplitude approximately 10 minutes before there was an increase in AE RMS. Although detected through vibration, outer race failures were undetectable through the use of AE which, as this is so readily detectable by many other researchers, is likely to be due to the low sampling frequency used.

The detection of subsurface cracking in bearings is something that has eluded researchers to date. This is mainly due to the focus on signal processing, enhancing the weak signals to try and show early damage as well as the inherent difficulty in such a noisy environment.

2.6 AE Frequency of Wear

As discussed previously, it is believed that the AE produced by the surface interaction of gears and bearings is by means of asperity contact. Research carried out by a number of authors has investigated the generation of AE within tribological systems, simplifying the sliding wear to single pair of surface interactions. Hase *et al.* (2012) carried out an investigation into the generation of AE from a reciprocating wear test rig, with the AE sensor mounted above the pin. Both adhesive and abrasive wear regimes were investigated. The adhesive wear investigation studied the AE produced by the sliding of iron-iron, copper-iron and silver-iron (pin-block) and the abrasive wear investigation studied that produced with an iron pin on emery papers of 400 and 800 grit respectively. The sensor used was a wideband AE sensor with a 0.5-4MHz operating range and was sampled at 100MHz. As a purely frictional experiment with a singular contact, the authors were able to successfully determine a number of frequencies which they believed were excited by frictional sources. Figure 2-21 was produced by Hase *et al.* (2012) and demonstrates not only the frequency range witnessed during his own study but also that of other researchers who have investigated various types of wear.

Ferrer *et al.* (2010) found that sliding friction between two steel surfaces produced AE peaks at 100kHz, with a frequency band of 50-200kHz. Wada & Mizuno (1989) have also shown that mild adhesive wear also excited frequencies within this region. Hao *et al.* (2009) investigated the frequency spectrum of a deep groove ball bearing and it was seen that the raw frequency spectrum of an outer race defect AE signal had distinct peaks at 100, 150 and 180kHz. By analysing the data with a scalogram, reducing the frequency resolution and increasing the time resolution, it was found that the continuous emission occupied the 100kHz frequency band whereas the burst type emission as the ball passed over the defect excited frequencies of 160 and 175kHz.

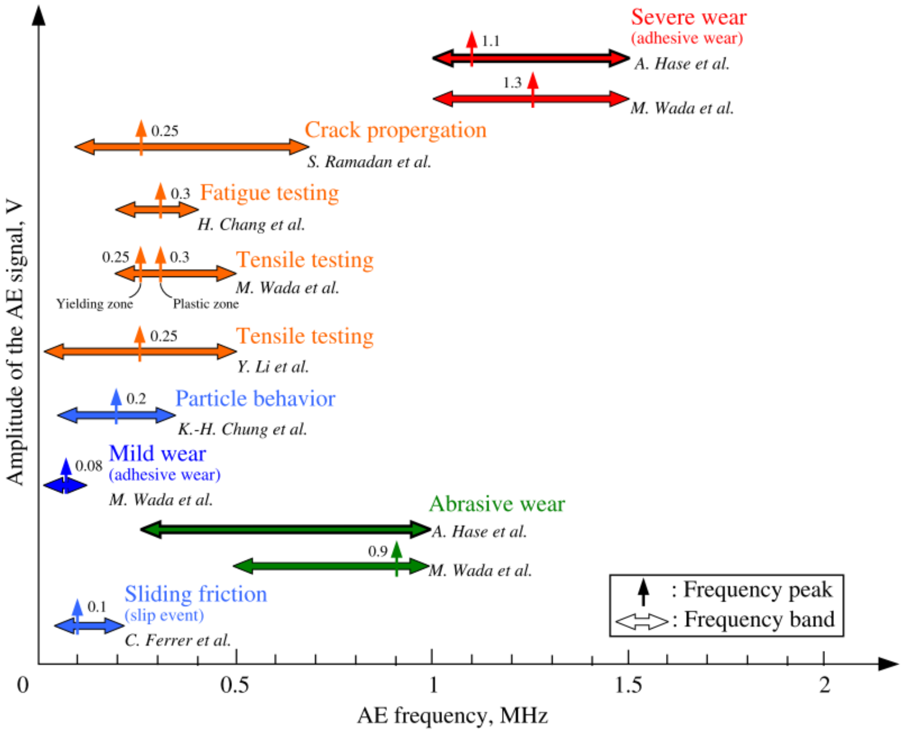

Figure 2-21 - Overview of the frequency bands excited for different sources of AE (Extracted from Hase *et al.* (2012))

2.6.1 Disadvantages of AE

For all of its benefits, AE also has a few limitations and disadvantages which have been well captured by the work of Mba and Rao (2006) who together produced a critical review of the application of AE technology to rotating machinery.

Mba and Rao (2006) discuss that the majority of published works investigating the use of AE as a condition monitoring tool have been carried out on test rigs specifically designed to reduce extraneous noise. As AE is a highly sensitive technique, it is thought that other sources of AE may affect the signal in real world applications. This is particularly apparent when trying to monitor gears because, quite often, the closest mounting point for a sensor is on top of a bearing housing. Therefore, all of the signals would have been modulated by transmission path through the bearing.

Another issue regards the high amount of attenuation faced by AE signals. Although the energy is high when the sensor is placed close to the AE source, as the distance increases, along with a number of boundary crossings, the signal becomes far weaker. Again, this is much more apparent in real world applications where there may be couplings and bearings, affecting the AE transmission.

The set-up of AE sensors also has the ability to jeopardise potential results. Shiroishi *et al.* (1997) states that inner race defects were undetectable via AE and it is thought that this is due to the lack of energy produced by the defects. It is also discussed that sources emitted from an inner raceway failure have further to travel, cross more boundaries and hence may become more quickly attenuated. A possible source of the problem with detecting the inner raceway defects in the manner that Shiroishi *et al.* (1997) tried to, is the way they filtered and demodulated the signal. Although the actual effects of the demodulation were not discussed, it was stated that the data was low-pass filtered at 1kHz. This has effectively removed the high frequency components of each individual burst of energy, meaning it is not possible to further analyse the high frequency components of the defect. This is a problem faced in most of the early work using AE as the signal is treated much like a vibrational signal rather than the full frequency spectrum produced being inspected.

Section 2.5.4 detailed how a number of analysis methods have been researched when post-processing AE signals for the purpose of damage detection. There are many 'hit-based' methodologies available including number of hits, thresholding, ringdown counts, energy, duration etc. but these analysis techniques are better suited to the application of discrete AE, unlike the continuous AE produced from gears and bearings. For the analysis of continuous AE, many authors have investigated the use of adaptive filtering techniques including, but not limited to, the Morlet Wavelet Decomposition and Empirical Mode Decomposition (Huang et al. 1998; Rai & Mohanty 2007; Dybała & Zimroz 2014; Wu & Chen 2006). Although able to demonstrate the ability to extract weak transient bursts from simulated 'noisy' signals, when applied to real signals there is a much larger variation in the accuracy and repeatability of the results. Although there exists potential for these methodologies in well-known sources and signal characteristics, like vibration for example, the application to continuous AE signals is hindered as the components within AE signals from gears and bearings are still not fully understood and require techniques that are readily adaptable (Feng et al. 2013).

2.6.2 Comparisons between Vibration and AE

Rogers (1979) compared the response of vibration and AE for a slow speed bearing and found that vibration was unable to detect any issues because of the lack of energy available to excite the accelerometer. AE however was able to detect the stress waves and hence demonstrate that damage was present.

Liu *et al.* (2011) conclude that AE analysis, when applied to a roller bearing under high rotational speed, is a better tool for detecting gross surface defects when compared with the vibrational analysis of the same defect. Many researchers have combined both vibration and AE detection techniques in the attempt to develop a better understanding of the signals emitted from a damaged bearing. Early work by Shiroishi *et al.* (1997) saw the combination of both vibration and AE whilst conducting experiments on a Timken tapered roller bearing at a speed of 1200rpm. The defect length was maintained at 2.54mm whereas the width was altered between 15.4 - 408.48μm. Each test saw the defect artificially seeded onto the outer raceway via a scribe. Vibrational analysis was able to show a strong correlation between the defect width against Kurtosis, RMS and Peak Amplitude, although the crest factor failed to provide any correlation at all. The spectral analysis of the raw vibrational signal has a large amount of floor noise present. Using the High Frequency Resonance Technique (HFRT) and an Adaptive Line Enhancer (ALE), the floor noise is significantly reduced and the defect frequencies become clearer in the spectral analysis. The AE analysis shows that, due to the burst of energy released as each roller passes over the defect, the spectral analysis is able to provide a much clearer representation of the bearing defect frequencies. However, the AE data presented by Shiroishi *et al.* (1997) has been low-pass filtered at 1kHz.

2.6.3 Frequency Content of AE Signals

AE is generally emitted at frequencies in excess of 100kHz. It is witnessed in multiple early studies that the AE spectrum presented fails to emit above 50kHz. In contrast to this Hao *et al.* (2009) used a PAC R15a sensor and witnessed frequencies of 100, 150 and 180kHz when detecting a 3mm circular defect on the outer raceway. Through the analysis of PAC R15 sensor responses it is seen that the sensor resonance occurs predominantly at 150kHz with a second peak at approximately 175kHz. It is thought that the detection of these frequencies is due to the sensor being excited at its resonant frequency, thus producing a strong signal. The main difference between Hao *et al.* (2009) and the earlier papers is the sampling frequency used. The highest sampling frequency used by the 'low-frequency' detecting papers was 96kHz. Hao *et al.* (2009)

used a 500kHz sampling frequency. Nyquist's theory states that the maximum detectable frequency is half of the sampling frequency. This would give Hao *et al.* (2009) the ability to detect frequencies up to 250kHz and the other authors up to 48kHz. Hao *et al.* (2009) although running a higher sampling frequency, only used grease to lubricate the bearings increasing the emission due to asperity contact as only a very small oil film will be produced, and the viscosity is unlikely to produce EHL between the contacting faces.

2.7 Chapter Summary

It has been shown that there is a significant amount of material surrounding the subject of using AE and vibration to detect damage within rotating machinery. There has been discussion on the effect of the Lambda ratio on the production of AE however the values of Lambda investigated were less than 3 and hence, the lubrication regimes consisted of boundary and mixed lubrication.

The identification of characteristic frequencies within the signal produced has aided the detection and location of defects within bearings however most of these signals have been produced by seeded defects, etched or engraved onto the bearing surface. Having knowledge of where the damage lies prior to analysis being conducted allows the researcher to focus their search, but little work has been done to demonstrate the detection and location of early stage damage that has naturally propagated. In addition to this, the characteristic frequency bursts generally occur at frequencies less than 1kHz, hence the suitability of vibrational transducers. There has however, been little investigation into the frequency content of these bursts in the range at which AE is sensitive (100kHz-1MHz).

3 Equipment and Supporting Materials

3.1 Chapter Overview

Section 2.3.2 introduces the fundamentals of AE as a whole, however this chapter explores the specific hardware and software used to record and process the signals produced by the transient waves demonstrated within this thesis. The chapter is split into two distinct sections, firstly detailing the equipment and software used followed by a section detailing numerical derivations for calculations used later in the thesis. The first section provides a brief overview of the AE and vibration hardware used throughout this study including the sensors and computers used, including a brief discussion on how to use such equipment. The section goes on to discuss the architecture of the software used to acquire the data as well as providing a brief explanation of the analysis codes developed by the author that were used to implement the different analysis techniques efficiently. The second section provides the reader with an in-depth derivation of the methods used to determine the dimensions of the Hertzian contact patch as well as the load distribution and lubricant film thickness at roller/raceway contact.

3.2 AE Hardware

3.2.1 AE Systems

This thesis uses two separate AE systems, a PCI-2 and an Autonomous Condition Monitoring System (ACMS). The PCI-2 system, (Physical Acoustics, 2017a), is an 8-channel AE system, manufactured by Physical Acoustics, and is capable of gathering data at up to 40 MSPS when collecting waveforms but is limited to a maximum of 10 MSPS when wavestreaming over four channels. The system is designed for research use and is versatile in application due to its core software, AEWin. AEWin allows the user to change the data-processing functions carried out internally, quickly plotting the number of hits as well as the energy, duration and rise time of the signals etc. This is useful when carrying out destructive testing within a laboratory environment as the user can tailor the information displayed on the screen in line with the experiment being carried out.

There is also the ability to connect external triggers to the PCI-2 system, allowing the system to be synchronised with load actuators and other NDT devices.

The ACMS system, (Physical Acoustics, 2017b) also manufactured by Physical Acoustics, is an 8 channel AE and vibration system designed specifically for commercial use within a wind turbine farm, where each wind turbine would be fitted with its own ACMS system. Each ACMS system is then connected to a server where the information is handled and processed accordingly. As there is the possibility that a significant amount of data would be produced by a single wind turbine, the system simplifies the data and, rather than allowing a user to plot the data required, instead produces warning signals once a pre-determined threshold is set. As a result, it is not possible to synchronise the data with load actuators or any other NDT system for direct comparison with a laboratory environment. Fortunately, however, the system is able to record and analyse both AE and vibration signals, collected through a Dual Function Sensor (DFS), although not concurrently. Instead, the system cycles between collecting AE hit data, AE wavestreams and vibration wavestreams. Each time a 'hit' occurs, waveforms are recorded on each channel and stored on the internal memory of the system with the '.DTA' file. This is to allow an engineer over-watching the wind farm to remotely access and analyse the data on the ACMS system. Unfortunately, as this system is to be used on test rigs where it is known that continuous emission occurs, the rate at which data is produced quickly exceeds the capacity of the systems internal memory, causing the system to over-write the historic data files including the AE and vibration wavestreams. In order to prevent information becoming deleted when using the system within a laboratory environment, a hard-drive was connected to the ACMS system and wavestreams were automatically transferred daily. The DTA files however were discarded due to their size and the inability to post-process the data contained within the file because of this.

3.2.2 Sensors

There exist a wide variety of AE sensors, with the characteristics of each type of sensor, i.e. resonant frequency, bandwidth and direction of sensitivity, tailored for specific applications. However, despite the characteristics of the sensor, at the core of each sensor there is a piezoelectric crystal that outputs a charge as pressure is applied due to the electric potential created as electrons within the crystal move relative to each other. The size, geometry and crystalline structure of this crystal determines the sensor characteristics and sensitivity. Piezoelectric crystals are commercially available as standalone components however a number of companies secure the crystals within metallic housings to protect the crystal against external forces as well as the surrounding environment. AE waves travel through the surface of the material and therefore it is important that the sensor face is well coupled to the surface, as if air gaps exists between the sensor face and the material, energy is readily absorbed by the air pocket. There exist a wide variety of coupling mediums and often it is down to personal preference and the test environment which determines the coupling medium to be used. If the sensor face is ceramic, then grease, ultrasound gel or silicone is often used to prevent damage to the sensor face. If the face is metallic then superglue is commonly used. It is important to note that when using grease or ultrasound gel, the sensor needs to be held in place with tape or a magnet however both silicone and super glue are able to secure the sensor to the material.

The quality of the bond between the sensor and material is determined by standardised techniques, making pencil lead breaks close to the sensor, commonly known as a Hsu-Nielson source (Hsu & Breckenridge, 1981; ASTM, 2010). The standards determine that the instrument required to perform the pencil lead break is a mechanical pencil, fitted with 0.3-0.5mm diameter 2H lead and equipped with a 'Nielson Shoe'. The shoe is a plastic component attached to the end of the mechanical component, the dimensions of which are determined in Figure 3-1, and is designed to produce a repeatable source by maintaining the angle at which the pencil lead is broken.

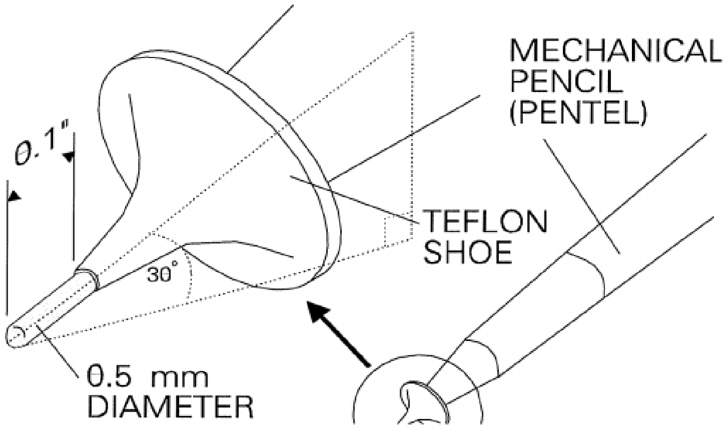

Figure 3-1 - Dimensions of the Hsu-Nieson shoe (Extracted from (Hellier, 2012))

There are two types of AE sensors used within this study. The first is a PAC Nano30 AE sensor (Figure 3-2) and these were selected due to their wide operating bandwidth, small size and availability. Nano30 sensors have a resonant frequency close to 300kHz and a typical calibration chart can be found in Appendix B. Nano30 sensors have ceramic faces and as such it is not possible to use super-glue to secure them to the test rigs under investigation. As the test rigs under investigation in this study are generally oily and operating at elevated temperatures for an extended period of time it was thought that brown lithium grease, a commonly used coupling medium, would melt and run out of the contact reducing the efficacy of the couplant. Therefore, a silicon based engine gasket sealant, Loctite 5910, was selected to secure the sensors to the test rigs. Silicon based sealants are commonly used to bond sensors to structures but the engine gasket was selected as it is designed not to deteriorate when exposed to oil and elevated temperatures for long periods of time. When applying the gasket sealant, both of the surfaces to be bonded were cleaned and degreased and a large blob of silicone was applied to the sensor. A magnet was used to hold the sensor in place for the 24 hours required for the silicone to cure fully.

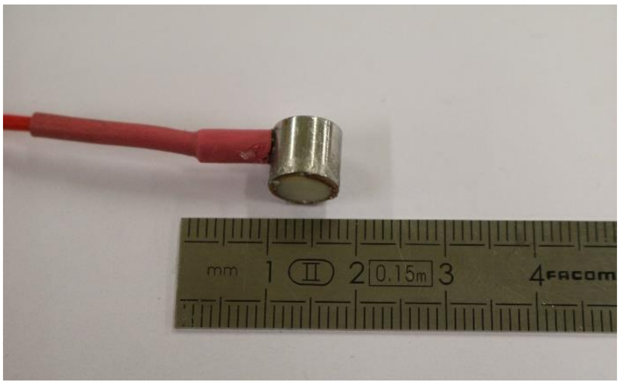

Figure 3-2 - Nano30 Sensor

The second sensor is a Dual Function Sensor (DFS-6000) manufactured by VibraMetrics and is capable of recording both vibration and AE, although not concurrently (Figure 3-3). Unlike traditional AE sensors, whose frequency ranges exist between 20 kHz – 1 MHz, the AE range is only sensitive up to 100kHz with a peak resonance at 30kHz. The vibration sensor produces a flat response between 1 and 10kHz. Example calibration sheets for both types of sensor can be found in Appendix B. The DFS-6000 sensors, as also shown in Figure 3-3, are designed to incorporate a small threaded shank that is used to secure the sensor to the wind turbine when used in the field. For the application of these sensors to the test rigs, threaded bosses were manufactured to allow for the boss to be secured to the test rig using super-glue and the DFS-6000 sensor was screwed into the boss with a smear of lithium grease to act as a couplant.

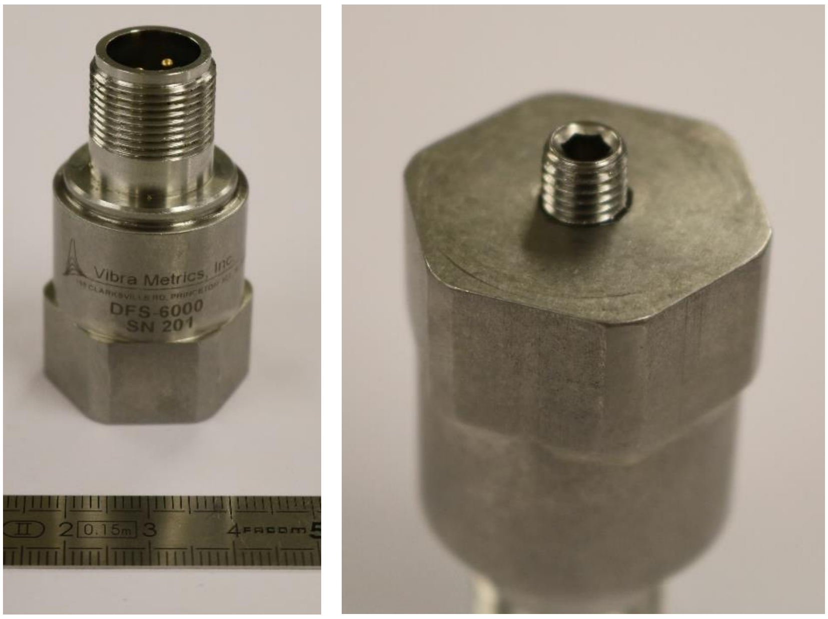

Figure 3-3 - VibraMetrics DFS-6000 sensor

3.2.3 *Amplifiers*

The AE sensor output is often connected to an amplifier before the signal is passed to the AE hardware. The amplifiers are able to apply a gain to the signal of 20, 40 or 60dB as well being able to apply filters to the incoming signals. Figure 3-4 is a typical PAC 20/40/60dB amplifier with an internal 20-1200kHz bandpass filter which is used in the majority of the experimental works herein. The ACMS system has an amplifier built into the internal electronics and is fixed at 40dB.

Figure 3-4 - PAC 2/4/6 Pre-Amplifier with built in bandpass filter of 20-1200kHz

3.2.4 Software

For the experimental work carried out in Chapter 4, a LabView Virtual Instrument (VI) was developed to allow for the acquisition of parametric data, including shaft speed and bearing temperature. The front panel allows for the user to specify the location to save the text file, the rate and length of data acquisition, as well as allowing a user to start and stop the acquisition system as required. As a load cell was not connected to the test rig to measure the applied load, the user is required to manually enter the applied mass in kilograms. Outputs from the data acquisition VI include shaft speed, total number of revolutions, number of data samples recorded, the temperature at each of the bearings and the oil bath as well as outputting a digital trigger to the PCI-2 system to align the parametric data acquisition with wavestream recording.

To increase the efficiency of the post-processing of the data, a number of scripts were developed within Matlab. The scripts were developed to allow the user to apply the analysis to a specific wavestream, or allow for the data to be batch processed, automatically writing image files and saving data sets. The analysis techniques investigated included Raw Signal plotting, RMS, Peak-to-Peak amplitude, Fast Fourier Transforms (FFTs), Binned FFTs and Order Analysis, some of which are briefly explained as follows:

3.2.4.1 FFT

The FFT equation (11) can used to determine the amplitude and phase of a frequency, *k*, within a signal expressed as a complex number, X_k,

$$X_k = \sum_{t=0}^{T-1} x_t \cdot e^{-i2\pi kt/T} \qquad (11)$$

where t is the current time sample, T is the total number of samples and x_t is the value of the signal at time t. Each signal recorded may be decomposed into a number of sinusoidal waves each with different frequencies and amplitudes by performing a Fourier Transform. The Fourier transform fundamentally breaks down the signal to display the amount of energy at each of the frequencies contained. Figure 3-5 illustrates how the FFT is determined where the signal is determined by (12),

$$y = \sin(5x) + \sin(10x) + \sin(20x) + \sin(50x) \qquad (12)$$

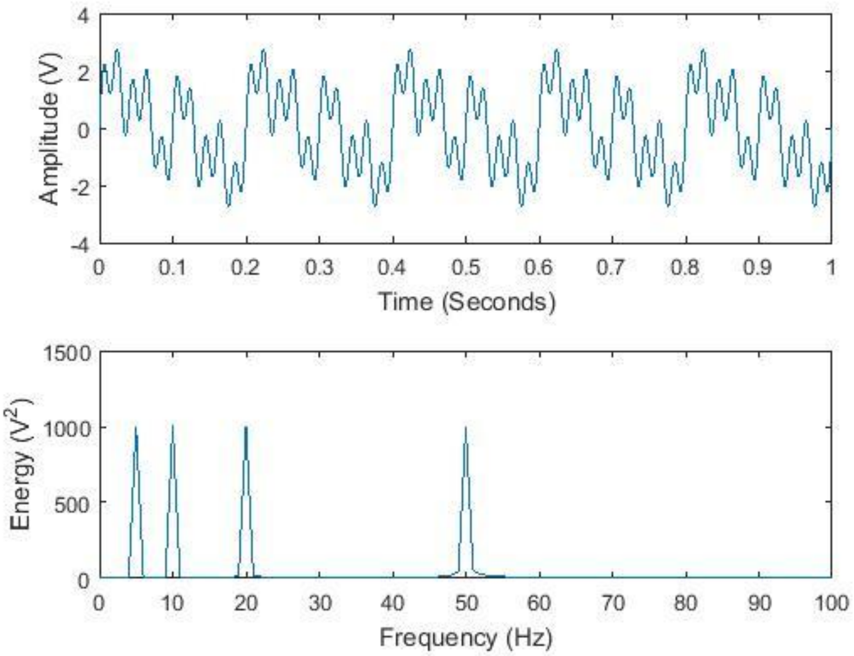

Figure 3-5 - Example of an FFT

3.2.4.2 Order Analysis

Order analysis is very similar to frequency analysis but, instead of plotting the frequency with regards to time (Hz), the frequency is plotted to the rotational frequency of a component. For example, using Figure 3-5 as the base signal again (Equation 12), however it is now known that the shaft is rotating at 5Hz. Plotting the signal with respect to the shaft frequency now demonstrates peaks at 1, 2, 4 and 10 orders demonstrating that for a single rotation of the shaft, pulses occur 1, 2, 4 and 10 times per revolution (Figure 3-6). The benefit of plotting with respect to orders is clear when the speed of the shaft is not constant. Following on from the example above, if the shaft speed is increased, the location of the orders in the frequency spectrum will remain the constant if their signal is dependent on shaft speed, i.e. a gear pair, or will change if the signal is independent of shaft speed i.e. an electric pump operated independently of a driveshaft (Figure 3-7).

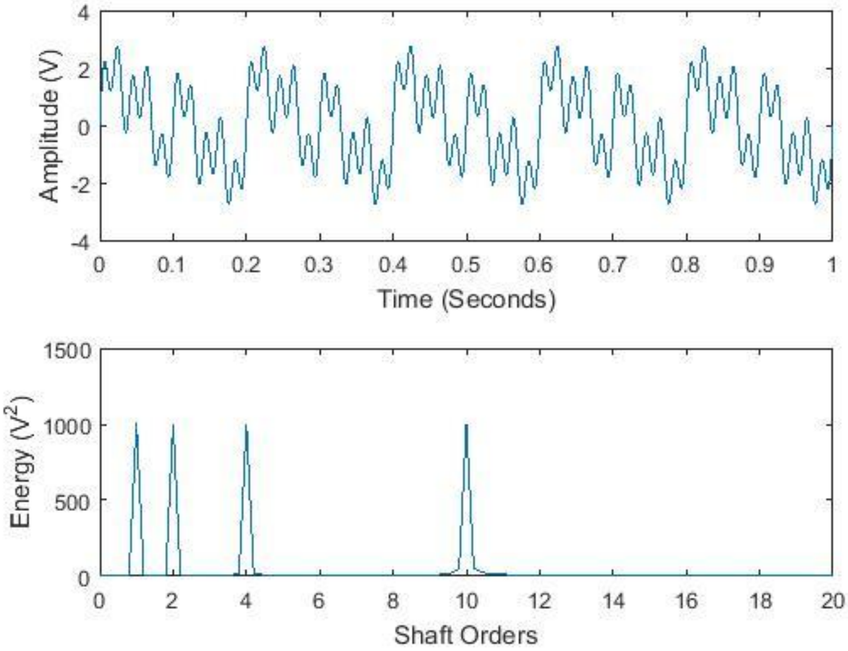

Figure 3-6 - Example of Order Analysis

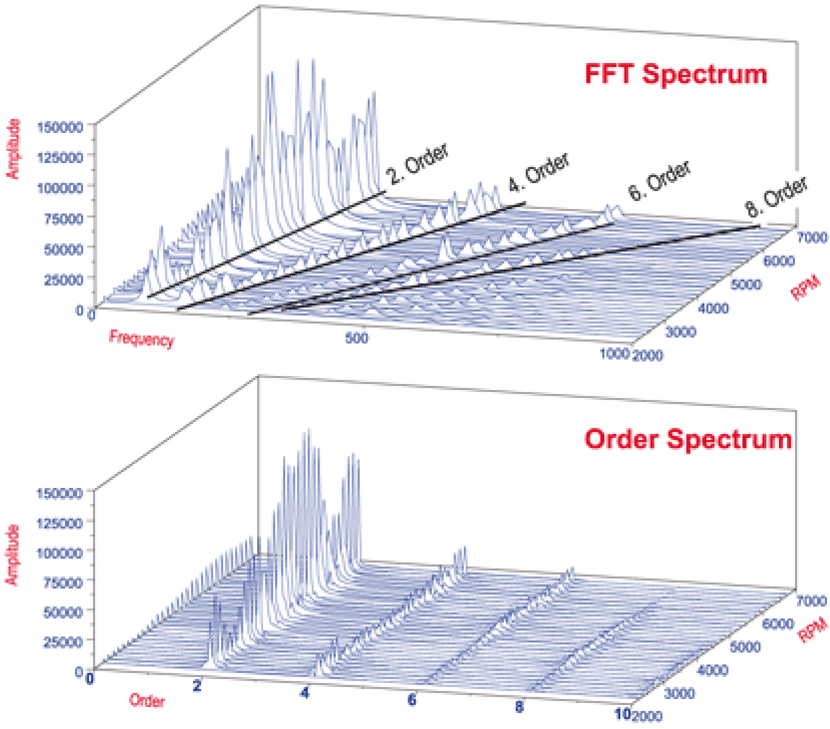

Figure 3-7 - Example of Order Analysis for a speed sweep (Extracted from (National Instruments, 2015))

3.2.4.3 Binned FFT

The binned FFT technique used throughout this thesis builds on the fundamental FFT as described in Section 3.2.5. When plotting the FFTs for a large amount of data, it is difficult to determine trends with such a high frequency resolution. The binned FFT collates the data between bands, generally separated at 1kHz, summing the amplitudes of all data within the 'bin'. The binned FFT is then meshed as a 3D plot and viewed from above to determine trends within the data.

3.3 Calculation of Tribological Conditions Within Bearings

It is important to know, when designing experiments, how variables such as speed, load and temperature affect the tribology of the bearings/gears under investigation so that accurate conclusions can be drawn. It is important that the amount of stress experienced by the both the rollers and raceways is determined prior to testing to ensure that the bearing/gear is not overloaded when trying to establish healthy bearing characteristics. Conversely, it is also important to know the contact stresses under higher loads to allow for accelerated bearing failure. In addition to the contact stress, the Lambda ratio also allows for determination of the extent of the surface separation and the level of asperity contact which may be present, the process of which is documented in Equations 13 - 45.

3.3.1 Hertzian Contact

For two bodies in contact, their combined radius, the relative radius of curvature, *R*, is determined by Equation (13) for a non-conformal contact,

$$\frac{1}{R} = \frac{1}{R_1} + \frac{1}{R_2} \tag{13}$$

and Equation (14) for a conformal contact,

$$\frac{1}{R} = \frac{1}{R_1} - \frac{1}{R_2} \tag{14}$$

where R_1 and R_2 are the radius of the body in a single axis (Figure 3-8). The relative radius of curvature is calculated for both the x and y axis, and as such determines the shape of the contact. For $R_x = R_y$ the contact is circular, $R_x \neq R_y$ the contact is elliptical and if either R_x or R_y are infinite, the contact is rectangular.

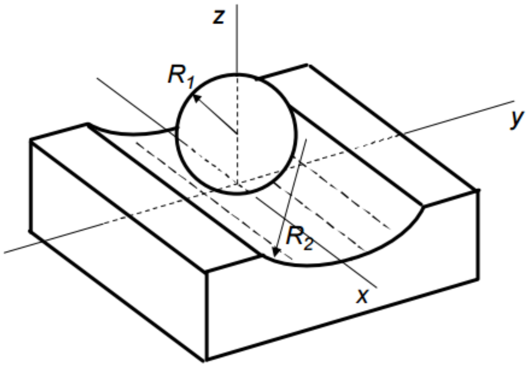

Figure 3-8 - Illustration to define Relative Radius of Curvature – Extracted from Evans (2013)

Hertz determined that for a line contact, the average contact pressure, p_m, over the contact region between two bodies, is a function of the Youngs' Modulus, E, Poissons ratio, ν, the deflection, δ, and semi-contact width, b, such that

$$p_m \propto \frac{E_n}{1-\upsilon_n^2}\frac{\delta_n}{b} \tag{15}$$

and therefore,

$$\delta_n \propto \frac{E_n}{1-\upsilon_n^2}\frac{p_m}{b} \tag{16}$$

As the pressure acts between two surfaces it is possible to say that

$$\delta_1+\delta_2 \propto \frac{E_1}{1-\upsilon_1^2}\frac{p_m}{b}+\frac{E_2}{1-\upsilon_2^2}\frac{p_m}{b} \tag{17}$$

also

$$\delta_1+\delta_2 = \frac{b^2}{2R_1}+\frac{b^2}{2R_1} \tag{18}$$

Therefore,

$$\left\{\frac{1-\upsilon_1^2}{E_1}+\frac{1-\upsilon_2^2}{E_2}\right\}p_m \propto \left\{\frac{1}{R_1}+\frac{1}{R_2}\right\}a \tag{19}$$

For simplicity, the right-hand side of Equation 16 can be simplified to produce a relative elastic modulus of the two bodies, E', such that,

$$\frac{2}{E'} = \frac{1 - v_1^2}{E_1} + \frac{1 - v_2^2}{E_2} \tag{20}$$

Therefore,

$$\frac{p_m}{E'} \propto \frac{b}{R} \tag{21}$$

Detailed Hertzian analysis determines that

$$b = \sqrt{\frac{8Rw'}{\pi E'}} \tag{22}$$

and,

$$p_m = \sqrt{\frac{\pi E' w'}{32R}} \tag{23}$$

As shown in Figure 3-9, the pressure varies semi-elliptically over the contact-width, *2b*, and the maximum pressure, *p₀*, is calculated as

$$p_0 = \frac{2w'}{\pi b} \tag{24}$$

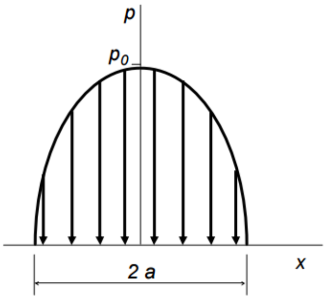

Figure 3-9 - Pressure distribution over contact width of *2a* – Extracted from Evans (2013)

3.3.2 *Load Distribution*

Equation (23) determines the maximum Hertzian contact pressure of a single contact, but within a rolling element bearing the load is distributed amongst a number of rollers, with the exact number determined by the bearings radial clearance (Figure 3-10). To determine the individual roller loads on each rolling elements within the bearing and hence the maximum roller load, the method of Harris & Kotzalas (2006) was used. This technique is complex but yields details information of the load distribution within the bearing.

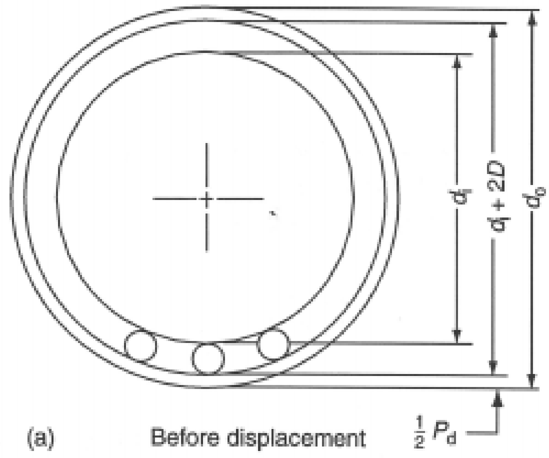

(a) Before displacement

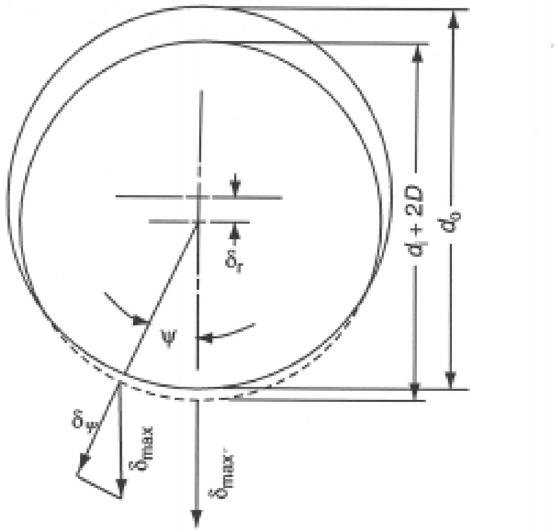

(b) After radial displacement

Figure 3-10 - Schematic demonstrating how the load distribution is calculated. Extracted from (Harris & Kotzalas 2006)

For a cylindrical rolling element under a pure radial load, *Q*, the load experienced at the inner raceway, Q_i, is equal to the load experienced by the outer raceway, Q_o, i.e.

$$Q = Q_i = Q_o \tag{25}$$

For a simple elastic contact between two bodies, the elastic deformation at the contact, δ, is proportional to the load, *Q*,

$$\delta \sim Q^n \tag{26}$$

where n=3/2 for ball bearings and n=10/9 for roller bearings. Therefore, it can be said that,

$$Q = K\delta^{n} \tag{27}$$

Where K_n is the load deflection factor.

The total deflection, δ_n, of two bearing raceways under load and separated by a rolling element can be expressed as,

$$\delta_n = \delta_i + \delta_o \tag{28}$$

where δ_i and δ_o are the defections between the roller and the inner raceway and outer raceway respectively.

Therefore,

$$K_n = \left[\frac{1}{(1/K_i)^{1/n} + (1/K_o)^{1/n}}\right]^{n} \tag{29}$$

and

$$Q = K_n\delta^{n} \tag{30}$$

When taking the contact geometry for a roller-raceway line contact into consideration,

$$K_p = 2.15 \times 10^{5}\Sigma\rho^{0.5}(\delta^{*})^{-1.5} \tag{31}$$

where $\Sigma\rho$ is a parameter relating to the contact geometry and δ^{*} is a non-dimensional deflection. Therefore, for a steel roller-steel raceway line contact,

$$K = 8.06 \times 10^{4} l^{8/9} \tag{32}$$

For a cylindrical roller bearing the radial load is distributed over a number of rollers and the radial deflection at each of the roller locations, δ_{φ}, can be calculated by,

$$\delta_{\varphi} = \delta_r \cos\varphi - \frac{1}{2}P_d \tag{33}$$

Where δ_r is the radial ring shift at $\psi = 0$ and P_d is the diametrical clearance. Rearranging Equation (33) in terms of maximum deflection,

$$\delta_{\varphi} = \delta_{max}\left[1 - \frac{1}{2\varepsilon}(1 - \cos\varphi)\right] \tag{34}$$

where,

$$\varepsilon = \frac{1}{2}\left(1 - \frac{P_d}{2\delta_r}\right) \tag{35}$$

The overall angle of the load distribution is determined by the diametrical clearance and re-arranging Equation (35),

$$\varphi_l = cos^{-1}\left(\frac{P_d}{2\delta_r}\right) \tag{36}$$

From Equation (27) the ratio between the angular load, Q_φ, and maximum load, Q_{max}, is equal to the angular deflection, δ_φ, and maximum deflection, δ_{max},

$$\frac{Q_\varphi}{Q_{max}} = \left(\frac{\delta_\varphi}{\delta_{max}}\right)^n \tag{37}$$

and therefore, substituting Equation (34) into Equation (37),

$$Q_\varphi = Q_{max}\left[1 - \frac{1}{2\varepsilon}(1 - \cos\varphi)\right]^n \tag{38}$$

For static equilibrium, the sum of the vertical loads at each of the rollers must be equal to the total applied load,

$$F_r = \sum_{\varphi=0}^{\varphi=\pm\varphi_l} Q_\varphi \cos\varphi \tag{39}$$

or

$$F_r = Q_{max} \sum_{\varphi=0}^{\varphi=\pm\varphi_l} \left[1 - \frac{1}{2\varepsilon}(1 - \cos\varphi)\right]^n \cos\varphi \tag{40}$$

Equation (40) can be written as an integral such that,

$$F_r = ZQ_{max} \times \frac{1}{2\pi}\int_{-\varphi_l}^{+\varphi_l} \left[1 - \frac{1}{2\varepsilon}(1 - \cos\varphi)\right]^n \cos\varphi \, d\varphi \tag{41}$$

or

$$F_r = NQ_{max}J_r(\varepsilon) \tag{42}$$

where

$$J_r(\varepsilon) = \frac{1}{2\pi}\int_{-\varphi_l}^{+\varphi_l} \left[1 - \frac{1}{2\varepsilon}(1 - \cos\varphi)\right]^n \cos\varphi \, d\varphi \tag{43}$$

and N is the number of rollers. From Equation (30) it is known that,

$$Q_{max} = K_n\delta_{\varphi=0}^n = K_n(\delta_r - \frac{1}{2}P_d)^n \tag{44}$$

and therefore

$$F_r = NK_n \left(\delta_r - \frac{1}{2} P_d\right)^n J_r(\varepsilon) \tag{45}$$

For a bearing under pure radial load, where the number of rollers and the inner race diameter are known, it is possible to calculate the load distribution integral, $J_r(\varepsilon)$. To estimate the first value of ε, a radial deflection, δ_r, is assumed and used to solve Equation (35). This value of ε is then used to solve Equation (45) and if Equation (45) fails to balance, the process is repeated through an iterative process until Equation (45) is balanced. Figure 3-11 illustrates an example of the load distribution integral, $J_r(\varepsilon)$, as calculated for a cylindrical roller bearing. Due to the nature of this calculation, a computational code was written to perform the calculations for the bearings used within this thesis (Appendix A).

The code outputs the maximum roller load as well as the load on each of the rollers in contact. The maximum roller load is used to calculate the maximum contact pressure, as described in Section 3.3.1, as well as within the Dowson-Higginson formula when determining the minimum fluid film thickness, as outlined in Section 2.4.1. The fluid film thickness is then used in combination with the RMS surface roughness to determine the lubrication regime which the bearing is operating in.

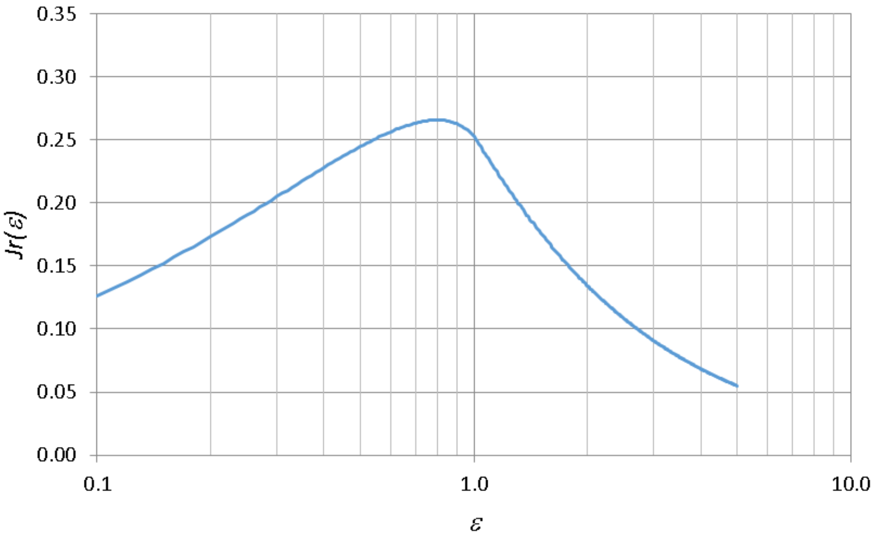

Figure 3-11 - Load distribution integral for a cylindrical roller bearing

4 AE Response of High Speed Bearings

4.1 Introduction

4.1.1 Chapter Overview

This chapter aims to determine the signals produced by both AE and vibration sensors when a roller bearing is operating at speeds ranging from 600-5980rpm. The chapter is divided into five main sections where the first section, Section 4.2, describes the design of the test rig before Section 4.3 describes the data acquisition hardware used and the experimental set-up as a whole.

Section 4.4 uses the data collected from a healthy bearing to investigate the effect of speed and load on data analysis techniques. This includes both statistical parameters such as the RMS, Peak to Peak amplitude and Kurtosis, as well as analysis in the frequency domain, comprising of High Order Frequency analysis and use of the signals Order Spectrum.

Section 4.5 discusses the sensitivity and repeatability of both AE and vibration hardware, and determines how reliant each method is on the test set-up.

Section 4.6 investigates the sensitivity of AE to artificial defects applied to the outer raceway of a test bearing. Simple analysis methods are used to demonstrate that the signal is influenced by artificial defects and weak signal extraction methods are explored to improve the detectability and identification of small defects.

The final sections, Section 4.7 - 4.9, go on to investigate the AE and vibrational response of a number of different bearings which were caused to fail naturally, albeit at an accelerated pace. The first life test investigates the failure of a heavily loaded, misaligned bearing that failed within 12 hours, and hence is classified as being rather aggressive. The second life test was carried out over an extended period of time, in excess of 5 months, and as such the bearing failed in a more controlled manner. The analysis of the life test data is compared to the seeded defects and demonstrates a large difference between natural and artificial bearing defects.

Section 4.10 then draws the main conclusions for the chapter.

The data collected in all of the sections, with exception for Section 4.6, has been collected using a PCI-2 AE System as well as the ACMS System. Section 4.6 however relied solely on the use of a PCI-2 AE System due to system availability.

4.1.2 Aims and Objectives

The experiments conducted in the following chapter aim to:

- Better understand the characteristics of continuous AE signals and determine the independent influences of both speed and load as well as the Lambda ratio.
- Demonstrate the difficulties in characterising bearings for use with AE condition monitoring and the reliance of AE on test set-up.
- Determine the effect on the AE signal when a series of artificial defects are applied to the outer raceway of a bearing and investigate the use of weak signal extraction methods to improve defect detectability.
- Monitor the natural damage propagation in roller bearings when subjected to accelerated life tests to compare the response of AE and vibration and determine the possibility of detecting the onset and propagation of raceway/roller damage.
- Demonstrate the key similarities/differences in analysis when detecting natural bearing damage and artificial bearing damage.
- Determine similarities and differences in using both AE and vibration techniques.

4.2 Experimental Design

4.2.1 Rig Design

As discussed within the literature review, Chapter 2, the majority of the test rigs designed and operated by other researchers to generate roller bearing data all share a similar design, an over-slung test bearing with two support bearings to the left of the test bearing. This design is popular as it allows for the bearing under investigation to be removed from the shaft for inspection, without the need to remove the support bearings. It also allows the test bearing to be of a smaller bore diameter (and hence more likely to fail) than the support bearings. This set-up however, places a greater radial load on the support bearing closest to the test bearing thus increasing the chances of causing damage to the wrong bearing.

For this research, the bearing test rig was designed with the test bearing placed in between two support bearings (Figure 4-1 and Figure 4-2). A radial load was applied to the test bearing via a loading arm, such that the load in each of the support bearings is half of that applied to the test bearing. Such an arrangement increases the likelihood that any natural bearing degradation occurs solely in the test bearing.

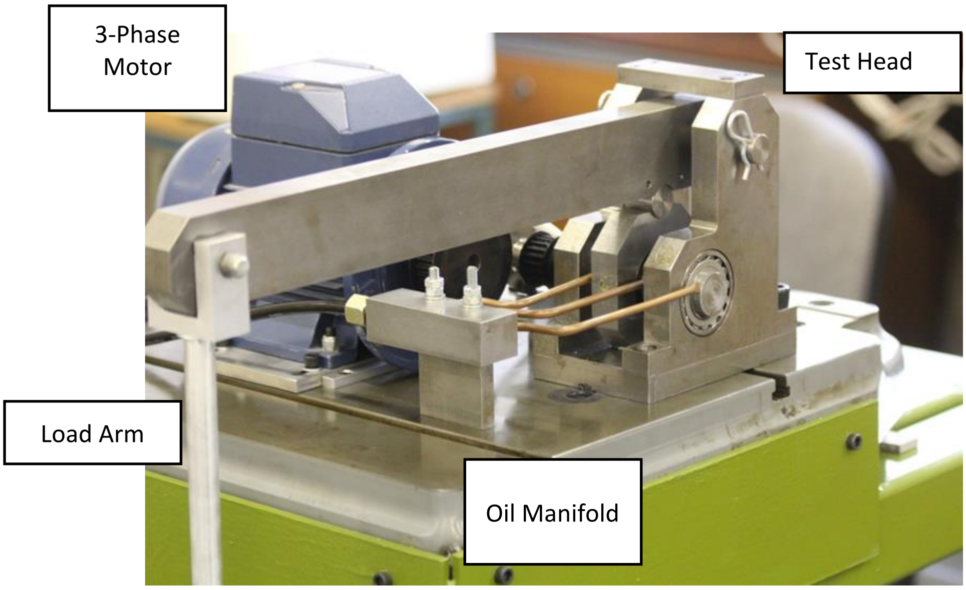

Figure 4-1 - Test Rig Overview

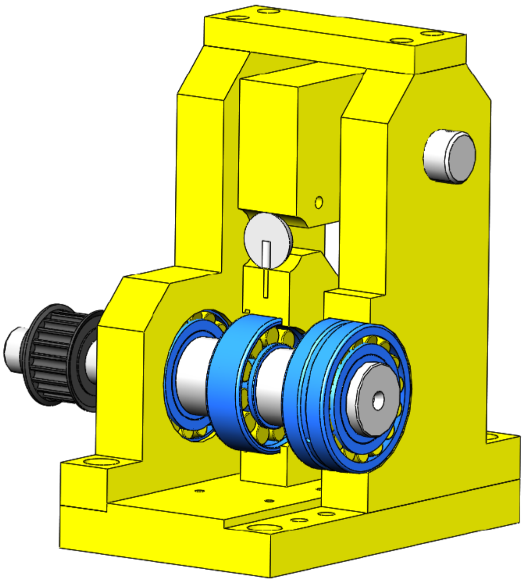

Figure 4-2 - High speed bearing test head schematic.

The load arm itself acts as a 10:1 lever arm, mechanically increasing the applied load from the masses used. Initially, the load was transmitted from the lever arm to the test bearing via a cylindrical roller spanning the length of the test bearing housing. This was installed to introduce misalignment within the test bearing, causing the load to become more concentrated on a localised region within the test bearing. To ensure that misalignment was minimised during the characterisation of healthy bearings, a 20mm ball bearing was placed between the load arm and the test bearing changing the contact from a line contact to a point contact. A constraining rail was placed either side of the test bearing housing to prevent axial movement.

The test bearing, an SKF N204ECP single row roller bearing, was selected due to the design of the outer raceway. As the bearing is of ‘N’ specification, the inner raceway encloses the roller/cage assembly whereas the design of the outer raceway allows the roller/cage assembly to be removed from within the outer race (Figure 4-3). Being able to remove the inner race and rollers from within the outer race allows for the bearing to be separated into its individual components without damaging the bearing. This is particularly advantageous when it comes to applying seeded defects onto the raceway, as well as being able to inspect the surface of the outer raceway of the bearing following an experiment.

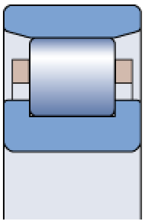

Figure 4-3 - Cross-sectional view of a cylindrical roller bearing of 'N' type specification - (SKF, 2016)

Unlike the test bearing, the support bearings do not need to be disassembled as their primary function is to react the load applied to the test bearing. To decrease the possibility of the support bearings degrading naturally, SKF 22205/20 E bearings were selected. These bearings are double row spherical roller bearings and due to the increased number of rollers, and hence improved contact geometry, they exhibit a much higher dynamic load rating, and hence higher L_{10} life, when compared to the test bearings (Table 4-1). In addition to the increased load capability, the design of the support bearings allows them to compensate for any small misalignments or shaft bending. SKF bearings were selected for the majority of the experimental work discussed due to their reputation of providing high quality, repeatable and reliable bearings.

Table 4-1 - Geometry and load rating of the test and support bearings

		N 204 ECP	22205/20 E
Number of Rollers	N	11	30
Roller Diameter (mm)	B	7.5	6.72
Roller Length (mm)	L	8.33	6.6
Inner Race Diameter (mm)	d_i	26.5	31.3
Diametrical Clearance (mm)	P_d	0.045	0.045
Dynamic Load Rating (kN)	C	28.5	49.9
Static Load Rating (kN)	C_0	22	44
Fatigue Load Rating (kN)	P_u	2.7	4.7

Each bearing was lubricated with mineral oil matching the specification of OEP-80. The oil was heated to 50˚C within the oil sump from where it is pumped to a central manifold and then distributed between individual oil jets, aimed at each of the bearings in the region of maximum load. The oil pick-up contains a strainer, removing any large foreign debris from the oil prior to it being passed through an inline oil filter with a 140-L-101H element with an absolute micron rating of 6µm. When the bearings are running under test conditions, the frictional energy dissipated within the bearing causes the raceways to heat up, hence increasing the oil temperature. To prevent the oil becoming too hot, a water-cooled heat exchanger was incorporated into the oil system, ensuring that the oil bath temperature remained stable at 50˚C.

The drive shaft, the drawings of which can be found in Appendix C, was manufactured from EN40B steel which was nitride hardened to 750-900 Vickers (62-68 Rockwell C) to a depth of 0.25mm to help ensure that it would last throughout the bearing life tests without itself becoming damaged through fatigue. The mounting faces for the bearings were ground to allow for a normal fit using tolerances based on SKF recommendations, allowing the bearings to be pressed on and removed without affecting the radial clearance within the bearing. An SKF KM4 self-locking lock nut was placed at the end of the shaft to secure the shaft relative to the bearings. The drive shaft was driven via an inverter driven 0.75kW, 2-pole, 3 phase motor with a maximum output speed of 2985rpm. To reach the bearing speeds required, the motor was coupled to the drive shaft via a pair of timing pulleys with a ratio of 1:2, increasing the maximum speed to 5980rpm. The speed itself was monitored using an optical light gate sensor combined with a trigger disc where the digital output is wired to a data acquisition system where digital signal analysis counts the number of pulses received over a period of time, thus calculating the shaft RPM.

4.2.2 Data Acquisition

It is important to keep an accurate record of the speed, load, number of rotations and temperature throughout the duration of each test. To determine both the speed and the number of rotations completed, a slotted disk, mounted at the end of the shaft, was used in conjunction with an optical light gate sensor to create a digital pulse. The bearing housings were drilled to allow for K-type thermocouples to be applied to the outer race of the bearing. These thermocouples were connected to OMEGA thermocouple amplifiers which produced a +/- 10V output. Each of the signals produced was connected to a National Instruments data acquisition module, USB-6008. The USB-6008 module is used to input data into a VI produced in National Instruments LabView.

The VI front panel, as shown in Figure 4-4, allows the user to determine the interval at which data will be logged.

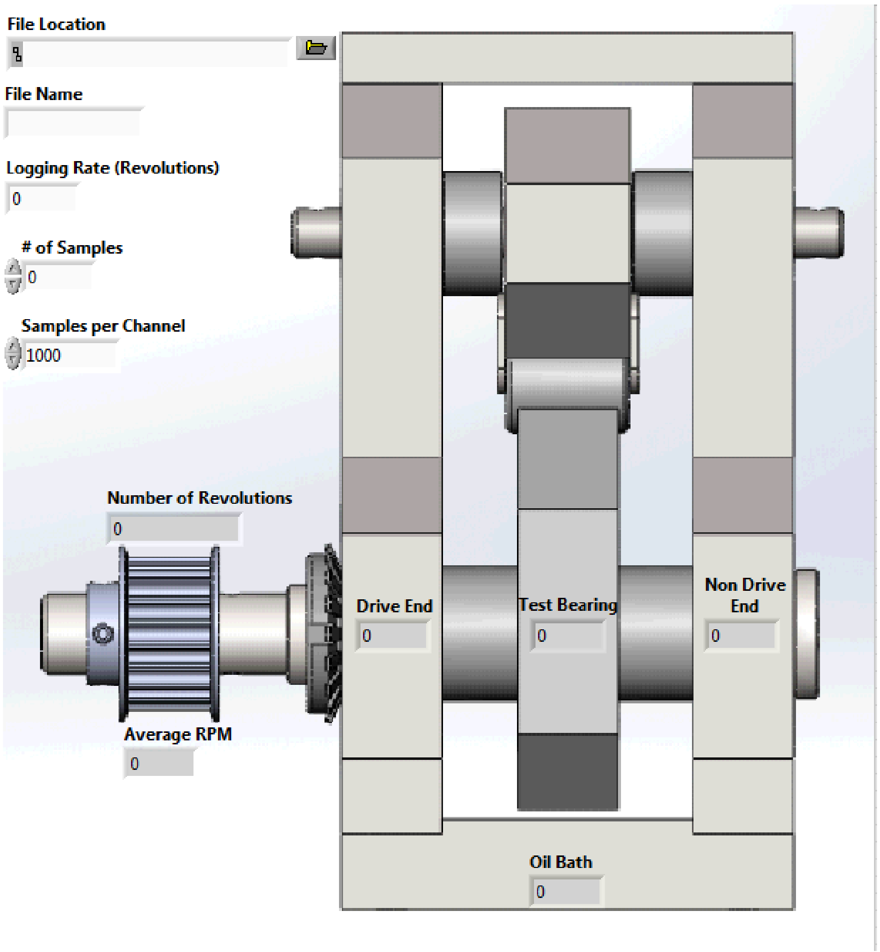
File Location

File Name

Logging Rate (Revolutions) 0

# of Samples 0

Samples per Channel 1000

Number of Revolutions 0

Average RPM 0

Drive End 0

Test Bearing 0

Non Drive End 0

Oil Bath 0

Figure 4-4 - LabView VI designed for use with the high-speed test rig.

To prevent the loss of any data, the VI is designed to open/create a text file, write the data to the text file by appending to the previous file, and then close the text file. As well as logging data, the VI is also able to trigger the PCI-2 AE system to record wavestreams at user defined intervals through a digital output on the USB DAQ. As it has been designed for use on an active wind turbine farm however, the ACMS system is designed to record wavestreams at pre-set time intervals rather than relying on an external trigger. As a result, there is a slight difference in the time that the data is collected between each system.

4.2.3 Bearing Operating Conditions – Load, Contact Dimensions and Film Thickness

As there are a number of variables possible when conducting a dynamic test, a number of factors were taken into consideration when designing the experiments to be conducted. These factors include: speed increments, load increments, increment duration, test duration, oil temperature and condition of the bearing. Initial experiments investigated the AE response of healthy bearings and, as such, it was important that the bearings loads were below the fatigue stress limit of the bearing, determined as 1500MPa by the ISO 281 Standard (2007), hence reducing the likelihood of any damage initiation. Using the iterative process outlined in Chapter 3.3, the load distribution across the individual rollers within the test bearing was determined allowing the maximum Hertzian contact pressure and semi-width to be calculated (Figure 4-5 and Figure 4-6). Due to the geometry of the bearing, and the roller/inner raceway contact being less conformal, the maximum contact stress will occur at the inner race/roller contact. To ensure that the inner race stress is kept below 1500MPa during the healthy characterisation, the radial load applied to the bearing was kept below 2500N by applying mass up to a maximum of 20kg, resulting in an overall radial load of 2266N when the load arm mass and applied mass are combined.

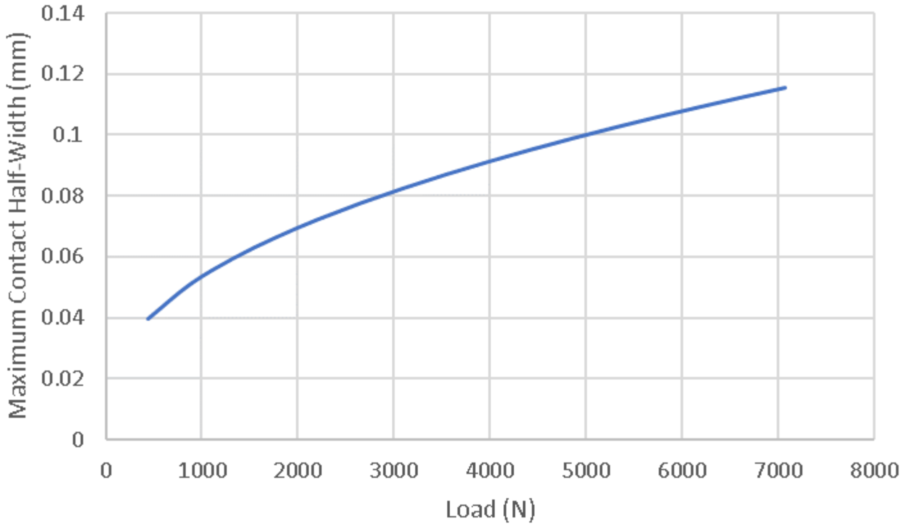

Figure 4-5 - Maximum contact half-width with respect to load for a SKF N20ECP bearing.

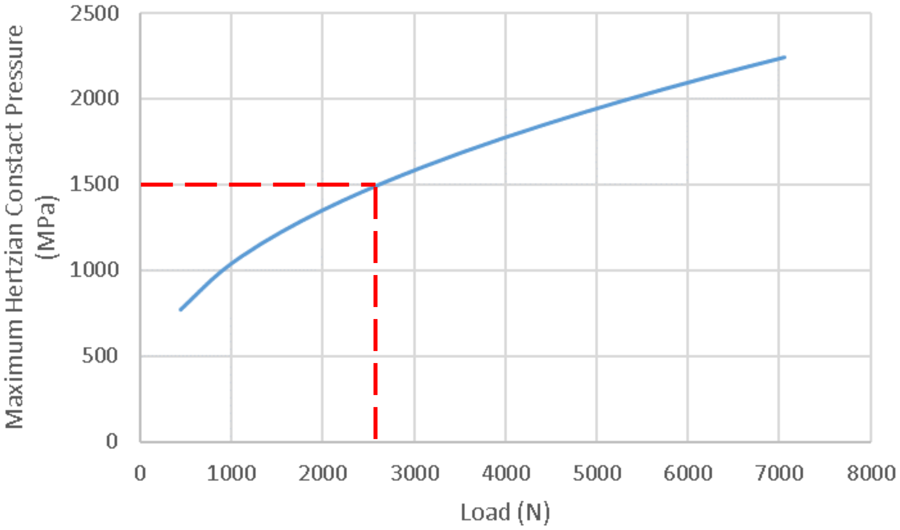

Figure 4-6 - Maximum Hertzian contact pressure with respect to load for an SKF N204ECP bearing

Table 4-2 uses Equations (7)-(10), presented in Section 2.5.1, to calculate the characteristic defect frequencies of both the test and the support bearings with respect to the frequency of the drive shaft. Of particular note is the similarity between the BPFO and BSF for the N210ECP bearing. This similarity makes it difficult to distinguish between the two locations through the frequency analysis but, as an inherent characteristic of the bearing's geometry, it is not possible to change this.

Table 4-2 - Characteristic defect frequencies of the test and support bearings with respect to shaft frequency

	N 210 ECP	22205/20 E
Ball Pass Frequency – Inner Race (BPFI)	6.71 x F	8.82 x F
Ball Pass Frequency – Outer Race (BPFO)	4.29 x F	6.18 x F
Ball Spin Frequency (BSF)	4.31 x F	5.36 x F
Fundamental Train Frequency (FTF)	0.39 x F	0.41 x F

In order to determine the minimum lubricant film thickness using the Dowson-Higginson formula, Equation (2), outlined in Section 2.4, the pressure-viscosity coefficient, α, and the oil viscosity at atmospheric pressure, η, need to be determined from the oil properties whereas the mean speed at the contact, ū, is calculated from the speed of the inner race and roller respectively as the outer raceway is stationary. For this application, however, as pure rolling is assumed, the roller and the inner race rotate at the same speed. Derived from data presented by Weeks (2015), Figure 4-7 illustrates the values of α and η for OEP-80 oil. For the experimental works carried out within this thesis it was decided that, where possible, the outer raceway temperature of the bearing would be used to infer the temperature of the oil within the contact zone. Due to the oil film thickness existing in the order of 10 microns it is thought that there will be sufficient heat transfer from the bearing raceway to the oil, elevating the oil temperature away from that of the oil supply. Further energy will also be added to the oil as it is compressed within the loaded region as well as during the shearing of the oil film.

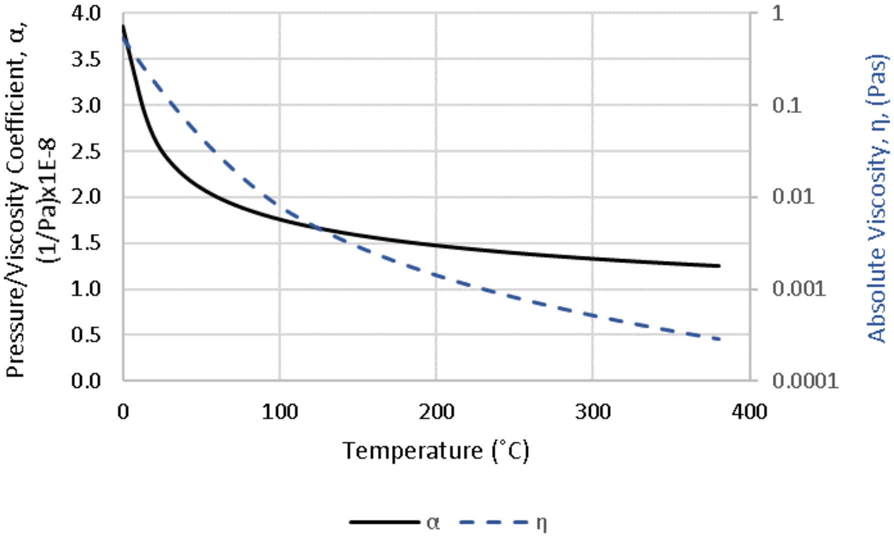

Figure 4-7 - Values of Pressure/Viscosity coefficient, α, and absolute viscosity, η, of OEP-80 oil with respect to temperature – Adapted from Weeks (2015)

4.3 Experimental Procedure

4.3.1 Characterisation Experiment Overview

To develop an understanding of the effects of load and speed on the AE and vibration signal for a healthy bearing, a number of characterisation experiments were carried out on a healthy bearing. For each experiment carried out, the first 10 minutes were conducted under the same conditions with the inner race rotating at a speed of 590rpm whilst under a radial load of 304N (i.e. the load applied due to the mass of the arm alone). This was to ensure that the bearings were brought up to the test speed and temperature in a controlled manner and hence preventing any initiation of premature damage. The different types of tests conducted are detailed in the following sections.

4.3.1.1 Phase 1: Run in test

Following running in guidelines determined by NSK (2017), the speed was increased from 590rpm to 5980rpm in stages of 590, 1190, 1790, 2380, 2980, 3580, 4180, 4790, 5380 and 5980rpm. The radial load was held constant at 794N (Figure 4-8).

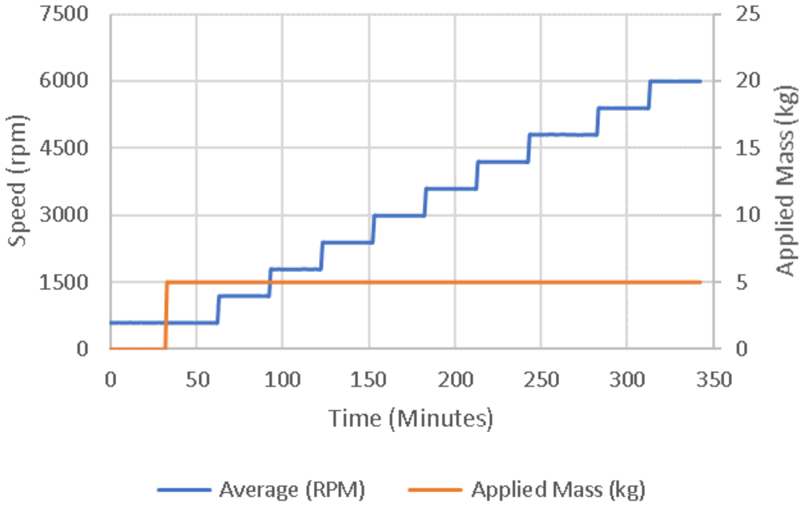

Figure 4-8 - Phase 1: Run in test

4.3.1.2 Phase 2: Speed ramped

The speed was increased up from 590rpm up to 5980rpm, and then back down to 590rpm, in stages of 590, 1190, 2380, 3580, 4790 and 5980rpm. The radial load was held constant at 794N (Figure 4-9).

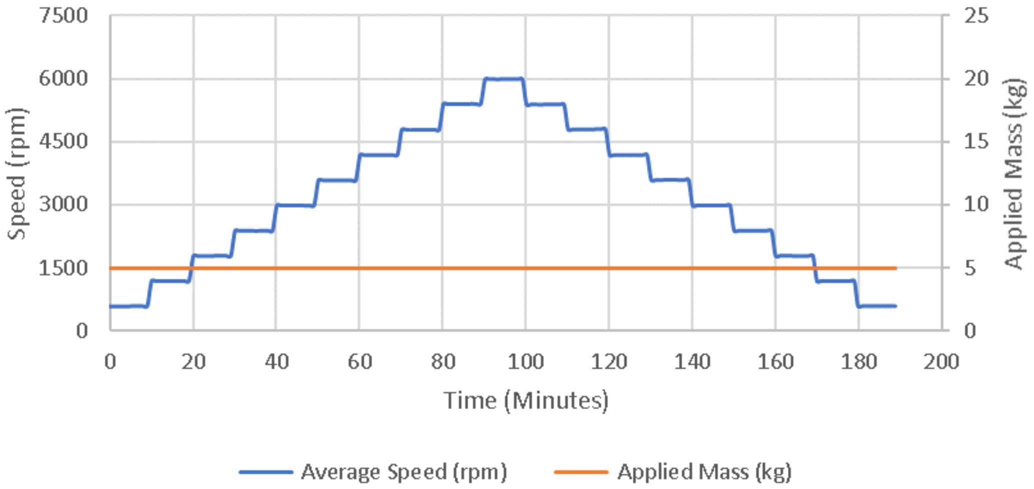

Figure 4-9 - Phase 2: Speed Ramp

4.3.1.3 Phase 3: Load ramped

With the speed held constant at 2980rpm, the load was increased from 304N to 2266N and back down to 304N in stages of: 304, 794, 1284, 1775 and 2266N (Figure 4-10).

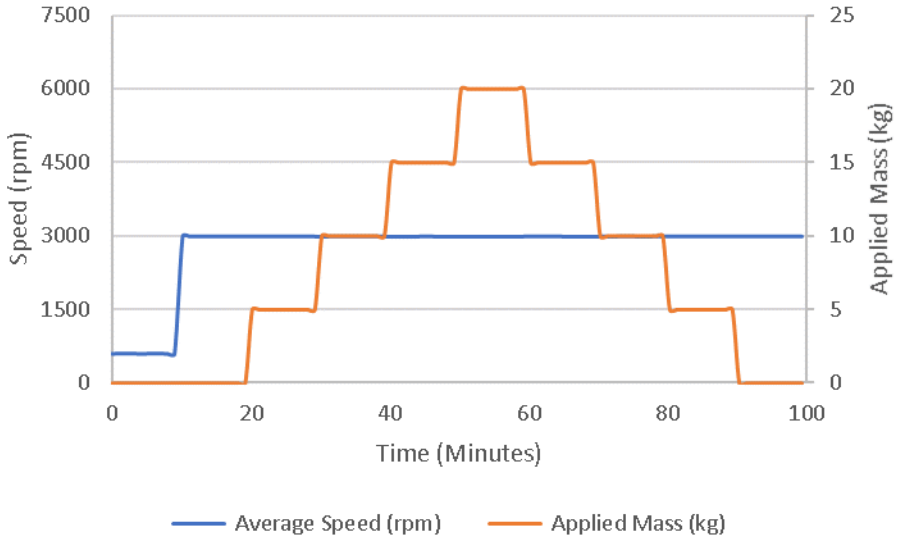

Figure 4-10 - Phase 3: Load Ramp

4.3.1.4 Phase 4: Mixed Test 1 - Speed ramped, load held

The speed was increased up from 590rpm up to 5980rpm, and then back down to 590rpm, in stages of: 590, 1190, 2380, 3580, 4790 and 5980rpm under an initial load of 304N due to the mass of the loading arm acting on the bearing. Once the speed ramp was completed under the first load, additional mass was added to the loading arm and the speed ramp started again. The loads under which the speed ramps were conducted were 304, 794, 1284, 1775 and 2266N (Figure 4-11).

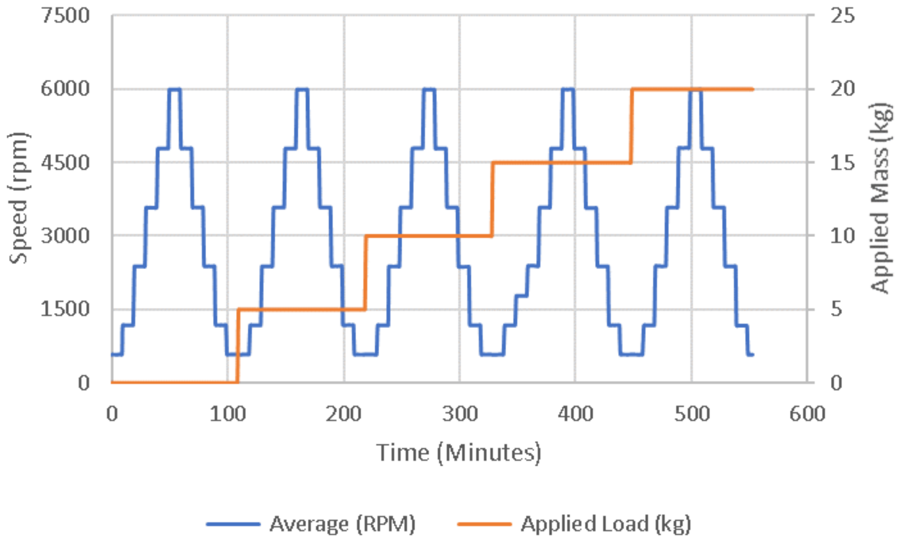

Figure 4-11 - Phase 4: Mixed Test 1 - Speed ramped, load held

4.3.1.5 Phase 5: Mixed Test 2 – Speed held, load ramped

The load was ramped from 304N to 2266N and back down to 304N in stages of: 304, 794, 1284, 1775 and 2266N under an initial speed of 590rpm. After the load ramp, up and down, was completed for the first speed, 590rpm, the speed was increased and the load ramp sequence was repeated at speeds of 1190, 2380, 3580, 4790 and 5980rpm (Figure 4-12).

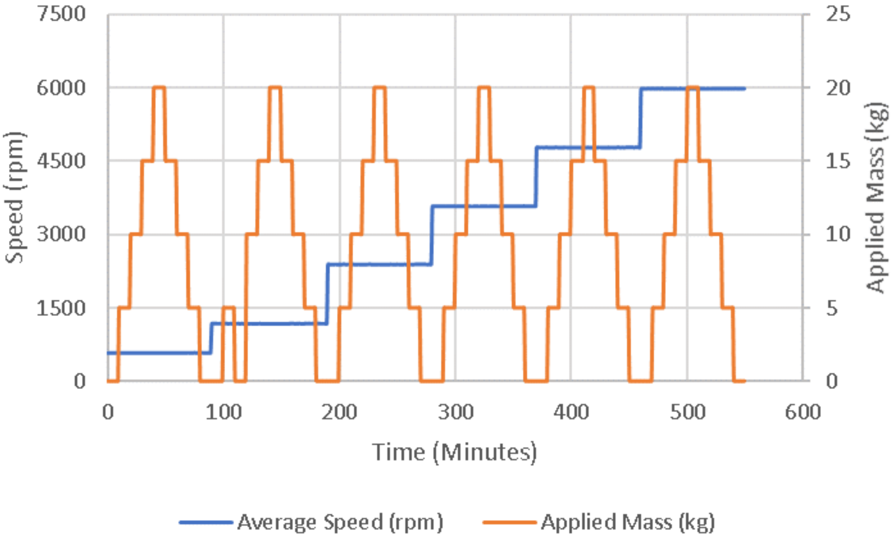

Figure 4-12 - Phase 5: Mixed Test 2 - Speed held, load ramped

4.3.2 Sensor locations

As illustrated in Figure 4-13, Nano30 AE sensors were applied to each of the bearing housings using techniques described in Section 3.2.2 and the quality of the bond was determined by standard techniques - making pencil lead breaks close to the sensor, commonly known as a Hsu-Nielson source (Hsu & Breckenridge, 1981; ASTM, 2010). The sensors were attached to PAC 2/4/6 amplifiers set at a gain of 40dB and a bandpass filter of 20-1200 kHz. DFS-6000 AE and Vibration sensors were also attached to each of the bearing housings in the locations shown in Figure 4-13 using the threaded bossed as described in Section 3.2.2. The six sensors mounted upon the bearing housings are used to provide relatively clean, undisturbed waveforms produced by the bearings. As it is not always possible in an industrial/commercial application to place the sensor so close to the bearings, a seventh and eighth sensor are mounted as far away as possible from the test bearing at the end of the load arm. This sensor is positioned as such to demonstrate exactly how signals attenuate over long distances, and hence, the ability to detect damage at such a position.

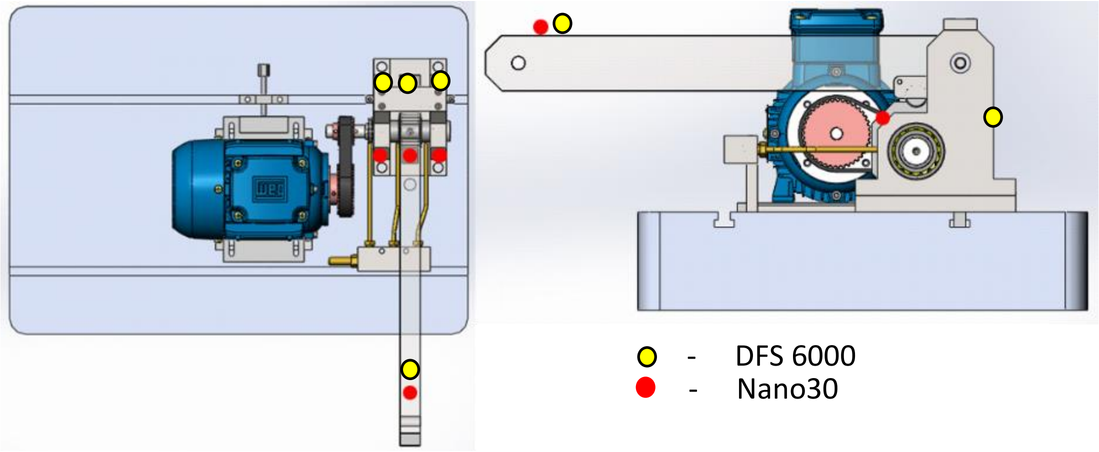

Figure 4-13 - Sensor locations

4.3.3 Data Acquisition

AE wavestreams were recorded for a length of 0.5 seconds once every minute using both a PCI-2 and ACMS system. In addition to this, using a Windows-based PC, parametric data including temperature and speed, was gathered and stored in a corresponding text file.

4.4 Healthy Bearing Test Results

4.4.1 Section Overview

For the healthy bearing characterisation, a large amount of data was gathered and it would be lengthy and repetitive if all of the data were analysed within this chapter. To help simplify the analysis process the following sections, unless stated otherwise, analyse the data collected during Phase 4: Mixed Test 1 - Speed ramped, load held. A number of analysis techniques are performed, including RMS, peak to peak amplitude, frequency analysis and order analysis.

4.4.2 Raw Signal

As discussed in Chapter 2, the main differences between modern vibrational transducers and AE sensors is the frequency band sensitivity and hence the sampling frequency signals necessary to avoid aliasing (Nyquist's theory). Figure 4-14, Figure 4-15, and Figure 4-16 are example signals from each of the three sensor types used within this experiment, AE (Nano30), AE (DFS6000) and vibration (DFS6000) respectively. Due to the way in which the data is recorded, the data shown is collected with a minimal difference of time between them as the data recording is not simultaneous. The speed and radial load applied to the test bearing for all three figures was 5980rpm and 1284N. The AE wavestreams for both the PCI-2 system and ACMS system are recorded for a length of 0.5 seconds but the length of the vibration wavestream is limited to 0.08 seconds. Therefore, to draw accurate comparisons between each of the three different types of wavestreams, the time window of Figure 4-14, Figure 4-15 and Figure 4-16 is limited to 0.08 seconds, which, at 5870rpm means that up to 4 revolutions of the inner race occur. The main differences between the three sensors are the amplitude and the frequency content. Although there are up to 4 rotations of the shaft, there are no distinguishable changes in the signal to highlight this. Some authors would describe the information within the continuous waveforms presented as noise, and would often describe the system as having a low signal to noise ratio (SNR). The waveforms presented however are the real signals and in order to filter out data effectively, the signal contents need to be understood fully as what may be classified as noise may in fact help with analysis.

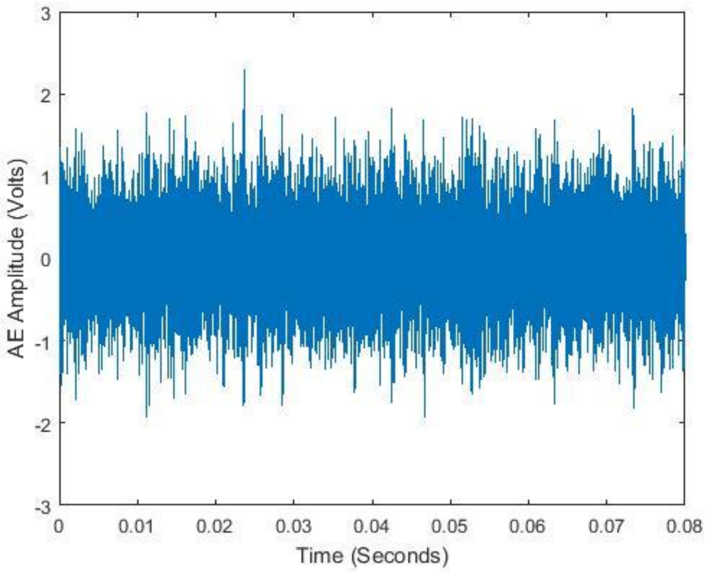

Figure 4-14 - Raw Signal recorded on the PCI-2 system, Channel 2 at 5980rpm and 1248N

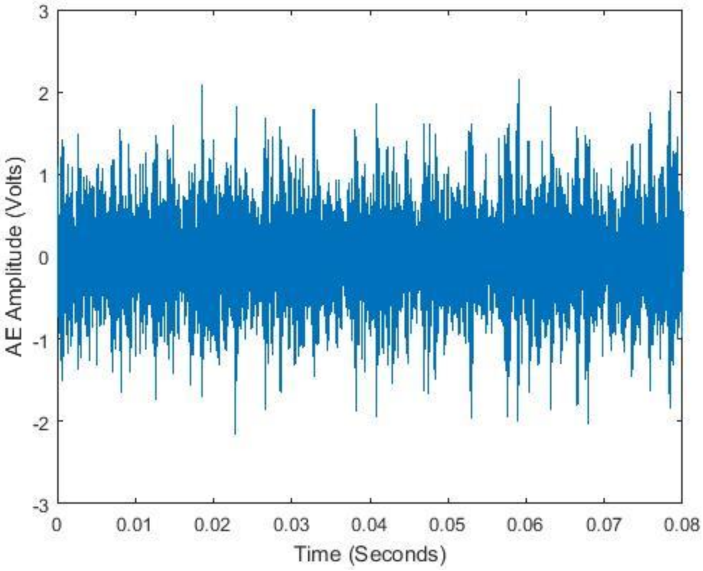

Figure 4-15 - Raw Signal recorded on the ACMS system, AE Channel 2 at 5980rpm and 1248N

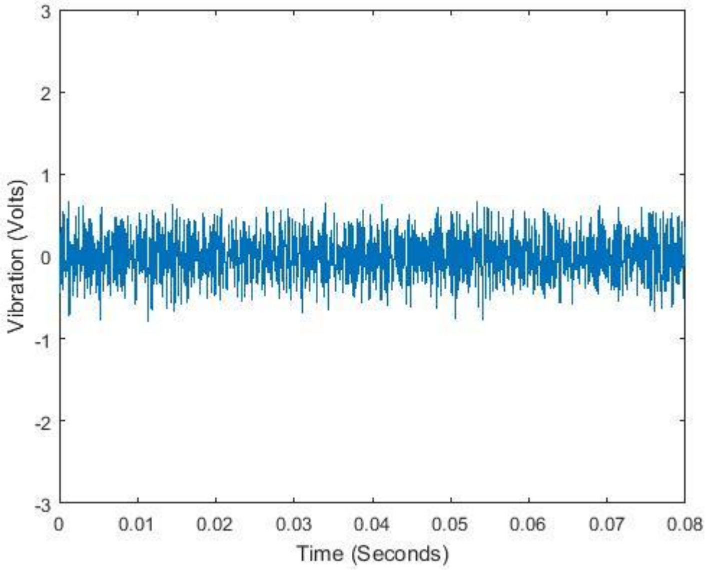

Figure 4-16 - Raw Signal recorded on the ACMS system, Vibration Channel 2 at 5980rpm and 1248N

4.4.3 Statistical Parameters

Although an extremely simple method of data analysis, RMS has been used successfully by a number of authors, including Boness *et al.* (1990), Serrato *et al.* (2007), Elforjani and Mba (2008), Raja Hamzah and Mba (2009) and Nienhaus *et al.* (2012), to average the signal to a single numerical value, and is hence able to quickly determine how the signal changes with respect to speed and load. Figure 4-17 plots the RMS of the test bearing waveforms, AE and vibration, as recorded on the PCI-2 and ACMS systems. The figure demonstrates the significant effect speed has on the RMS amplitude, producing a step response as the speed is increased/decreased for both AE and vibration and in agreement with observations made by Couturier and Mba (2008). As the load is increased from 304N to 2266N, the RMS amplitude of the AE sensors increases steadily whereas the vibrational response remains relatively constant, providing evidence that the load may have a more significant effect on the higher frequency components of the signal.

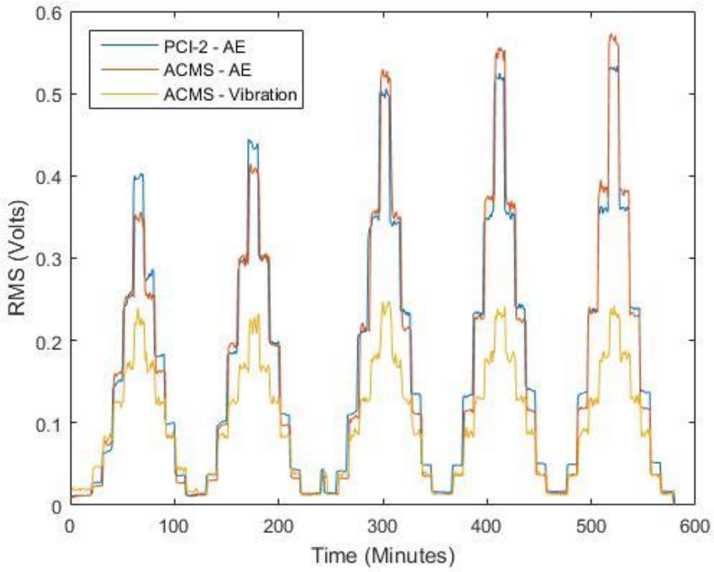

Figure 4-17 - RMS amplitude of test bearing wavestreams from PCI-2 and ACMS systems.

As both are statistical parameters of the recorded wavestreams, it is appreciable that the trends observed between the applied speed/load on the RMS amplitude stand true for the Maximum Peak to Peak amplitude (Figure 4-18). However, unlike the stability of the RMS amplitude, the peak to peak amplitude fluctuates significantly over the 10-minute period during which the speed is held constant, before being increased/decreased. As shown in the discussion of the raw signals, the wavestreams are composed of a number of high frequency transients that extend beyond the base level 'noise floor'.

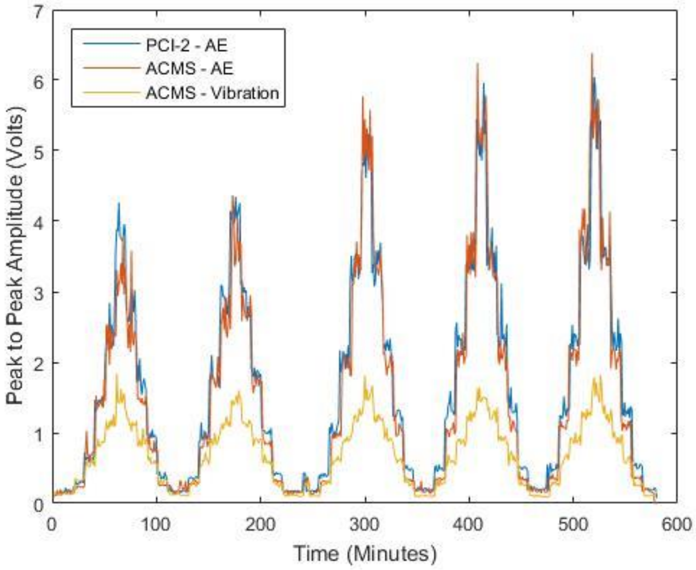

Figure 4-18 - Maximum Peak to Peak amplitude of test bearing wavestreams from PCI-2 and ACMS systems.

Increasing speed changes the amplitude of both the noise floor and the individual transients. As RMS is the average of the wavestream, the effect of the increasing transient amplitudes is minimal relative to the signal average. As witnessed in Figure 4-17, the vibrational signal, which is free of high frequency transients, demonstrates less variation as the load is increased.

The trend of RMS vs. speed compliments the surrounding literature as Al-Ghamd and Mba (2006) found that for a healthy bearing the RMS of AE and vibration increases with the rotational speed of the system. This is considered to be due to the amount of energy supplied to the system and Couturier and Mba (2008) suggest that the increased energy is due to increased asperity contact at the bearing surfaces. The Lambda values investigated experimentally by Couturier and Mba (2008) were below 3 and hence the lubrication regime was both boundary and mixed lubrication. The parametric data recorded during the running of Phase 4 was used to provide the temperature history of the test bearing throughout the experiment (Figure 4-19).

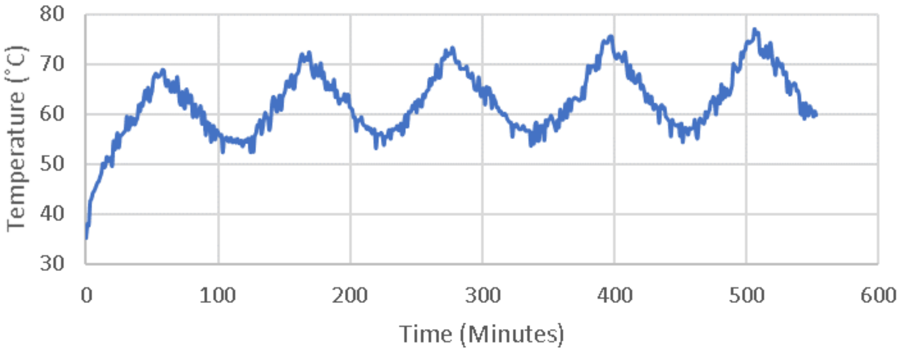

Figure 4-19 - Temperature readings from the test bearing during Phase 4

Combining this with the oil specifications, Figure 4-7, and Equations (2)-(4) it is possible to plots the theoretical Lambda values against the AE_{RMS} values for this test Figure 4-20. The surface roughness of the bearing was measured using a Taylor Hobson profilometer before the testing began and the RMS surface roughness, Rq, of the inner raceway and rolling element was found to be 0.077μm and 0.074μm respectively. It can be seen that as the test starts, the bearing is cold and hence, with the increased viscosity of the oil, there exists a theoretical full film between the roller and the inner raceway. It can also be seen over the first 10 minutes that as the oil quickly heats up, the Lambda value drops below 3 and the lubrication regime becomes mixed.

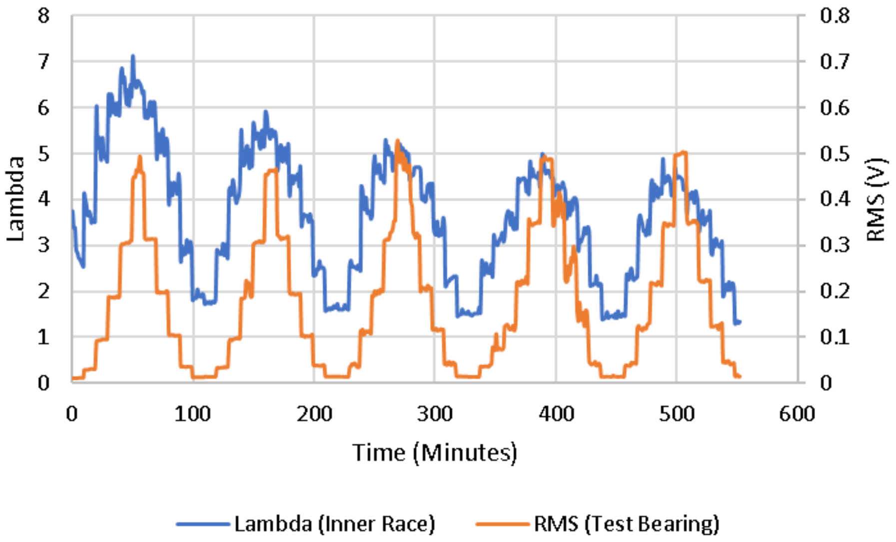

Figure 4-20 - Response of Lambda and RMS for the test bearing during Phase 4: Mixed Test 1 - Speed rampled, load held

As the speed is increased incrementally, the Lambda and RMS values also increase with the lubrication regime becoming Elastohydrodynamic. This lubrication regime is consistent throughout the test apart from when the speed is reduced down to speeds below 2380rpm, giving rise to mixed lubrication conditions. The strong positive correlation of RMS value with Lambda ratio therefore suggests that, under these operating conditions, asperity contact is not the cause of the increase in signal average. Indeed, if the signals were predominantly caused by asperity contact, one would expect the signal levels to increase as Lambda *decreases*. Even if the higher speeds produce more AE as the few most aggressive asperities make contact more frequency, one would expect the thicker films to somewhat negate this effect, and not see the strong AE/speed correlation To investigate this further, controlled tests would be required where temperature (and hence lubricant viscosity and therefore Lambda ratio) is adjusted independently of speed, producing tests where the lubrication conditions are changed independently of the level of (speed related) energy in the system.

There are a number of other hypotheses presented by the author that may explain why the RMS increases with Lambda ratio and speed:

- As a bearing rotates, the rollers themselves only start to rotate as they enter the loaded region of the bearing. Therefore, as the roller starts with zero velocity, the initial contact will start as boundary/mixed lubrication as the roller slides rather than rolls. Only as the roller starts to spin is an elastohydrodynamic oil film established between the roller and raceway and hence asperity contact may actually be occurring despite the theoretical Lambda value being greater than 3. It is also thought that this may be worse as the speed is increased as the length of time a roller is in the contact region is significantly reduced, and hence the roller may not be able to achieve its maximum rotational velocity.

- As the roller passes through the loaded region a wake is formed at the front of the roller allowing for oil to be drawn into the contact zone to form the elastohydrodynamic film. This however causes oil to be forced out of the rollers path and as the speed of the bearing increases, the rate at which oil is ejected by the rollers will increase, and if the oil jet is not able to replace the lost oil fast enough, the amount of oil available to form a fluid film will be reduced significantly.
- Based on the Stribeck curve, if a sufficient fluid film thickness exists friction may be generated due to shearing of the oil within the contact zone.
- The vibration caused as the bearing rotates in turn excites the bearing housing due to the change in bearing stiffness as the number of rollers in contact changes. As the speed increases, the amount of excitation energy into the housing increases and the resonant frequencies of the bearings and housings may be excited.

4.4.4 Frequency Analysis

To better understand the effect that variations in speed and load have on the AE signal, trends in the frequency spectrum were investigated. To determine such trends, Fast Fourier Transforms (FFTs) were calculated for each of the recorded wavestreams. To improve the resolution of the data for visual analysis, the FFT frequency axis was split into a number of bins, each with a width of 1 kHz. Each bin is the summed energy of all the frequencies contained within that frequency range. The binned FFT's are then stacked together to produce a 3D plot of Time vs. Frequency vs. Energy.

Similar to the response of the RMS and peak-to-peak amplitude, the energy amplitude of the binned power FFT's is heavily influenced by the speed, and hence, the amount of excitation energy supplied to the system. Figure 4-21 is a sample of the binned FFT viewed isotropically and it demonstrates that although the amount of energy increases with speed, there is no significant change in the frequency content. This is important to note as the binned FFT's that follow will be viewed in the x-y plane (Frequency-Time) and the frequency bands at lower speeds will not be visible although they do exhibit the frequency excitations as the higher speeds, albeit at lower amplitudes.

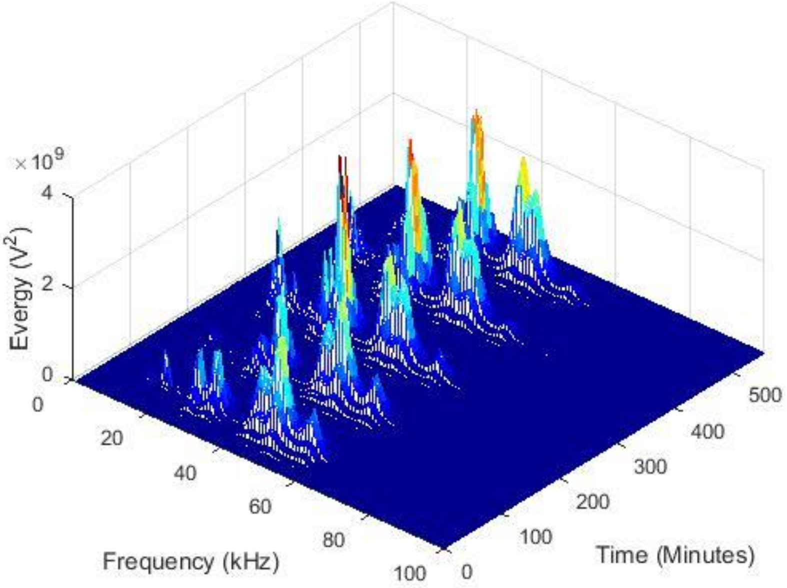

Figure 4-21 - Isotropic view of an example binned FFT

The sampling rate of the AE wavestreams was 1MHz and therefore, due to Nyquist's theorem, the binned FFT's for the PCI-2 and ACMS wavestreams were only presented up to 500kHz. There exists a large difference in the energy amplitude of signals as the frequency increases and therefore the binned FFT's are split up into three different sections, 0-100kHz, 100-200 kHz and 200-500kHz, allowing for a better interpretation of the results. The sampling rate of the vibration sensors was limited to 51.2kHz and therefore the maximum frequency of the vibration FFT was limited to 25kHz.

Figure 4-22 plots the binned frequency of the AE wavestreams between 0-100kHz and Figure 4-23 plots the vibration frequency response between 0-20kHz. Figure 4-24 and Figure 4-25 plot the binned FFT's of the PCI-2 and ACMS wavestreams between 100 – 200kHz and 200 – 500kHz respectively. It should be noted that the scale of the colour-bar representing the FFT energy amplitude in Figure 4-24 and Figure 4-25 are an order of magnitude higher for the PCI-2 data than the ACMS data due to the difference in energy levels between the two different systems.

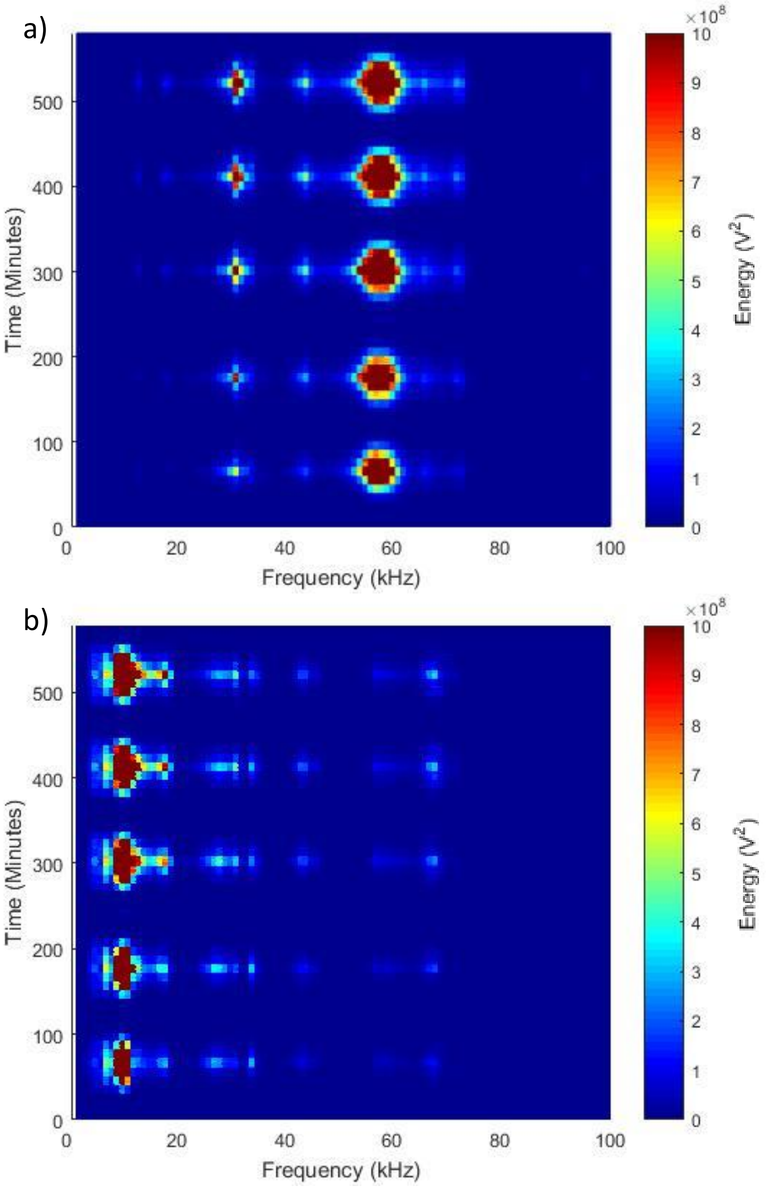

Figure 4-22 - Binned Frequency of test bearing between 0-100kHz for a) PCI-2 AE and b) ACMS AE

Figure 4-22 shows that the PCI-2 system has a dominant excitation at frequencies between 53-62kHz as well as medium level excitation frequencies at 30 and 43kHz and low energy excitations at 18, 66 and 71kHz. The ACMS system however has a dominant excitation frequency at 10kHz, a comparatively medium level excitation at 18 and 27kHz and low energy excitations at 34, 43, 58 and 67kHz.

It can be seen that there exist some similarities in the frequencies excited, however the fundamental low frequency response is vastly different between the two sensors due to their construction. The DFS-6000 sensors are sensitive between 0-100kHz and the Nano30 AE sensor has a sensitivity between 125-750kHz. Therefore, to excite the Nano30 sensor at these low frequencies indicates that there must be a significant amount of energy available within this region. Also of note is that the signals received at the Nano30 sensor are passed through a 20-1200kHz bandpass filter when they are amplified. The ACMS signals however, are not filtered and hence there is clear excitation between 0 and 20kHz.

Further clarity of the low order frequency excitation is seen in Figure 4-23 where the excitation bands are at 2, 4, 6 and 8-10kHz. It is thought that these low level frequency bands excited are related to the HNBFRI's as discussed by Graney and Starry (2012). As the speed is increased, the amount of energy supplied to the system as a whole increases thus exciting the resonant frequency modes of the system.

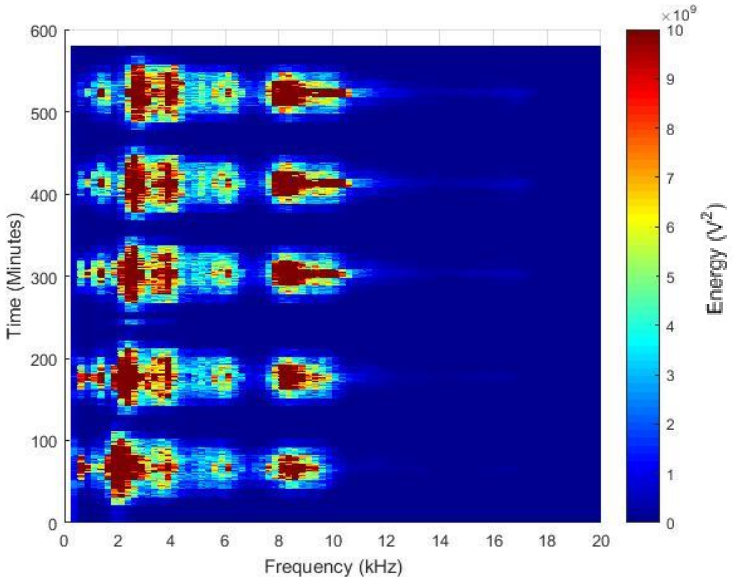

Figure 4-23 - Binned frequency of test bearing between 0-20kHz for vibration signals

The energy at 27kHz for the PCI-2 system shows a strong correlation with the increasing load values. It is thought that this is because as the load is increased, there exists an increased amount of energy potential to be released as the stiffness of the bearing changes with the number of rollers in contact. Further evidence of the change in stiffness affecting the excitation frequency is visible in the vibration spectrum as the excitation at 2kHz drifts to a maximum frequency of 2.5kHz as the load is incremented. As the frequency range is increased to 100-200kHz (Figure 4-24) the PCI-2 system shows a large amount of energy between 112-120kHz whereas the ACMS system is excited between 103-108kHz, albeit at energy levels an order of magnitude lower. It is possible

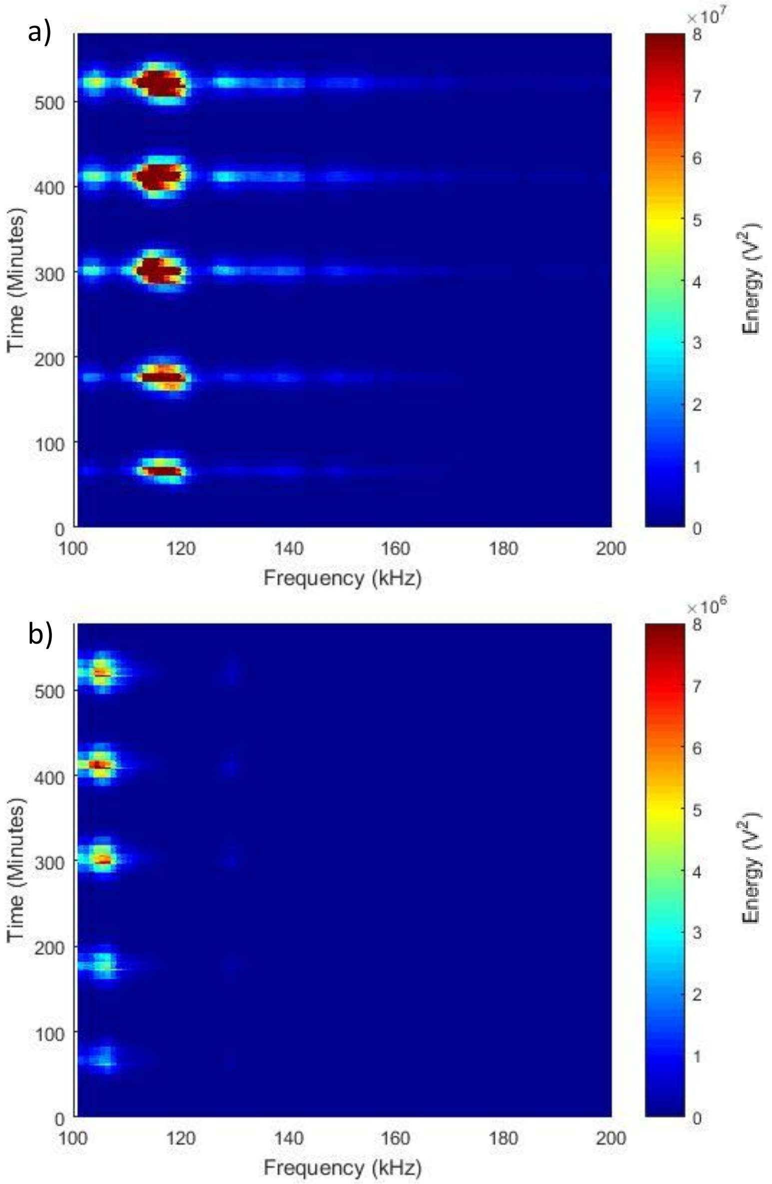

Figure 4-24 - Binned Frequency of test bearing between 100-200kHz for a) PCI-2 AE and b) ACMS AE

that these frequencies occur as second harmonics of the frequencies witnessed in Figure 4-22.

Although it is difficult to know for certain, it is also possible that these peaks are related to the propagation of small cracks and plastic deformation occurring within the loaded region of the test bearing as it is run in. Ramadan *et al.* (2008) performed a tensile test on a 12.5mm diameter braided steel wire that was formed of 7 wires in total. After 815 hours of the test beginning, the number of AE hits increased and these were linked to crack initiation due to local corrosion. The frequency of the AE waveforms linked to these hits demonstrated a peak excitation centred around 100kHz. It is also possible that this frequency band may be linked to friction within the bearing. Ferrer *et al.* (2010) determined that the AE released during a stick-slip friction event between sliding steel samples released bursts of transients whose energy was concentrated around 100kHz. Although the test bearing is lubricated at all times, there still exists an amount of friction within the bearing and it may be possible that this is the detection of it. Both theories, small crack propagation and friction are possible as the amount of energy released at this frequency increases as the load, and hence the contact pressure, is increased.

Figure 4-25 plots the frequency response between 200-500kHz and there now exists two orders of magnitude difference between the cumulative energy of the PCI-2 and ACMS systems. This is mainly due to the fact that the DFS-6000 sensor's operating range is up to 100kHz and, although the sampling rate allows for information to be gathered up to 500kHz, the sensor is not sensitive at high frequencies.

The PCI-2 system demonstrates strong frequency excitation at 202, 237 and 277kHz as well as slight excitation around 340-350kHz, close to the sensor's resonant frequency. The ACMS system shows excitation at 220kHz. These frequencies are close to the second harmonic of the frequencies witnessed in Figure 4-24 and as such it is not considered that these frequencies are directly linked to any AE phenomena.

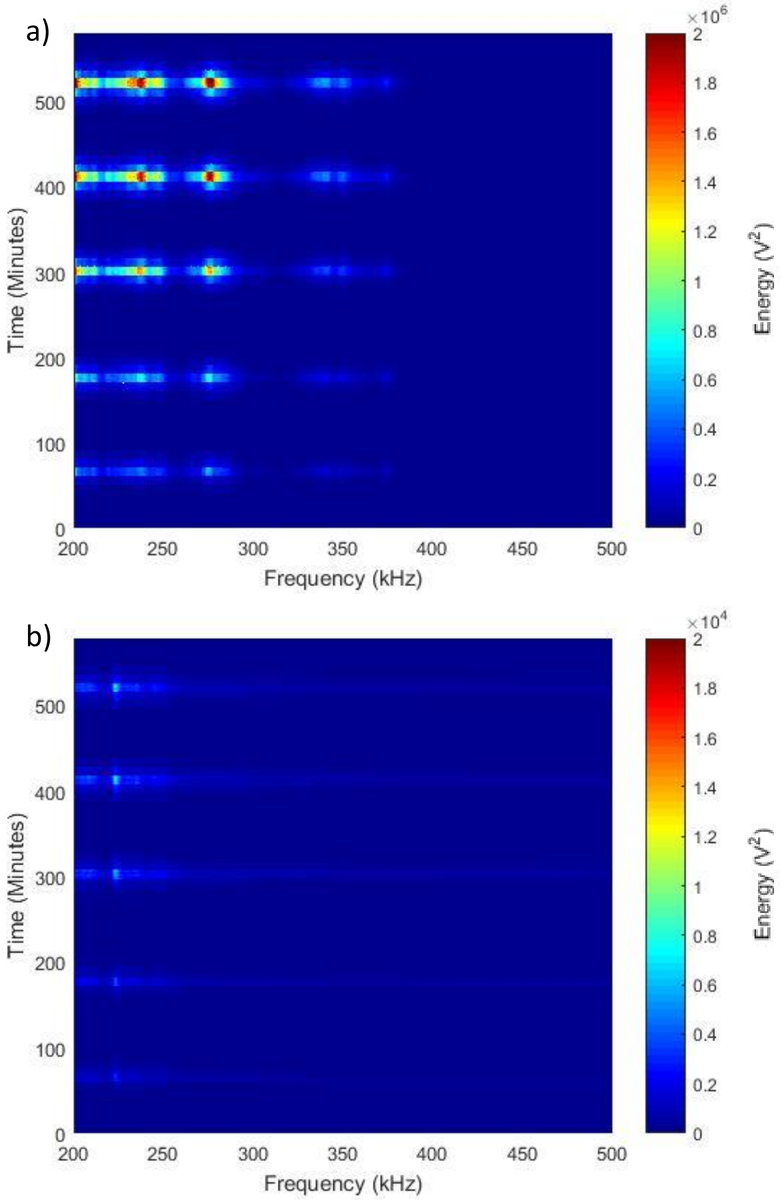

Figure 4-25 - Binned Frequency of test bearing between 200-500kHz for a) PCI-2 AE and b) ACMS AE

Figure 4-26.a-c plots the order analysis of the wavestreams recorded during the healthy characterisation as recorded on the PCI-2, ACMS AE and ACMS Vibration systems respectively. It can be seen that the orders excited changes with what system, or sensor, is used. For the order analysis of the data recorded on the PCI-2 system it can be seen that an order of 4.3, the test bearing BPFO, is excited as the speed is incremented, increasing in energy as the load is increased. The large benefit of using order analysis can be shown as, although the speed of the shaft is fluctuating, the characteristic frequency of the bearing remains the same. It is discussed widely that the BPFI is difficult to detect by previous researchers, (Mba and Rao, 2006; Shiroishi *et al.,* 1997; Tan and

Mba, 2005) however Figure 4-26 demonstrates that the PCI-2 signal demonstrates a small amount of energy at the test bearing BPFI, 6.7 orders, but only as the applied load is increased. This increased transmission is thought to be due to the increase in contact area between the roller and inner raceway, allowing for more of the energy from the signal being able to be transmitted through to the bearing housing. The order analysis of the ACMS wavestream also demonstrates some excitation at the test bearing BPFO but there is a greater amount of energy at 6.2 orders, the BPFO of the support bearings. This means that the energy generated at the support bearing BPFO is transmitted through the shaft and into the sensor on the test bearing. Although taken from the same test rig, with the wavestreams recorded only seconds apart, it is difficult to explain why there is no detection of this order in the analysis of the wavestreams recorded on the Nano30 sensors connected to the PCI-2 system. It could be argued that the operating frequency of the DFS6000 sensor being lower than that of the Nano30 sensor may cause it to be more sensitive to lower frequencies, although it would be thought that if this were the case, the energy amplitude at the test bearing BPFO would also be greater on the ACMS AE sensor than on the PCI-2 system. This is a feature witnessed in the order analysis of the vibrational wavestreams, where the energy amplitude is similar for the BPFO of the test bearing and support bearing.

Another benefit of order analysis can also be seen in the order analysis spectrum of the vibration data where characteristic ‘C’ shapes are witnessed between 0.5-1.5 orders, as the speed in ramped up and then back down. This is due to the detection of a frequency that does not change with shaft speed, such as the heater/stirrer or lubrication pump motor.

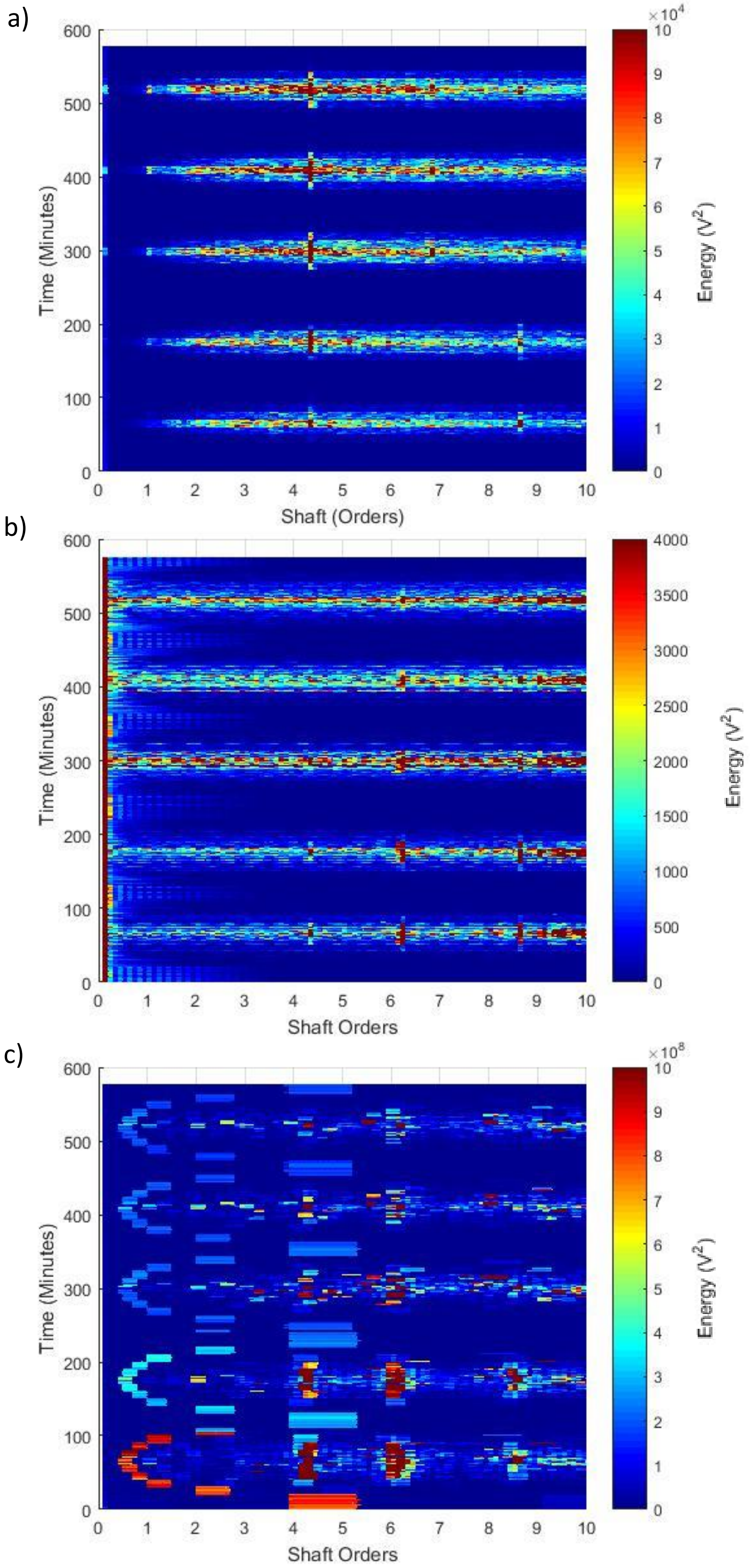

Figure 4-26 - Order analysis of healthy wavestreams as recorded on a) PCI-2, b) ACME AE and c) ACMS Vibration

4.5 AE Sensitivity

The majority of the experimental works presented in the literature review, Section 2, focus solely on the response of a single test bearing and the reports fail to discuss the AE and vibrational response of the support bearings also attached to the system. When analysing the support bearing data acquired during the experiment detailed in Section 4.5 it was found that the AE and vibrational response of the support bearings differed from that of the test bearing.

Figure 4-27, the RMS plot of the PCI-2 response for all four sensors connected to the test rig, demonstrates that the RMS value of the wavestreams recorded for the two support bearings is far higher than the test bearing, although the two support bearings are operating at the same speed as the test bearing and only subjected to half of the radial load. This suggests that, although the speed of the bearing has a significant effect on the signal amplitude, the geometry and design of the bearing may also be responsible for differences in the bearing response.

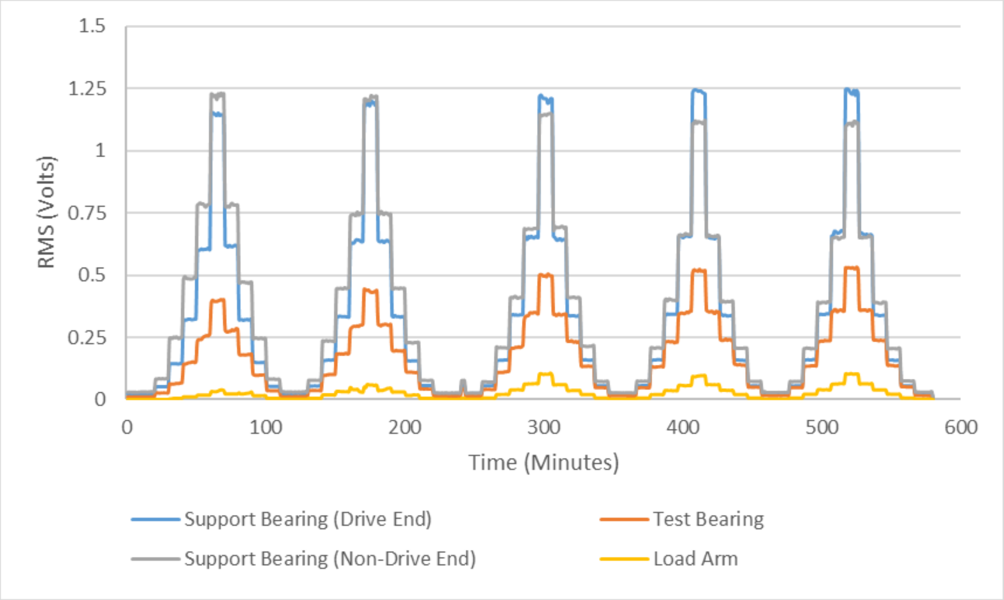

Figure 4-27 - RMS of all channels - PCI-2

However, Figure 4-28 plots the RMS of the AE wavestreams recorded on the ACMS system at a similar time to those shown in Figure 4-27. It can be seen that the ACMS AE response for the Non-Drive End support bearing has a larger RMS amplitude than the test bearing, as previously seen in Figure 4-27, however there is a difference in the AE response of the Drive End support bearing which exhibits an RMS amplitude similar to that of the test bearing.

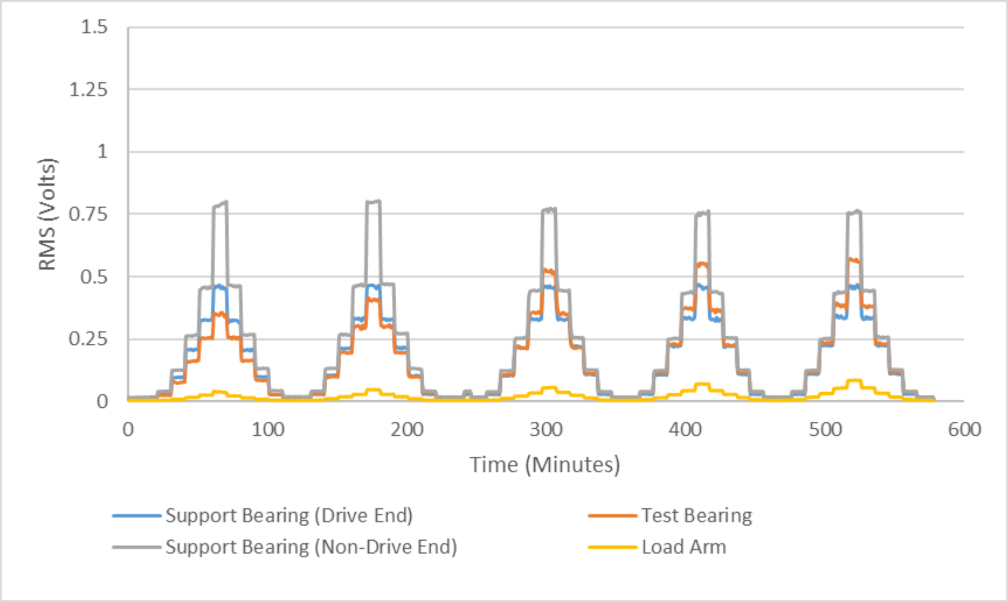

Figure 4-28 - RMS of all channels - ACMS AE

Finally the ACMS vibrational response for the same experiment, Figure 4-29, differs completely from the two AE plots, Figure 4-27 and Figure 4-28, demonstrating instead that the test bearing has the highest RMS amplitude, followed by the Drive End support bearing with the second highest RMS amplitude and the Non-Drive End support bearing having the lowest response out of the three bearings monitored.

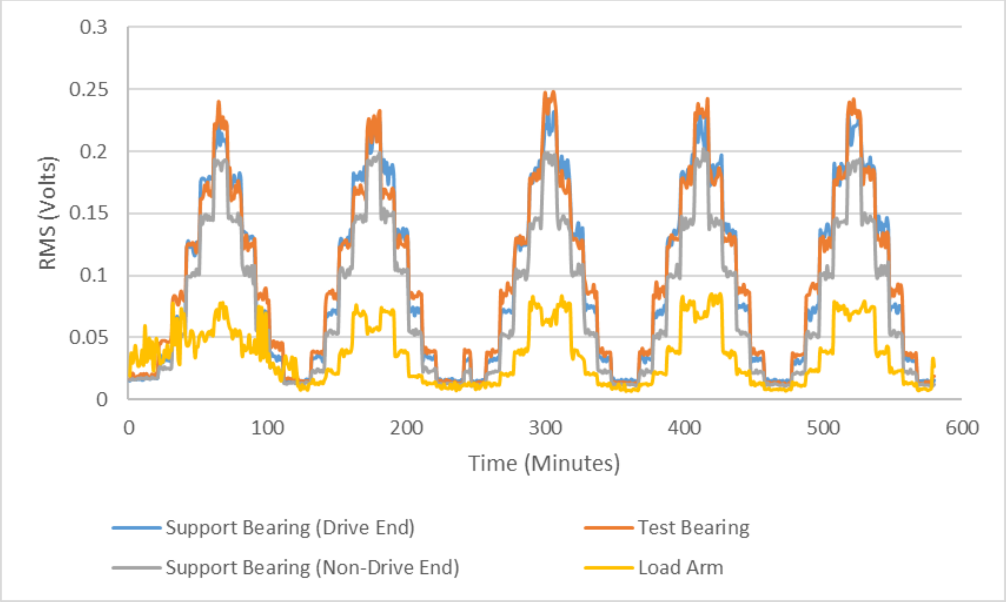

Figure 4-29 - RMS of all channels - ACMS Vibration

Although the step change in RMS value remains somewhat proportional to the increasing/decreasing speed across all three bearings for each of the data acquisition systems, there is a noticeable difference across both the bearing and system as the load is increased.

With increasing levels of bearing load, the AE response of both the PCI-2 and ACMS system show an ***increase*** of RMS amplitude in the test bearing and a ***decrease*** in the Non-Drive End support bearing. The Drive-End support bearing shows no change with increasing load, similar to the vibrational response of all of bearing locations. With no visible changes in the vibration analysis, there is further evidence that the effect of load causes changes in high frequency bands possibly due to increased friction.

This demonstrates how the sensor type, location and acquisition system used *all* have a contribution to the signals produced. As well as this, the coupling medium, coupling quality and the set-up of individual experiments can also have a significant effect on the signal produced (Colombo *et al.*, 2005).

A direct comparison of the **healthy** data gathered from two separate experiments, where the test rig, including sensors, had been completely dismantled and the test bearing exchanged for another but with the same support bearings in place, demonstrates the high sensitivity of AE and its dependency on test set up.

Figure 4-30 and Figure 4-31 plot the RMS amplitude for the PCI-2 and ACMS systems respectively, for the AE wavestreams recorded during a mixed test on a different test bearing than that previously analysed in Figure 4-27 and Figure 4-28. It can be seen that the PCI-2 RMS values of the Drive End bearing are significantly higher than the Non-Drive End bearing and the test bearing not only in this experiment, but also compared to the values shown in Figure 4-27. However, when comparing the ACMS AE RMS values of Figure 4-28 and Figure 4-31, it can be seen that the RMS values of Non-Drive End support bearing are comparable, but the Drive End support bearing values have decreased albeit only slightly. If AE is to be used as a commercial health monitoring system, the characteristics of a healthy set-up need to be determined every time the system is modified. Having a threshold against which new data can be compared helps to reduce the number of false positives and is often used within vibrational condition monitoring systems.

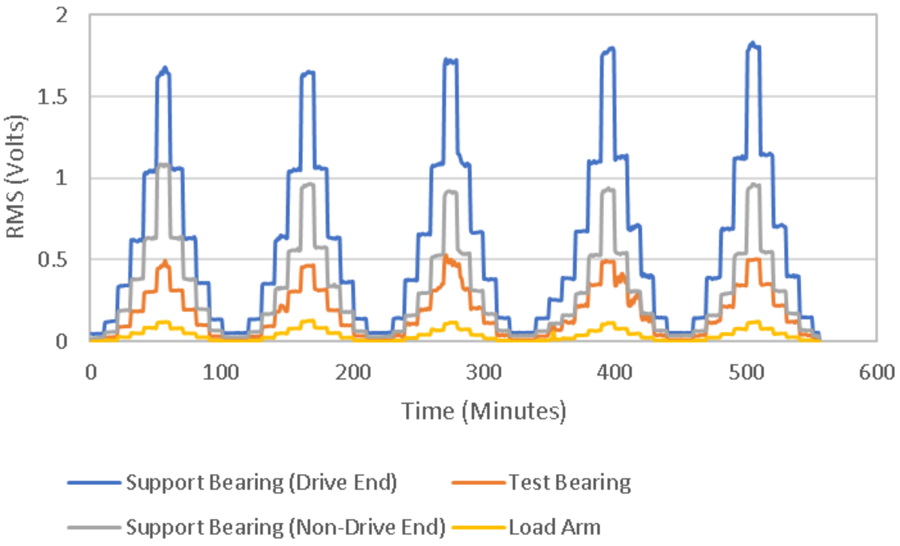

Figure 4-30 - RMS response of the AE wavestream recorded on the PCI-2 system for a separate Mixed Test

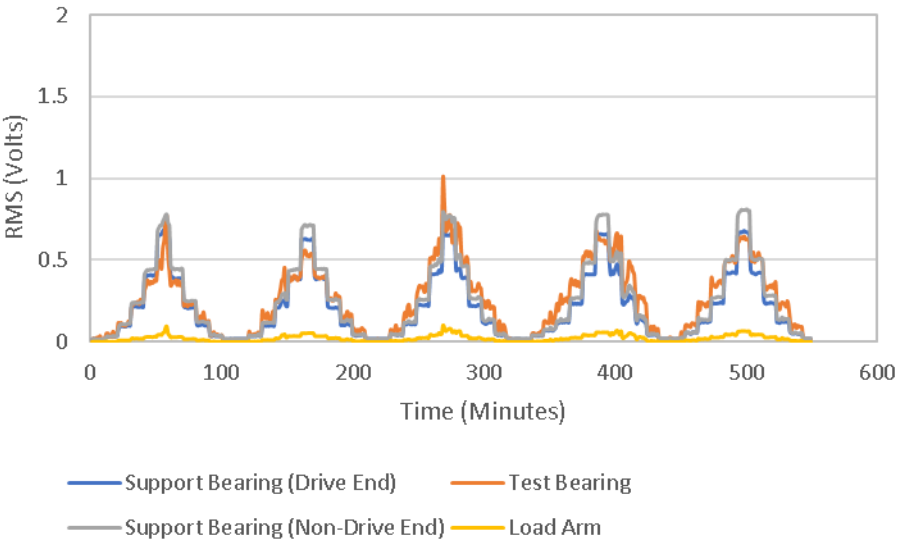

Figure 4-31 - RMS response of the AE wavestream recorded on the ACMS system for a separate Mixed Test

4.5.1 Healthy Bearing Discussion Points

Section 4.5 has demonstrated that, for a healthy bearing, the speed at which the bearing is operating affects the response of the RMS and the energy content within the frequency spectrum. The effect of Lambda ratio on the RMS value was also investigated and it was shown that for this experiment, the bearing mainly operated with an EHL lubrication regime with short periods in mixed/boundary lubrication conditions. This puts the findings of Couturier and Mba (2008) under scrutiny as there was no disparity between the AE response when under the two lubrication regimes.

Through the frequency analysis, the cause of high frequency components within the PCI-2 and ACMS AE signals was hypothesised and only through further investigations can these be clarified.

The final part of Section 4.5 demonstrated the reliance on the experimental set up as well as how the sensors mounted to different bearings within the system differ. Also, for the work carried out in this research, it was not always possible to ensure that the same sensors were used for each test and, as shown by the example calibration charts in Appendix A, it is known that there exists a difference between each individual sensor. That, coupled with the knowledge that the repeatability of sensor mounting is not necessarily accurate, is a further reason as to why it is recommended for future tests that an initial period of running is conducted to determine the operating amplitudes of all sensors attached for a given set up.

4.6 Seeded Defects

4.6.1 Section Overview

A vast majority of the surrounding literature concerns the AE produced in damaged bearings by artificially seeding damage to the raceways or rollers. Among the various techniques available, there are two popular methods, engraving and EDM. In order to determine the effect that seeded damage has on the AE signals produced, seeded defects were applied to the outer raceway of an SKF N204ECP test bearing. Similar to the presentation of the results in Section 4.5, the analysis methods include RMS amplitude, peak to peak amplitude, and binned frequency content.

4.6.2 Experimental Set-Up

Four Nano30 AE sensors were placed on the bearing housings in the same location as the healthy bearing characterisation, however instead of silicone, a brown lithium based grease was applied to act a couplant, with magnets used to keep the sensors in position. The couplant was changed from silicone to grease to allow for quick change over between tests as it takes 24 hours for the silicone to cure completely. Colombo *et al.* (2005) demonstrated the difference in response for a number of couplant materials although the two couplants used in this study, silicone and grease, were not considered as part of their investigation. Visual analysis of the raw wavestreams however, found that there was little difference between the visual characteristics in them. All of the tests were conducted at a speed of 5980rpm with radial loads of 0.29, 0.79, 1.29 and 1.79kN applied to the test bearing (Figure 4-32).

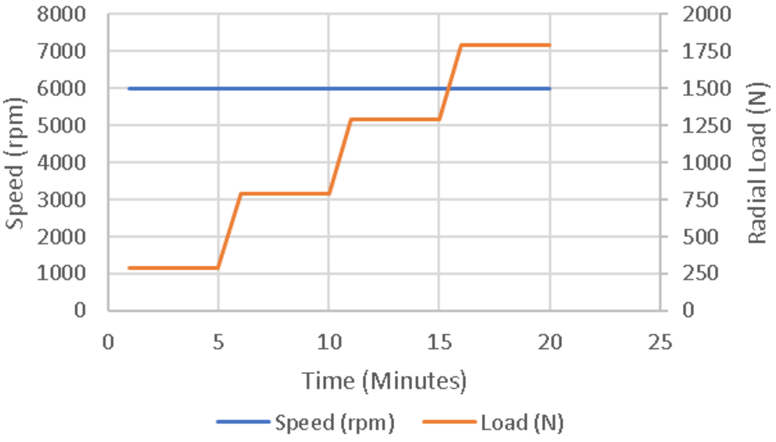

Figure 4-32 - Test schedule for a seeded defect test

For each load increment a total of four wavestreams were recorded for a length of 0.25 seconds with a sampling frequency of 1MHz. Following each load increment, the test was allowed to settle for 10000 revolutions until the first wavestream was recorded. The wavestreams following this were then recorded after a further 2000 revolutions of the shaft. The process repeated itself for each load increment.

An engraver was used to apply seeded defects, of increasing size and number, to the outer raceway of a SKF N204 ECP bearing. Due to the design of the test rig, disassembly/assembly was required after each of the individual tests to increase the size of the defects on the outer raceway. The size of the defects investigated was measured using a Taylor Hobson Talysurf surface profilometer and 'Mountains' software was used to process the measurements as well as calculating the peak volume and valley volume, by calculating the amount of material above and below the mean surface respectively Table 4-3. The measurements made by the Talysurf also allow for an image to be produced for each defect, detailing the extent of the damage applied to the surface as well as demonstrating how the defect changes before and after being run (Figure 4-33 - Figure 4-43).

Table 4-3 - Seeded Defect Description

Defect Name	**Defect Schematic**	**Pre-Test Volume (μm^3)**	**Post-Test Volume (μm^3)**	**Figure Name Pre/Post**
Defect 1	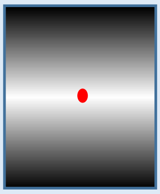	**Peak** 154413 **Valley** 317543	**Peak** 113954 **Valley** 285719	Figure 4-33 Figure 4-34
Defect 2	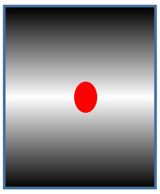	**Peak** 133685 **Valley** 629639	**Peak** 58926 **Valley** 646754	Figure 4-35 Figure 4-36
Defect 3	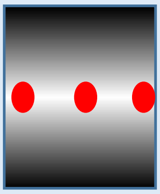	**Peak** 166135 **Valley** 465806	**Peak** 115047 **Valley** 505060	Figure 4-37 Figure 4-38
Defect 4	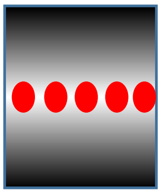	**Peak** 148595 **Valley** 679192	**Peak** N/A **Valley** N/A	Figure 4-39 N/A
Defect 5	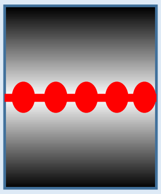	**Peak** 188414 **Valley** 687111	**Peak** 179024 **Valley** 696703	Figure 4-40 Figure 4-41
Defect 6	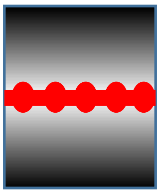	**Peak** 475880 **Valley** 1302331	**Peak** 106083 **Valley** 1615745	Figure 4-42 Figure 4-43

Figure 4-33 and Figure 4-34 are three-dimensional representations of the first defect, Defect 1, before and after the bearing was run respectively. The approximate dimensions of the engraved defect are 0.4 x 0.6mm and it is placed in the centre of the outer raceway. The engraver produces a characteristic pattern on the surface of the raceway and it can be seen where the engraver has impacted the surface a total of four times, producing a series of valleys with material raised around the periphery of the defect forming a series of peaks. These peaks, as seen for all of the defects tested, can be seen to reduce in height following the bearing defect being tested.

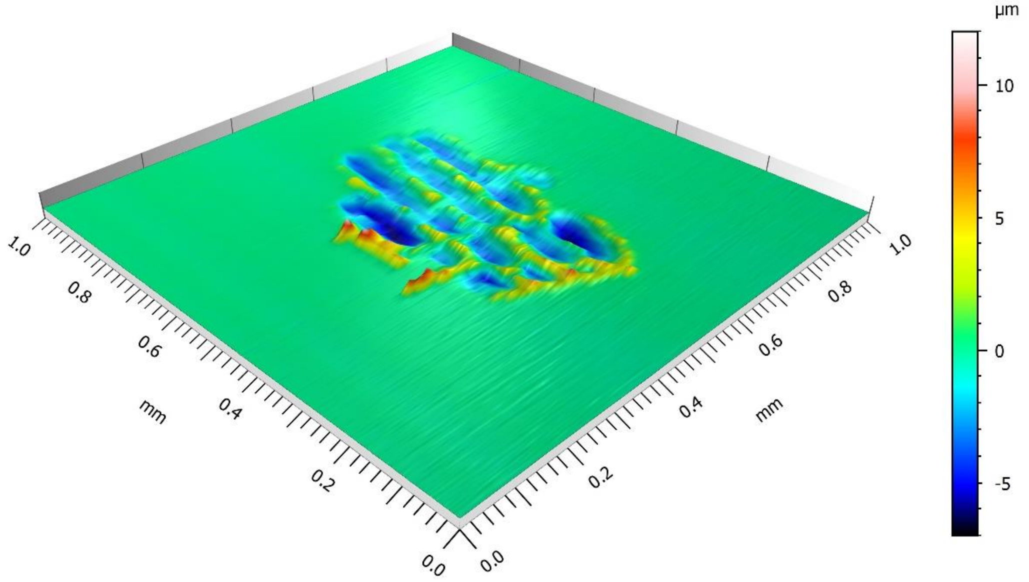

Figure 4-33 - Defect 1 Pre-Test

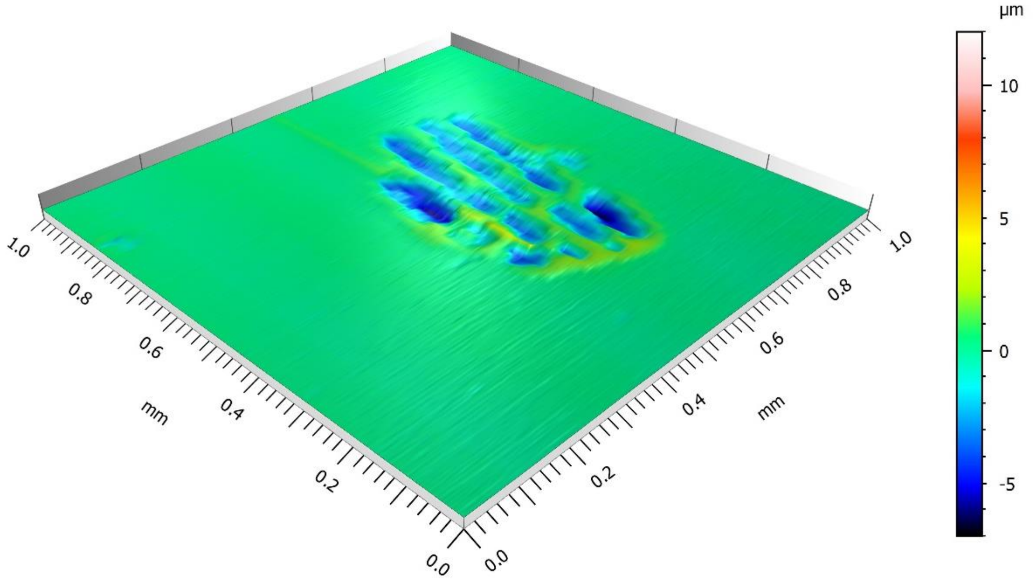

Figure 4-34 - Defect 1 Post-Test

Figure 4-35 and Figure 4-36 plot the 3D measurement of Defect 2 before and after being tested respectively. Defect 2 expanded on the first defect, Defect 1, and it can be seen that an increased amount of damage is applied slightly lower than where the initial defect was placed although the two still intersect. The dimensions of the defect are increased to approximately 0.6 x 1mm.

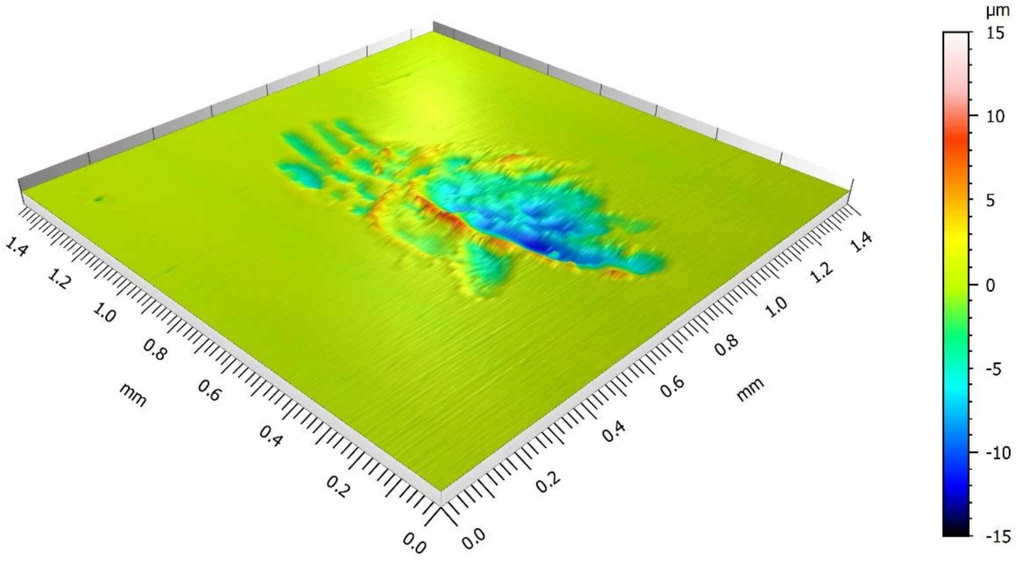

Figure 4-35 - Defect 2 Pre-Test

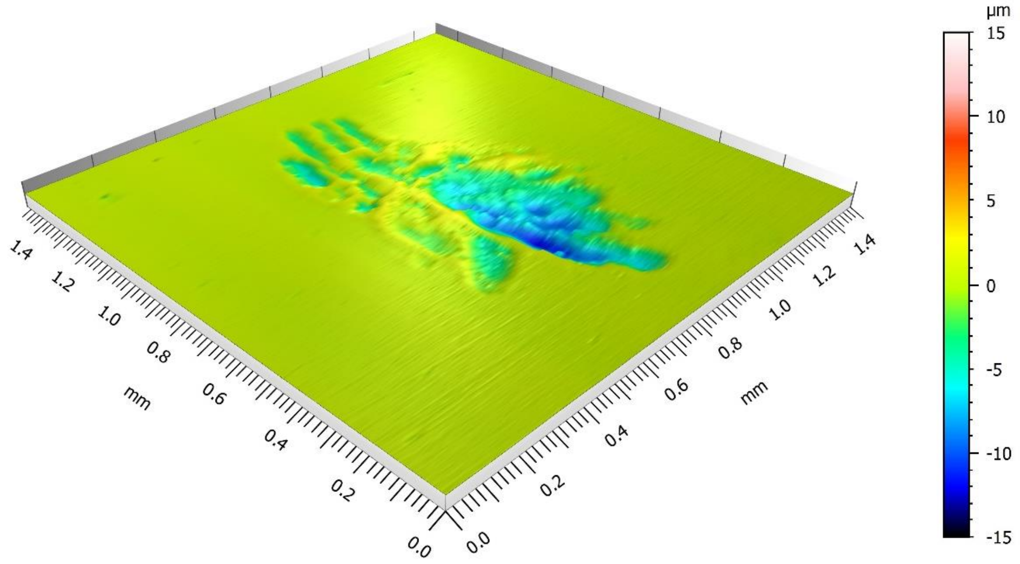

Figure 4-36 - Defect 2 Post-Test

Figure 4-37 and Figure 4-38 plot the 3D representation of Defect 3 before and after being tested respectively. For this iteration of the defect, the centre defect was left unchanged, and two further defects were added on the outer edges of the outer raceway, however still within the path of the roller contact. The far left defect was much larger than the other two, both in dimension and depth at 0.8 x 1mm and approximately 20µm deep. The increased size and depth of this defect also meant that more material was placed around the defect periphery. The defect introduced on the right hand side was the smallest of the three defect at approximately 0.5 x 0.5mm.

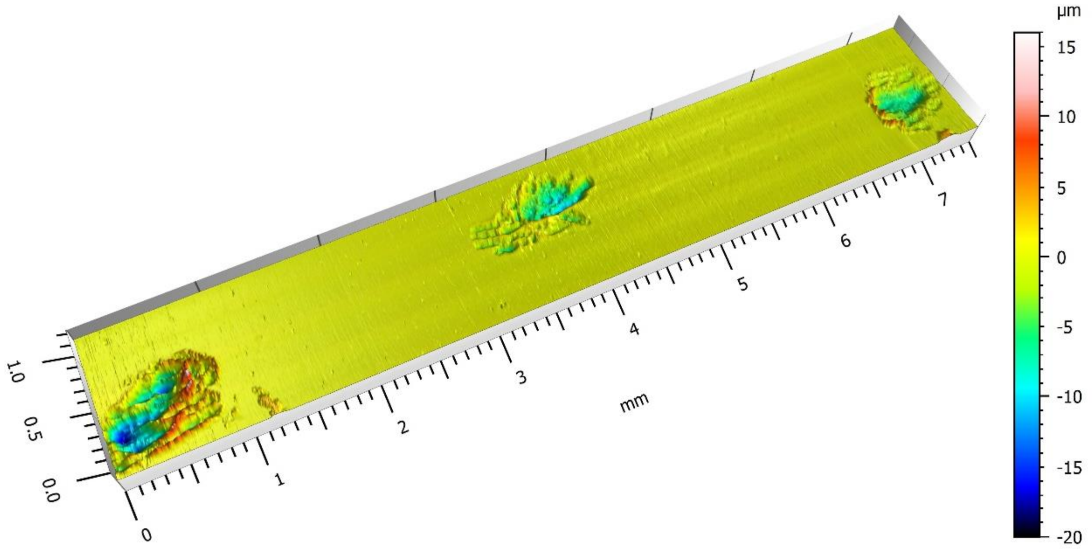

Figure 4-37 - Defect 3 Pre-Test

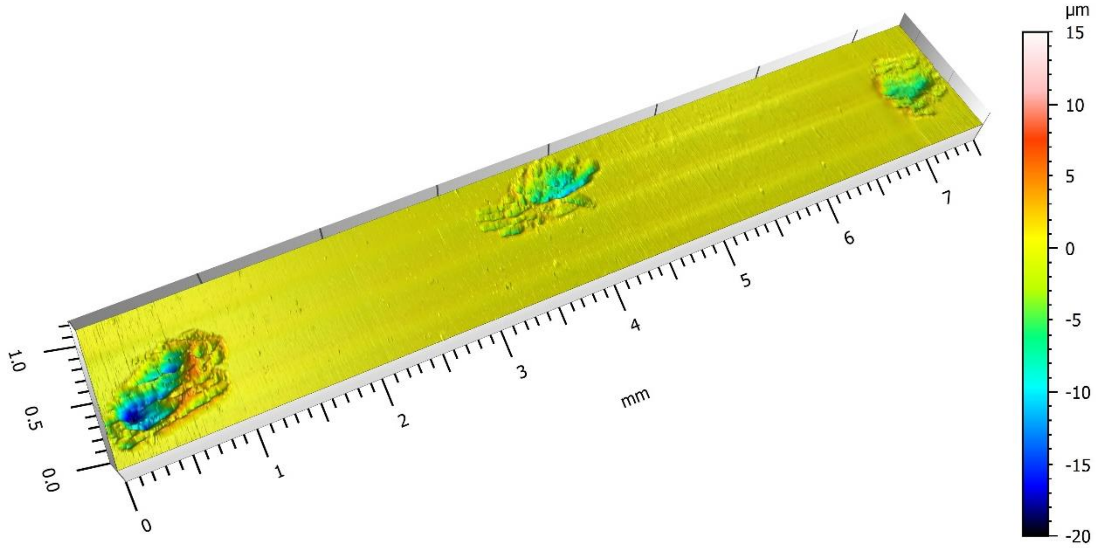

Figure 4-38 - Defect 3 Post-Test

Figure 4-39 plots the 3D representation of Defect 4 prior to testing commencing. Unfortunately, the Defect 4 post-test Talysurf file became corrupted and, due to the nature of the way the defect was grown by building on top of previous defects, the author was unable to re-measure the post-test defect. Defect 4 introduced a further two engraved defects in between the left hand defect and the centre defect as well as the right hand side defect and the centre defect. The dimensions of each defect remained relatively constant although it is worthwhile to note that the defects were not in a straight line due to the inherent inaccuracy of using a hand operated engraver.

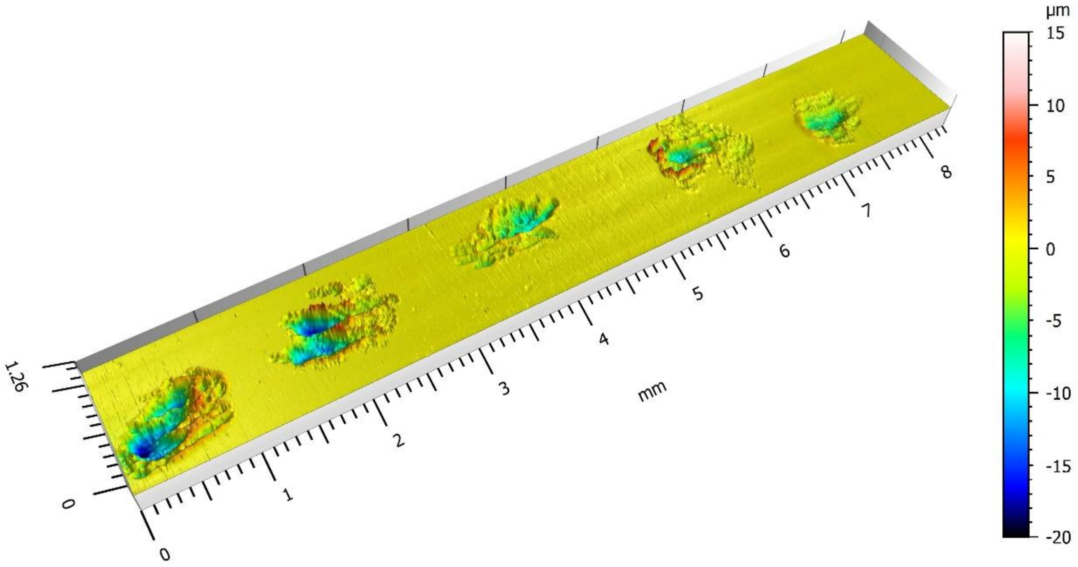

Figure 4-39 - Defect 4 Pre-Test

Figure 4-40 and Figure 4-41 plot the 3D representation of Defect 5 before and after being tested respectively. Defect 5 saw the introduction of a thin line connecting each of the 5 separate defects and the characteristic form of an engraved defect, where material is pushed away, can be seen in the chevron pattern as the line extends from left to right.

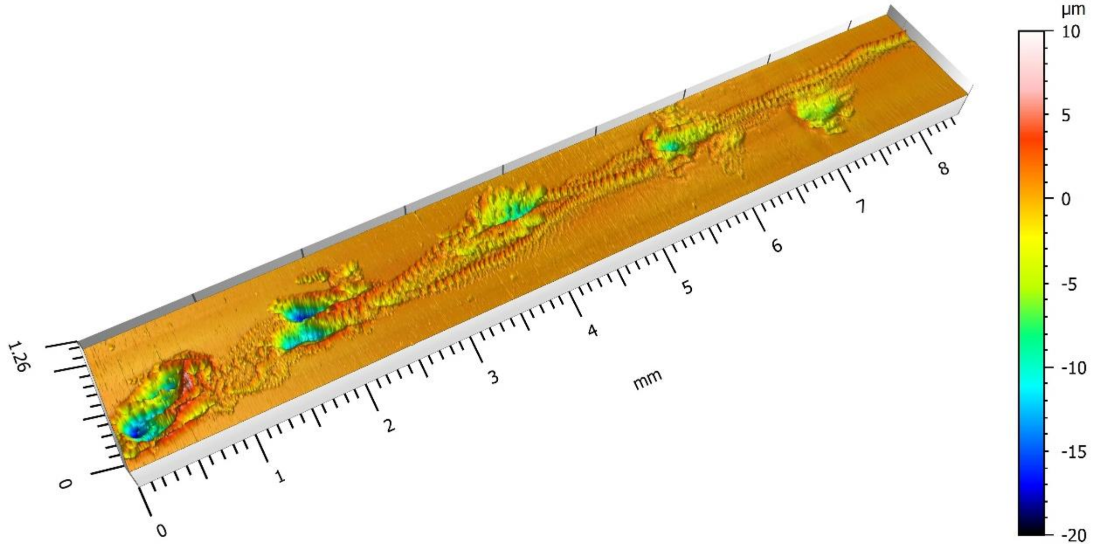

Figure 4-40 - Defect 5 Pre-Test

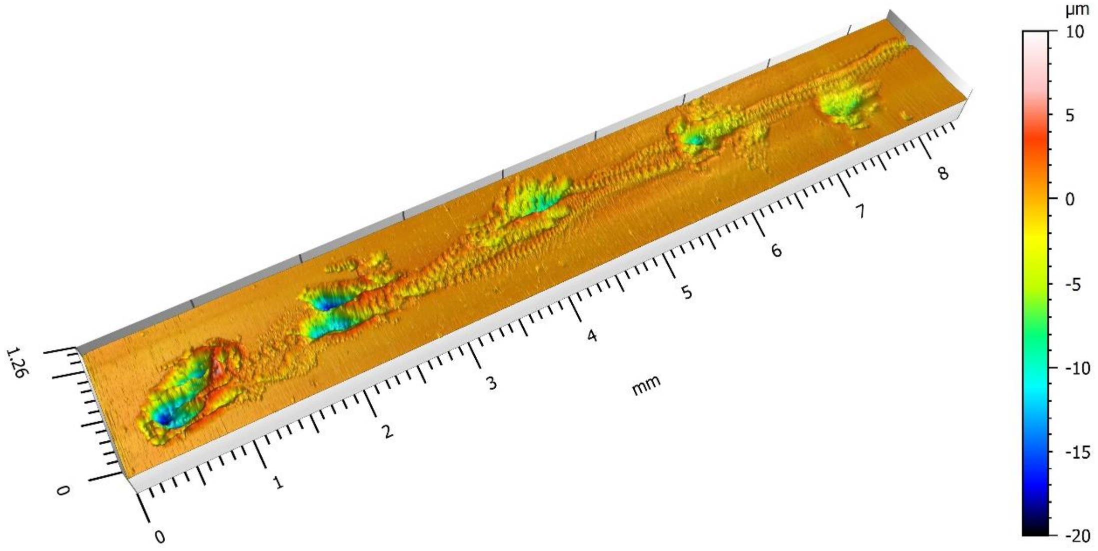

Figure 4-41 - Defect 5 Post-Test

Figure 4-42 and Figure 4-43 plot the 3D representation of Defect 6 before and after the test respectively. Defect 6 increases the size of the defect by passing the engraver repeatedly over the surface of the raceway. As a result, it is difficult to identify the individual defects applied from Defect 1 – Defect 4, however the effect of over-rolling is particularly clear as all of the large peaks have been removed in the post test scan.

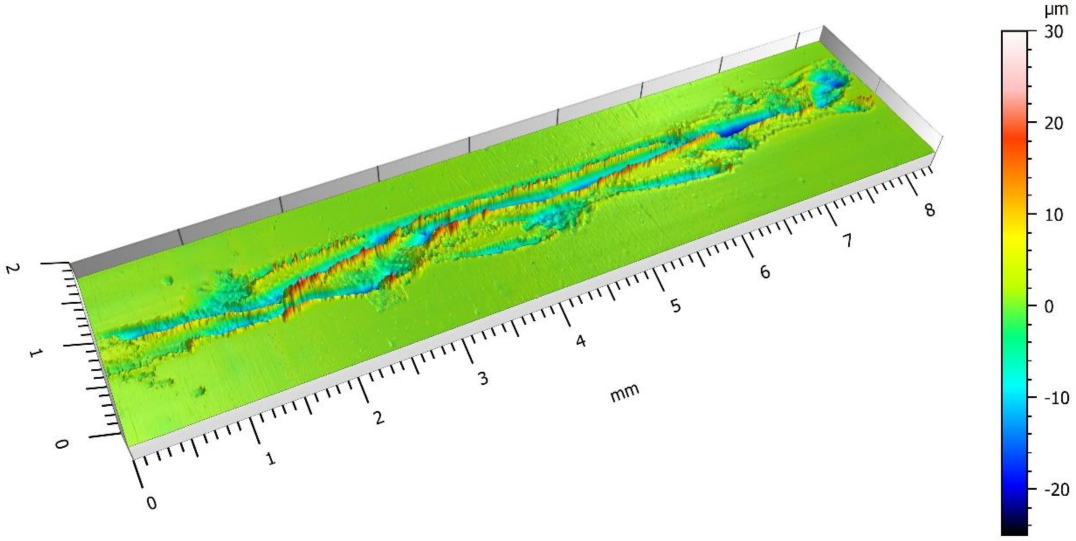

Figure 4-42 - Defect 6 Pre-Test

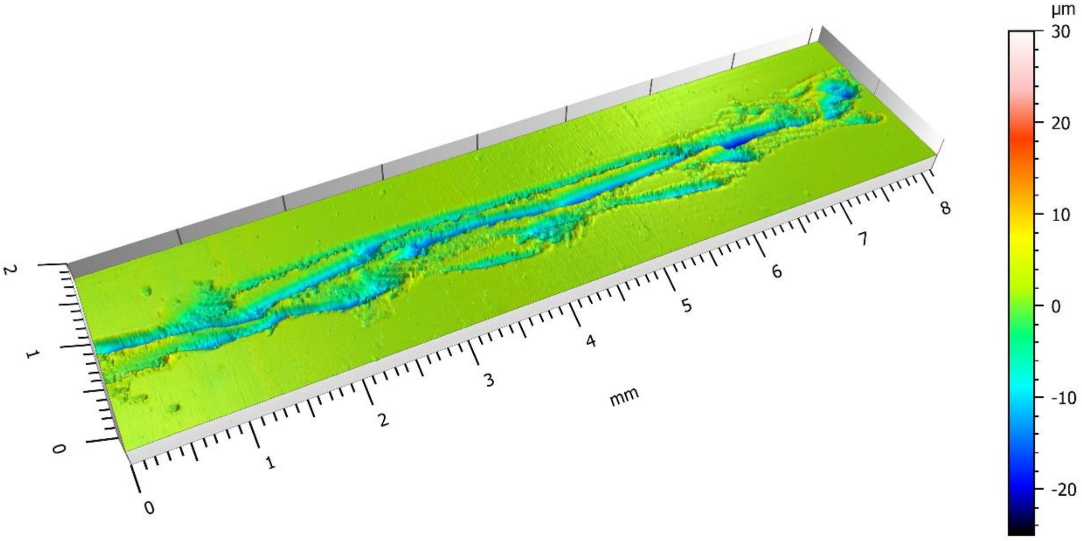

Figure 4-43 - Defect 6 Post-Test

4.6.3 Results

Figure 4-44 plots the RMS amplitude of the wavestreams recorded for Defects 1-6 as well as healthy data. It can be seen that with the addition of the smallest defect, Defect 1, the RMS amplitude increases. The same occurs with Defect 2 but there is a sharp decrease in RMS as the seeded defect is altered from being a single point defect, to multiple surface defects across the surface of the outer raceway. It was initially thought that the decrease may be due to erroneous data, but it can be seen that as the defect was expanding from Defect 3-6, where the damage remained at the same width across the raceway but increases in severity, that the RMS value also increases. If the response of Defect 3 was in fact erroneous, the author would expect to see a larger difference between Defect 3 and 4, as well as the other two defects applied after this. Therefore, it is thought that by spreading the damage across the raceway, there is a greater contact area available for stress distribution.

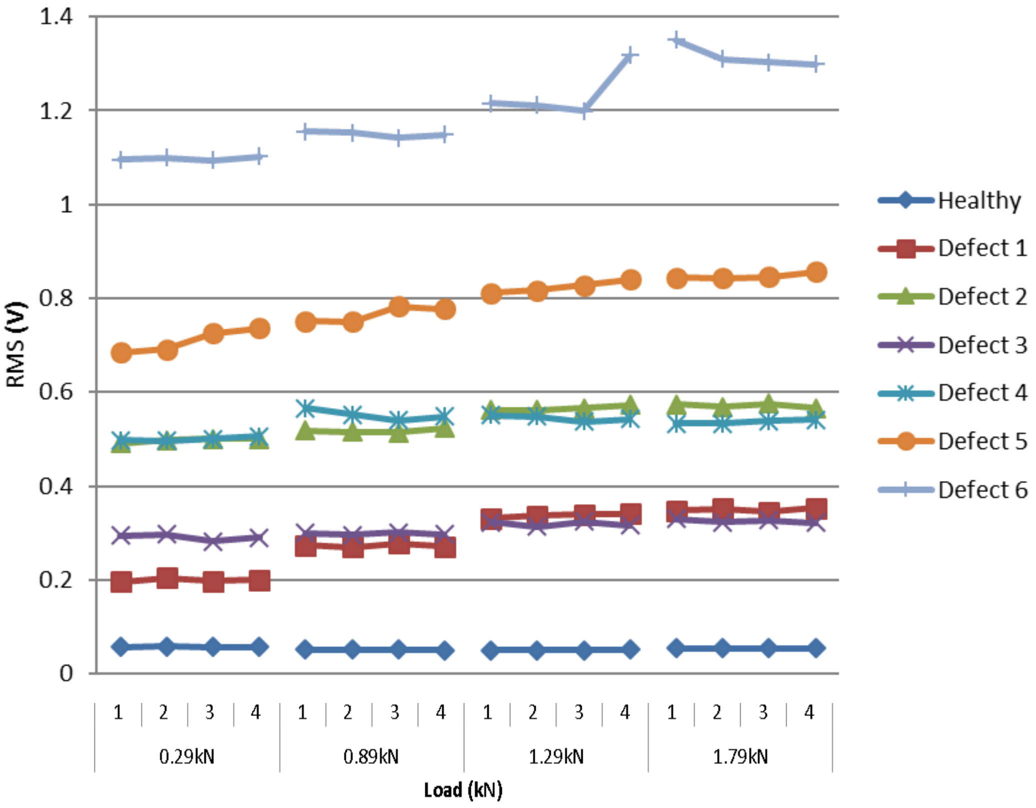

Figure 4-44 - RMS Amplitude of Defects 1-6 from wavestreams recorded on PCI-2 AE System

As shown in studies by other researchers, Al-Ghamd and Mba (2006) and Al-Dossary *et al.* (2009), the analysis of the seeded defects investigated in this experiment demonstrates that even the smallest of irregularities on the raceway of a bearing has the potential to be detected through condition monitoring techniques. The RMS values clearly show that there is a distinct difference when a defect is introduced to the outer raceway however, as shown in Section 4.5, the disassembly/reassembly process plays a pivotal role in the signals produced, potentially changing the response with each iteration. Therefore, it is important to analyse the response of individual signals using binned frequency analysis to determine high frequency response and order analysis combined with, where necessary, weak signal extraction methods in an attempt to detect the characteristic defect frequencies associated with artificial defects on the outer raceway.

4.6.3.1 Raw Signals

Figure 4-45 plots a raw signal for each of the six defects, demonstrating how the signal changes with increasing defect size. Even to the naked eye, periodic transients are witnessed within Figure 4-45.a, the smallest of the defects seeded onto the outer raceway. The resolution of these transients compared to the background noise however produces a very low SNR. The SNR of Defect 2 however, is much greater even though the background noise has also increased in amplitude. As seen in Defect 1, Defect 3 has low amplitude, periodic transients visible and the reduction in amplitude of both the transients and background noise is also reflected in the RMS values. Once the defects are joined up with an engraved line running through all three spalls, all of the periodic transients increase in amplitude, Defects 4, 5 and 6.

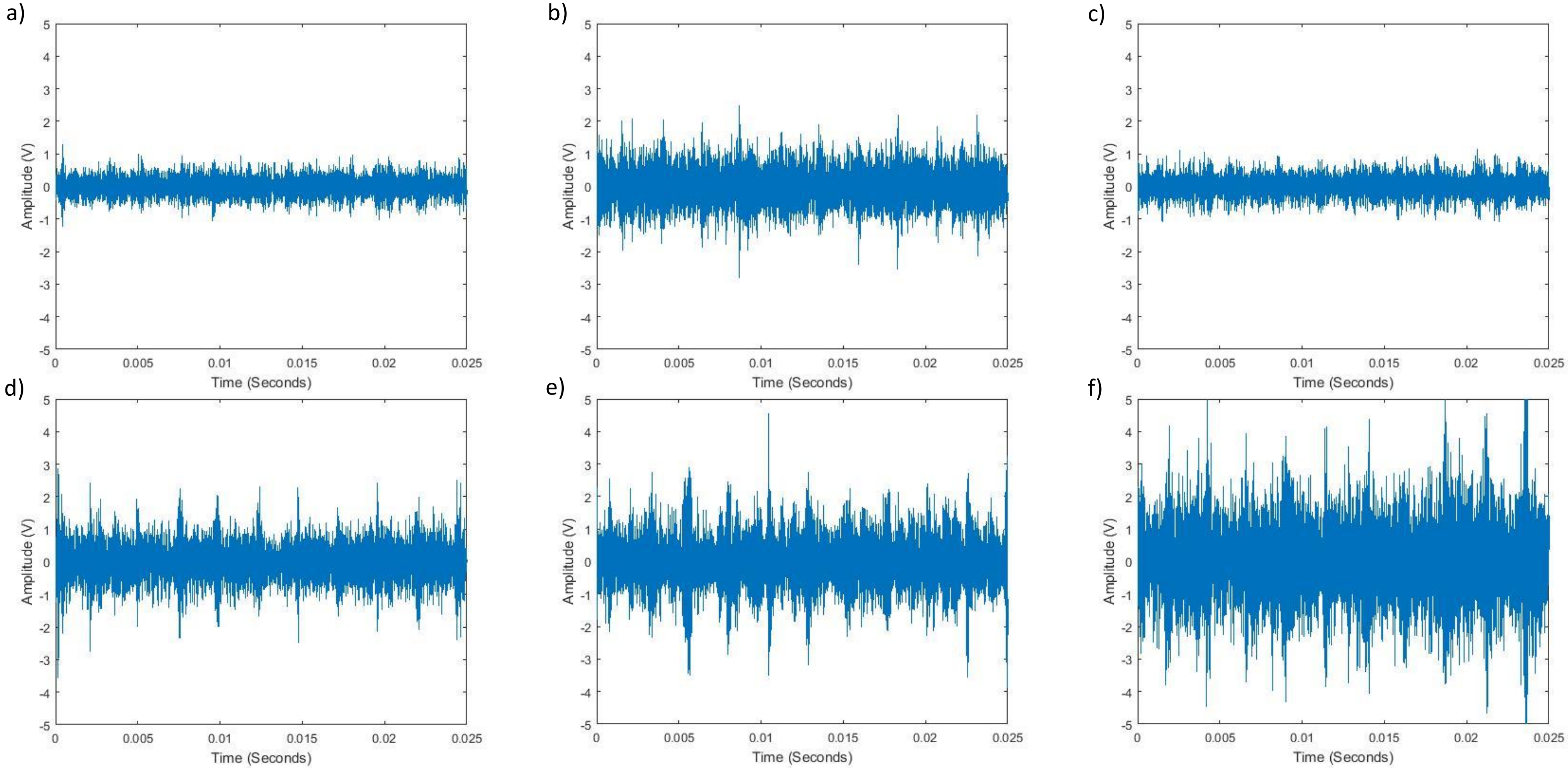

Figure 4-45 - Raw wavestreams recorded for a) Defect 1, b) Defect 2, c) Defect 3, d) Defect 4, e) Defect 5 and f) Defect 6

4.6.3.2 Binned Frequency

Figure 4-46, Figure 4-47 and Figure 4-48 plot the binned frequencies of the PCI-2 AE data between, 0-100kHz, 100-200kHz and 200-500kHz respectively. When analysed between 0-100kHz it can be seen that all of the defects, regardless of size, demonstrate increased amplitude at approximately 27kHz although from Defect 4 – Defect 6, where the defect was extended from individual spalls to a line across the width of the raceway, the dominant excitation frequencies are increased to 40 and 60kHz.

In the analysis of healthy bearings, Figure 4-22, it was seen that the signals RMS values were closely related to the energy amplitude at low level frequencies. Comparing the frequency spectrum of Defect 2 and Defect 3 however, the energy amplitude seems to be unaffected although a large drop was witnessed in the RMS values between Defect 2 and 3. There does however exist a significant difference in the spectrum when plotted between 100-200kHz where, for clarity, the scales are not consistent for all 6 defects. Instead, Defect 1, 3 and 4 are plotted with a maximum energy of $1x10^8$ V^2, Defect 5 is scaled to $3x10^8$ V^2, and Defects 2 and 6 have a scale of $2.5x10^9$ V^2.

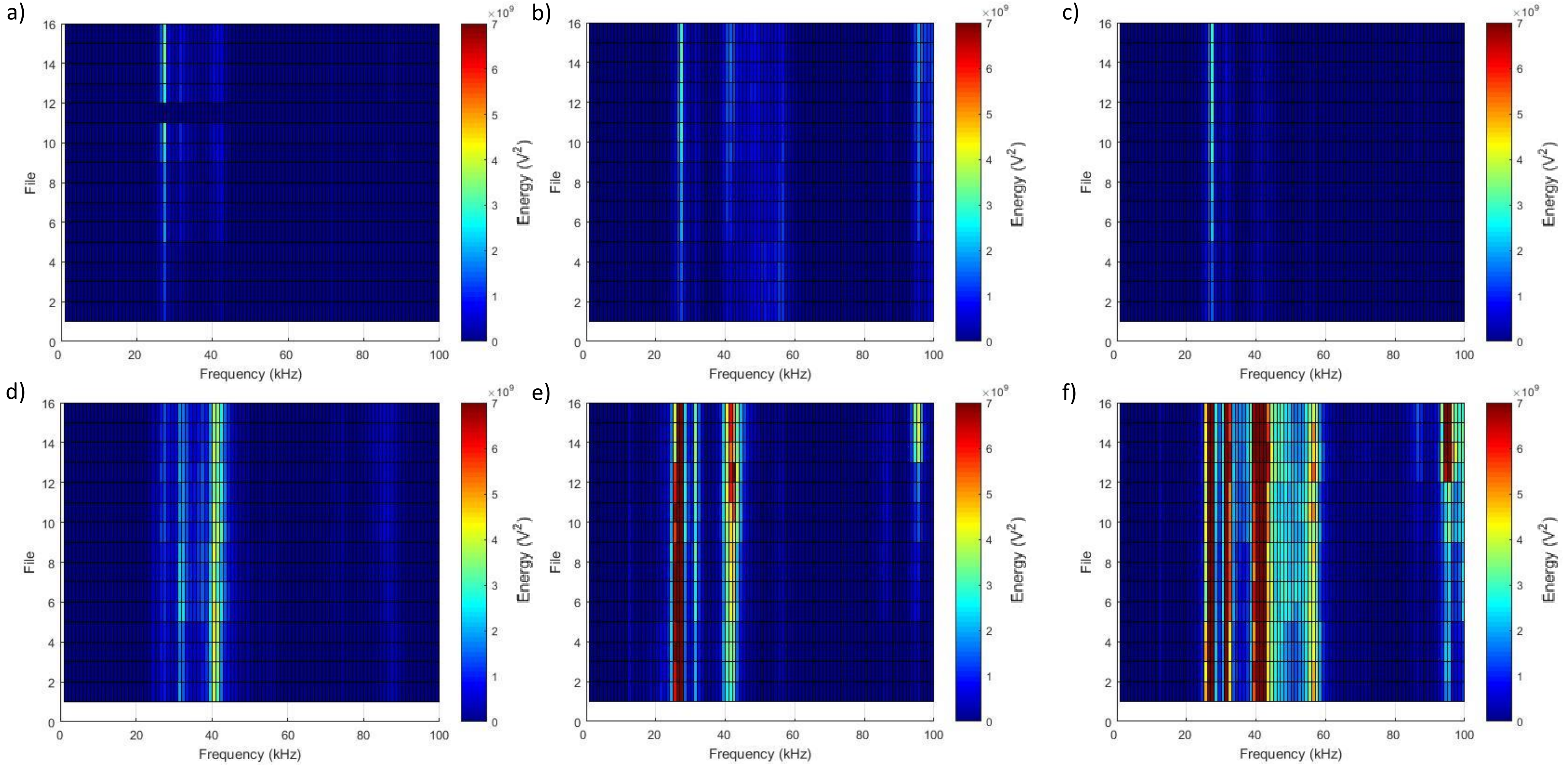

Figure 4-46 - Binned frequency plots of PCI-2 AE data between 0-100kHz for a) Defect 1, b) Defect 2, c) Defect 3, d) Defect 4, e) Defect 5, and f) Defect 6.

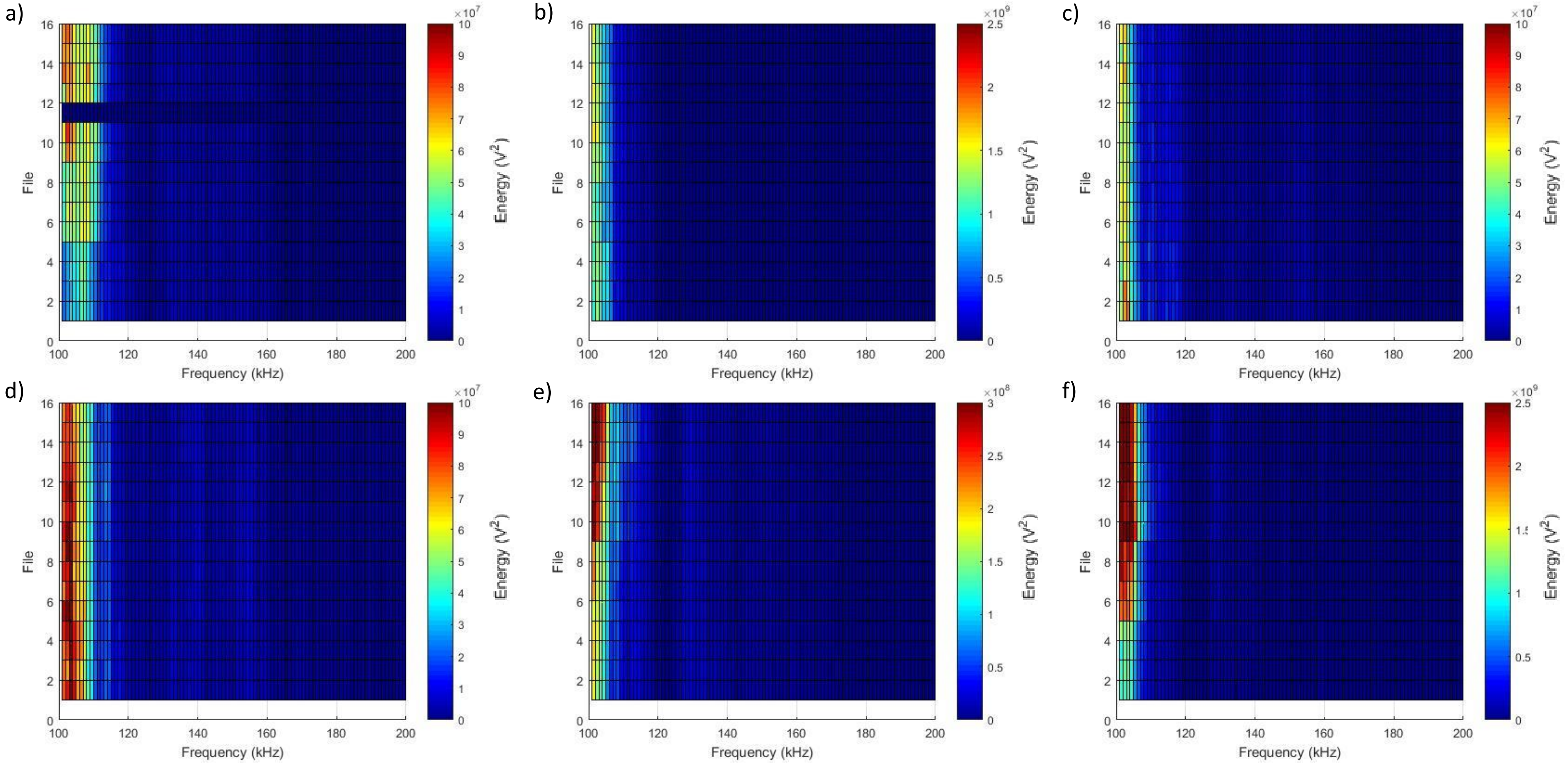

Figure 4-47 - Binned frequency plots of PCI-2 AE data between 100-200kHz for a) Defect 1, b) Defect 2, c) Defect 3, d) Defect 4, e) Defect 5, and f) Defect 6.

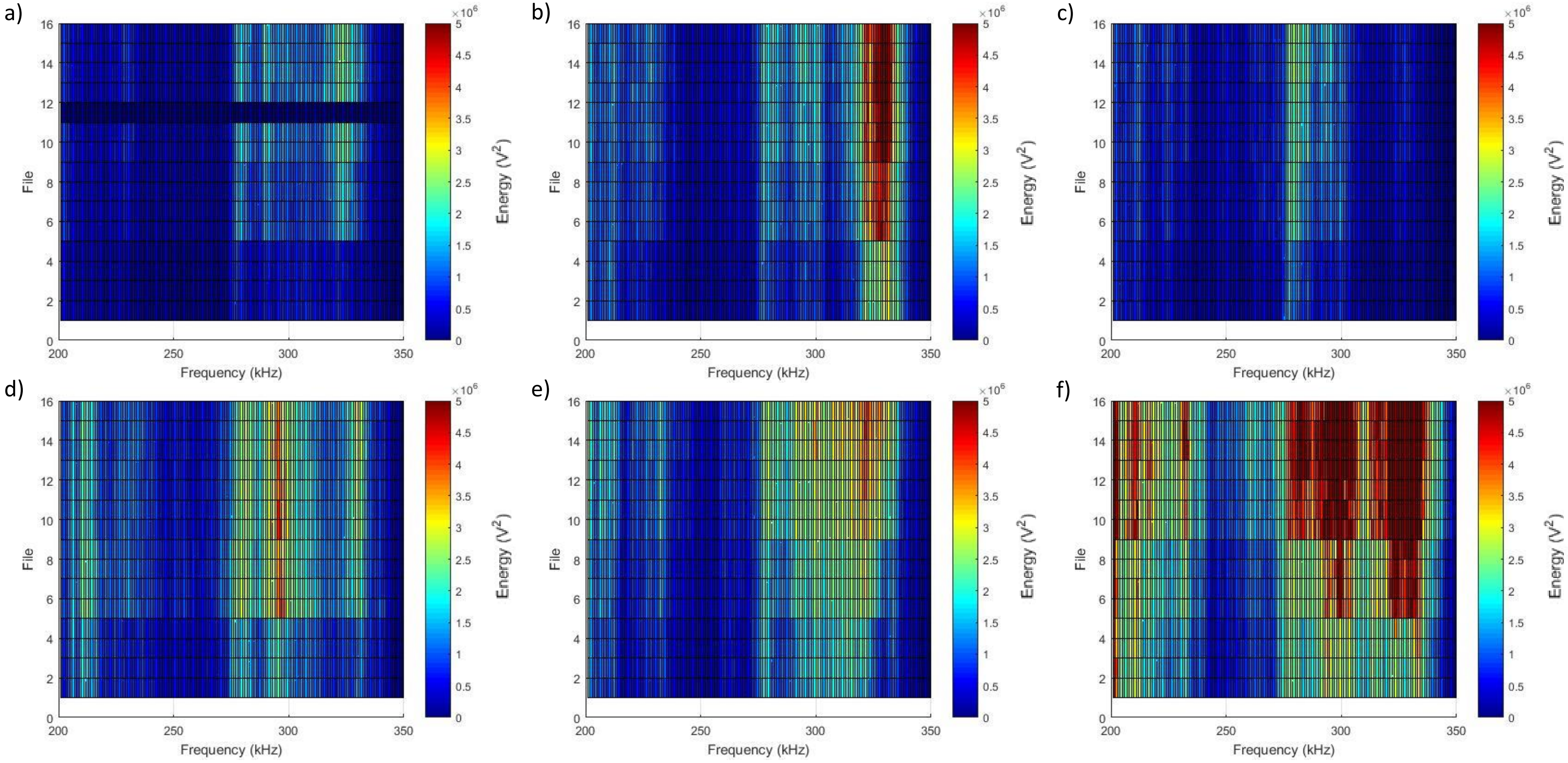

Figure 4-48 - Binned frequency plots of PCI-2 AE data between 200-350kHz for a) Defect 1, b) Defect 2, c) Defect 3, d) Defect 4, e) Defect 5, and f) Defect 6

The significant contrast in the amount of energy at frequencies around 100kHz between Defects 2 and 3 indicates that the type of defect affects the frequencies excited. Defect 2 had a large number of peaks around the valley created as material was forced away through engraving and was centred in the raceway as shown by Figure 4-49.a, the surface measurement prior to the test commencing. Surface measurement following the running of Defect 2 however demonstrates that the peaks have been smoothed by over-rolling Figure 4-49.b and this is common across all six defects as previously witnessed in Figure 4-33 - Figure 4-43.

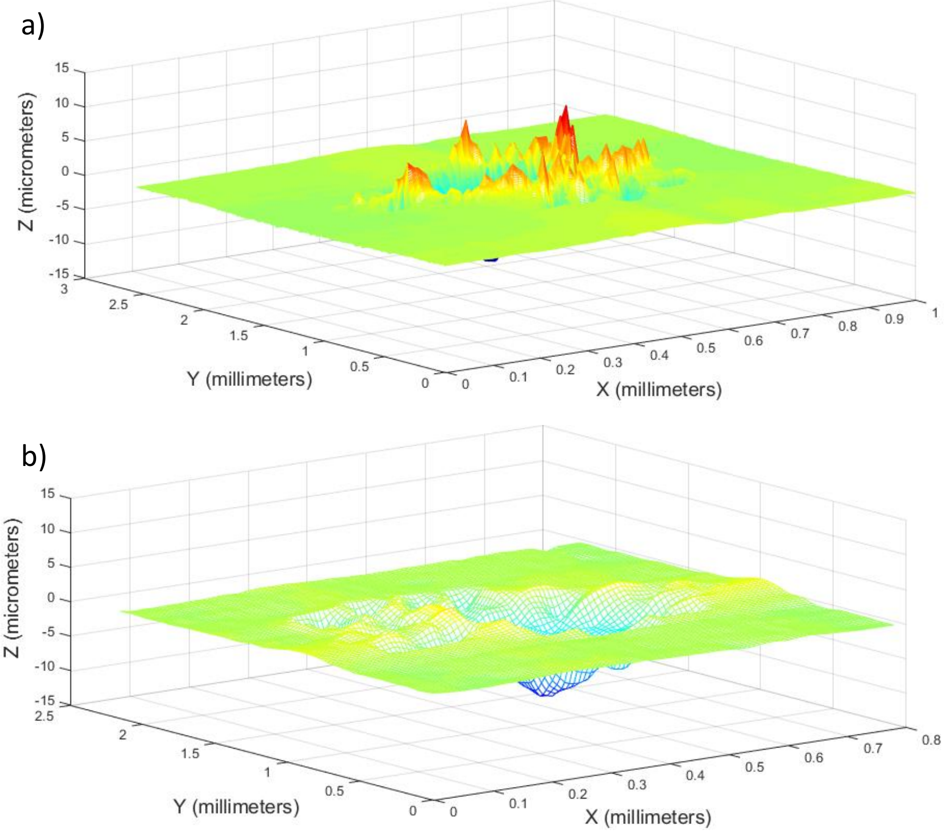

Figure 4-49 - Talysurf image of Defect 2 a) pre- test and b) post-test

As previously discussed in Section 4.5, the increase in energy amplitude of the frequencies around 100kHz may be attributed to the amount of plastic deformation occurring, as seen by Ramadan *et al.* (2008), as well as the build-up and over rolling of debris particles as the peaks are flattened by over-rolling, as demonstrated by Chang *et al.* (2009) in their study of particle interaction in the sliding contacts within a hard disk drive. Also, as the amount of debris increases, the bearing friction will also increase, complementing the work of Ferrer *et al.* (2010).

Although also seen in other frequency ranges, the spectral range of 200-350kHz demonstrates an increased sensitivity of the sensor's resonant frequency to changes in the radial load applied. When the radial load is applied by only the mass of the load arm, (i.e. no additional masses are added), the energy is relatively low but as the additional masses are added, there is a significant increase in the amount of spectral energy between 300-350kHz. As this is load related, and the increase is more significant than that previously witnessed in the healthy bearing frequency response, Figure 4-25, there may be a link between higher frequencies and plastic deformation during asperity contact.

Figure 4-50.a-f plots the order spectrum of the raw wavestreams recorded during the experimentation of Defects 1-6 respectively. It can be seen that for Defects 1 and 3, there is significant lack of periodicity in any of the first 10 orders. Defect 2 demonstrates energy at 4.3 orders, corresponding to the BPFO of the outer raceway. The cumulative energy of the BPFO in Figure 4-50b is relatively low despite the periodic bursts being easily visible within the raw signal (Figure 4-45.b). As the size of the defect was increased, Defects 4, 5 and 6, the energy at the BPFO, 4.3 orders, increases significantly, and there is also energy at the second BPFO harmonic, 8.6 orders. It is thought that the detection of the BPFO for Defect 2 within an order plot is difficult due to the high frequency components, contained within the periodic bursts of the raw signal, masking the low frequency bursts.

In order to enhance the visibility and detection of orders within the damaged signal, the raw signals were passed through a Hilbert Transform in order to envelope the signal, and hence improve low frequency resolution. A Hilbert Transform produces an analytical signal formed of both real and imaginary parts and can be used to provide information about the instantaneous amplitude and instantaneous phase of the signal. The instantaneous amplitude is the part of the Hilbert transform used to envelope the signal.

Figure 4-51.a-f plots the order spectrum of the enveloped data, helping to improve the visibility of low frequency components across all of the defects. As the binned frequency plots now contain higher energy levels, the envelope order spectrums of Defects 4,5 and 6 are plotted with an order of magnitude difference in z-axis when compared to Defects 1,2 and 3. When analysed with a Hilbert transform, the order analysis of the enveloped signal allows for the first two harmonics of the BPFO, 4.3 and 8.6 orders to be distinguished for Defect 1, which was previously undetectable in the order analysis of the raw signal.

This, however, does not determine the positive detection of the damage on the outer raceway. As seen in Figure 4-26, the order analysis of a healthy bearing also demonstrates frequencies at the BPFO. This is because the BPFO is a geometrically determined frequency and hence exists with or without the presence of damage. The only difference is in the amplitude of the BPFO. Other characteristic frequencies of the bearing components are not visible so therefore, this does demonstrate that for a seeded defect, the BPFO for a very small defect on the outer raceway can be detected using AE. There is also significant energy at approximately 2 orders, which also increases in energy as the defect grows. It is thought that this may be the detection of the 2nd harmonic of the shaft frequency.

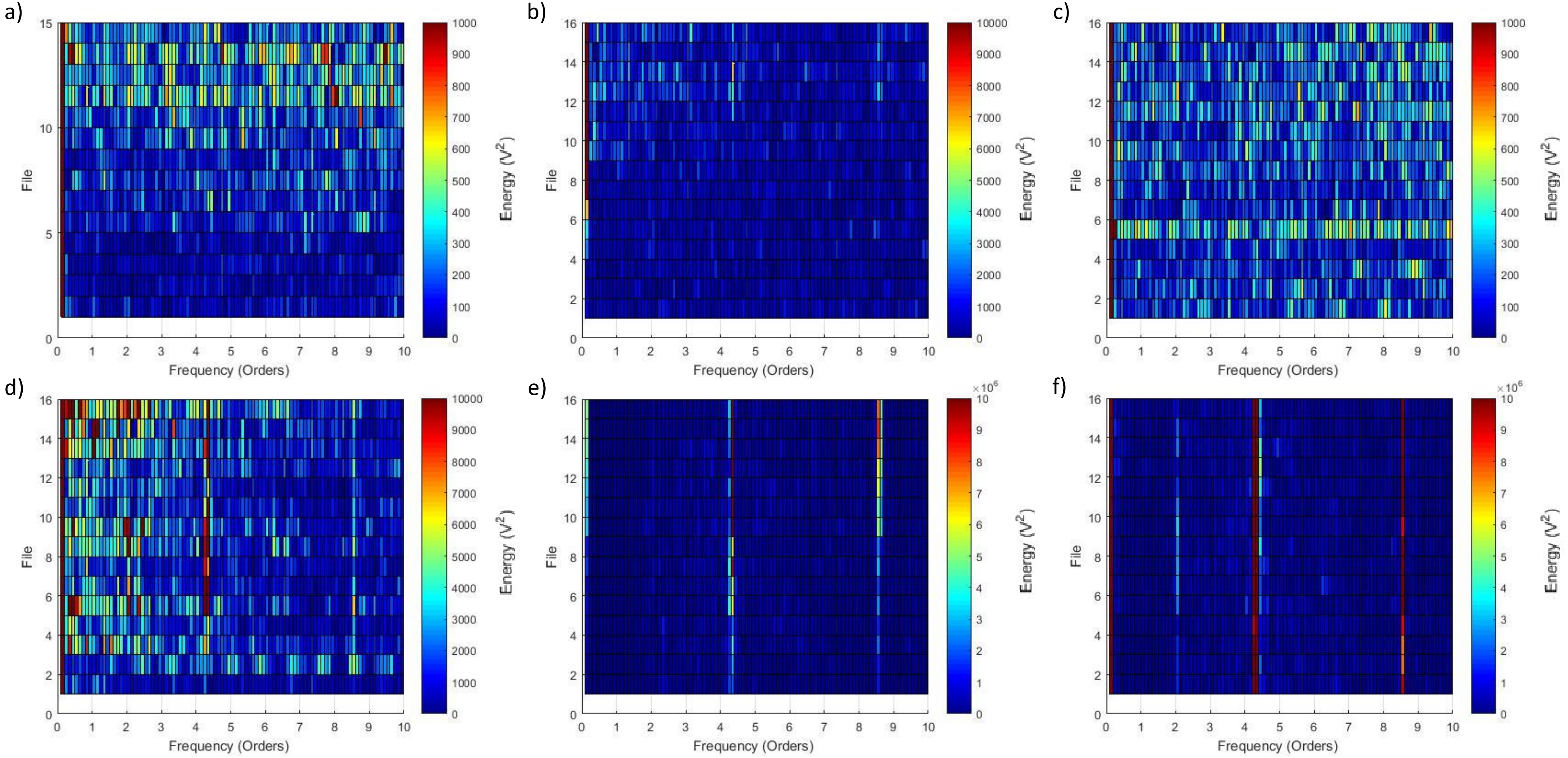

Figure 4-50 - Frequency plots with respect to shaft orders of raw PCI-2 AE data for a) Defect 1, b) Defect 2, c) Defect 3, d) Defect 4, e) Defect 5, and f) Defect 6

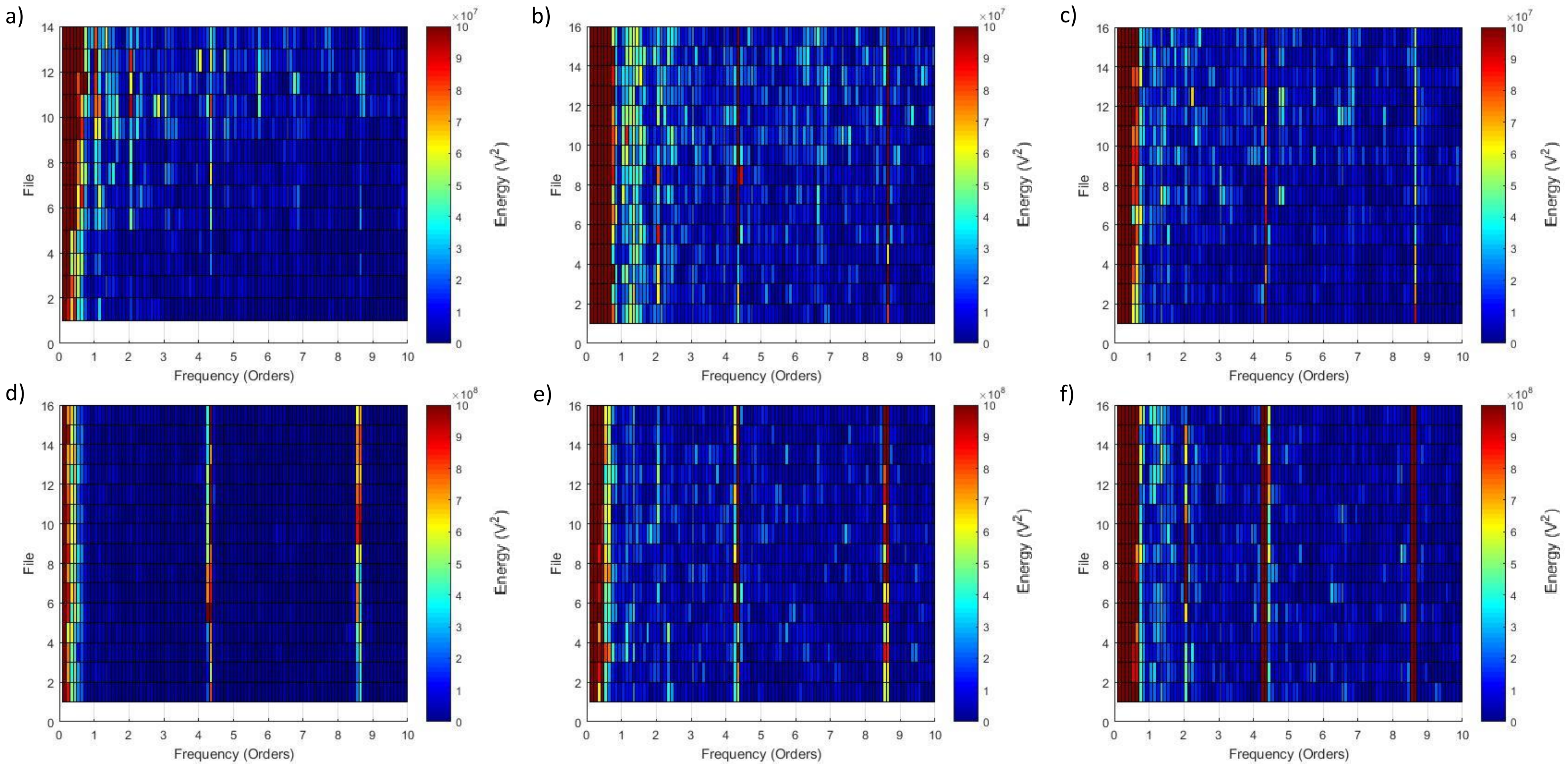

Figure 4-51 - Frequency plots with respect to shaft orders of Hilbert transformed PCI-2 AE data for a) Defect 1, b) Defect 2, c) Defect 3, d) Defect 4, e) Defect 5, and f) Defect 6

4.6.4 Discussion

Through the analysis of seeded defects engraved onto the outer raceway, it has been demonstrated that AE is able to detect small seeded defects through the analysis of the raw signal by means of RMS amplitude, increases in spectral energy and the excitation of orders relating to the BPFO. An enveloping technique, the Hilbert transform, was able to enhance the detection of the smallest of defects, Defect 1, and may prove to be useful in detecting damage initiation when allowing a bearing to degrade naturally through life tests.

The drop in both RMS amplitude and transient periodicity between Defect 2 and 3 raises questions about what exactly is being detected from the seeded defects. In Al-Ghamd and Mba (2006) it was shown that a smooth defect showed significantly less energy when compared to one where material was raised above the average asperity height within the raceway. The increase in energy and RMS for coarse defects determines that the AE signals are produced by the contacts of raised edges, plastic deformation, over-rolling of debris and debris being entrained through the contact. Comparing the frequency spectrum of Defect 2 and 3 there was little difference in the spectrum between 0-100kHz but orders of magnitude difference in energy between 100-200kHz. As seen in the healthy bearing analysis, the lower frequency bands are excited more with increasing speed as this is the region when bearing/system resonant frequencies are excited. The difference in excitation energy at 100-200kHz further suggests that the over rolling of debris, plastic deformations, debris entrainment and potentially increased friction excite frequencies in this bandwidth.

The initial, simple analysis of the raw signal using RMS shows that even small defects on the bearing surface can produce a change. These AE measurements, however, are taken directly above the bearing and it is thought that when the machine becomes more complex, it will become less and less possible to be able to use RMS to detect bearing damage as there may be influential factors from gears, shafts, seals etc. Also, as with all seeded defect research within the literature, the effect that the disassembly and reassembly process has on the recording of AE is largely unknown. As demonstrated in Section 4.5, the AE response can change dramatically with each test rig set up and, as a result, in order to determine if defects can successfully be detected using AE, life tests are required.

4.7 Life Tests

4.7.1 Section Overview

Section 4.6 demonstrated that, although not representative of how true bearing defects occur or look, seeded defects are able to demonstrate how AE responds to changes on the bearing raceways. However, as the test rig is disassembled between each test, there is a large amount of uncertainty as to the validity of the results. Therefore, the following section performs accelerated life tests on an SKF N204ECP bearing in order to determine the sensitivity of each condition monitoring technique to naturally propagated bearing damage. Two types of accelerated life tests were conducted, altering the length of time taken until the test bearing failed.

The first life test, Section 4.8, applied the radial load with a cylindrical roller placed between the load arm and bearing housing. This arrangement caused the load to be unevenly distributed along the outer-raceway as the load applied to the load arm was misaligned due to a stack up of manufacturing tolerances. Overloading in this manner increases the stress concentration in the area of contact, resulting in the quick initiation of a bearing failure which, for this example, occurred after a total of 12 hours of operation.

The second life test, Section 4.9, transferred the radial load from the load arm to the bearing housing via a ball bearing, eliminating any misalignment between the load arm and the bearing housing as the contact between the two was altered from a line contact to a point contact. Being a far less aggressive method of bearing testing, the bearing was run for a much longer period of time, approximately 2800 hours, before signs of bearing failure became apparent.

Prior to each of the life tests being performed, a healthy bearing characterisation was carried out to the same test schedule as in Section 4.5, and therefore the data gathered during the life test can be compared to the characterisation data which is used as a healthy benchmark. Being able to examine the damaged bearing following the test aids in the data analysis process as it is known where the defect occurred and its severity. The first life test, Life Test 1, resulted in test bearing failure at both the inner and outer raceway and the second life test produced a rolling element failure, also resulting in pitting of the outer and inner race way.

4.8 Life Test 1

4.8.1 Experimental Set-Up

Following a healthy bearing characterisation test, the speed and load were increased incrementally until a final speed and radial load of 5980rpm and 5700N respectively were achieved at 1.75 hours after the start of the test (Figure 4-52). These conditions remained constant until the bearing had failed. The bearing failure was determined through the rise of signals on the data acquisition systems as well as there being an audible difference.

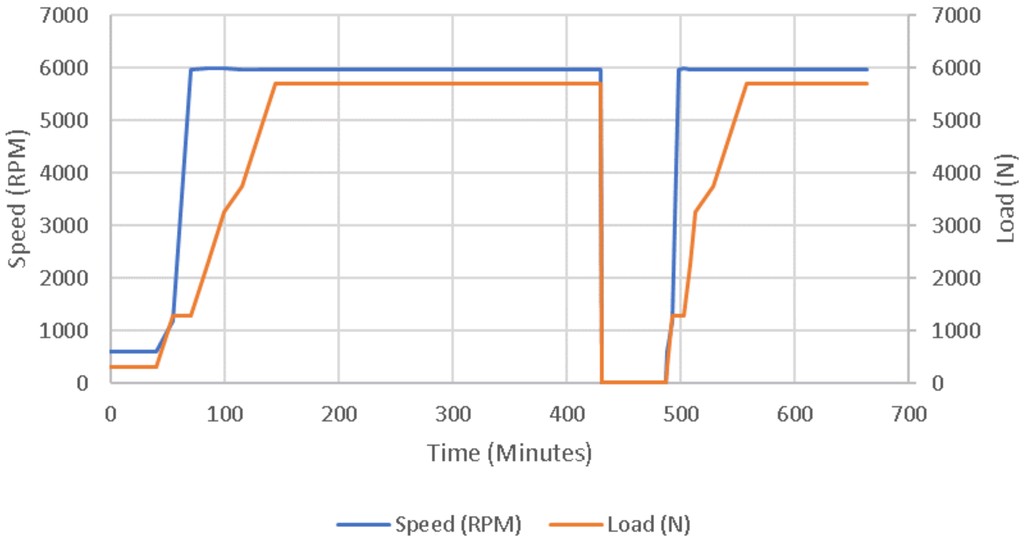

Figure 4-52 - Experimental overview for Life Test 1

For comparison, AE was recorded on both a PCI-2 and ACMS system and vibration was also recorded using the ACMS system with the wavestreams recorded every 15 minutes throughout the test duration. Sensor type and location remained the same as those described in Section 4.3.2. As this experiment hoped to induce significant wear within the bearing, the pre-amplifier gain for the PCI-2 was set to 20dB to prevent the potentially high signal levels being amplified beyond the range of the AE system. It was not possible to change the gain levels of the ACMS system and hence these remained at 40dB.

4.8.2 Bearing Failure Overview

Figure 4-53 shows the extent of the damage observed on the inner and outer raceway upon being disassembled after a running period of 12 hours. The damage on the outer raceway is localised to the point of maximum load and it can be seen that the front face of the outer race as viewed in Figure 4-53 was overloaded through misalignment due to the shape of the damage area. The damage on the inner raceway covers over 270˚ of the bearing surface due to the point of maximum load on the inner raceway changing as the shaft, and hence inner race, rotates (with a fixed outer raceway). Despite such extensive damage occurring on each of the two raceways, there was no visible damage on any of the rollers.

Figure 4-53 - Test bearing damage post-test

4.8.3 Results

4.8.3.1 Data Overview

Figure 4-54, Figure 4-55 and Figure 4-56 are the RMS amplitude plots of all four bearings over the accelerated life test calculated from wavestreams recorded on the PCI-2, ACMS AE and ACMS Vibration systems respectively. It can be seen in all figures that, as discussed in Section 1.5, when the speed is low, the RMS amplitude of the signal also remains low. However, once the speed reached 5980rpm after a period of 1.75 hours, the RMS signal levels increase to values similar to those witnessed in the healthy bearing characterisation for each system respectively. The RMS amplitude remains constant for approximately 5.5 hours, and after the experiment has been running for a total of 7 hours, the test bearing RMS amplitude increases significantly across all systems. The test was paused at this point to allow for visual observations of the test bearing in an attempt to determine if the bearing was damaged. The test was then allowed to continue to run until catastrophic failure had occurred as the experimental time surpassed the 11-hour mark.

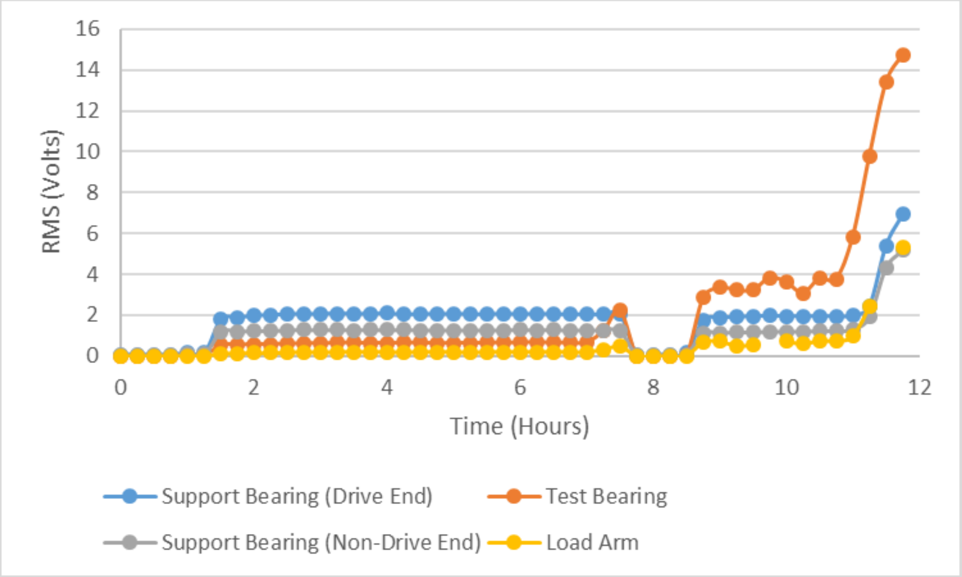

Figure 4-54 - RMS amplitude of PCI-2 AE life test data

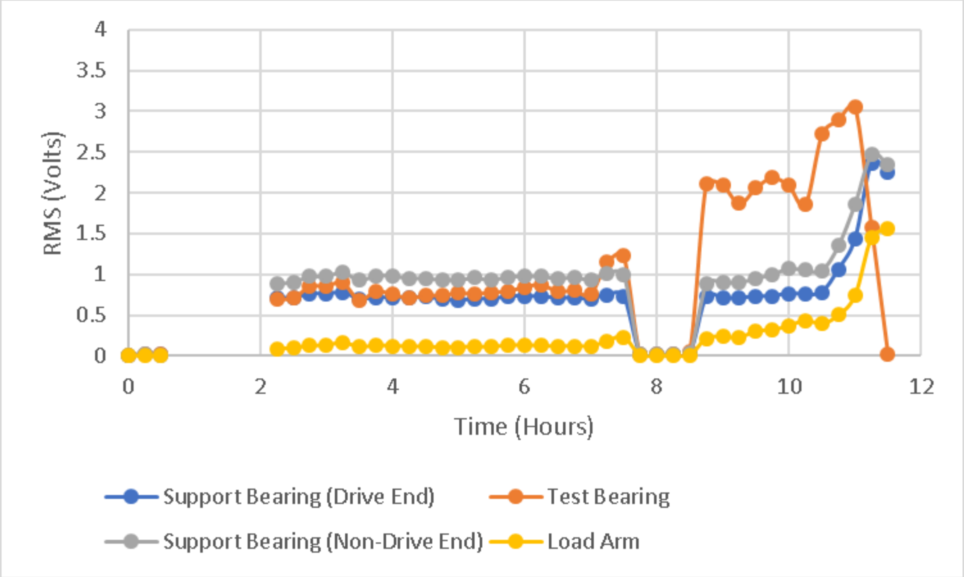

Figure 4-55 - RMS amplitude of ACMS AE life test data

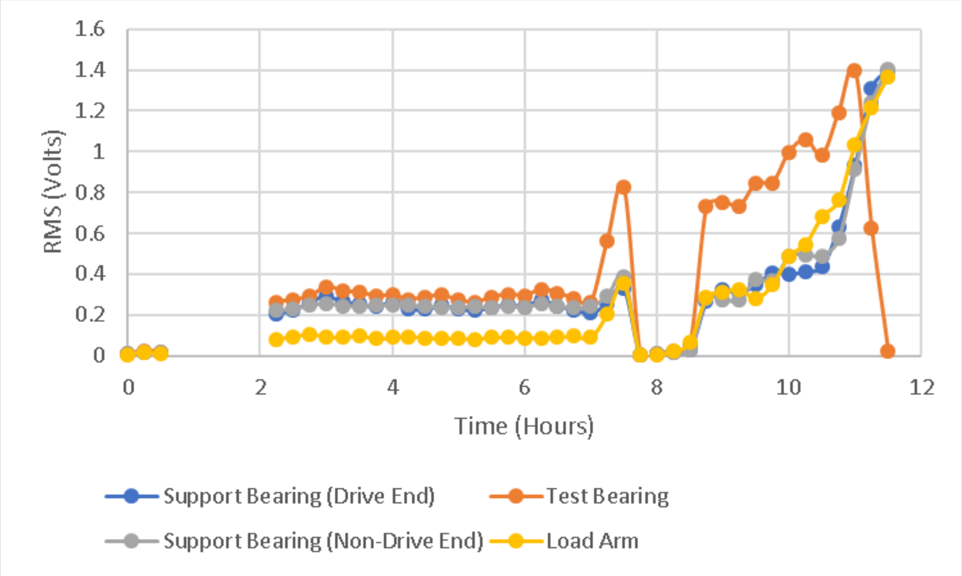

Figure 4-56 - RMS amplitude of ACMS Vibration life test data

The RMS amplitude plots show that on all three systems used, a change in bearing condition was detected after approximately 7 hours. The RMS response of the AE and vibration signals differs as the damage initiates. For the vibration sensors, whilst the largest increase in RMS amplitude can be seen in the two sensors connected to the test bearing and load arm, there is, however, also a small increase in the RMS amplitude of the two support bearings. For AE however, the RMS response seems to only increase in the channels monitoring the test bearing and load arm. Following a short period of inactivity, where the test rig was stopped for inspection, it can be seen that the RMS amplitude continues from its previous peak and continues to grow as the damage propagates further. It can also be seen in Figure 4-55 and Figure 4-56, the response of ACMS AE and Vibration respectively, that as the damage increases in severity, the sensor mounted to the test bearing became uncoupled from the bearing housing due to the large oscillations experienced, causing the RMS to drop to zero at approximately 11 hours.

4.8.3.2 Raw Signals

Figure 4-57, Figure 4-58 and Figure 4-59 plot the raw signals recorded from the PCI-2 AE, ACMS AE and ACMS Vibration systems respectively, where figure ‘x.a’ is the signal before the initial rise in RMS amplitude after 7 hours and figure ‘x.b’ is the signal recorded 15 minutes after and, hence, is responsible for the rise in RMS amplitude.

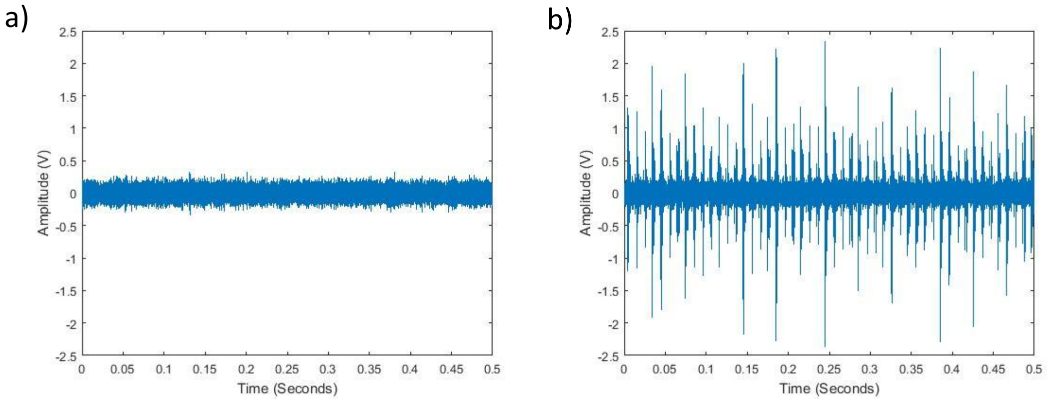

Figure 4-57 - Raw signals from PCI-2 AE system a) before initial increase in RMS amplitude, and b) after initial increase in RMS amplitude.

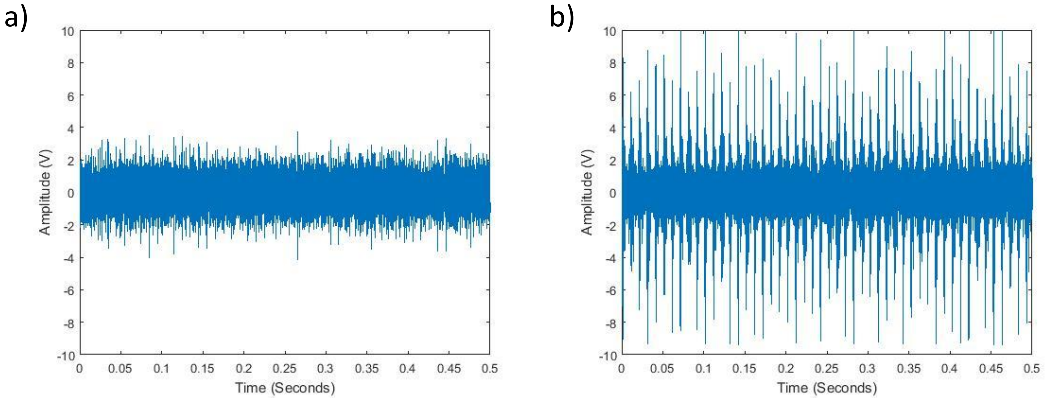

Figure 4-58 - Raw signals from ACMS AE system a) before increase in RMS amplitude, and b) after increase in RMS amplitude.

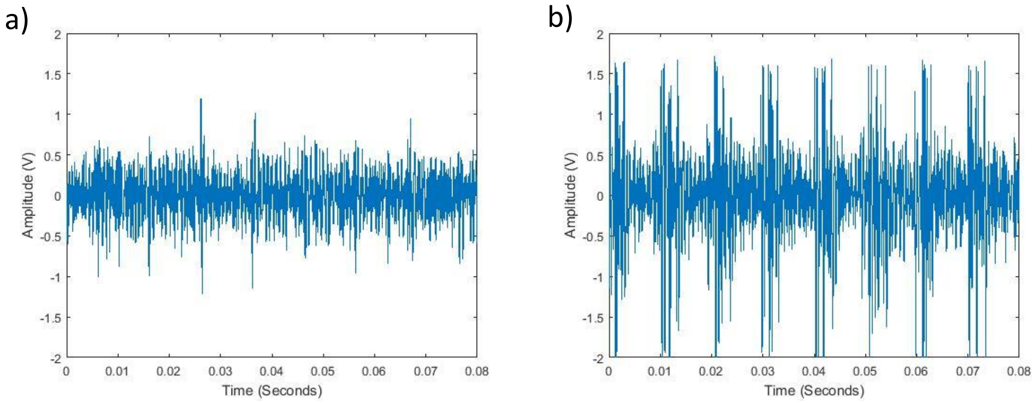

Figure 4-59 - Raw signals from ACMS Vibration system a) before increase in RMS amplitude, and b) after increase in RMS amplitude.

Through visual analysis of all ‘a’ plots, it can be seen that there exist weak periodic transient bursts within the background noise however, these periodic bursts are masked in the PCI-2 AE, less so in the ACMS AE but become much better pronounced in the vibration signal. Being monitored over two different systems it is difficult to know with certainty the exact time difference of recording for the two systems and hence whether the ACMS wavestreams were recorded a short while after the PCI-2 wavestream when the damage had begun to propagate. That said, with the maximum difference between the time of recording on the two systems at less than a minute, it is doubtful that the signals would have changed significantly. However, the signal to noise ratio of ACMS vibration vs. ACMS AE, two wavestreams recorded in succession on the same system, is highly significant. This demonstrates the difference in sensitivity due to the operating frequency range of the sensor as the vibration sensor will require less energy in order to excite low level frequencies when compared to the AE sensors.

The ‘b’ plots show the periodic transient bursts commonly associated with bearing failure and, through order analysis of each of the ‘b; plots, it was found that, for the PCI-2 data the frequency band containing the most energy existed at 6.8 orders, relating to the BPFI of the test bearing, with separate peaks occurring at a separation of 1 shaft order (Figure 4-60).

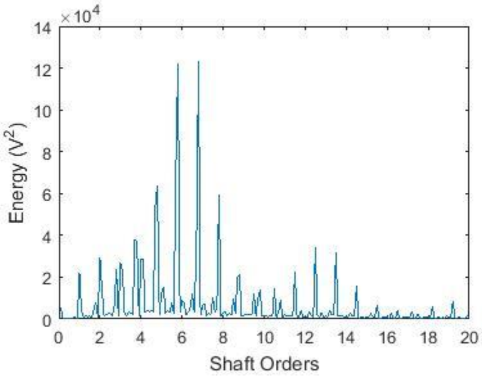

Figure 4-60 - Order analysis of Figure 4-57.b

This is a clear indication that damage initiation began upon the inner raceway, and literature suggests that the damage must be significant at this point as transients have a large number of interfaces to pass through (Morhain & Mba 2003). Order analysis of the AE and vibration data presented in the ‘b; designation of Figure 4-58 and Figure 4-59 fails to show any large peaks in the orders below 12 shaft orders (Figure 4-61).

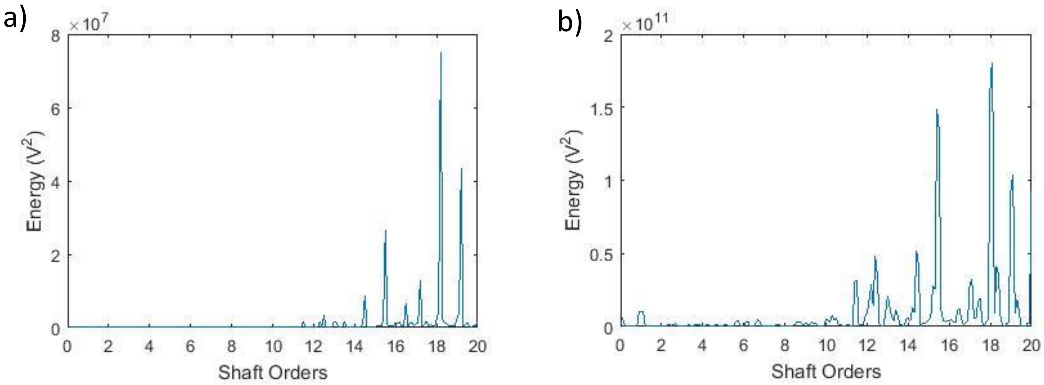

Figure 4-61 - Order analysis of a) Figure 4-58.b and b) Figure 4-59.b

Instead, the energy peaks at approximately 18 orders although there is a small amount of energy at 6.9 orders for the order analysis of the vibration data Figure 4-61.b. Visual analysis, manually counting the number of peaks between two set times, however confirms that the transient bursts present in Figure 4-58 and Figure 4-59 do occur at the BPFI. It is thought that the clipping of the signals as they reach the maximum range of the sensor may be responsible for the lack of detection of the BPFI from the raw signal. The wavestreams on all systems were gathered every 15 minutes and, due to the way bearing damage propagates it is likely that the damage initiated due to a small spall, smooth defect or subsurface defect on the inner raceway. It is thought by the author that in the 15 minutes between the two wavestreams being recorded that the damage has become significant enough to affect a whole roller, and has perhaps spread across the width of the raceway. That is not to say that the damage was not present beforehand, as it can be seen in the raw signals of all channels that low amplitude periodic bursts occurred in the wavestreams similar to those of Defect 1 in the seeded analysis tests (Figure 4-45.a).

4.8.3.3 Frequency Analysis

Figure 4-62, Figure 4-63 and Figure 4-64 are the binned frequency plots between, 0-100kHz, 100-200kHz and 200-500kHz respectively where the designations ‘a’ and ’b’ refer to data recorded on the PCI-2 and ACMS AE data respectively. As with the analysis of healthy bearings in Section 4.5, when running at slow speeds the energy content is significantly lower than when being run at 5980rpm and as a result there is no visible energy for the first 1.75 hours.

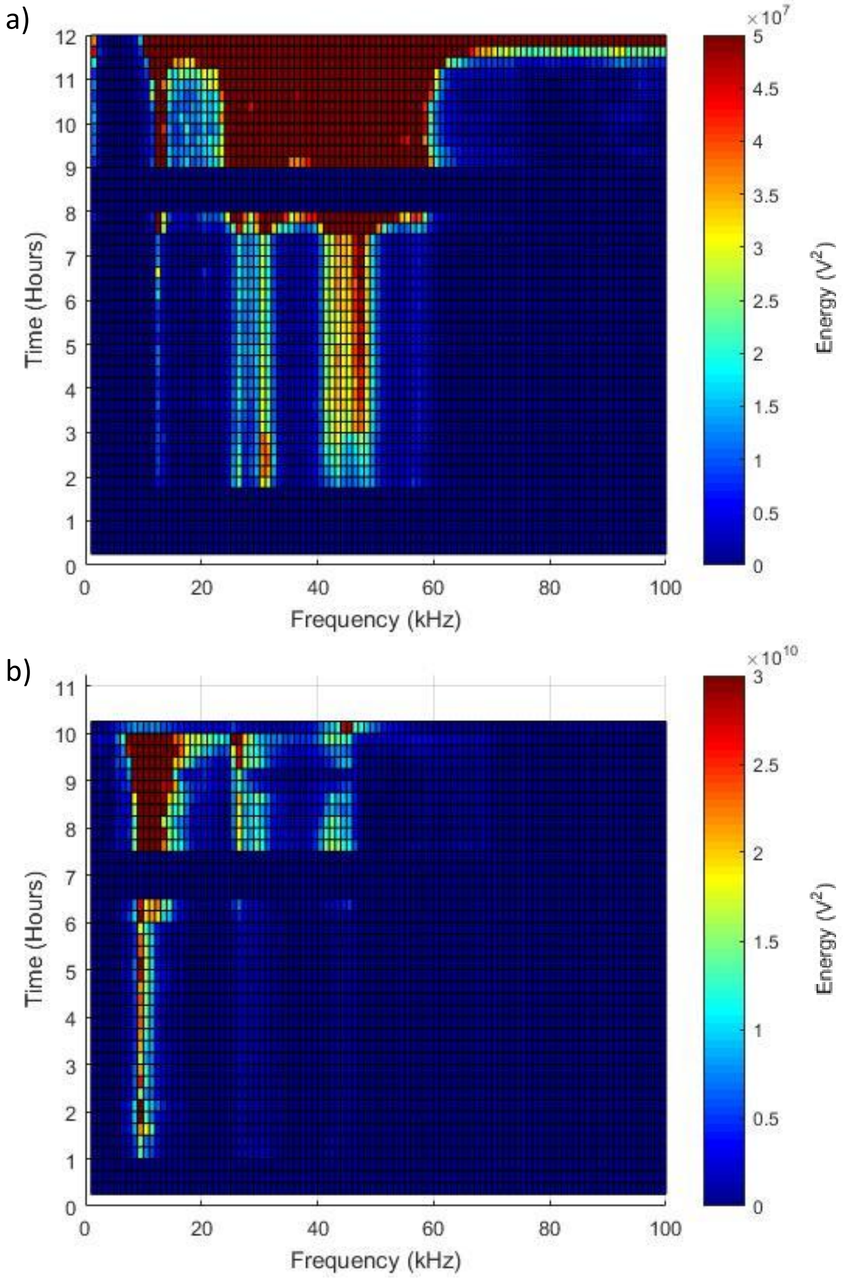

Figure 4-62 - Binned Frequency plot between 0-100kHz for a) PCI-2 AE data and b) ACMS AE data

Once the speed is set at 5980rpm however, Figure 4-62.a, the frequency response of the PCI-2 system shows strong excitation at 30kHz but as the load is increased, the energy amplitude at 30kHz reduces and instead higher excitation occurs at a band of 48kHz. The ACMS system however, Figure 4-62.b, is excited at 9kHz and this frequency band is excited regardless of the load applied. The change in excitation level for the PCI-2 system occurs as the maximum radial load is reached. Experimentation prior to this, in the healthy and seeded test, failed to load the bearing past 2.2kN and it may naturally be thought that the change in frequency is due to the change in resonant frequency as the overall bearing stiffness changes with load. However, if this were the case then the same trend would be likely to be witnessed across all data acquisition systems. Figure 4-22, the frequency plot of the healthy bearing characterisation data, demonstrated that as also seen in Figure 4-62, the ACMS AE signals were excited at approximately 10kHz whereas the PCI-2 data saw excitation at 60kHz. It is thought that the change in excitation frequency may be due to a change in the test rig setup, mainly due to the introduction of misalignment of the load although this cannot be confirmed without further testing (Section 4.9). It is also of note that as the damage propagates, the energy at all frequencies increases. Figure 4-62, Figure 4-63 and Figure 4-64 have had their scales changed in order to demonstrate more clearly the increase in frequency amplitude between 0-7.5 hours, as the damage is thought to be growing.

The dominant frequency band excitation remains consistent at 114kHz for the PCI-2 AE response between 100-200kHz, with a secondary excitation band at 127kHz (Figure 4-63.a). The ACMS AE response demonstrates excitation between 100-116kHz with the energy amplitude peaking at 101 and 107kHz. A significantly lower frequency band excitation can also be seen in Figure 4-63.b at 127kHz, matching the secondary frequency band of excitation of the PCI-2 system (Figure 4-63.a). During the healthy bearing analysis in Section 4.5, it was originally considered that the AE emitted between 100-200kHz, Figure 4-24, may be due to 2nd harmonics of the frequencies witnessed between 0-100kHz. However, as the dominant frequencies in Figure 4-62.a are below 50kHz, it is not possible that these are 2nd harmonics. There would also, in this circumstance, be a shift in the frequencies excited as the dominant frequency in Figure 4-62.a changes from 30kHz to 48kHz although there is no apparent shift in dominant frequency over the test duration in Figure 4-63.a.

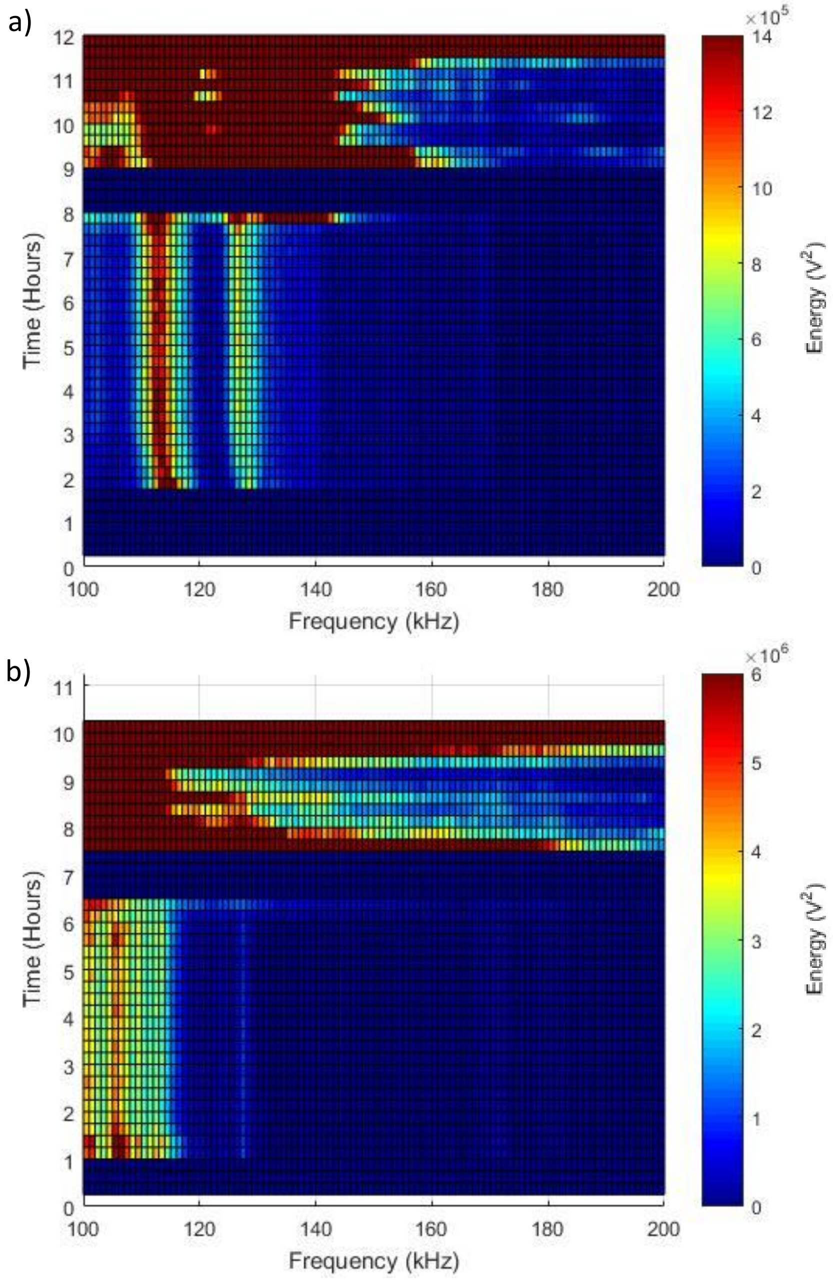

Figure 4-63 - Binned Frequency plot between 100-200kHz for a) PCI-2 AE data and b) ACMS AE data

Analysis of the frequency band between 200-500kHz during the healthy bearing analysis also suggested that these were harmonics and possible excitation of the sensor's resonant frequency. However, unlike what was previously seen in Figure 4-25, it can be seen in Figure 4-64.a that the energy at the frequency band of 330-340kHz seems to grow in amplitude between the 2nd and 8th hour of running. This frequency band is close to the resonant frequency of the Nano30 sensor used and may provide evidence of the bearing surface conditions changing during this time period as plastic deformation is often released at high frequencies. In contrast, Figure 4-64.b shows that the ACMS AE sensor has excitation bands at 220kHz and 230kHz but these bands do not grow in energy as seen in Figure 4-64.a. Instead they mirror the energy amplitudes seen in Figure 4-63.b and hence it is thought that these are in fact their 2nd harmonics. This is understandable however as the DFS6000 sensor, although it is marketed as an AE sensor, only has a working range up to 100kHz. Therefore, it is difficult for the ACMS sensor to detect anything above this frequency unlike the Nano30 sensor which has a much larger operating window.

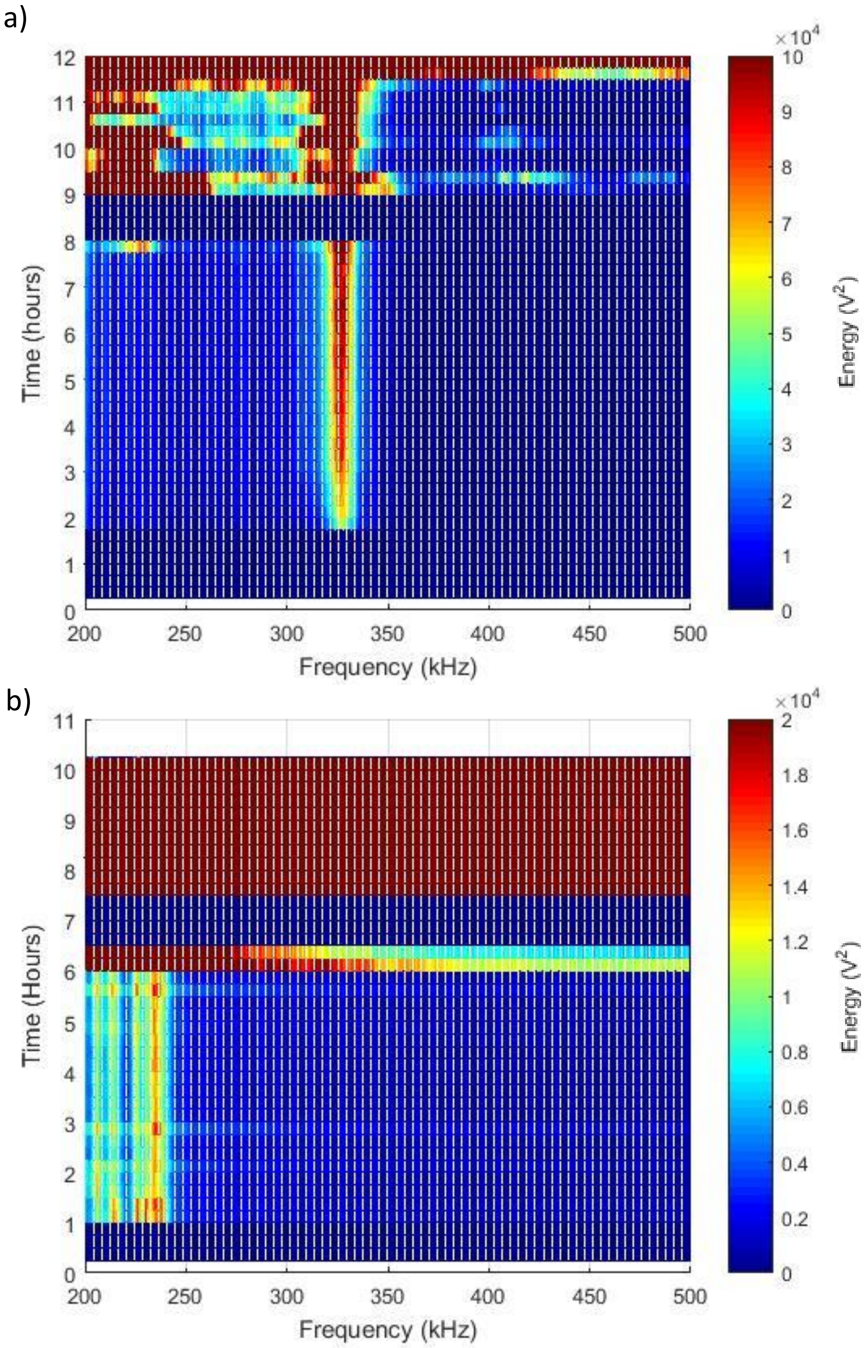

Figure 4-64 - Binned Frequency plot between 200-500kHz for a) PCI-2 AE data and b) ACMS AE data

4.8.3.4 Order Analysis

Figure 4-65, Figure 4-66 and Figure 4-67 plot the order spectrum of raw PCI-2, ACMS AE and ACMS Vibration signals respectively for the files leading up to the detection of damage after 7.5 hours. The data was only plotted up to the 7.5 hour mark as, after this point, the energy became so large that no information can be determined as seen in the binned FFTs. The energy amplitude of each order spectrum varies with the type of transducer used due to the sensitivity of the sensors to low frequencies.

For the PCI-2 AE, Figure 4-65, there exists sporadic energy at the BPFO, 4.3 orders, as well as at the shaft order and its harmonics, 1, 2 and 3 orders. When analysing the order spectrum before and after the rise in RMS after 7 hours, Figure 4-60, it was seen that the majority of the energy was focussed at 6.8 orders, close to the test bearing BPFI, with further peaks separated at 1 shaft order away. In the order spectrum for the whole life test however, it can be seen that there is a strong detection of the BPFO throughout indicating the potential source of failure to be the outer raceway.

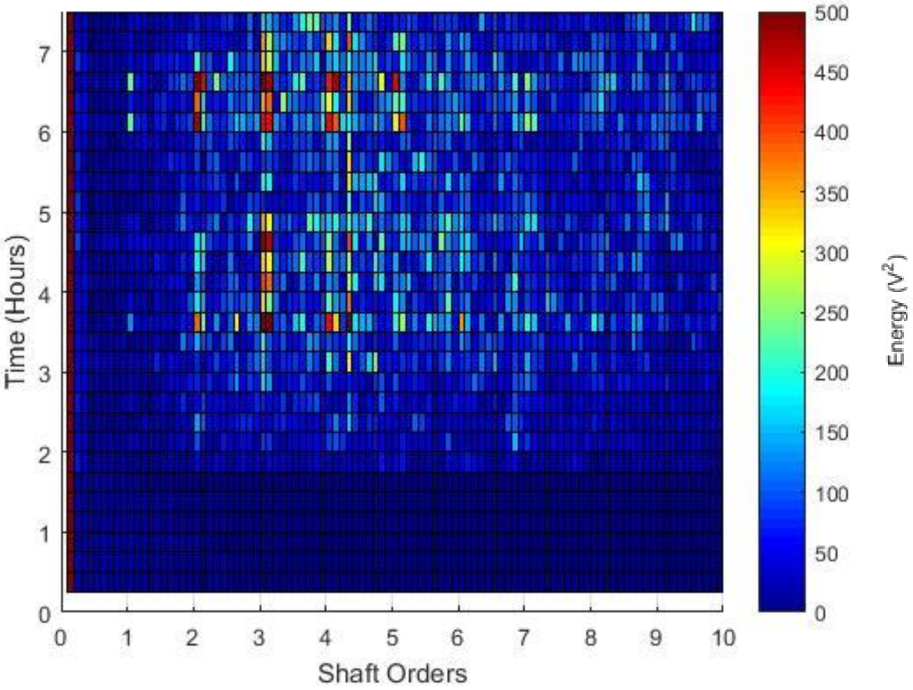

Figure 4-65 - Order Analysis of Raw PCI-2 Signals

In the order spectrums for the ACMS AE and Vibration (Figure 4-66 and Figure 4-67), both systems demonstrate excitation of orders at the BPFO, although the 2nd harmonic of the BPFO, 8.6 orders, has a higher energy than the 1st order. An order of 6.2 is also excited within the order spectrums which is lower than the BPFI for the test bearing by 0.5 orders. Instead, it is thought that this excitation relates to the BPFO of the support bearing which was calculated to be 6.18 orders.

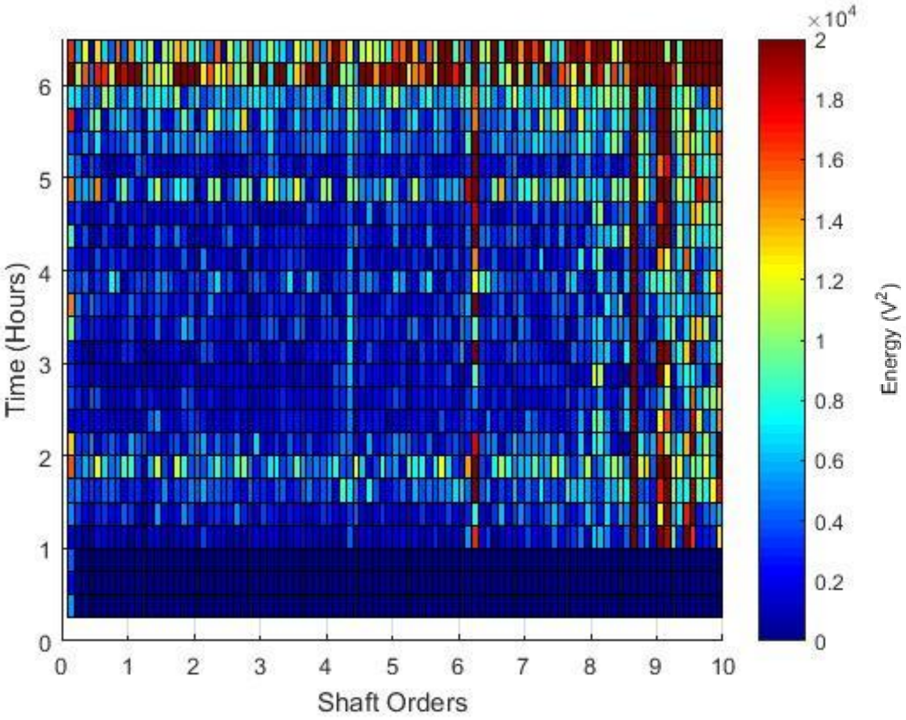

Figure 4-66 - Order Analysis of Raw ACMS AE Signals

These orders were not previously witnessed in the healthy characterisation test, Section 4.5, and it is thought that, as the shaft deflection increases with load, the amount of energy transmitted from the support bearings via the shaft to the test bearing will increase dramatically. If this is the case, then it is demonstrated that although this data is collected from sensors connected to the test bearing, the signals produced by a single bearing are also influenced by nearby bearings which may prove problematic when trying to diagnose failure location in the field. Also visible within the vibration spectrum is the FTF at a frequency of 0.4 orders, a frequency not seen in the ACMS AE and PCI-2 AE spectrums.

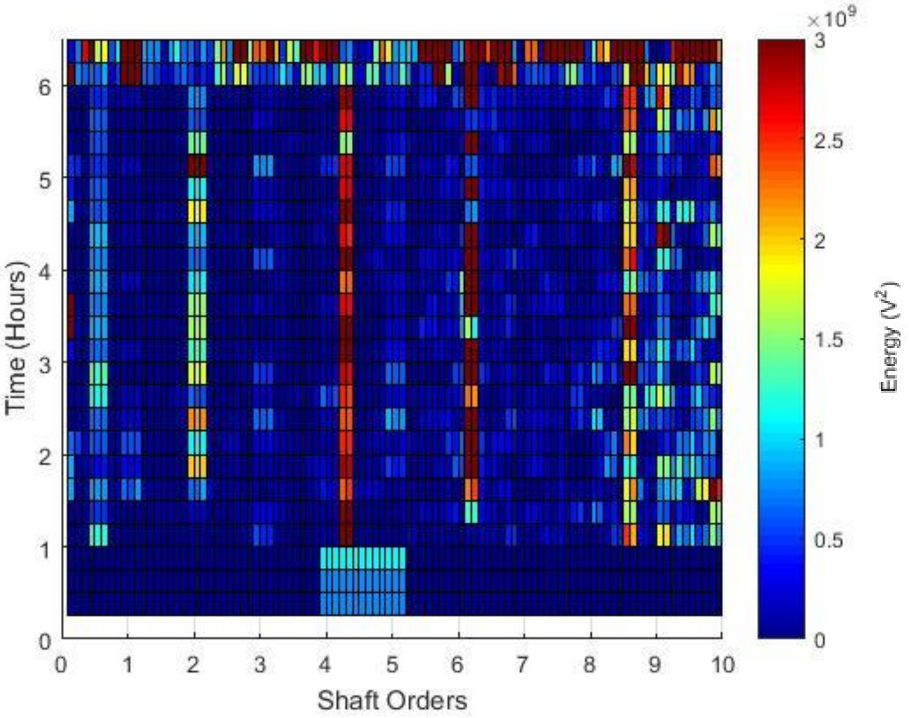

Figure 4-67 - Order Analysis of Raw Vibration Signals

Section 4.6 demonstrated that the Hilbert transform could be used to enhance the detection of weak periodic bursts within the signal for detection within an order spectrum. Figure 4-68, Figure 4-69 and Figure 4-70 are the order spectrums of the enveloped waveforms of the signals recorded on the PCI-2, ACMS AE and ACMS vibration systems respectively, where the envelope is formed by processing the data with a Hilbert Transform.

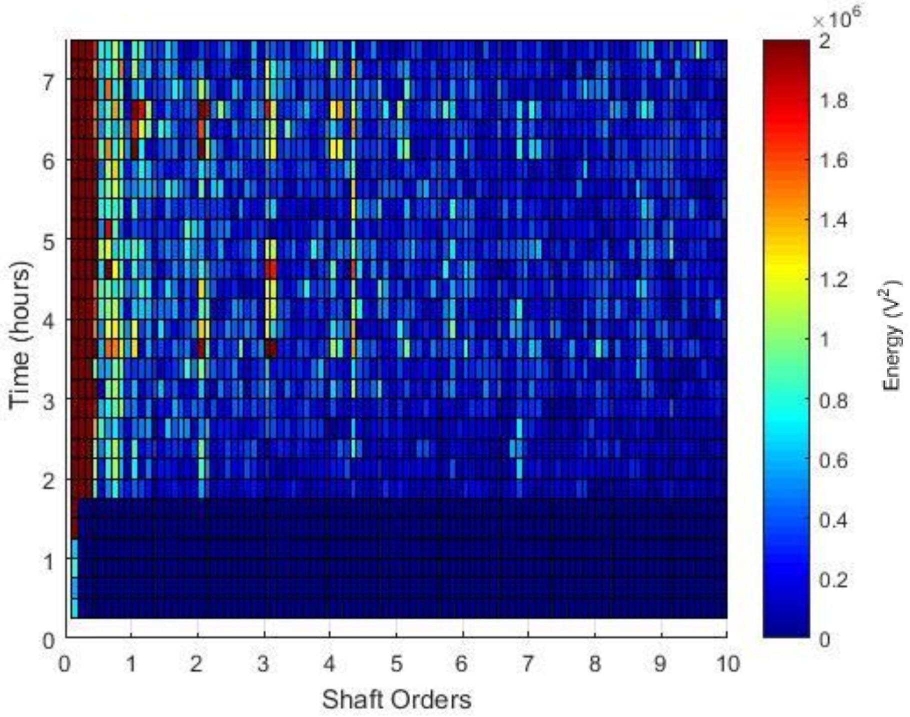

Figure 4-68 - Order Analysis of Hilbert Transformed Data - PCI-2 AE

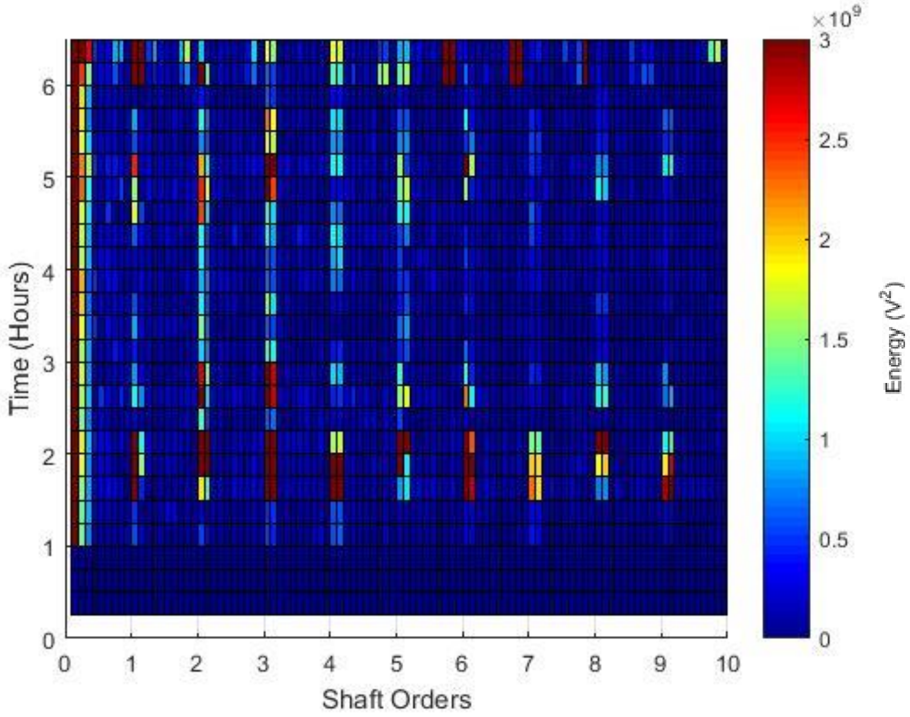

Figure 4-69 - Order Spectrum of Hilbert Transformed Data - ACMS AE

As the high frequency content of the bursts is removed, there is an increase in energy at the lower frequencies within the order spectrum of the PCI-2 data. Similar, albeit smaller, increases are also seen when comparing the order spectrum energy content of the ACMS AE and ACMS vibration raw signals to their Hilbert Transformed counterparts. The orders excited by the PCI-2 AE data are similar to those seen within the raw signal order spectrum, Figure 4-65, although there now also exists new excitation energy at an order of 6.8, corresponding to the BPFI of the bearing that was previously unseen in the early wavestream files. The energy contained within this order is significantly lower than that of the BPFO and fluctuates in amplitude throughout the experiment. When compared to the raw signal, the Hilbert transform has increased the strength of the BPFO when compared to the shaft order harmonics. The BPFO order, 4.3, also increases and decreases in energy between different files. The RMS amplitude of the raw data previously remained relatively constant, however, this change in energy between different files in the order domain may be related to the propagation of defects, increasing in energy as they become larger and are still rough, and then decreasing in energy when smoothened or when debris has been ejected from the contact path.

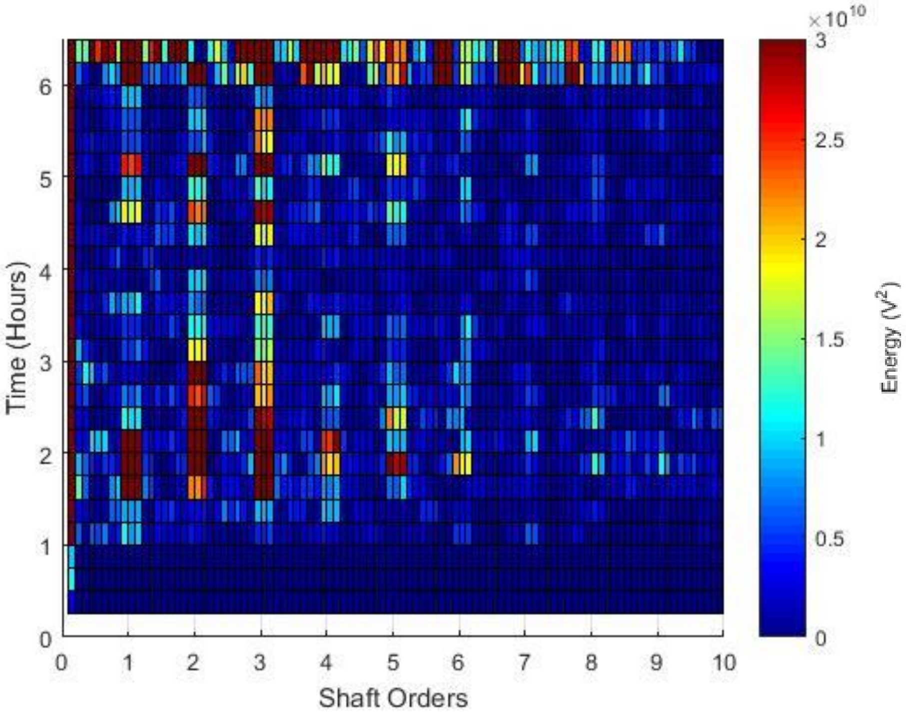

Figure 4-70 - Order Spectrum of Hilbert Transformed Data - Vibration

The application of a Hilbert transform to the data collected from the ACMS AE and vibration data respectively, increases the number of shaft order harmonics excited within the order spectrum. This is to the detriment to the order representing the BPFO of the test bearing which, at the scale plotted, is no longer visible. This may be attributed to the excitation width of the shaft harmonics as these span up to 0.3-0.4 orders away from the harmonic, potentially including the BPFO order.

Although there is little/no visible indication of the characteristic bearing frequencies in the ACMS AE and ACMS vibration spectra, the strength of the shaft rotation harmonics may indicate damage to the inner raceway when analysed following the post processing of the PCI-2 AE data which shows signs of the BPFI. As discussed within the literature review, the BPFI is excited when damage on the inner raceway makes contact with a roller. The amplitude of this excitation varies however depending on the number of degrees through which the shaft has travelled, 0-360˚, with the greatest amplitude witnessed once per revolution as a point on the inner raceway passes through the area of maximum load.

4.8.4 Discussion

Overall, this life test was extremely aggressive and, because the data was collected at 15 minutes intervals, it is difficult to confidently determine the point of damage initiation. Nor is it able to demonstrate, with confidence, any slow increase in value, RMS or frequency energy amplitude, as one would expect as the damage propagates. What is successfully determined through this life test however is that, when a bearing is misaligned, damage propagates quickly. This quick damage propagation is detectable via both AE and vibration and, using simple data analysis techniques. The difficulty lies in diagnosing where the damage initiated as there is contradicting evidence over the two data acquisition systems, with one stating that the damage could have initiated in the outer race and the other the inner race.

Analysis of the wavestreams recorded during the life test demonstrate there is clear evidence of weak periodic transients within the signal before the significant rise in RMS occurs. Comparing these wavestreams with those collected during the analysis of seeded defects, Section 4.6, there is a correlation between the weak bursts shown in Defect 1. It is highly possible that as the defect initiated, micro and macro pitting of the surface would have begun, producing debris that could, in turn, be rolled into the raceway surface. It is thought that this is likely to have produced the low level transient bursts witnessed with the background noise and, only as the damage had spread across the raceway, as with the seeded defects, that the level of RMS rose significantly with clear transients within the signal.

To understand with confidence the benefit of using RMS and frequency analysis to determine defects that are slow to grow within the bearing, a significantly less aggressive test is required.

4.9 Life Test 2

4.9.1 Experimental Set-Up

This life test used the same support bearings as used in 'Life Test 1' but the test bearing was exchanged for a new SKF N204ECP single row, cylindrical roller bearing. Following a run in period and healthy bearing characterisation, the life test was begun. The test rig was first warmed up, running at 590rpm under a radial load of 304N for a total of 10 minutes. The speed was then increased from 590rpm to 5980rpm in stages of 590, 2300 and 5980rpm under a radial load of 794N, with each stage held constant for 10 minutes. When a speed of 5980rpm had been achieved, the load was then increased from 794N to 3244N in stages of 794,1284 2264, 2754 and 3244N, each held for 10 minutes before being increased.

During both the speed and load increments, wavestreams were recorded once per minute on each of the three systems used. Once the final speed of 5980rpm and radial load of 3244N had been achieved, the acquisition rate was decreased to every 5 minutes (reduced from the 15 minutes used in Life Test 1 in an attempt to improve resolution during the bearing failure). The radial load was held constant for a total of 280 hours, approximately 100 million revolutions of the inner raceway, before the load was increased to 5204N. This load was held constant for a further 1400 hours, after the bearing had sustained a total of approximately 500 million revolutions, before the load was increased further to 6184N. After a further 1130 hours of operating under 6184N, the test was stopped following the increase of RMS amplitude on the Non-Drive End support bearing. Figure 4-71 illustrates the variation of test parameters over the duration of the test.

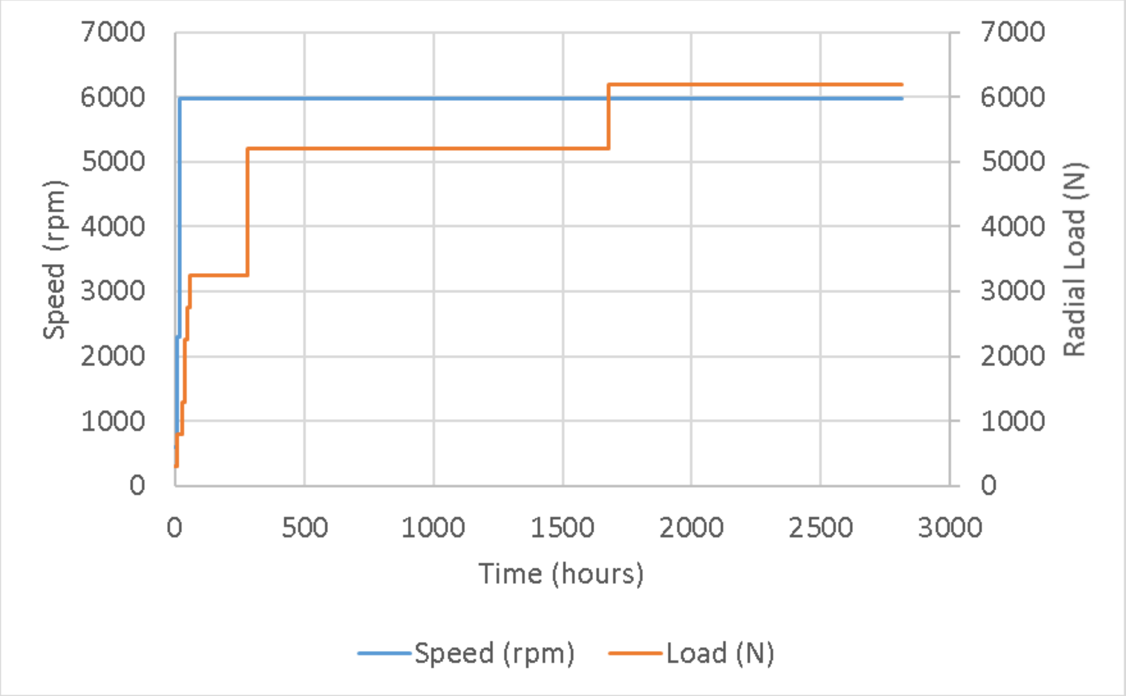

Figure 4-71 - Variation of test parameters during Life Test 2

4.9.2 Defect Images

Figure 4-72.a-c provides images that detail the bearing damage following the 2810 hours of testing. Although both the outer and inner raceway had developed wear marks demonstrating where the roller had been running, this damage is not thought to be the cause of failure. The roller however, had suffered from a significant amount of surface fatigue, characterised by the shape of the craters formed in the surface as previously demonstrated by SKF (1994) (Figure 2-12). The shape of the fatigue failure on the roller indicates that, although misalignments were negated as much as possible, the load still may not have been evenly distributed over the roller.

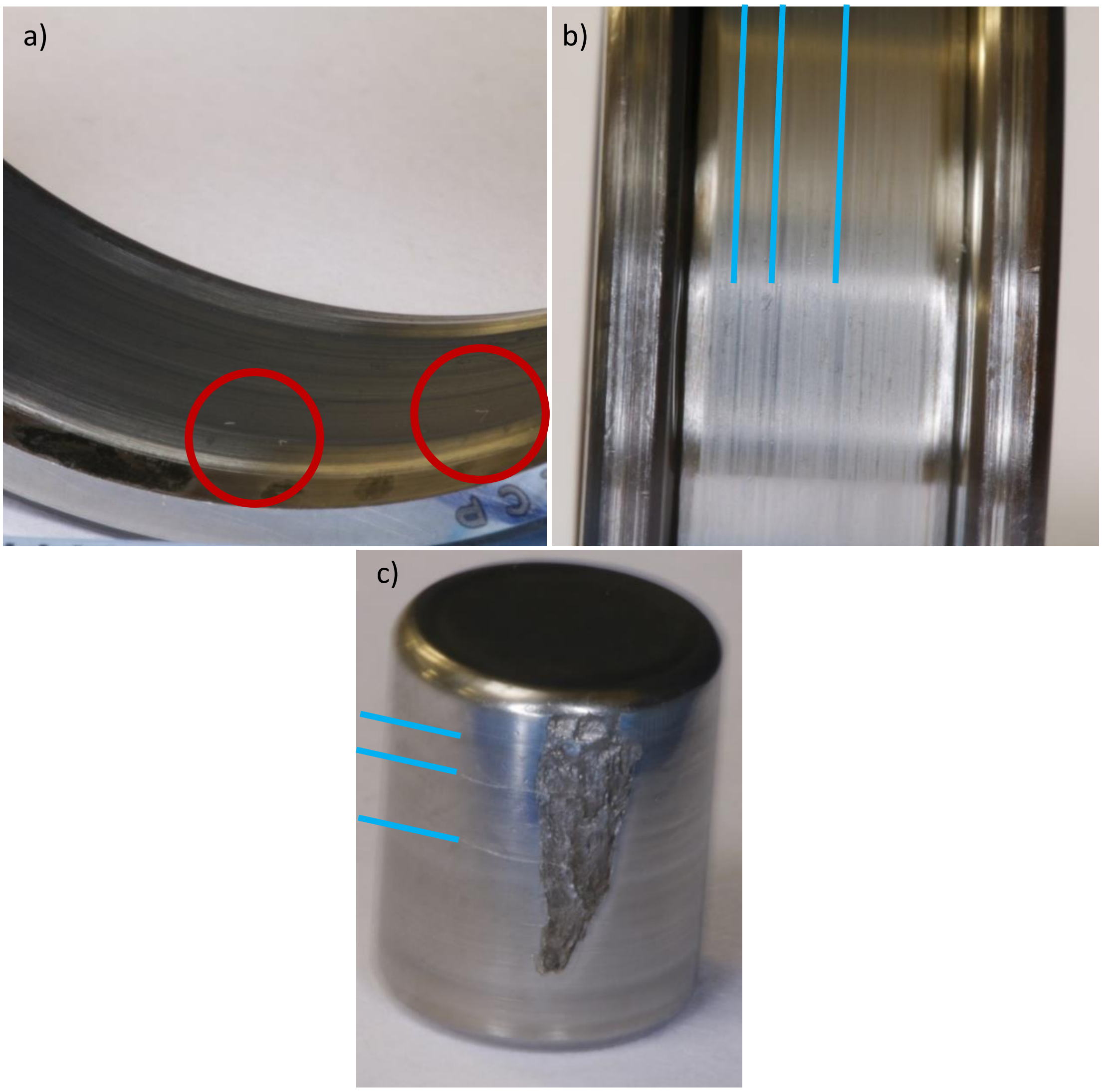

Figure 4-72 - Test Bearing condition after 2810 hours of operation for a) Outer Raceway, b) Inner Raceway and c) a roller element

Within the wear scars on the inner and outer raceway, there exist a series of smaller lines and characteristics which demonstrate areas of increased wear. These lines are similar to the rifling effect found on bullets during forensic investigations and, as demonstrated by the blue lines, they can be matched up with characteristics on the roller. The image shown of the inner raceway demonstrates these extra wear scars to the left of the raceway and, it is deduced from the rifling effect that the roller, if rotated 90˚ counter-clockwise would be in the correct orientation to the inner raceway. These areas of increased wear are likely to be due to debris being trapped and scraped along the surface of the inner and outer raceway. Highlighted by the red rings is also evidence of micro-pitting of the outer raceway where it is thought the over-rolling of debris may have produced localised regions of plastic deformation.

Figure 4-73 is the surface profile of the damage to the rolling element as described in Figure 4-72.c. It can be seen that the dimensions of the damaged region are approximately 8.5mm x 2.5mm with a maximum depth of 210µm although, for much of the area the depth rarely exceeds 110µm.

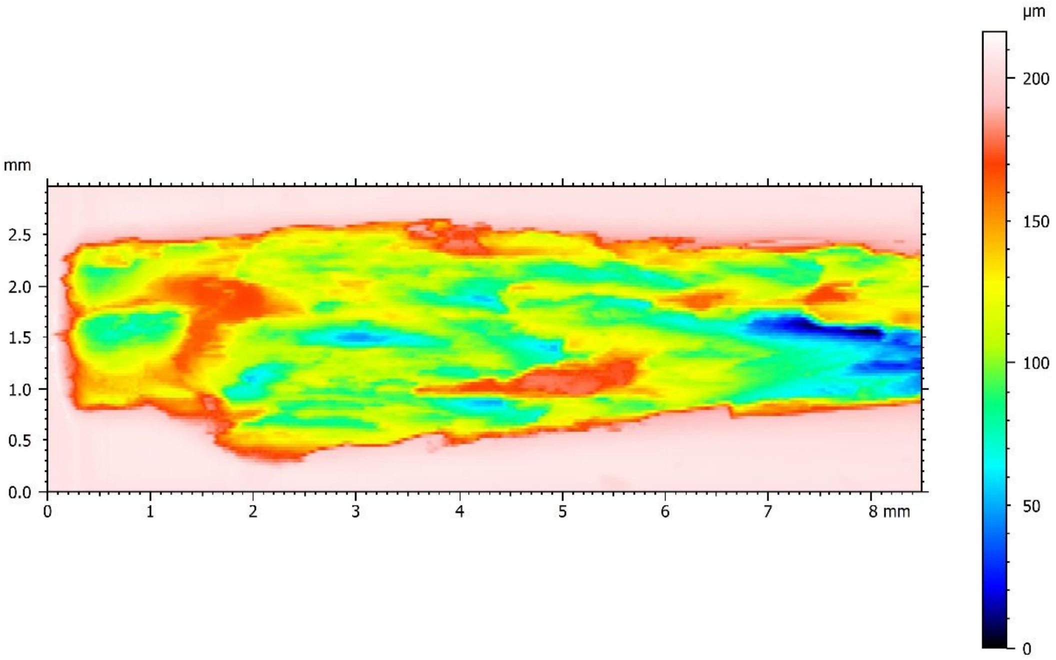

Figure 4-73 - Talysurf image of the surface fatigue damage on the rolling element

4.9.3 Results

Figure 4-74 plots the RMS trend as recorded on the PCI-2 system where each point is calculated from the first signal of each day. It can be seen that after the first day, once the test speed and load have been reached, that the RMS amplitude starts at 0.72V, increasing over the first 40 days to a level of 0.82V. It is thought that this increase may occur due to bearing faces bedding in and may also be attributed to the polymerisation of the couplant as it continues to cure, hardening and hence improving the transmission of the signals from the bearing housing to the sensor. This level of RMS amplitude is maintained at approximately 0.82V until after 79 days have passed, there is a significant jump in the RMS value which continues to increase in amplitude until the final failure occurs after 110 days.

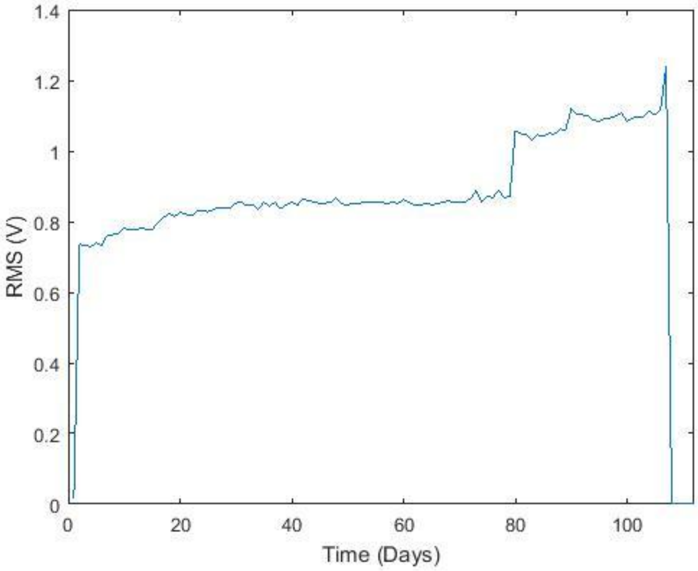

Figure 4-74 - Daily RMS plot for the PCI-2 System

Based on the trend produced by the daily RMS plot (Figure 4-74) three windows of data, each approximately 50 hours in length, were considered for the analysis of data recorded on the PCI-2 and ACMS systems. Figure 4-75, determines the RMS trend at the start of the test, Figure 4-78 determines the RMS trend over the RMS jump after 1912 hours and Figure 4-79 determines the RMS before the final failure occurs after 2807 hours. The data plotted in these three figures is derived from wavestream recordings taken once every five minutes. That is apart from the start of the test, in Figure 4-75, where the data recorded for the first 2 hours was recorded at 1-minute intervals.

It can be seen in Figure 4-75, between 0 and 0.5 hours there is an increase in RMS amplitude in the signals recorded on all three systems. This is due to the increases in speed from 590 – 5980 rpm. Following this initial increase, the RMS amplitude of the ACMS AE and vibration continues to increase, albeit slowly, as the radial load is increased from 794 to 3244 N. The RMS of both the ACMS AE and vibration both stabilise at 0.67 and 0.22 volts respectively. The RMS amplitude of the PCI-2 system however decreases as the load is increased until a radial load of 3244 N is achieved, where the PCI-2 AE RMS amplitude then stabilises at 0.75V. This drop in RMS amplitude is contrast to the RMS signals witnessed in the healthy bearing analysis detailed in Section 4.4 where RMS levels were seen to increase with radial load.

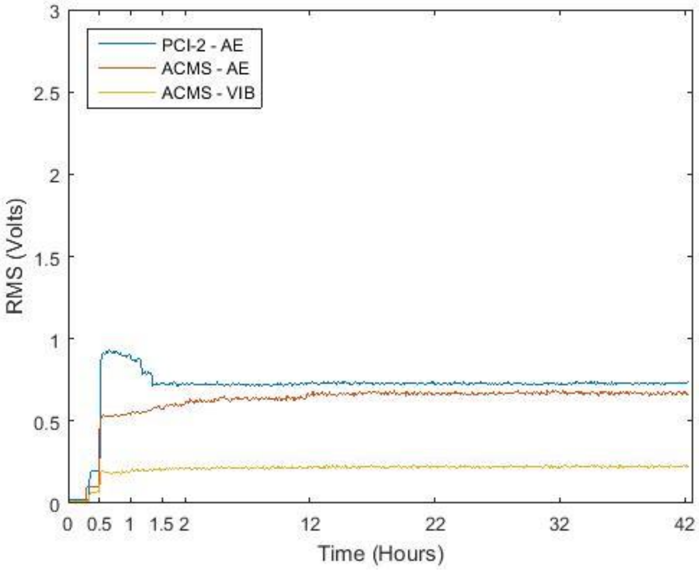

Figure 4-75 - RMS trend for all three systems at the start of life test

Figure 4-76 plots the raw signals recorded 17 hours into the life test once all of the three signal levels had settled to a constant level. It can be seen that, similar to the raw signals of healthy data depicted in Sections 4.5.2 and 4.8.3, there exists a continuous emission with amplitudes of approximately +/- 2V for the PCI-2 and ACMS AE systems and +/- 0.5-0.75 for the ACMS vibration signals. The signals in Figure 4-78 are formed of a number of low amplitude transient bursts although it is difficult to determine any periodicity within the signals through visual analysis alone. As discussed in Section 2.5.1, the characteristic bearing frequencies exist for healthy bearings as it is a function of the bearings geometry and the frequencies are excited as the stiffness of the bearing increases and decreases periodically. Figure 4-77 plots the order spectrum of the raw signals in Figure 4-76 at it is shown clearly in both the PCI-2 and vibration orders that there exists a large amount of energy at 4.3 orders, which is far larger than the energy at this order when compared to previous tests. For the signals from the AE ACMS system however, there is very little energy at 4.3 orders, with the peak energy existing at 18.8 orders. The excitement of an order at 4.3 corresponds to both the BPFO or BSF of the bearing. The existence of this frequency in the 'healthy state' of the bearings is more prominent in this Life Test as, unlike Life Test 1, at the end of the test the outer raceway was generally undamaged, apart from some micro-pitting thought to be due to the over-rolling of debris emitted from the damaged roller. The failure mode however was due to the damage to a single roller. Although not checked extensively prior to the test commencing, SKF bearings are of high quality and it is not thought that a surface defect would have been present on this bearing at the start of the test. This is confirmed further by the length of the accelerated test as, if the roller was damaged prior to the test commencing, it is thought that the test would have finished significantly earlier, especially after witnessing how quickly the RMS increased at the end of the test. It is also unknown as to why the peak energy at 4.3 orders is detectable within the spectral

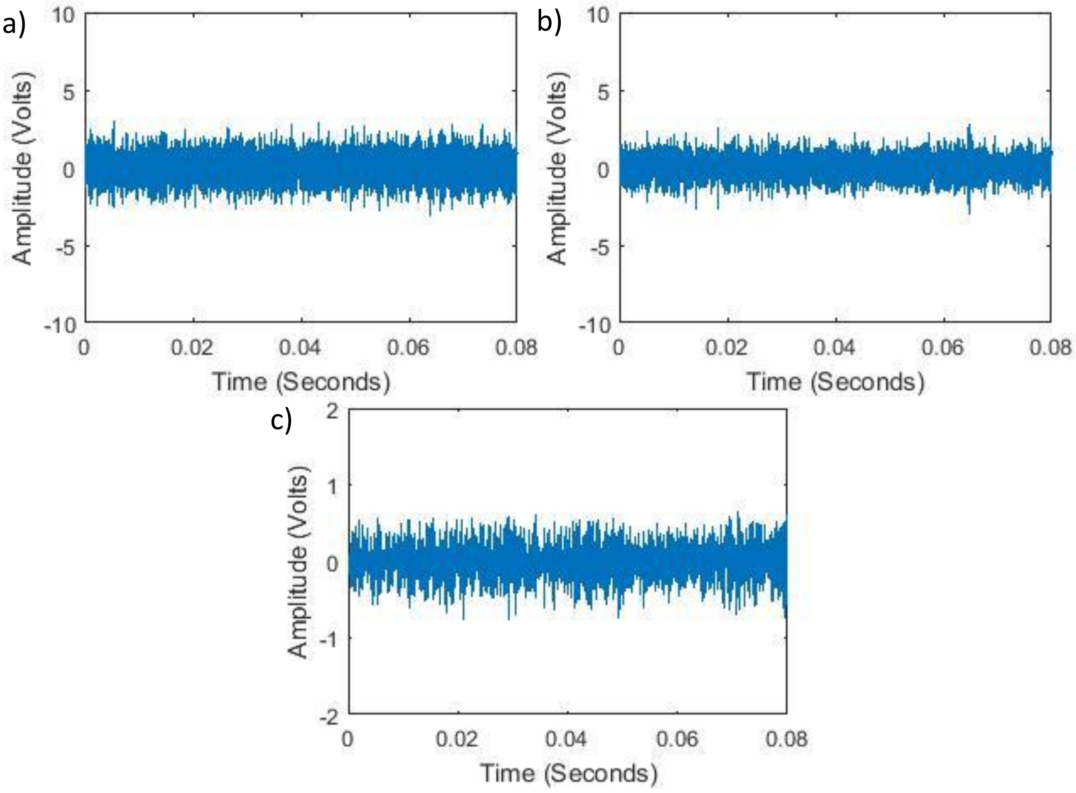

Figure 4-76 - Raw Signals after 17 hours as recorded on a) PCI-2 System, b) ACMS AE System and c) ACMS Vibration System

plots of PCI-2 AE and ACMS vibration whereas the ACMS AE shows little energy in this region.

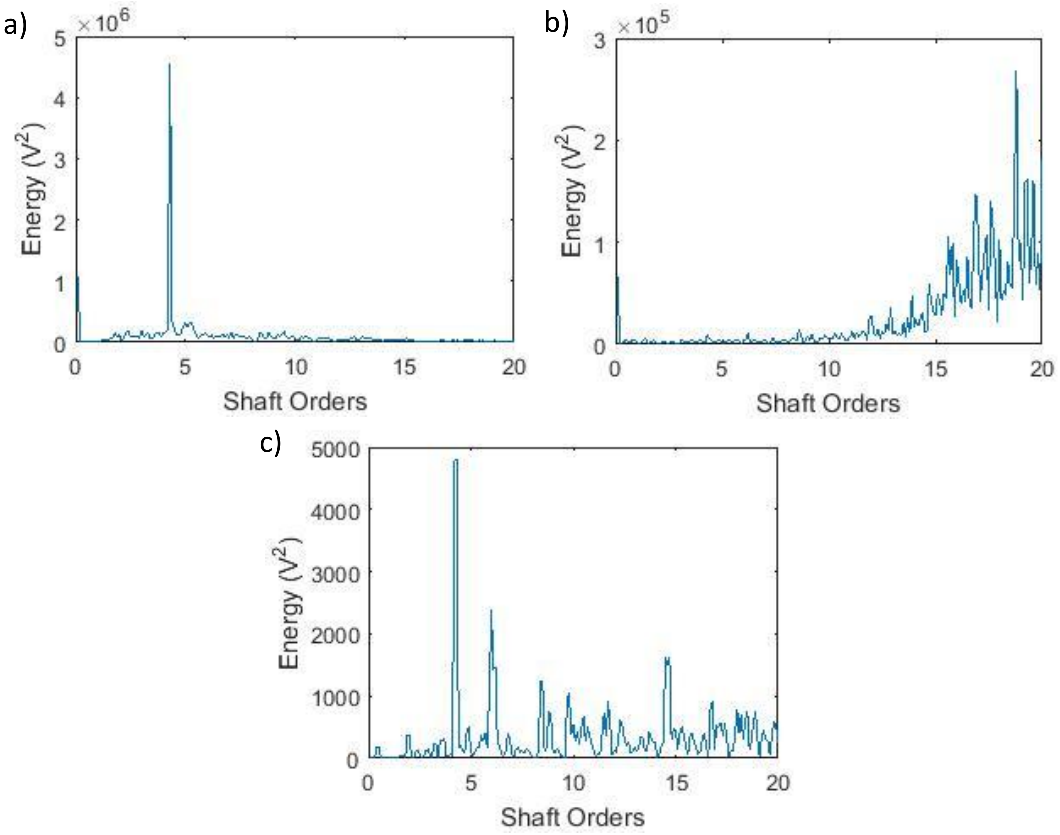

Figure 4-77 - Order analysis of the images in Figure 4-76 a-c respectively

Figure 4-78 shows that the RMS amplitude of the signals at the start of the observation window has changed slightly from the values witnessed at the end of the initial window (Figure 4-75). 125 hours into the second window, after a total of 1922 hours into the test overall, the RMS amplitude drops down to 0V for approximately 4 hours. This is due to the power supply to the test rig motor, as well as the oil supply system, being stopped during a power cut. The data acquisition systems, on a separate power supply ring, continued to run during this period. Once the power resumes, the motor quickly returns to full speed and the RMS amplitude of the ACMS AE and vibration signals return to the same level as they were prior to the power interruption. The RMS amplitude of the AE wavestreams recorded on the PCI-2 system however increases to 1.06 volts as the system is restarted. This RMS level is maintained for the rest of the window of observation. It is thought that this is due to slight changes in the running condition. The power supply to the system is used to provide power to the oil pump as well as the heater-stirrer unit. Without power for 4 hours, but with the oil/water heat exchanger still running since this is fed from a piped water supply, the oil within the sump would have cooled considerably. Then, as the system is restarted, the bearings were initially run with a limited oil supply as, due to the oil being considerably more viscous at cooler temperatures, it takes time for the oil feed pipes to fill up and hence supply the oil jet to the bearings. As neither of the two ACMS acquisition systems increase in amplitude upon restarting, it is thought that the change in PCI-2 RMS amplitude is due to the influence of higher order frequencies.

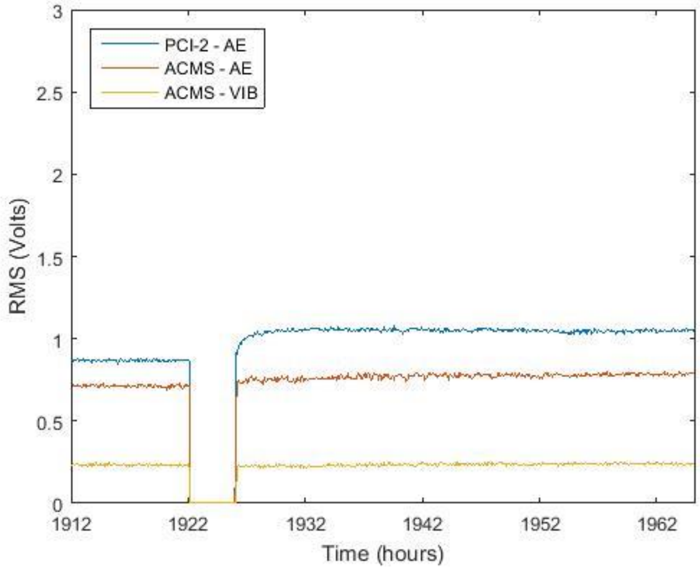

Figure 4-78 - RMS trend for all three systems after 1912 hours into the life test

At the start of the third and final window of observation, Figure 4-79, the RMS amplitudes are similar to the amplitudes seen at the end of the second window, Figure 4-78. After 2789 hours the RMS amplitude begins to increase slowly in amplitude in both the ACMS vibration and PCI -2 AE. There is however a small but notable step change in the ACMS AE response. The amplitude increases steadily from 2789 hours to 2804.5 hours in both the ACMS vibration and PCI-2 AE signals whereas there is a considerable amount of variation in amplitude, increasing and decreasing in amplitude until a sharp increase is witnessed in all three sensors until the final failure of the bearing after 2807.5 hours.

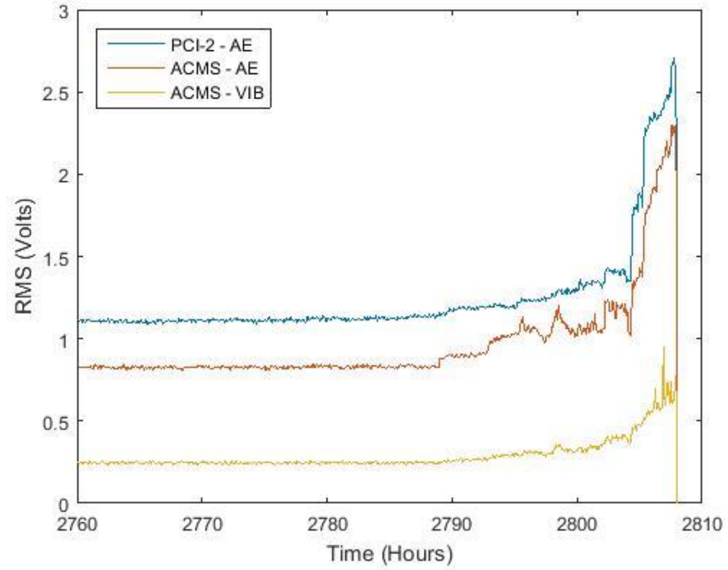

Figure 4-79 - RMS trend of all three systems after 2760 hours

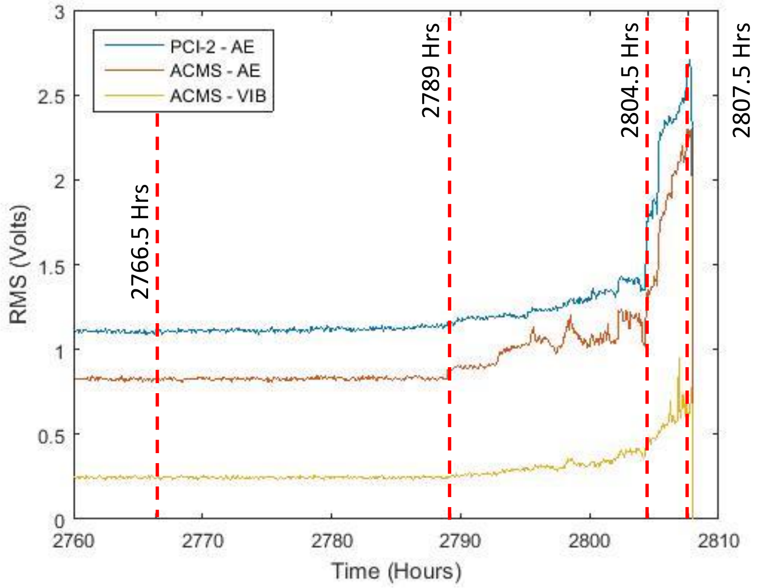

Figure 4-80 - Annotation of Figure 4-79 demonstrating the location of the raw signals used for further analysis

Figure 4-81 - Figure 4-86 illustrate the raw signals of each of the three systems at each of the key changes in the RMS amplitude discussed above. The location of these points is illustrated further in Figure 4-80, which is an annotation of Figure 4-79. The raw signals after 2766.5 hours, Figure 4-81, are similar in amplitude to the signals recorded at the start of the life test, Figure 4-76. Unlike the early signals however, the transient bursts that make up the signal are more prominent within the signal although it is still not possible to determine the periodicity of them.

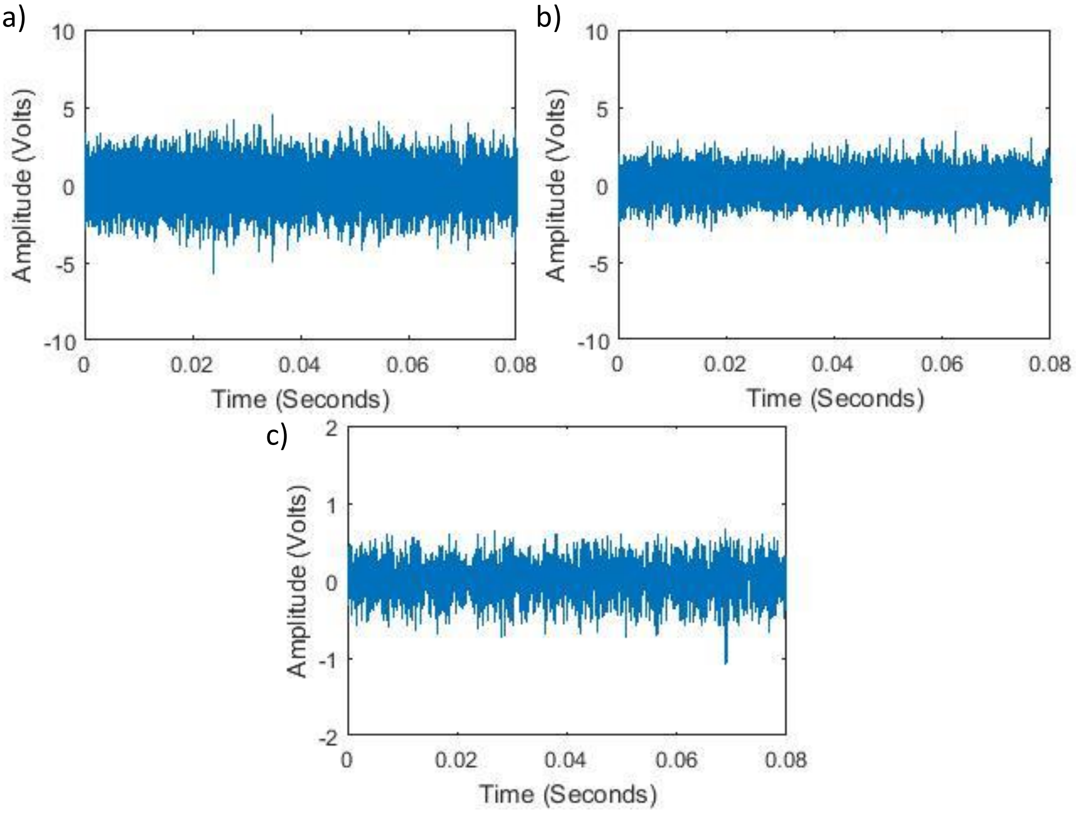

Figure 4-81 - Raw Signals after 2766.5 hours as recorded on a) PCI-2 System, b) ACMS AE System and c) ACMS Vibration System

Figure 4-82 demonstrates the order spectrum of the raw signals in Figure 4-81 and it can be seen that although the raw signals are similar in appearance, the amount of energy at the BPFO/BSF has increased for the PCI-2 AE and ACMS vibration spectrums. There is also visibility of a 2nd harmonic at 8.6 orders within the ACMS AE and ACMS Vibration spectrums. The increase of energy at the 1st and 2nd harmonic of the BPFO/BSF is an indication that, since the beginning of the life test, the condition of the bearing may have begun to change. The visibility of the 2nd harmonic also indicates that this may indeed be the detection of the BSF as the BSF represents a complete revolution of the roller. However, due to the construction of the bearing, a burst will be emitted twice per revolution as the defect/discontinuity on the surface of the roller makes contact in turn with both the inner and outer raceway. Detection of this frequency, coupled with the knowledge of the final failure mode, increases confidence that this is the detection of the BSF. It is unclear however, as to why the ACMS system, both AE and Vibration, are able to detect the 2nd BSF harmonic whereas the PCI-2 system is unable to.

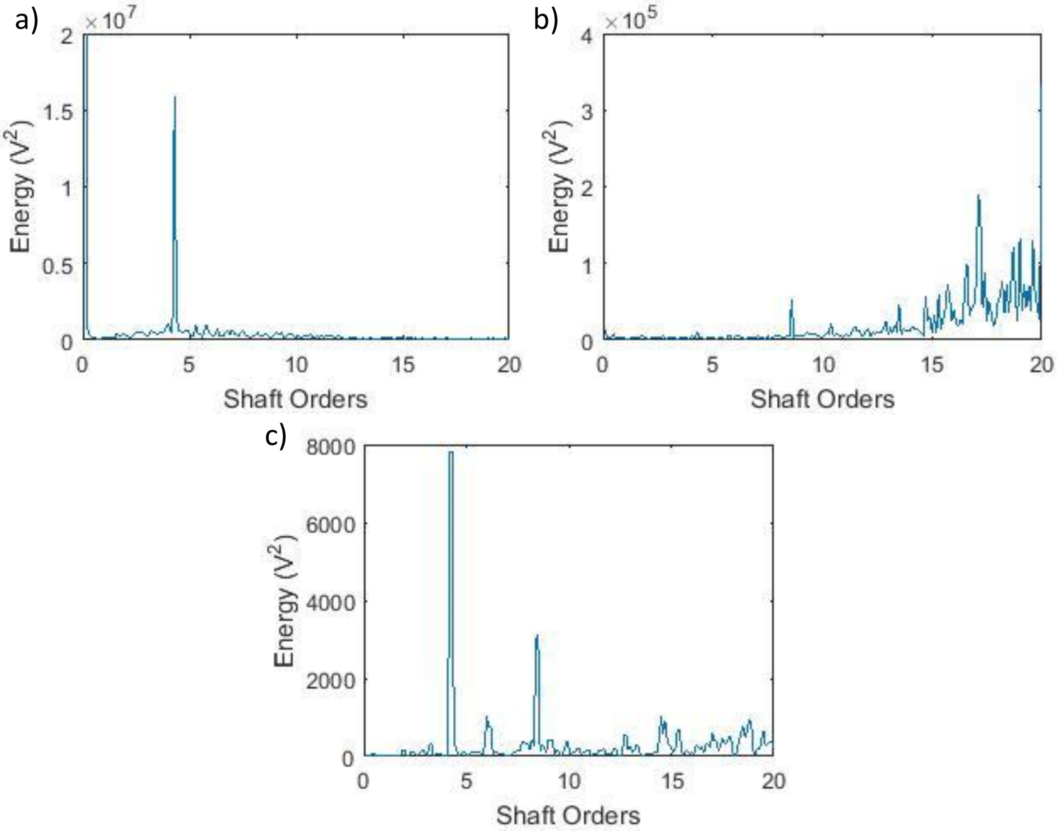

Figure 4-82 - Order analysis of the images in Figure 4-81 a-c respectively

The raw signals recorded after 2789 hours (Figure 4-83) are again, similar to the signals recorded at the beginning of the test, Figure 4-76, in terms of the amplitude of the general noise floor however, the number of transients exceeding the amplitude of the noise floor has increased significantly, indicating changes in the running conditions of the bearing. Spectral analysis, Figure 4-84, continues to show that as the bearing condition deteriorates, the energy at the BSF continues to increase in all three systems however the corresponding harmonics are still only visible in the ACMS AE and vibration spectrum.

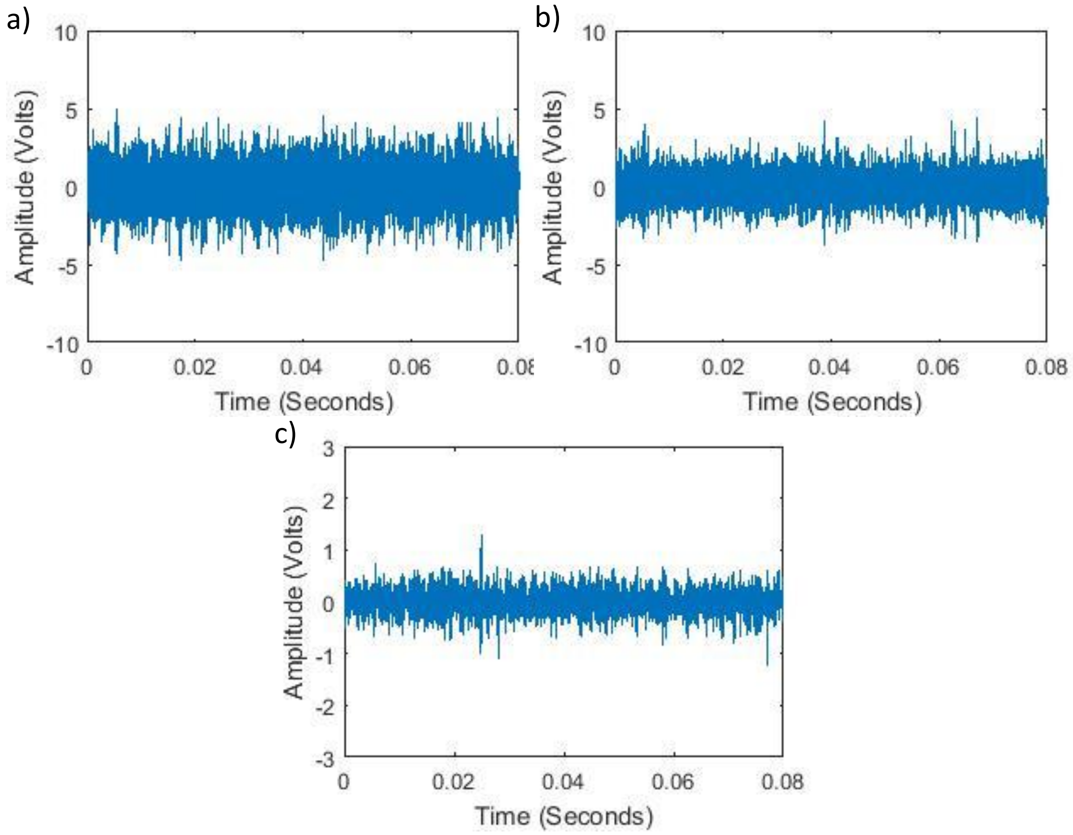

Figure 4-83 - Raw Signals after 2789 hours as recorded on a) PCI-2 System, b) ACMS AE System and c) ACMS Vibration System

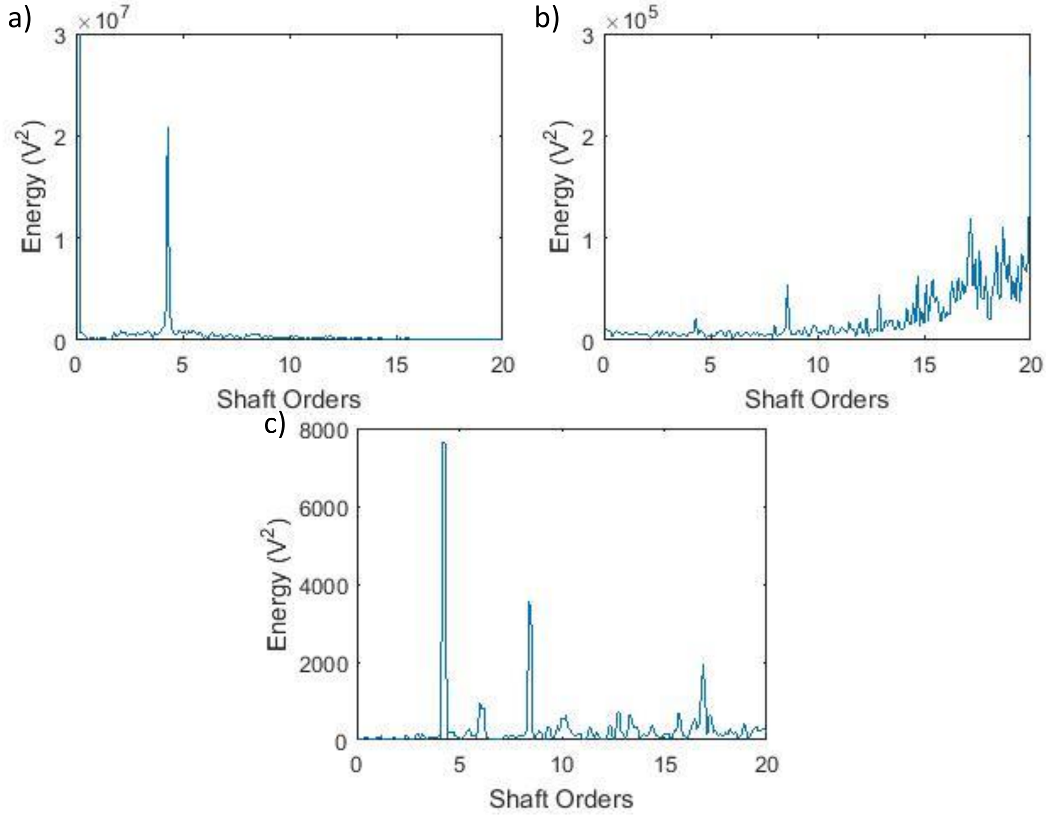

Figure 4-84 - Order analysis of the images in Figure 4-83a-c respectively

Figure 4-85 illustrates the raw wavestreams after 2804.5 hours and it can be seen that for all three systems, the amplitude of the transient bursts has increased significantly and the frequency of their occurrence has increased to a point where it is possible to determine some periodicity between them. Spectral analysis shows a number of new frequencies being excited, particularly in the PCI-2 AE and ACMS vibration spectrums, Figure 4-86. The increase in energy at the higher orders within the ACMS AE spectrum however reduces the visibility of the lower level orders.

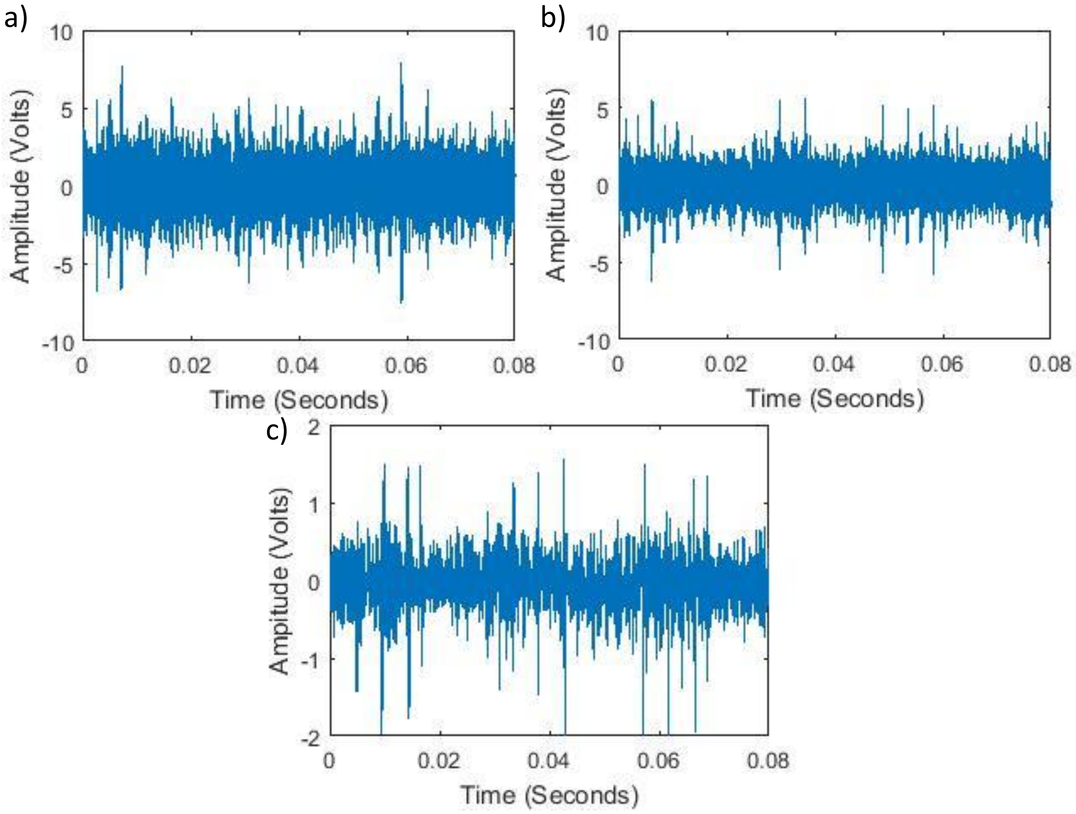

Figure 4-85 - Raw Signals after 2804.5 hours as recorded on a) PCI-2 System, b) ACMS AE System and c) ACMS Vibration System

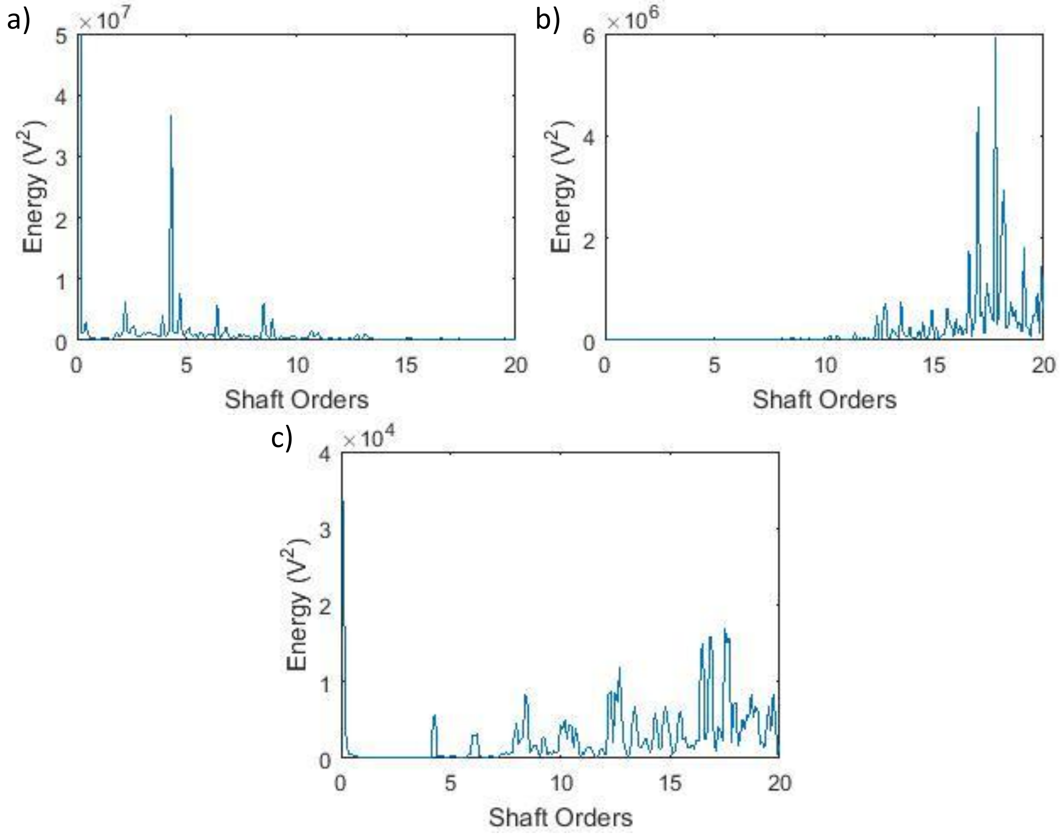

Figure 4-86 - Order analysis of the images in Figure 4-85 a-c respectively

The final wavestreams, recorded after 2807.5 hours shows that the amplitude of the transient bursts recorded on each of the systems exceeds their input limits. There is clear periodicity between each of the transients, with each burst separated at the BSF. This is, as it has been throughout the analysis of the raw signals, confirmed through spectral analysis. The BSF and the 2nd, 3rd and 4th harmonic are visible in the PCI-2 and ACMS AE plots. The ACMS vibration spectrum however, similar to the order spectrum of the earlier ACMS AE signals, demonstrate a large amount of energy in the higher orders, reducing the visibility of the lower orders.

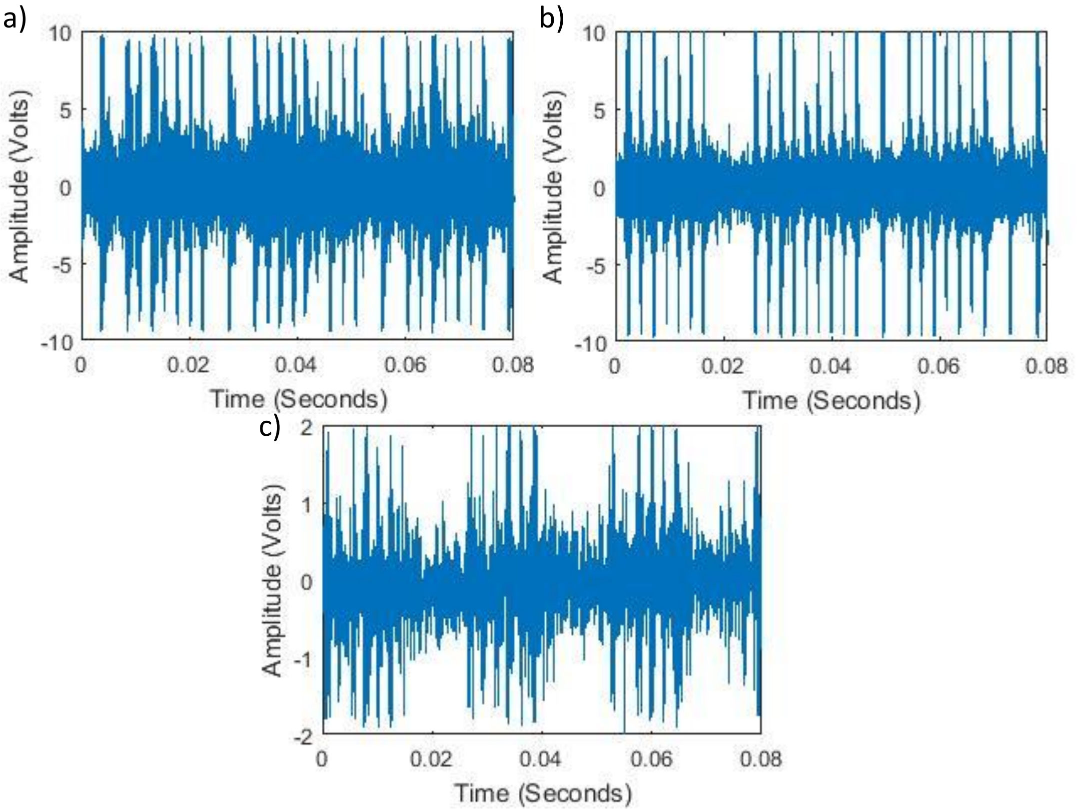

Figure 4-87 - Raw Signals after 2807.5 hours as recorded on a) PCI-2 System, b) ACMS AE System and c) ACMS Vibration System

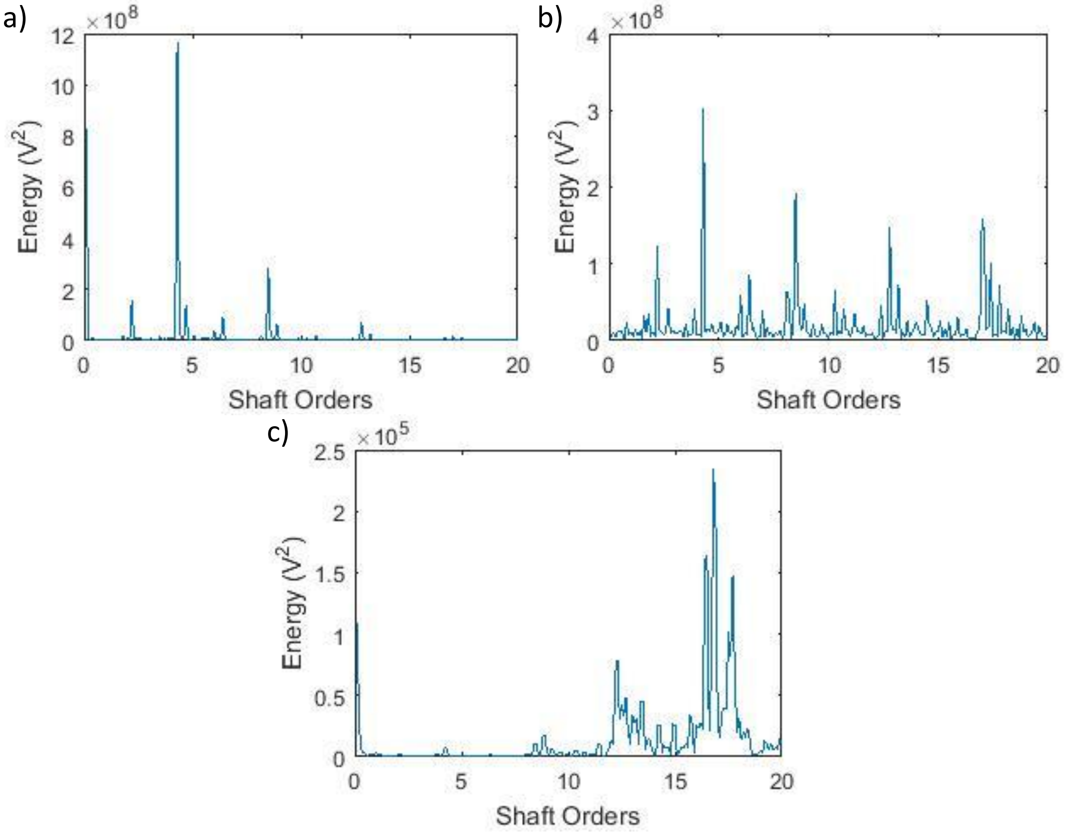

Figure 4-88 - Order analysis of the images in Figure 4-87 a-c respectively

It has been shown through the analysis of the raw signals above that, throughout the life test, excitation at 4.3 orders increases in the data recorded in all three systems used. Figure 4-89 determines the order spectrum between 0 and 10 orders for the data collected on each of the three systems starting from 2760 hours at it can be seen that the excitation at 4.3 orders is constant in the PCI-2 and ACMS vibration plots. There is also visibility of 8.6 orders in both ACMS AE and vibration throughout the plot and this differs from the order analysis of the individual signals above as the x-axis has now been reduced to show data between 0-10 orders. As a result, the scale of the z-axis has been changed to highlight the dominant frequencies in this region clearly.

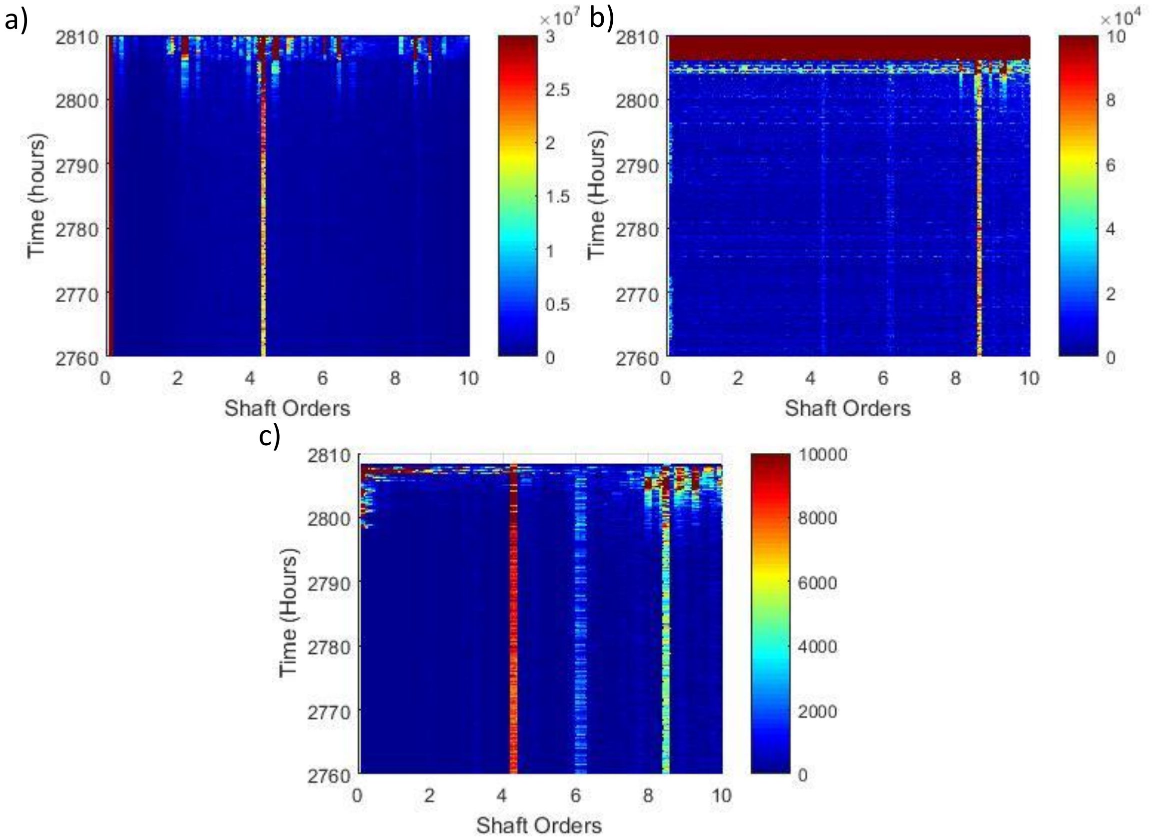

Figure 4-89 - Order analysis after 2760 hours for a) PCI-2 System, b) ACMS AE and c) ACMS Vibration – where the unit of the Z-axis scale is Energy (V^2)

Figure 4-90 plots the binned FFT spectrum between 0-100kHz for both the PCI-2 and ACMS system. It can be seen that the dominant frequency excited in the PCI-2 system is approximately 56kHz whereas the ACMS AE system demonstrates an excitation at 10kHz. The frequency bands of excitation for the ACMS AE data are similar to the excitation bands witnessed in the healthy bearing characterisation, Figure 4-22, and the beginning of Life Test 1, Figure 4-62.

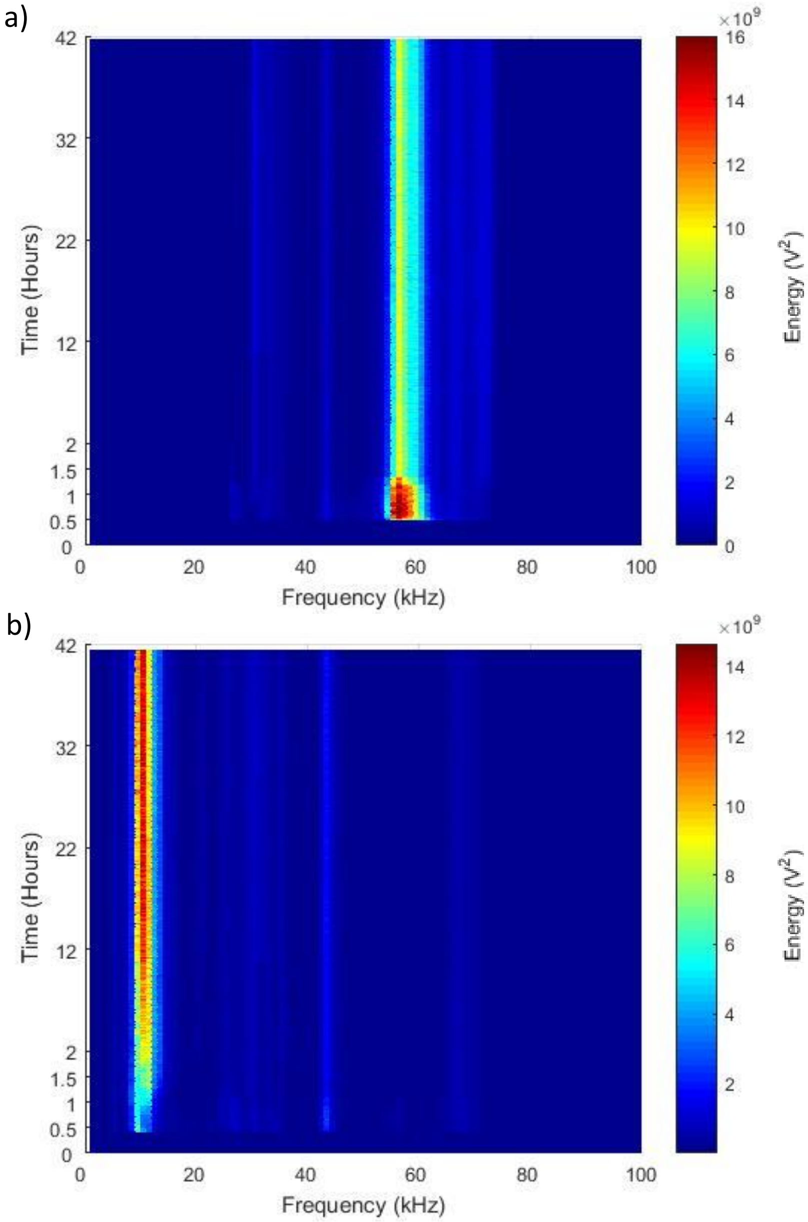

Figure 4-90 - Binned FFT between 0-100kHz for a) PCI-2 System and b) ACMS AE System at the start of Life Test 2

The bands of excitation for the PCI-2 data are also similar to the band witnessed in the healthy bearing characterisation but differs from the frequencies excited in Life Test 1. It was hypothesised in Section 4.8 that the introduction of misalignment to the bearing had an impact on the excitation frequency in the PCI-2 signals and it is shown that, for two different bearing tests each with a reduced level of misalignment, the excitation frequency remains constant. Also of interest is that the ACMS AE data appears to be insensitive to changes in the test setup. The energy at the excitation frequency band of 56kHz for the PCI-2 data increases in line with the increase in bearing speed before reducing in amplitude as the load is increased as previously discussed when analysing the RMS data, (Figure 4-75). A similar comparison can be made for the ACMS AE data which continues to increase in amplitude until 12 hours into the experiment where a 'steady-state' is achieved.

Figure 4-91 plots the binned frequency spectrum of the ACMS vibration data between 0-25kHz and, similar to the excitation levels of the ACMS AE system, the peak excitation exists at 9.2kHz with further bands separated at approximately 500Hz either side. It is thought that these separation bands are due to the excitation at the BSF, 4.3 orders or 428Hz, as shown to be excited in the order plots of the initial vibration data, Figure 4-76c. This would present itself at 500Hz bands because the frequency plot Figure 4-91 is developed from summed bins with a width of 100Hz. Therefore, any frequency information between 400-500Hz will be summed and presented at 500Hz.

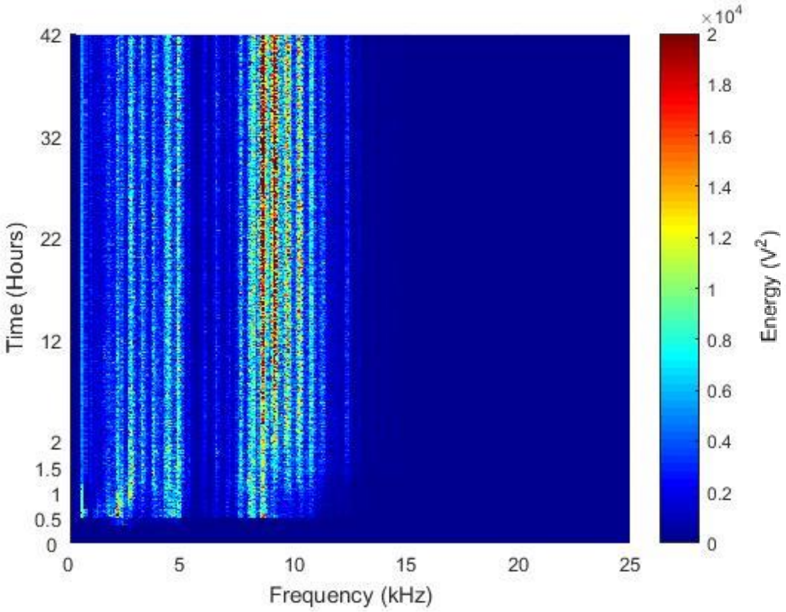

Figure 4-91 - Binned FFT of the Vibration signals between 0-25kHz at the start of Life Test 2

Figure 4-92 plots the frequency spectrum of the initial data from the life test between 100-200kHz. The main frequencies of excitation are 116kHz and 105kHz for the PCI-2 and ACMS AE systems respectively. For both systems, these frequencies are similar to the bands of excitation seen previously within the analysis of the healthy bearing test and life test 1. Discussion up until this point has presented contrasting views on the origin of frequencies emitted at this frequency level. It was originally thought in the healthy bearing analysis that the excitation was due to the 2nd harmonic of the data presented in the 0-100kHz region. It was argued during the analysis of Life Test 1 however that it was unlikely that they were the 2nd harmonics as the dominant frequency band for the PCI-2 data between 0-100kHz shifted from 30-48kHz but no similar shift was witnessed in the analysis between 100-200kHz. Instead, the excitation of 116kHz and 105kHz has been constant throughout all of the experiments conducted and analysed and it is thought that the origin of this frequency may be linked to friction within the bearing as the frequency band is similar to that observed by Ferrer *et al.* (2010).

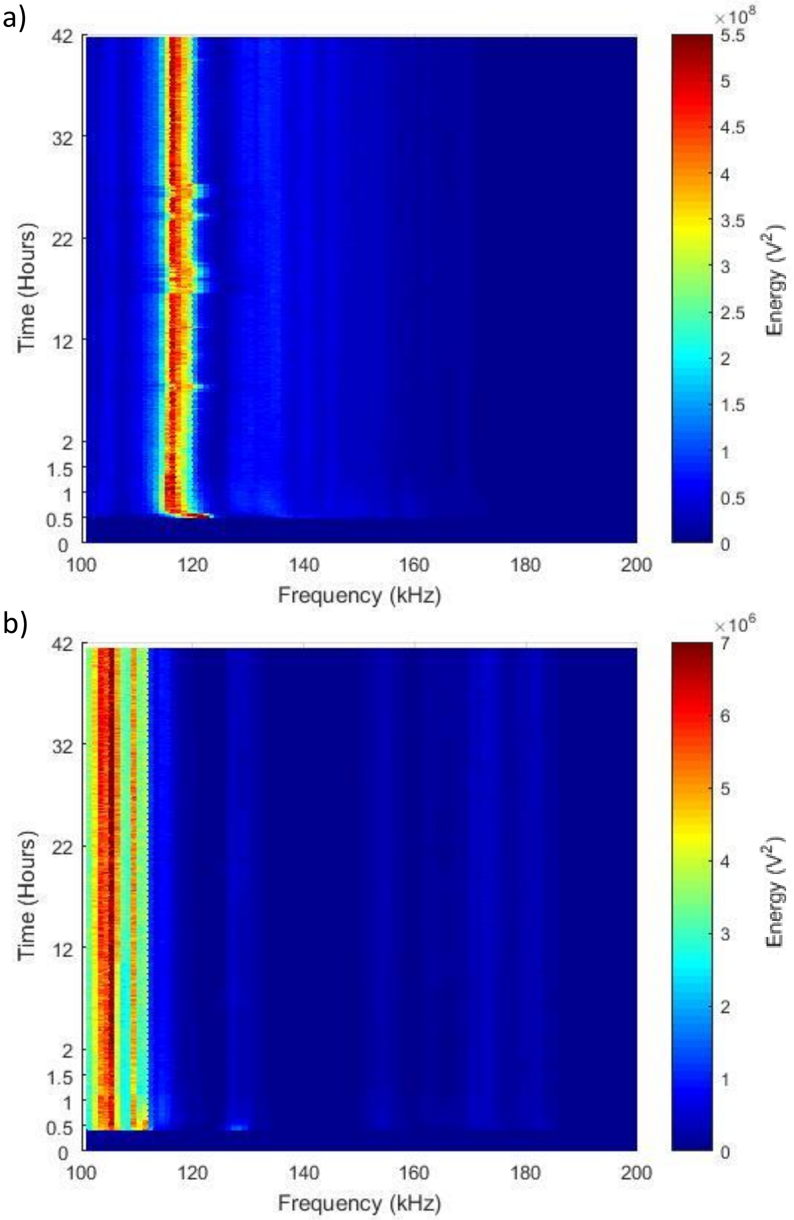

Figure 4-92 - Binned FFT between 100-200kHz for a) PCI-2 System and b) ACMS AE System at the start of Life Test 2

A similar discussion exists regarding the origin of excitation frequencies between 200-500kHz. Figure 4-93 demonstrate that there is excitation at 238kHz and 223kHz for the PCI-2 and ACMS system. The energy amplitude of the PCI-2 system differs from the amplitude trends witnessed between 0-100kHz and 100-200kHz as well as the RMS amplitude. Instead of increasing with the speed followed by a reduction in amplitude as the load is increased, it appears that the excitation at this frequency is more sensitive to load, increasing in energy after 1.5 hours as the load is increased to its maximum level of 5.7kN.

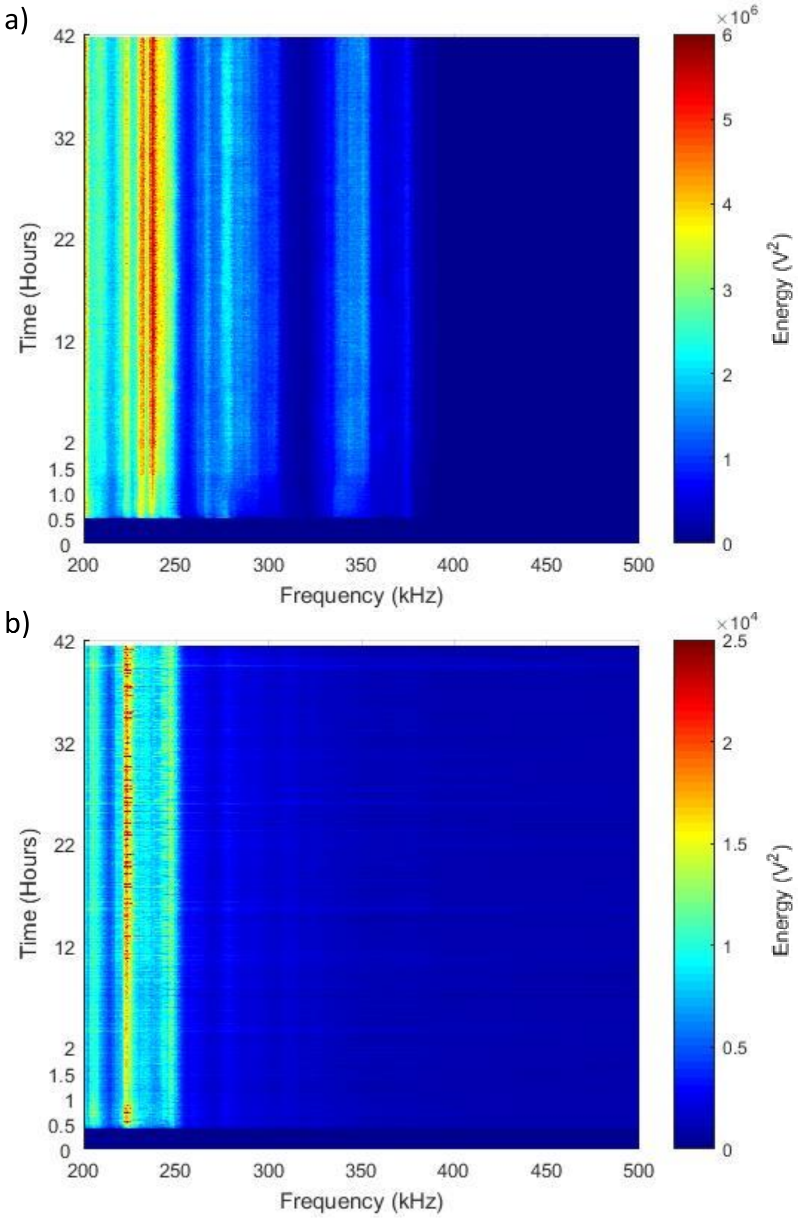

Figure 4-93 - Binned FFT between 200-500kHz for a) PCI-2 System and b) ACMS AE System at the start of Life Test 2

There is also a difference in the amplitude of the ACMS AE signals which show a large amount of energy as the test is started which reduces as the load is increased, before rising again as the system reaches a steady state. These trends are in complete contrast to those witnessed in Figure 4-92, the plot between 100-200kHz, but it may be possible that the amount of load applied alters the level at which each harmonic is excited.

It can be seen that for all three regions of the binned FFT investigated, 0-100kHz, 100-200kHz and 200-500kHz, the dominant frequency bands that were excited at the start of the life test continue to be excited throughout the test until final failure occurs at 2810 hours, Figure 4-94, Figure 4-95 and Figure 4-96 respectively.

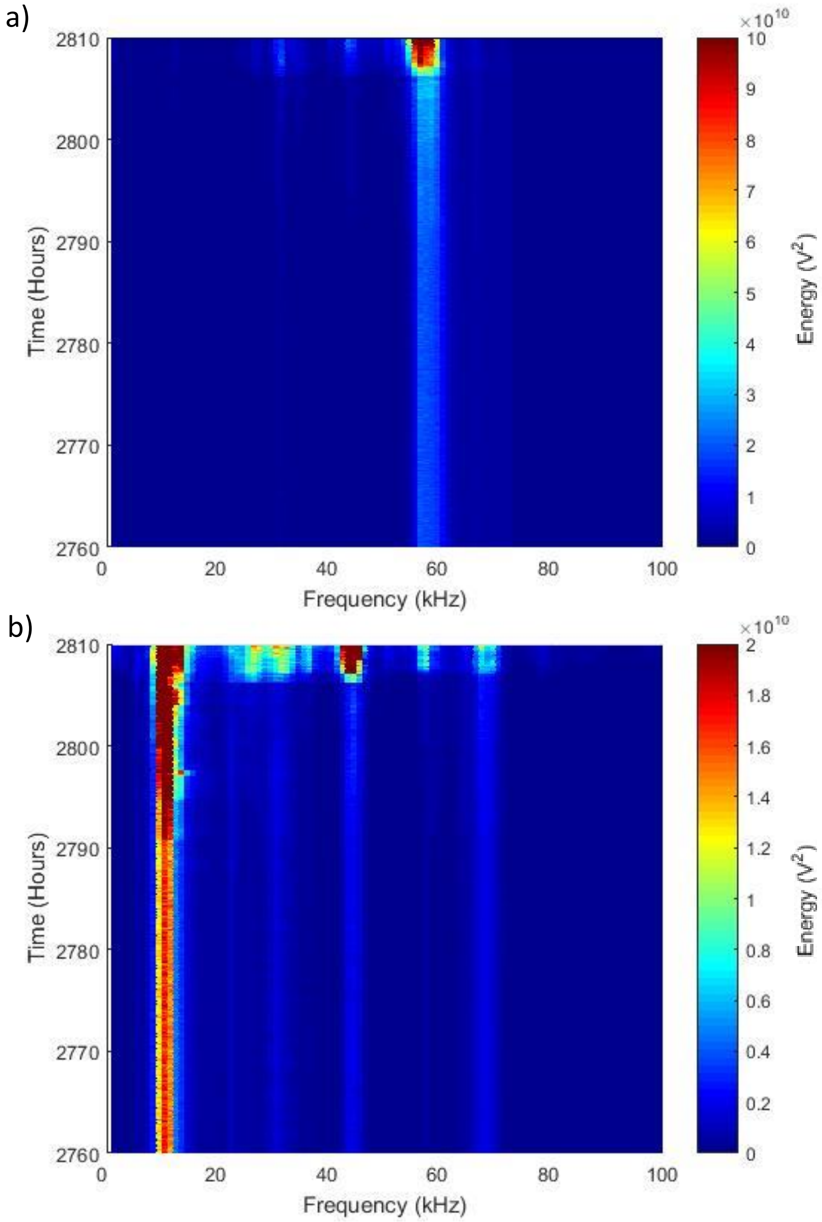

Figure 4-94 - Binned FFT between 0-100kHz for a) PCI-2 System and b) ACMS AE System after 2760 hours into Life Test 2

It can be seen that for each of the separate windows, including the vibration analysis (Figure 4-97) the amplitude of the dominant frequencies increases in line with the RMS amplitude, Figure 4-79.

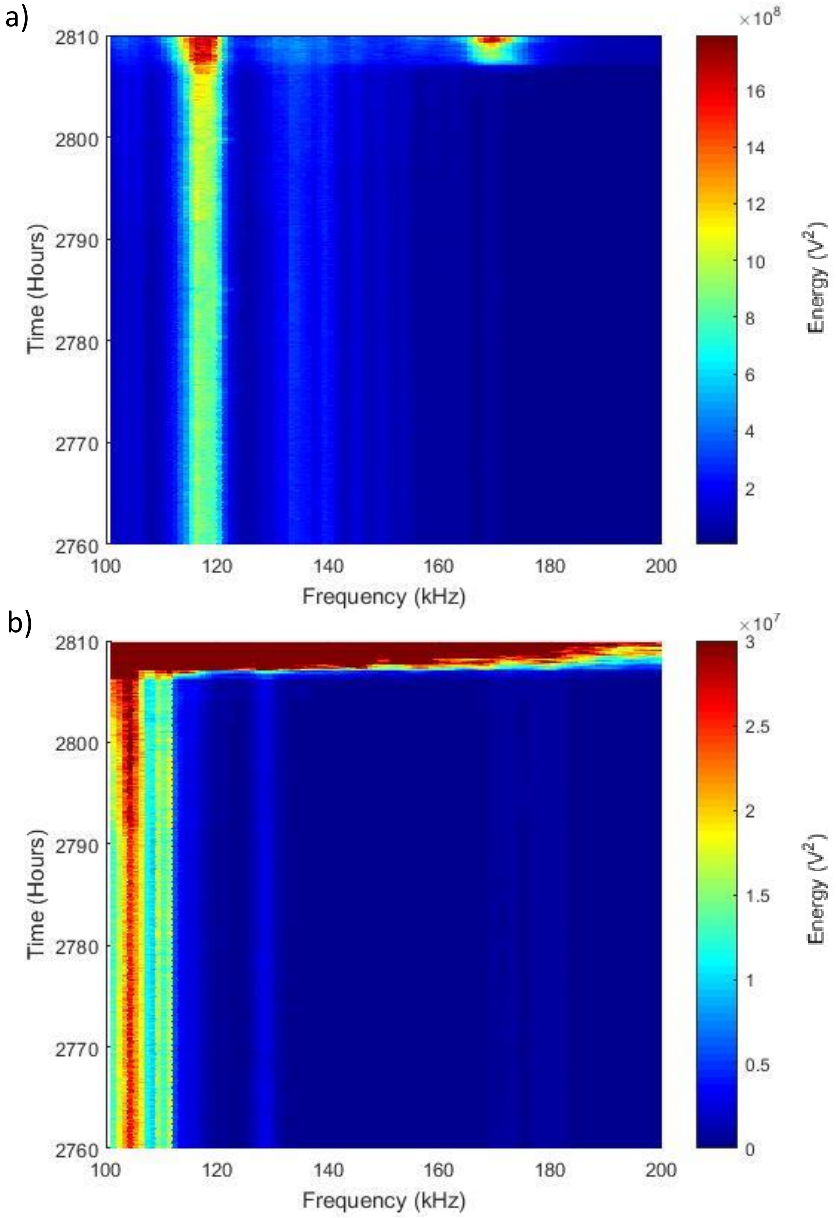

Figure 4-95 - Binned FFT between 100-200kHz for a) PCI-2 System and b) ACMS AE System after 2760 hours into Life Test 2

This is in contrast to the findings during Life Test 1, particularly in the region of 200-500kHz. It was seen in the analysis of Life Test 1 (Figure 4-64) that for the PCI-2 data the energy at 330kHz increased in amplitude between 2 and 7 hours although the RMS amplitude remained relatively constant. It is thought that this is due to the source location as Life Test 1 concluded with extensive damage to the inner and outer raceways. Signal propagation from both of these raceways, particularly the outer raceway, is known to be far stronger than emission from a roller due to the attenuation over multiple contact interfaces as well as the location of the damage relative to the loaded zone.

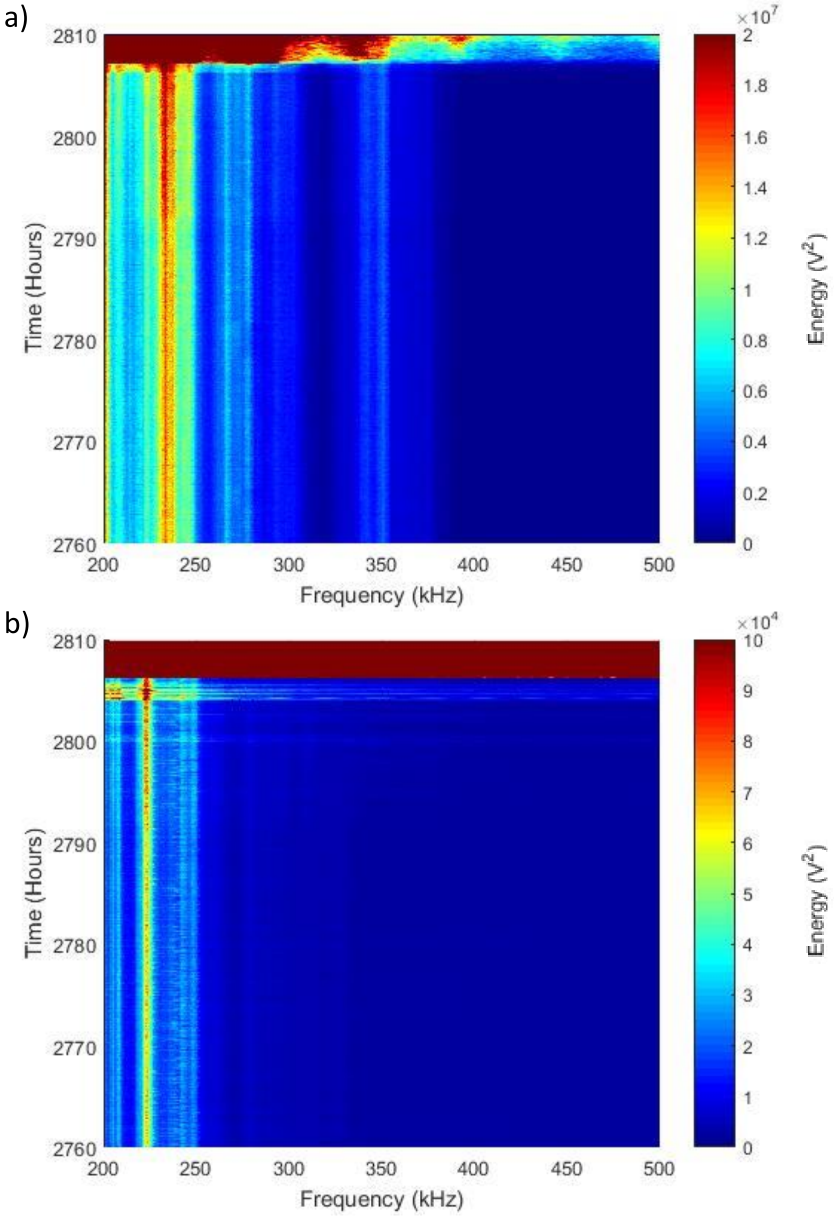

Figure 4-96 - Binned FFT between 200-500kHz for a) PCI-2 System and b) ACMS AE System after 2760 hours into Life Test 2

As a result of this, the advantage that AE demonstrated during the first life test is negated as for this failure mode, the detection of damage is possible on all three of the systems, with neither of them showing a clear advantage over the other types. It is however positive that a relatively small amount of damage to a roller could be detected by all three systems.

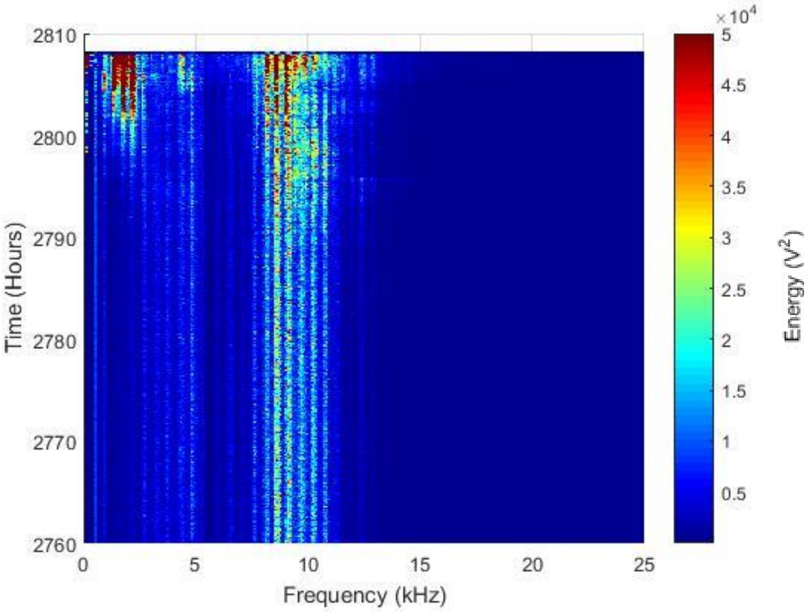

Figure 4-97 - Binned FFT of the Vibration signals between 0-25kHz after 2760 hours of Life Test 2

4.10 Chapter Conclusion

It has been shown that the for each of the tests conducted that when analysing the signals with RMS or frequency analysis, an increase in shaft speed has a far greater effect on the signal amplitude than when the load is increased. For all three systems, an increase in load also produced an increase in RMS amplitude and spectral energy although in Life Test 2, an increase in load caused both analysis techniques to reduce in amplitude. This has not previously been discussed by other authors however it is thought that it is due to small changes in the signal produced namely the amplitude of the signal. The different sets of vibration data gathered during the healthy bearing characterisation, Figure 4-17 and Figure 4-29, demonstrated very little change in the RMS amplitude with increasing load whereas the AE data recorded on the PCI-2 system demonstrated both increases and decreases in RMS amplitude. Although this leads to a hypothesis that the increase in load may be influencing the frequency content of the signals, this is not reflected in the frequency plots.

Section 1.5.5 discusses the continuity of data between each test set up and it has been demonstrated that there is a large variation in the results that are presented. However, throughout the rest of the chapter a number of similarities are drawn between different test setups, particularly between the excitation bands within the frequency analysis. It has also been shown throughout the analysis process that in general, the RMS amplitude of both AE and vibration data is able to detect the gross damage present within the bearing. It has also been shown through the study of seeded defects that PCI-2 AE system is highly sensitive to changes in the running condition. However, when running life tests, it is thought that due to the way damage propagates that the seeded defects produce a false sense of the actual sensitivity. For most of the tests carried out, it was seen that the frequency energy amplitude was proportional to the RMS, showing no clear advantage of analysing the frequency of the signals. However, through a heavily accelerated life test, it was shown that for damage propagation existing on the outer/inner raceway, the sensitivity of AE is better than vibration, but only when the sensor has a high frequency operating range. It was shown through the frequency plot that the energy at 330kHz for the PCI-2 system increased in amplitude independent of the RMS trend. For the following life test however, there was no indication within the frequency plot that there existed a change in running condition other than the increase in line with RMS increase.

5 AE Monitoring of Large, High Load Bearings

5.1 Chapter Overview

5.1.1 Introduction

Whereas Chapter 4 applied AE sensors to a relatively small test rig which was designed specifically to ensure the sensors were able to be positioned close to the source of AE, this chapter applies the technique of AE to a third-party test rig that was not designed for the sole purpose of detecting AE from bearings. The test rig, based at the Newcastle University Gear Design Unit, was instead designed to investigate the fatigue characteristics of large roller bearings which are normally used to support the planet gears of 1.5-2.5MW wind turbines.

Section 5.2 introduces this test rig beginning by summarising its overall design, followed by a more in depth description regarding the fundamental characteristics of the machinery and equipment that is used to operate it. Section 5.3 describes a preliminary study performed prior to the full test commencing which determined the wave propagation characteristics within the bearing housing. Section 5.4 then details how the main experiment was set up, followed by Section 5.5 which analyses and discusses the results gathered throughout the main experimental works. The chapter then concludes with Section 5.6 where the observations made throughout the chapter are summarised.

5.1.2 Aims and Objectives

The chapter as a whole aims to:

- Apply the technique of AE to a test rig much larger, more complex and hence closer to an industrial application than the test rig outlined in Chapter 4.
- Determine if it possible to diagnose the location of a bearing failure without prior knowledge of its failure mode.
- Investigate the response of a double row roller bearing without a cage constraining the rollers in place.

5.2 Rig Overview

The high load bearing test rig, situated within the Design Unit at Newcastle University, was designed to simulate the operating conditions faced by the planet bearings of a 1.5-2.5MW offshore wind turbine. It can be seen in Figure 5-1 that, as a general concept, the test rig is similar in design to that of the bearing test rig detailed in Chapter 4, where a test bearing is placed between two support bearings and loaded radially whilst rotating.

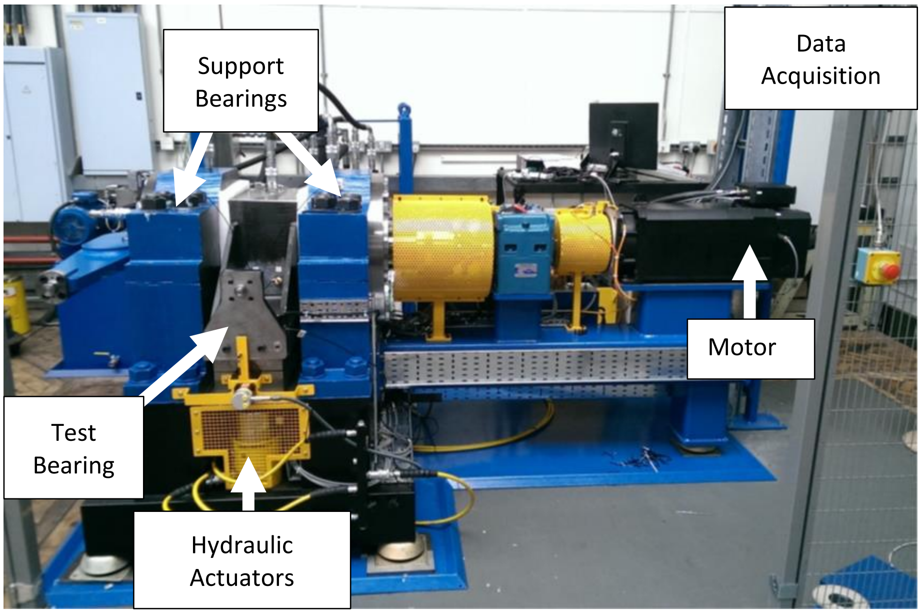

Figure 5-1 - Overview of Test Rig

For this investigation, an SKF NNCF 5044 CV double row, full complement rolling element bearing, the details of which are summarised in Table 5-1, was used (Figure 5-2). The bearing surfaces are coated with Diamond-Like Carbon (DLC), helping to provide the bearing with increased wear resistance as well as aiding in the prevention of adhesive wear (Doll & Kotzalas, 2010). The test bearing is a full complement bearing and, as there is no roller/cage assembly present, the rollers are prone to skewing producing an axial force within the test bearing. In order to react and measure the axial force produced, a reaction arm, instrumented with strain gauges, is applied to the test bearing, with its pivot point aligned with the centre of the shaft (Figure 5-3). Table 5-2 lists the bearing defect frequencies in terms of shaft frequency.

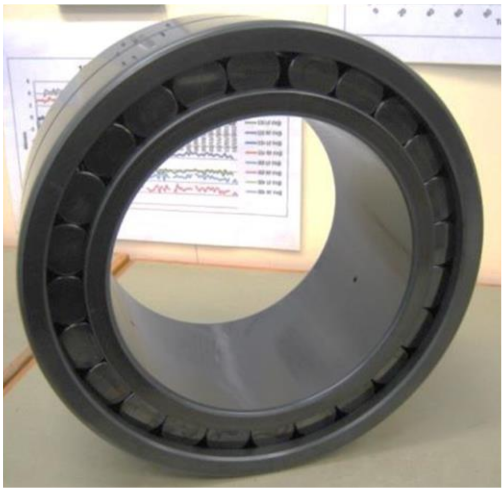

Figure 5-2 - A SKF NNCF 5044 CV roller bearing

Table 5-1 - Geometry and specifications of SKF NNCF 5044 CV roller bearing

Pitch Diameter, mm	277. 5
Roller Diameter, mm	36
Number of Rollers, Per Row	24
Static Load Rating, kN	2010
Dynamic Load Rating, kN	3600
Fatigue Load Limit, kN	375
Speed Rating, rpm	1100

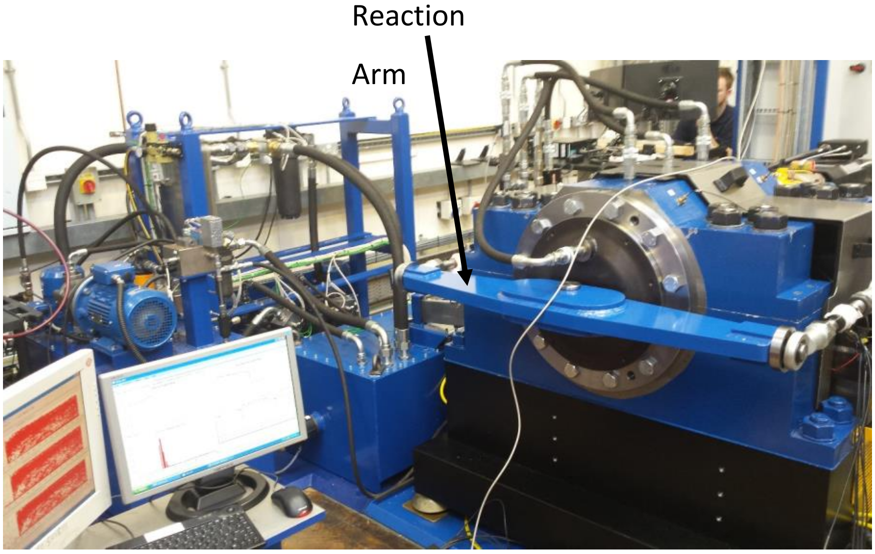

Figure 5-3 - High Capacity Bearing Test Rig

Table 5-2 - Characteristic defect frequencies in terms of shaft frequency, F

Characteristic Frequency	Theoretical Frequency (Hz)
BPFO	10.4 F
BPFI	13.6 F
BSF	7.54 F
FTF	0.43 F

The test rig is designed to operate up to a speed of 650rpm whilst applying a radial load of up to 3.5MN (350t.f) to the test bearing through a combination of hydraulic actuators located beneath the test bearing housing. There is one 100 bar hydraulic actuator located at the centre of the test housing with a further six 700 bar hydraulic actuators, distributed evenly either side of the 100 bar actuator (Figure 5-4). The main load is provided by the six 700 bar actuators with the 100 bar actuator allowing for the load to be 'fine-tuned' or 'trimmed'. The combined force of all seven actuators is distributed evenly to the bearing through a large roller, which also allows for the prevention of any misalignment between the bearing housing and the load cells.

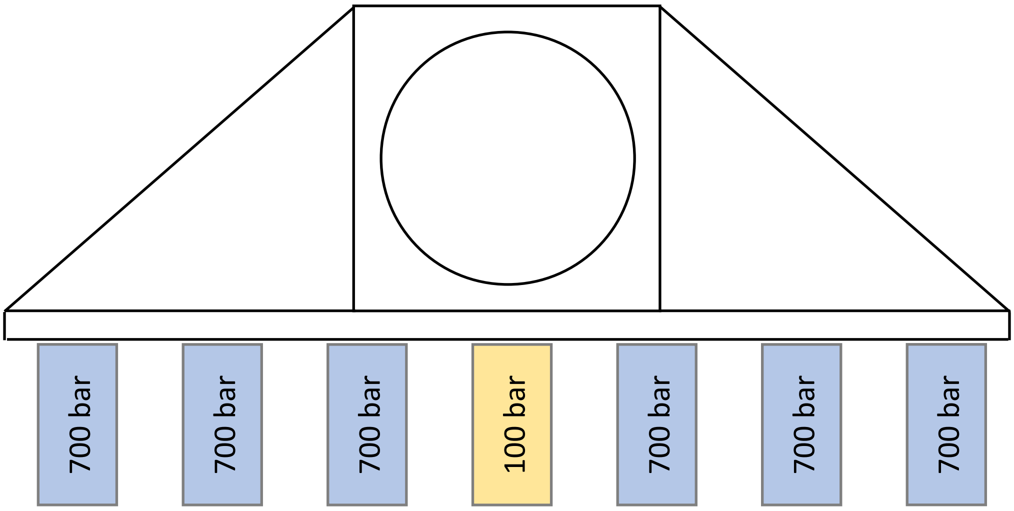

Figure 5-4 - Schematic of hydraulic actuator position

A mineral oil of specification ISO VG 220 was supplied to the bearings at a temperature of 45°C, kept constant through a heated oil sump as well as a water-cooled heat exchanger. The oil system contains a number of oil strainers and filters to ensure that the cleanliness of the supplied oil is to ISO 4406-/17/14 standard. In addition to this, several magnets were located on the underside of the oil return tray to catch ferrous particles within the oil, allowing for visual inspection as well as easy recovery of any particulates for further analysis.

A National Instruments data acquisition system was used to record and monitor a number of parameters detailing the running conditions of the test rig at a rate of 10Hz. There are over 40 different sensors monitored and they include the load, speed, temperature, vibration, oil feed flow rate and oil feed pressure of each bearing.

5.3 Preliminary Study

This test rig is considerably larger than the test rigs previously used and therefore a preliminary investigation was carried out to determine if signals were detectable, and if so, how different sensor types responded depending on their location upon the test housing. To determine the response of the system, artificial AE bursts or HN sources, were carried out upon the test bearing (Hsu & Breckenridge, 1981; ASTM, 2010).

As illustrated in Figure 5-5, three main locations were investigated; the top of the bearing housing (1), the front face positioned axially relative to the race (2), and the side face located radially to the race (3). WDI-AST, Nano 30 and P15 sensors were attached at locations 1 and 2 with magnets and a coating of ultrasound gel between the sensor face and housing to act as a couplant. Due to sensor and channel availability within the system, one WDI-AST sensor was placed at location 2, with another WDI-AST sensor located on the opposite face, to determine how symmetrical the wave propagation was through the material. Table 5-3 summarises the sensor locations.

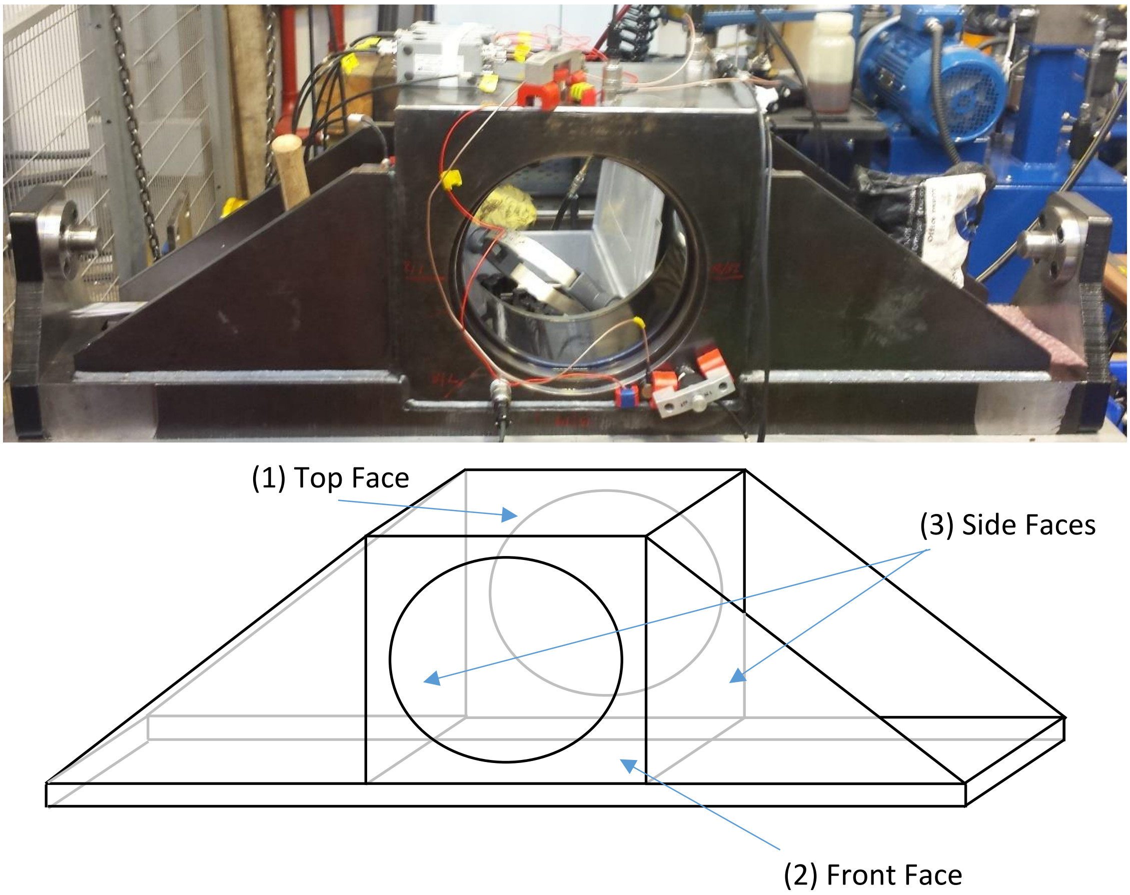

Figure 5-5 - Test Bearing Housing Schematics

Table 5-3 - Sensor Locations

Location	Sensor Type	Channel
(1) **Top Face**	Nano 30	2
	WDI – AST	4
	P15	7
(2) **Front Face**	Nano 30	1
	WDI – AST	3
	P15	8
(3) **Side Face**	WDI – AST	6
	WDI - AST	5

Five HN sources (pencil lead breaks, PLBs) were carried out at each sensor location to ensure adequate coupling before carrying out further characterisation. The first experiment was then conducted with PLBs carried out across the width of the bottom-most region of the bore in the test housing whilst the outer raceway was removed. The bottom region of the bore was selected for the HN sources as this is the region where rollers will be most heavily loaded during the operation of the bearing. Ten sources were carried out for every 22mm of axial movement along the 155mm width of the raceway.

Figure 5-6a-c plots the amplitude response, averaged over the ten PLB's conducted, for locations 1-3 respectively whilst the outer raceway was removed. It can be seen that when comparing the response of the two Nano30 sensors attached to Channel 1 and 2, mounted on the front and top face respectively, there is a larger amplitude in the axially located sensor as opposed to the sensor mounted on the top face. This is due to the relative distance of the sensor to the source, with the wave attenuating as it travels further through the material. In general, the standard error for the averaged HN sources was between 0.2 and 0.5 dB and because of this, it was not feasible to plot the error bars with the data.

It is also noted that both faces have a similar trend of response with respect to the lead break locations, albeit at different amplitudes. Unlike the Nano30 sensors, the WDI (Channels 3 and 4) and P15 (Channels 7 and 8) sensors exhibit less of a difference between the two mounting locations and this is thought to be due to their sensitivity to lower frequencies as shown in the calibration curves of the individual sensor types (Appendix B).

Finally, the response of channels 5 and 6, both WDI sensors mounted ± 90˚ relative to the lowest point of the raceway have very similar average amplitudes, albeit lower than the response of the sensors on the front and top face. It would be thought that the sensors mounted in this location, midway between the top face and bottom plane, would have a corresponding change in amplitude. However, the surface finish of these mounting locations was poor with the material being left as cast, increasing the attenuation of the signal as it is transmitted through the couplant and hence lowering the overall amplitude response of the sensors. Normally the surface could be prepared for the sensors, with the face being machined or sanded flat. However, modifications to the pre-existing test rig itself were limited and therefore it was not possible to improve this surface.

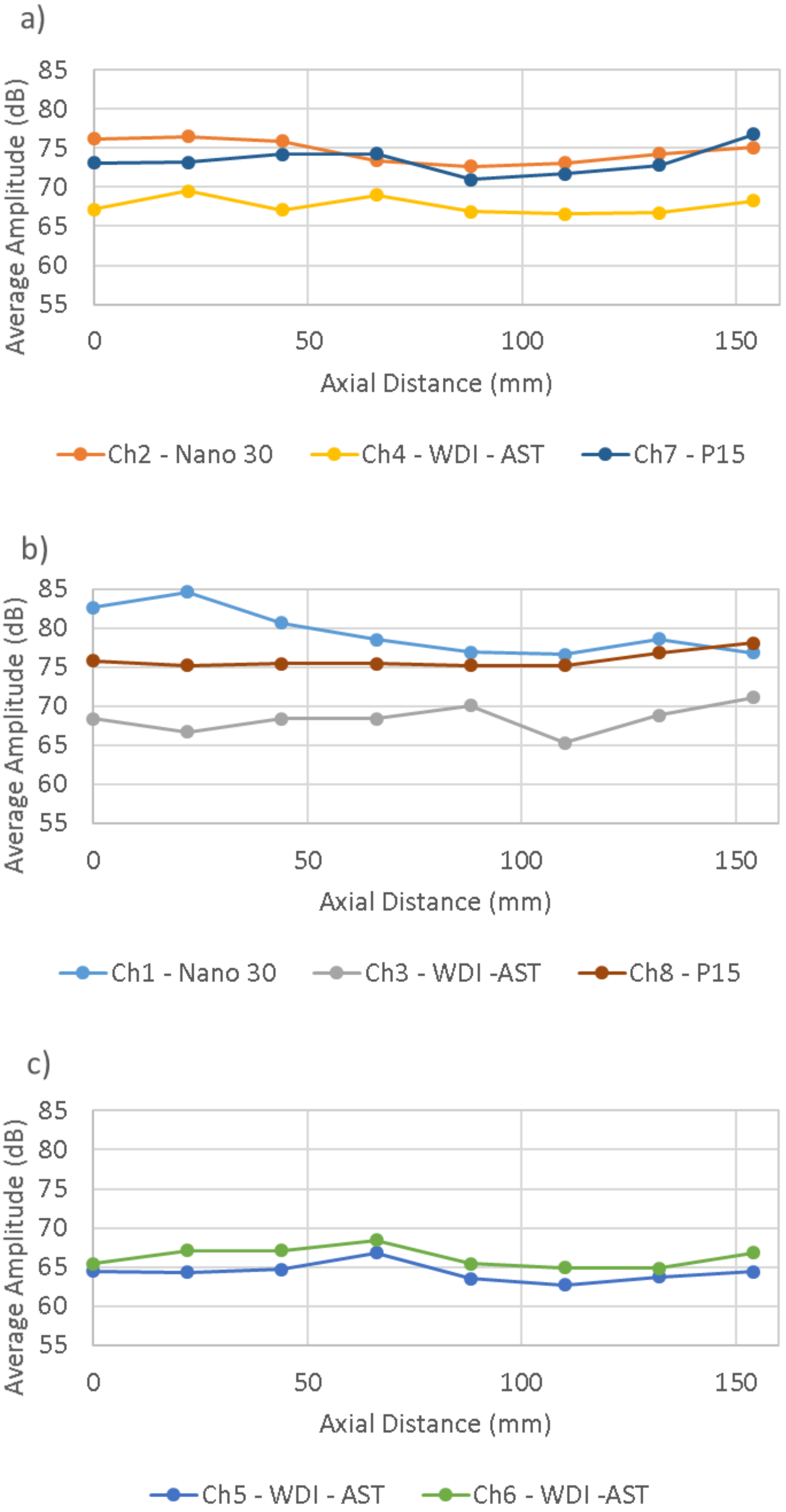

Figure 5-6 - Average amplitude of pencil lead breaks with the outer race removed at sensors mounted on a) Location 1, b) Location 2 and c) Location 3

The second test was carried out with the outer raceway installed in order to determine the amount of energy reduction as the wave propagated through the boundary between the two surfaces. The outer raceway was coated in oil prior to installation to allow the race to slide into the bore more easily, this has the added benefit of aiding coupling between the surfaces. Like the previous experiment, the HN sources are able to provide some indication of the energy loss as the wave travels through the material but when under real loading applications, the attenuation due to the boundary between the raceway and housing bore will be much reduced as the extreme loads force the two bodies together, deforming them elastically. Therefore, it is thought that the pencil lead breaks are in fact a ‘worst-case scenario’ in terms of the level of attenuation between the two bodies. Again, ten pencil lead breaks were carried out every 22mm along the width of the raceway. Figure 5-7.a-c plots the averaged amplitude response for the eight channels used.

With the outer raceway installed within the bearing housing, it can be seen that the average amplitude of all eight sensors has reduced. This is due to the extra boundary through which the wave must travel between the outer raceway and housing. As with the raceway removed, there is also a reduction in the average amplitude between the axially mounted Nano30 sensor and the sensor mounted on the top face. The two other sensor types however, the WDI and P15 sensors, demonstrated a reduced amount of attenuation in the average amplitude in the top face sensors compared with the axially mounted counterparts. This may be due to the sensitivity of the different sensor types to the signal frequency. With the inner raceway installed, the signal will change from being broadband to individual narrow band frequencies depending on the material properties. With the inner raceway installed, the dominant frequencies will change and some frequencies may even be attenuated as they pass through the oil film between the raceway and housing hence exciting the lower frequency sensors more.

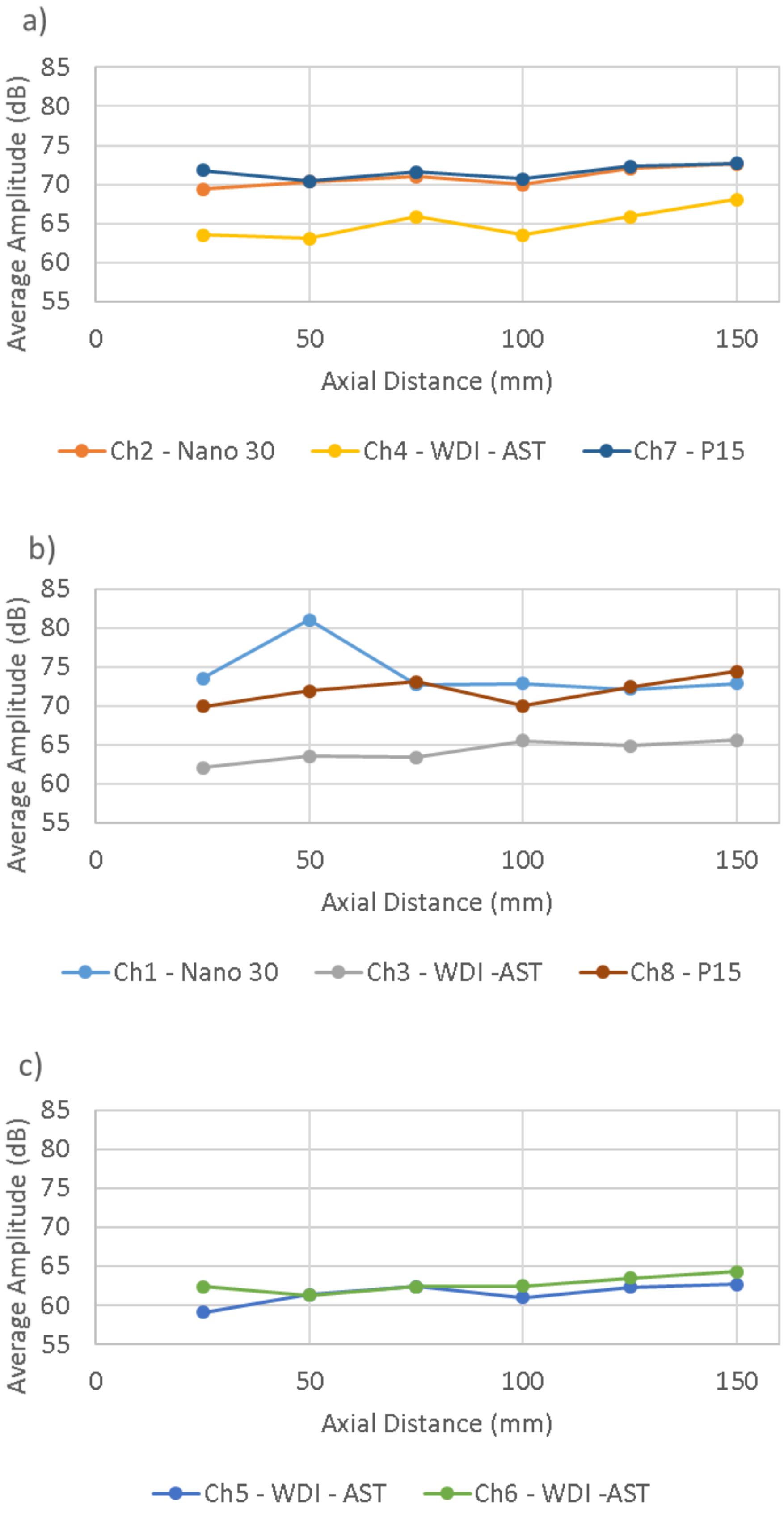

Figure 5-7 - Average amplitude of pencil lead breaks with the outer race installed at sensors mounted on a) Location 1, b) Location 2 and c) Location 3

Based on the results of the preliminary study it was decided that Nano30 sensors would be used as they demonstrated the strongest amplitude response both axially and on top of the bearing housing. Also, due to their small size they were able to be located close to the outer raceway in small, machined pockets. To ensure that the sensors would not become entangled within the test bearing in the eventuality of the sensors becoming dis-bonded, tapped holes were machined either side of the pockets, allowing for a securing plate to be fastened over the top of each sensor.

5.4 Experimental Set Up

Based on the information gained in the preliminary study, the test rig was reassembled along with both Nano30 AE sensors and DFS6000 vibration/AE sensors placed upon the test bearing housing (Figure 5-8). Two of the Nano30 sensors were positioned on either side of the test bearing housing as close to the outer race as possible in small, machined pockets. A third Nano30 sensor was placed on the top face of the bearing housing next to the oil inlet manifold. Two DFS6000 sensors were also placed on the top face, one near a pair of existing accelerometers and another next to the Nano30 sensor, whilst a third sensor was placed away from the main test housing, mounted to the loading base. Due to their size, it was not possible to place the DFS6000 on the front face where the Nano30 sensors were mounted. Engine gasket silicone, Loctite 5910, was used to secure the Nano30 sensors into place as well as acting as a couplant between the test head and sensor face. Like the previous bearing tests, the engine gasket silicone was selected due to its resistance to elevated temperatures and lack of deterioration in the continual presence of mineral oil. Cyanoacrylate adhesive was used to mount the DFS6000 mounting bosses into which the sensors were screwed into with a film of grease acting as a further couplant between the sensor and the boss.

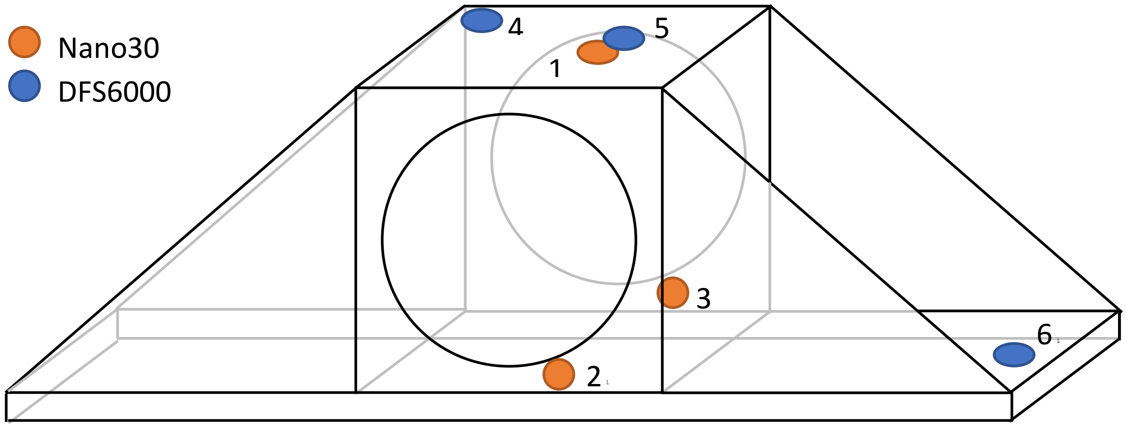

Figure 5-8 - Sensor location for main experiment

5.4.1 Data Acquisition

To minimise file size, the sampling frequency of the recorded wave streams for both the PCI-2 and ACMS was set at 1MHz and they were recorded every 15 minutes with the PCI-2 triggered based on the number of rotations. As discussed in Section 2.6.3, due to Nyquists theory the maximum possible detectable frequency when sampled at 1MHz is 500kHz. 500kHz was deemed an acceptable frequency threshold as the Nano30 sensor has a resonance at approximately 300kHz and DFS sensor had a resonance at 60kHz. The sampling frequency was also limited by the potential size of the files as the length of wavestreams recorded on the PCI-2 system was set at 1 seconds, whereas the ACMS system has a permanent length of 0.5 seconds. There is a disparity between the length of time for which each wavestream was recorded between the two different systems as it was deemed beneficial to record as many continuous shaft revolutions as possible to determine periodicity between them.

The gain of the PCI-2 system was initially set at 40dB but because of the high voltage amplitude witnessed during the early tests, the gain was reduced to 20dB. As this is simply a change of scaling factor, all of the data has been adjusted to the equivalent of a 40dB gain. For the ACMS system however, the internal gain is fixed at 14dB. The top Nano30 sensor was attached to a 100-1200kHz bandpass filter and the two side-mounted Nano30 sensors were initially attached to an inline 20-1200kHz bandpass filter. As the test progressed however (Run 2), the two inline filters were swapped for 100-1200kHz bandpass filters as the gain was fixed at 40dB on the inline filters.

5.4.2 Test Overview

Prior to the AE sensors being applied to the test rig, the bearing had already been run to its theoretical L_{10} life, after which the rig was disassembled and inspected for any damage/wear to the races. Upon inspection, it was found that the DLC coating upon the surface of the bearing had become scored in some regions within the contact area on the outer raceway (Figure 5-9). The scoring was located at the end of the roller path and it is thought to be caused by the large stress concentrations present at the end of the contact zone (Johnson, 1987). Although rollers are usually barrelled to minimise the effect of roller end stresses, the stresses are not completely eradicated. These large scores were located only on the outer raceway at the point of maximum load however, a number of smaller areas of scoring were distributed on both of the races (Figure 5-9.a and Figure 5-9.b). These smaller scoring marks were generally located close to small indentations or spalls on the raceway and are thought to be due to debris particles being rolled over and dragged through the contact region (Figure 5-9 d). Although there was some surface damage present, there existed no evidence of white etching failure, the failure mechanism the test was designed to initiate, and it was deemed that the bearing was not damaged significantly enough to justify its replacement. The drive shaft and support bearings were also visually inspected for any damage and as none was found, the rig was re-assembled.

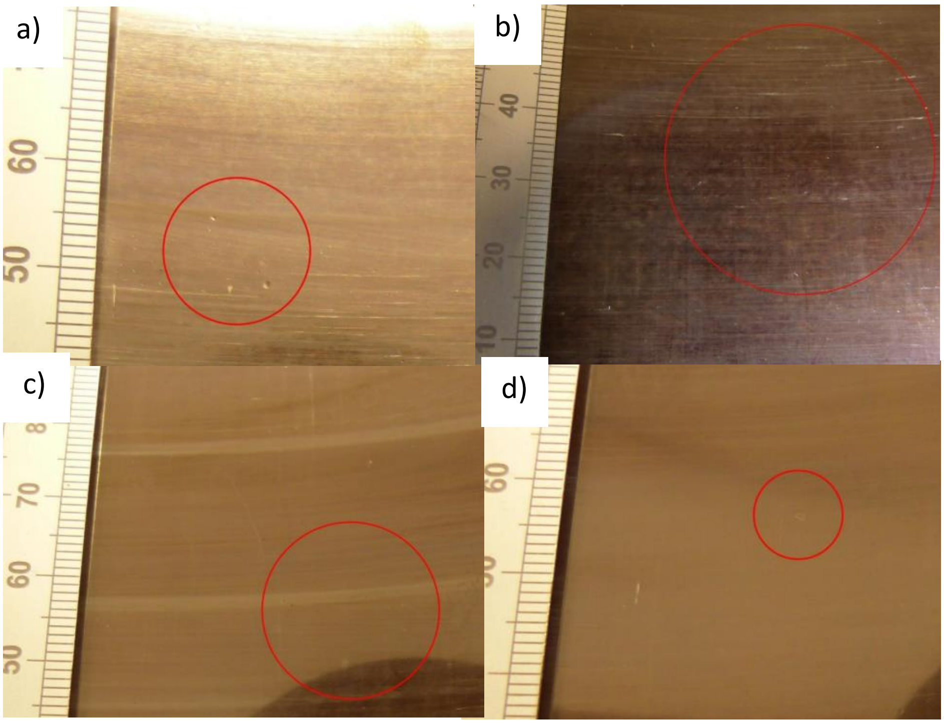

Figure 5-9 - Visual damage to the surface of the outer raceway before resuming the experiment

Between 10th March – 18th March the rig was monitored using AE sensors whilst being run for short intervals to ensure that the test rig, including its multiple sub-systems, were functioning correctly. The test rig, as previously described in Section 6.2, continually monitored a number of parameters and if any parameter exceeded a pre-determined threshold, the test rig was automatically shut down. The automatic shutdown was triggered a number of times, with the two main reasons for this being increased oil temperature and foreign debris detected in the oil return tray. Table 5-4 demonstrates how the data has been split up into a series of 'Runs' and determines the operating conditions of each run, as well as the cause of the run being ended.

Table 5-4 - Overview of runs 1-5

	Revolutions (cycles)	Speed (rpm)	Load (kN)	Stoppage Reason
Run 1	9168	100	500	Temperature & Debris
Run 2 (Static test)	0	0	0-1500	End of Test
Run 3	10941	450	1500	Temperature
Run 4	29163	250	1500	Temperature & Debris
Run 5	49713	450	1500	Debris

5.5 Results

The following results section is divided into a number of sections detailing the main findings in each of the runs conducted. Over the duration of the testing period the operating conditions, both speed and load, were changed continually between 0-450rpm and 0-1500kN respectively. Also, as the bearing had previously been run to its L_{10} life it is not possible to determine a healthy baseline to compare the bearing with. Therefore, for simplicity, the analysis of the following data will focus on discussing the visible characteristics within individual wavestreams. The data will be discussed chronologically, demonstrating the typical signal analysis conducted when trying to determine the location and severity of any damage within the bearing. Then to conclude the results section, photographic evidence of the actual damage produced during this set of experiments will be discussed, relating it to the key findings within the wavestream analysis.

5.5.1 Run 1

The first time the test bearing was run following re-assembly of the rig, the speed was set to 100rpm with a load of 500kN (+/- 20kN). Figure 5-10 illustrates the raw wavestreams recorded on the three channels of the PCI-2 system. As the test rig was running at a speed of 100rpm (1.67Hz) each PCI-2 wavestream only contains 1.6 revolutions of the shaft. It can be seen throughout the signal there exists a number of transient waves, each varying in amplitude. Each transient event is recorded on all three channels, with Channels 2 and 3, exhibiting a larger amplitude than Channel 1 and hence is indicative of the source being closer to the two sensors positioned close to the outer race, i.e. from within the highly-loaded contact region.

Visual analysis determines that the transients are spaced at a frequency of approximately 22Hz, corresponding to the ball pass frequency over a single location on the inner raceway (BPFI). Frequency analysis of the raw signal, Figure 5-11.a, is not able to determine this frequency however when the signal is enveloped using a Hilbert transform the frequency plot is able to determine the second harmonic of the BPFI at 44Hz (Figure 5-11.b).

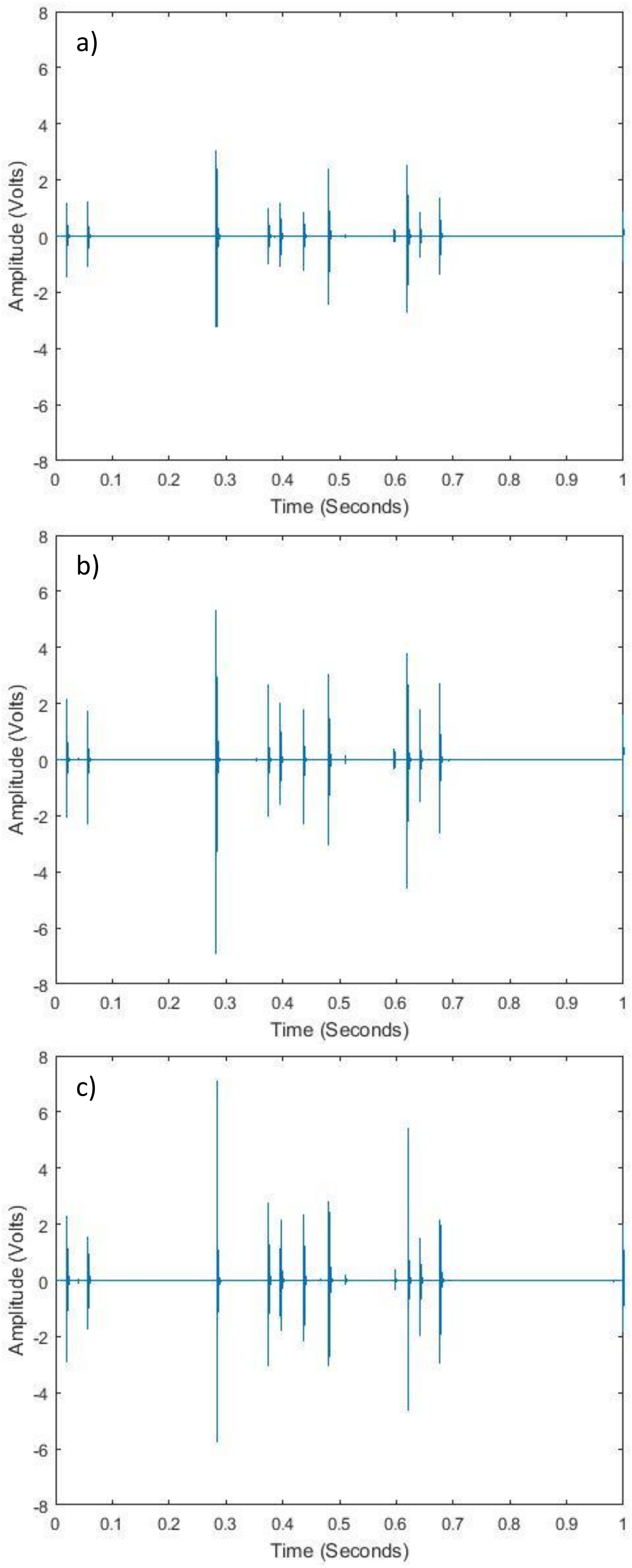

Figure 5-10 - Wavestreams of Channels 1-3 at 100rpm and 500kN after 3366 revolutions on a) Channel 1, b) Channel 2 and c) Channel 3

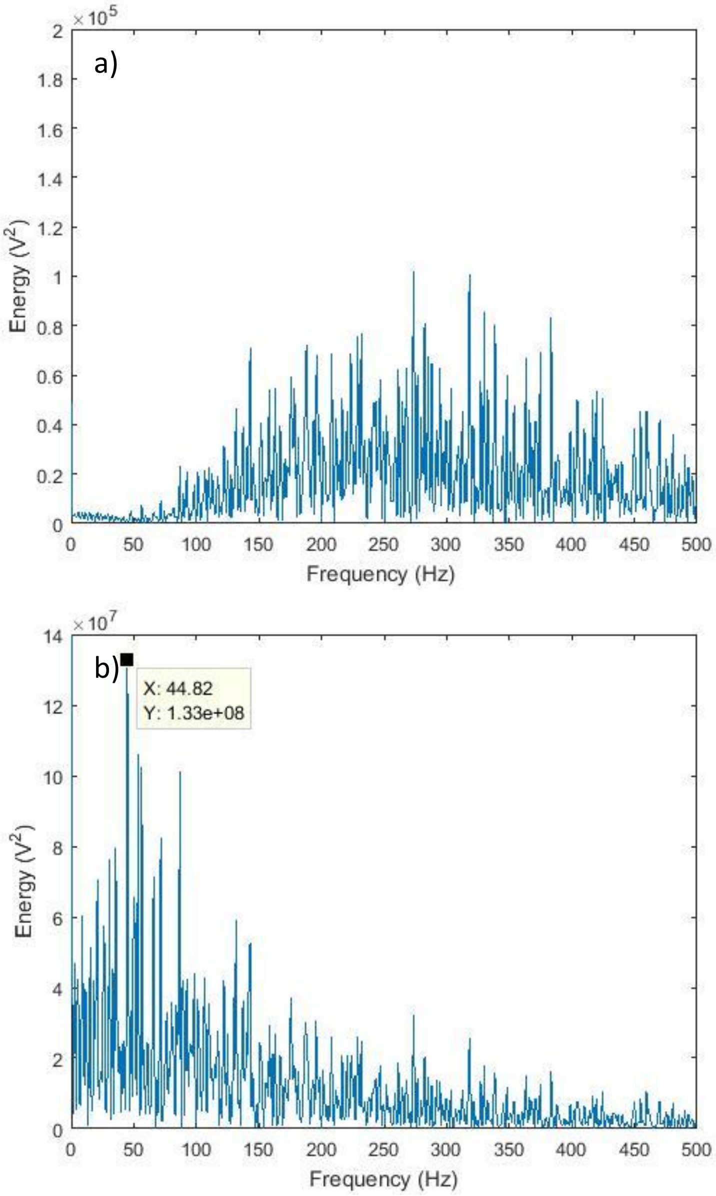

Figure 5-11 - Frequency analysis of Channel 2 a) Raw Signal and b) the Hilbert transformed signal after 3366 revolutions.

Although the spacing of the transients corresponds to the BPFI, the literature determines that when studying the vibration signal produced by damage on the inner raceway, the amplitude of the transients should be increasing and then decreasing as the inner race passes in and out of the area of maximum load, Figure 5-12 (Halme & Andersson, 2010). The transients witnessed in Figure 5-10 however do not demonstrate the common pattern and instead feature sporadic bursts of transients throughout the revolution of the bearing. This is an indication that the source of the transient bursts is not producing a transient every time it makes contact with a roller.

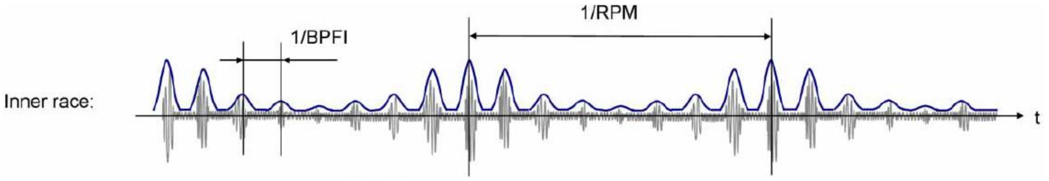

Figure 5-12 – Typical vibration wavestream produced by damage on the Inner Raceway of a bearing - (Halme & Andersson, 2010)

This suggests that the source is not constant, for example, it may be caused by the over-rolling of debris, flaking of the DLC coating, or other sources of plastic deformation. If the debris is being ejected from the contact zone or sticking to surfaces due to being rolled in, then emission will not occur periodically. Shiroishi *et al.* (1997) discussed that the data analysis technique employed through their research, peak ratio, was unable to detect debris denting because of the lack of strong characteristic defect frequencies. There is also the possibility that the source of the emission occurs on the subsurface of the inner raceway. As there will only exist a few subsurface crack locations to begin with, bursts will be sporadic and only emit energy when in the most heavily loaded region of the bearing.

Evidence of this non-periodic nature of the AE source is even more prominent in the following wavestream, Figure 5-13, recorded after a further 1100 revolutions of the inner race while still running under the same operating conditions. The signal now contains only three large transients, with the first two spaced at approximately 0.2seconds and the second and third transients spaced approximately 0.3 seconds apart (0.315Hz). Curiously, the gap of 0.3 seconds is a similar spacing to the larger amplitude transients witnessed in Figure 5-10, 0.336 seconds (2.976Hz). Running with a shaft speed of 100rpm, 1.6Hz, these larger bursts are occurring at approximately twice the shaft frequency and may indicate the source entering and leaving the loaded region. Although the spacing between these transients is similar after 3366 and 4459 revolutions of the inner race, the transient amplitude has decreased in the latter of the two wavestreams.

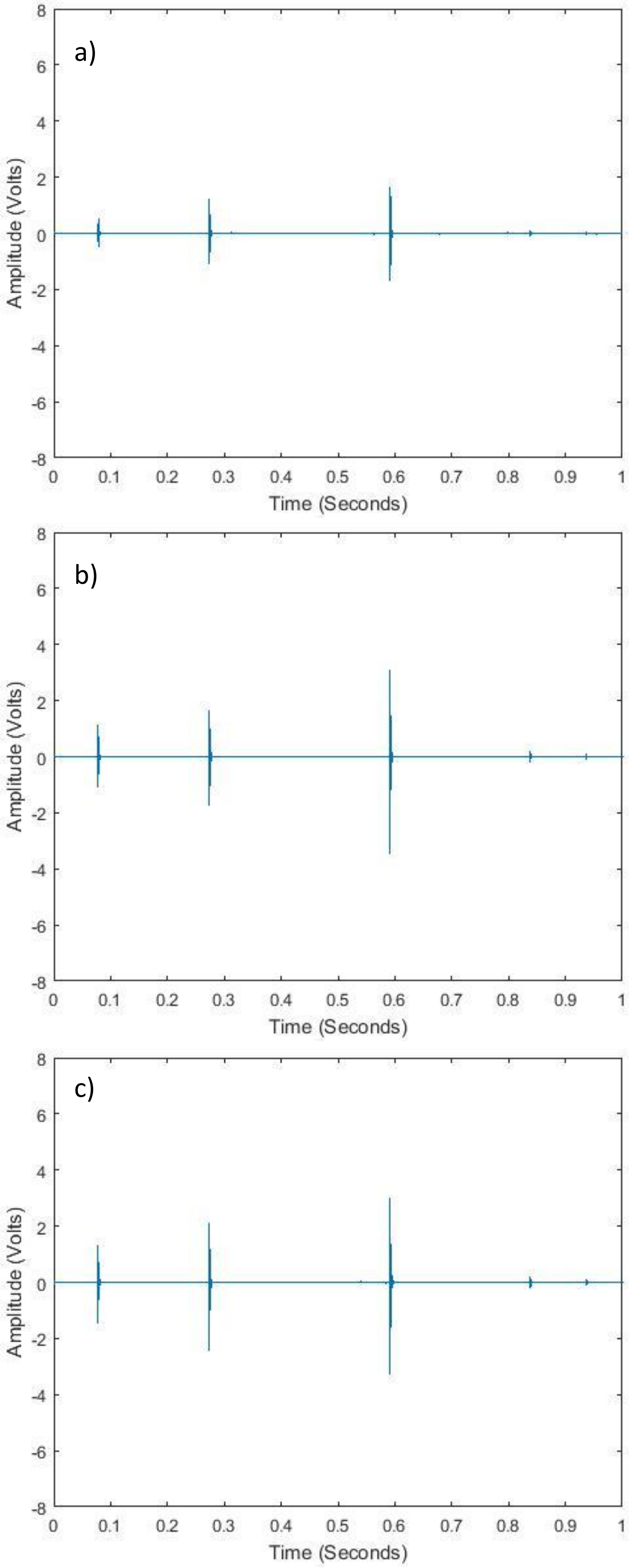

Figure 5-13 - Wavestreams of Channels 1-3 at 100rpm and 500kN after 4459 revolutions on a) Channel 1, b) Channel 2 and c) Channel 3

It can be seen in both Figure 5-10 and Figure 5-13 that the recorded wavestreams are similar across all three channels, although they vary slightly in amplitude. Therefore, Figure 5-14.a and b plot the raw PCI-2 wavestreams of only channel 2 after a total of 4970 and 7299 revolutions respectively. Although the transient bursts are not occurring continually throughout the single revolution of the driveshaft, and are therefore not easily detectable via order analysis, it is possible to develop a better understanding of the source mechanisms by closely investigating the relationship between individual transients within a wavestream.

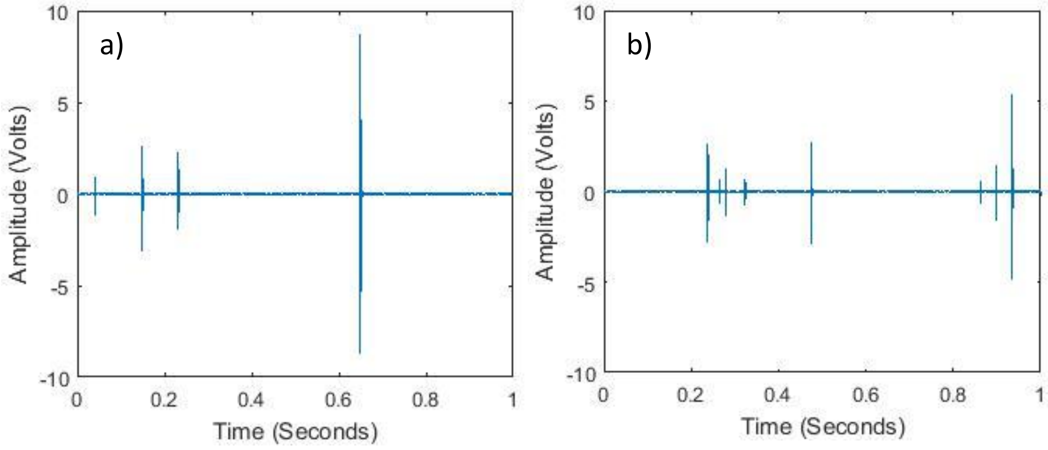

Figure 5-14 - Channel 2 raw waveforms after a total of a) 4970 and b)7299 revolutions

A typical wavestream demonstrating this is illustrated in Figure 5-15.a-c, where Figure 5-15.a is a magnification of Channel 2 after 4970 revolutions (Figure 5-14.a) and Figure 5-15.b-c are both magnifications of Channel 2 after 7299 shaft revolutions (Figure 5-14.b). In Figure 5-15.a, the time delay between two of the transients is 0.0832 seconds, or 12.02Hz. With a shaft speed of 1.6Hz, this equates to 7.51 orders, corresponding closely to the BSF of 7.54 orders. The BSF itself relates to a full rotation of the ball or roller and as such, there are usually two transient bursts, differing in amplitude and occurring at twice the BSF as the defect produces a transient on the outer raceway and then the inner raceway. In this instance however, the transient has only been produced on one of the races. This may be due to the transient burst produced at the inner raceway being too weak to excite the sensor. With that said however, Figure 5-15.b&c both produce the characteristic double occurrence of the BSF with transients spaced at 24.8Hz, where Figure 5-15.b is characteristic of a roller leaving the loaded region and Figure 5-15.c is a different roller entering the loaded region. This can be deduced by the change in amplitude of the roller as it contacts what is assumed to be the outer raceway, where reduction indicates a roller leaving and an increase indicating the roller entering the loaded region. It is possible that the surface of individual rollers may be damaged however, as the transients are not produced throughout the time that the roller is within the loaded region, the transients are more likely to be produced by foreign debris and this debris is either being rolled into the raceways or being ejected with the oil. It is also noted that in earlier wavestreams there existed a presence of the BPFI (Figure 5-10), however, after only just over 1000 revolutions, the BPFI is no longer a dominant signal characteristic.

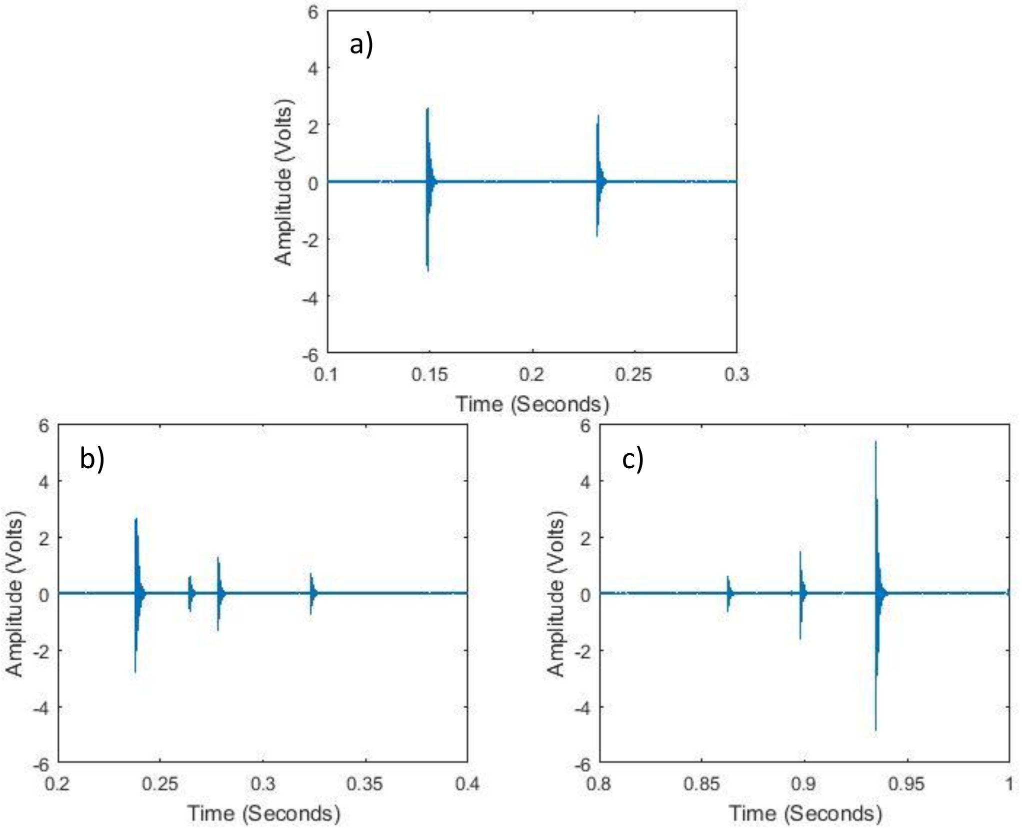

Figure 5-15 - Demonstration of the Ball Spin Frequency with the wavestreams after a) 4970 revolutions and b-c) 7299 revolutions.

Also visible in Figure 5-15.b is a transient after approximately 0.26 seconds that occurs in between the transients released at the ball spin frequency. Without any further information surrounding this transient, as in successive transients to which a frequency can be linked, it is not possible to know for sure the true origin. Although there are a number of potential sources, it is possible that this burst may be due to the over rolling of extra debris on the roller or raceway. Transients are also visible within the wavestreams recorded by the ACMS system, Figure 5-16.a and Figure 5-16.b. Recorded after a total of 5142 and 7648 revolutions respectively, the transients in Figure 5-16.a and Figure 5-16.b are recorded only a couple of hundred revolutions after each of the two PCI-2 wavestreams depicted in Figure 5-14. However, the transients witnessed in Figure 5-16.a and Figure 5-16.b do not occur at the same rate, i.e. there is no detection of the orders representing the BPFI or BSF.

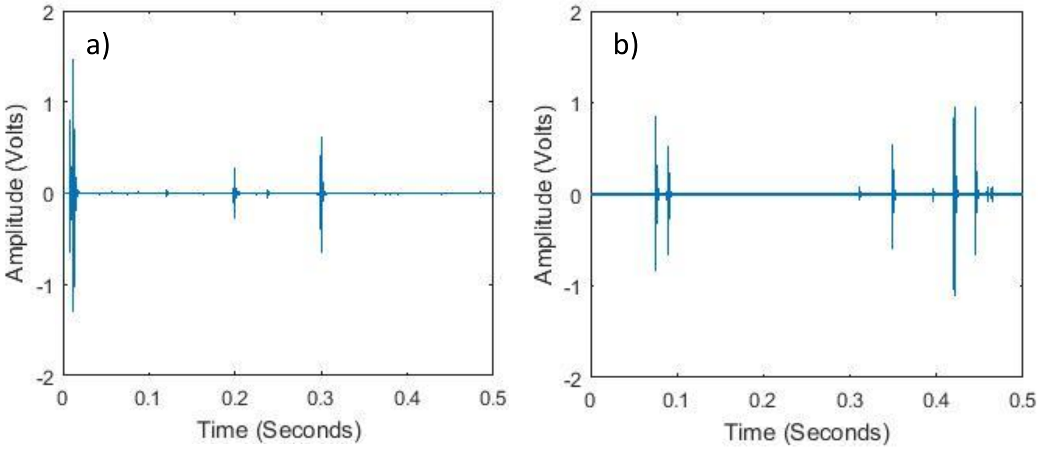

Figure 5-16 - ACMS raw waveforms after a total of a) 5142 and b) 7648 revolutions

This may be because wavestreams only allow for a snapshot of what is happening within the bearing at any one time and, if the length of that time window is not long enough then it is possible that information can be missed. The ACMS system, with a fixed window length of 0.5 seconds, only captures 80% of a revolution at a shaft speed of 100 rpm. As the two different systems are operating independently, the wavestreams are not collected simultaneously. As both systems are monitoring the same bearing however, it is thought that the sources producing transients in PCI-2 data are the same sources detected by the ACMS. As witnessed in the PCI-2 wavestreams, the early transients appeared for only short durations within the wavestreams and therefore it is thought that if it was possible for the ACMS wavestreams to be longer, then more relevant data may have been collected in the early damage detection phase.

Observations of the low level noise floor in the early wavestreams recorded on the PCI-2 system reveals that periodic transients also occur on all channels at what was initially thought to be the outer race frequency (17Hz or 10.2 orders). Figure 5-17 demonstrates this phenomenon in the wavestreams recorded after a total of 9168 shaft revolutions.

Upon further inspection, it can be seen that in contrast to the high amplitude transients witnessed in Figure 5-10 and Figure 5-13, the amplitude and clarity of these transients is greater in Channel 1, the sensor mounted on top of the bearing housing, than when compared to Channels 2 and 3, the sensors mounted close to the outer race in loaded region.

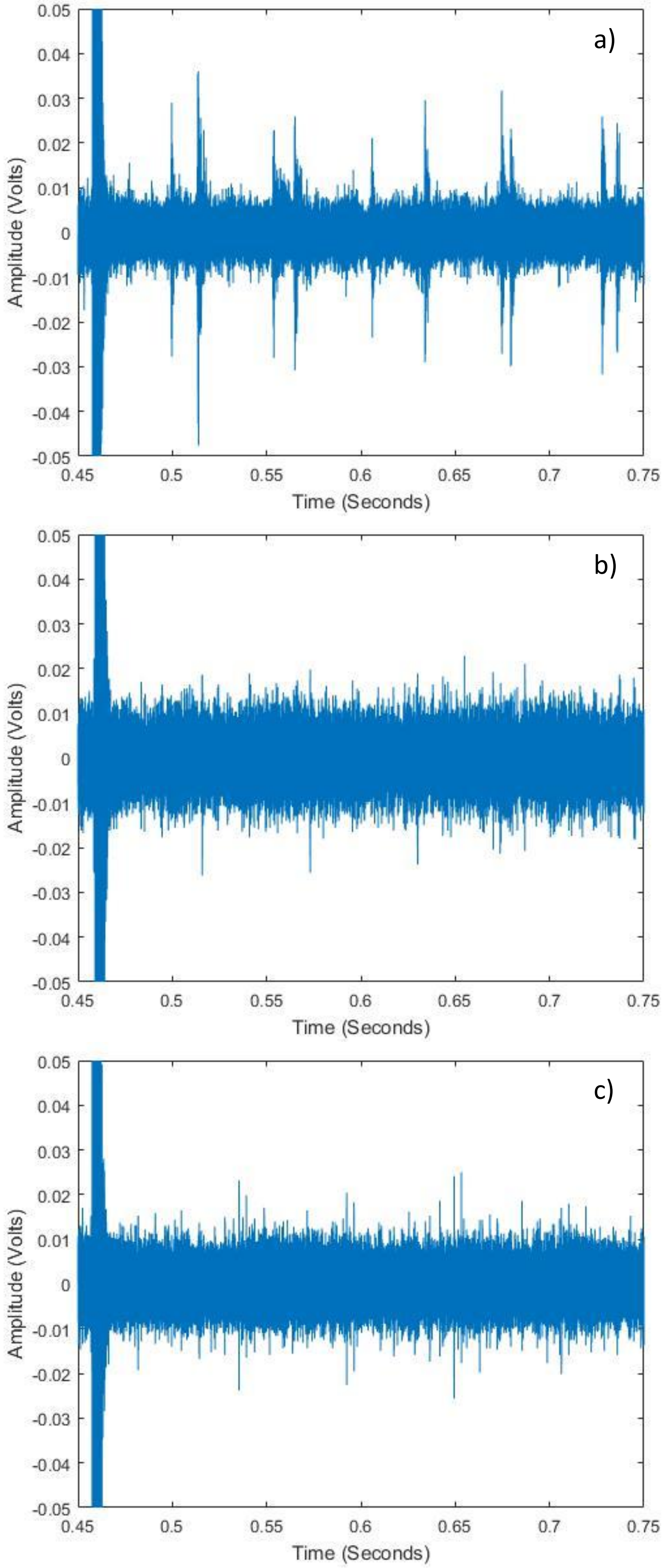

Figure 5-17 - Detection of low amplitude transients within wavestreams recorded on a) Channel 1, b) Channel 2, and c) Channel 3.

Low level AE, as seen in earlier chapters, is produced at the characteristic defect frequencies even without there being any damage on the raceway. This is because of the energy released as a roller passes through a region of maximum load. Although this may be the cause of these transients, it is thought that if they were caused by the roller passing through the loaded region of the outer raceway, the amplitude in Channels 2 and 3 would be greater than that of Channel 1. It is true that the direction of the sensors may also play a part in this as the sensors will have a greater sensitivity to waves propagating out of the plane however, as seen in the preliminary study, Channel 2 was more sensitive to artificial sources in the lower region of the outer race when compared with Channel 1.

Therefore, it is thought that rather than corresponding to the outer race frequency, these transients relate instead to the roller slap frequency, a phenomenon witnessed in full complement bearings when a roller/ball ‘falls’ into the preceding roller as it passes the highest point in its arc of rotation. Bearings with a cage installed do not suffer from this as their rollers/balls are constrained at a fixed angular spacing. Full complement bearings on the other hand, without a cage, have space for an additional roller but also exhibit a small gap as the total diameter of all rollers is slightly less than the pitch diameter.

Being loaded from below, there also exists a slight clearance between the rollers and the outer raceway at the top of the bearing and hence the event will occur closer to the top sensor, Channel 1, than the sensors mounted next to the bottom of the outer raceway, Channel 2/3.

As the test bearing is a double row roller bearing, it is appreciated that there are two separate occurrences of the roller slap frequency as the rollers become out of phase, as illustrated in Figure 5-18. Figure 5-18 also provides further evidence of roller slap occurring as the time between each of the transients continually fluctuates. If this was detection of the BPFO then it would be thought that the time spacing would be more constant because, as the rollers enter the loaded region, all rollers are touching and hence, periodically spaced. With both roller skew and the dynamic forces acting on the rollers themselves, there will exist a greater amount of fluctuation in the time it takes for a roller to fall as it passes its maximum height.

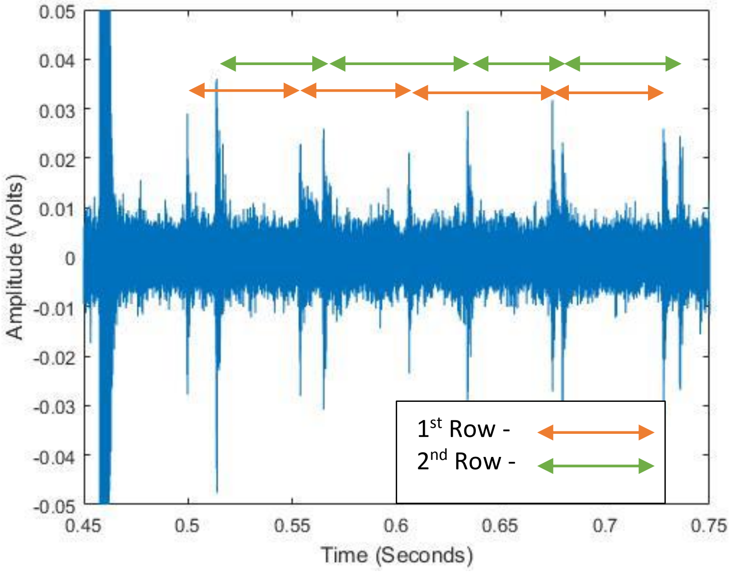

Figure 5-18 - Demonstration of transients produced by each individual row of rollers

To investigate the plausibility of the hypothesis that this is the detection of transients due to roller slap, simple analysis of the dimensions of the inner raceway and rolling elements can be carried out to determine a band of theoretical times which a roller could take to fall.

It is known that the Inner Race Diameter = 241.5mm, Roller Diameter = 36mm and therefore, Pitch Diameter = 277.5mm and the Pitch Diameter Circumference = 871.80mm. As there are 24 rollers, they occupy 864mm of the pitch diameter circumference, leaving a maximum gap width of 7.80mm. At a shaft speed of 100rpm, or 1.6 Hz, the fundamental train frequency (FTF) of the rollers, i.e. the time it takes for a single roller to complete a full revolution, is 0.43 x F. Therefore, at 1.6 Hz, FTF = 0.7166. As there are 24 rollers per row, the frequency for roller slap will equal 24 x FTF = 17.2Hz or 10.32 x F.

At 100rpm, one revolution of the roller train takes 1.4 seconds. A minimum and maximum time between subsequent rollers passing over the top of the bearing can be calculated by determining the time it would take if there was no gap present and if there exists a 7.80mm gap. For the minimum time, where two rollers are touching the roller has to travel 36mm of the arc, taking a total of 0.057 seconds. However, if there is a gap, the maximum time between rollers passing through increases to 0.072 seconds. For the impacts witnessed in Figure 5-18, the time delay for each individual row of rollers is summarised in Table 5-5.

Table 5-5 - Summary of the difference in time of transient burst detection due to roller slap

Row 'A'	Row 'A' Delta T	Row 'B'	Row 'B' Delta T
0.4992		0.5132	
0.5533	0.0541	0.5645	0.0513
0.6054	0.0521	0.6337	0.0692
0.6741	0.0687	0.6792	0.0455
0.7273	0.0532	0.7353	0.0561

Although none of the transients occur at a greater time delta than the maximum permissible time, 0.072 seconds, it can be seen that the time delta between most transients is lower than the minimum time albeit by only a few thousandths of a second. There are a few reasons as to why this may occur:

- The time of arrival for each transient event is determined by the first time the transient burst exceeds the noise floor level. It is possible that the transients occur earlier within the signal but due to the noise floor, it is not possible to observe the start of the wave.
- Although the speed is well monitored and controlled, if there happens to exist a scaling error in the data acquisition software then the speed could be a few rpm higher than the readings suggest.

These transients are only visible in the wavestreams recorded on the PCI-2 system. Investigation of the frequency response reveals that the transients are occurring low down on the frequency spectrum and hence should be in the detectable range of the DFS6000 sensors. However, due to the size of the sensors, it takes significantly more energy to excite the larger sensors than the smaller Nano30's. If this is indeed the detection of roller slap, then it is thought that the sensitivity of the DFS6000 is too low.

Due to an increase in oil temperature, the test rig was shut down automatically after a total of 9322 shaft revolutions at a speed of 100rpm and was not restarted again until the following day.

5.5.2 Run 2

As this experiment, as a whole, is conducted under higher loads than previously investigated, a static load test was conducted in order to determine if transient bursts of AE are due to increasing load or if they are produced by the rolling motion of the bearing instead. The static load capacity of a NNCF 5044 CV bearing is 2010kN and therefore the maximum load should not exceed 1500kN in an attempt to prevent causing any damage to the bearing.

Without rotating the main shaft, all the sub-systems, i.e. oil feed and hydraulic load actuators, were started and wavestreams were recorded to determine the influence of each of these sub-systems. It was found that under normal operation, with negligible load applied to the test bearing, there existed only the background noise. The load was then increased from 0 to 1500 kN in increments of approximately 25kN for loads between 0 – 150kN and 50kN for loads between 150-1500kN, with each load held for approximately 30 seconds (Figure 5-19).

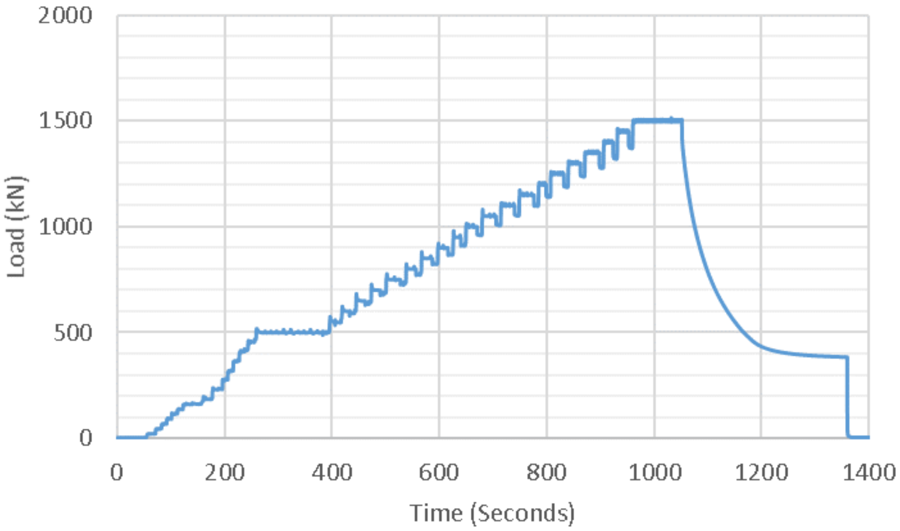

Figure 5-19 - Load increments during Static Load test

Due to the sensitivity of the hydraulic actuators having to produce load via displacement, it was found that as the load was increased further it became increasingly difficult to apply such small load changes. Therefore, the load was instead reduced by 50kN and then increased by 100kN thus producing the 50kN differential required. The load was held stationary at 500kN for a period of 2 minutes to allow for a visual inspection of the test rig to ensure there were no problems before exceeding the load further as well as allowing any stresses to settle.

Once the maximum load of 1500kN had been achieved, the load was held for a total of 90 seconds before being quickly reduced back to 400kN, a known safe load. Once this load had been achieved, the load was then removed completely and the test was concluded. Only the PCI-2 system was used during this investigation as the ACMS system is designed to be applied to a wind turbine and hence, does not allow for static experiments to be carried out easily.

Figure 5-20 illustrates the hit amplitude vs. time for all three channels attached to the test head. It can be seen that as the system is turned on at time zero, there were a large number of hits on the system. It is thought that this may the detection of transients as the hydraulic pumps and oil systems are started. The test was begun after 160 seconds and as the two systems, the PCI-2 system and the PC controlling the test rig, were not connected, a time mark was used to indicate when the target load was changed on the PC, corresponding to the load increments in Figure 5-19. The first hit was recorded when the load increment was paused briefly after 250 seconds although, when observing the waveform produced, there is little/no information contained within these hits.

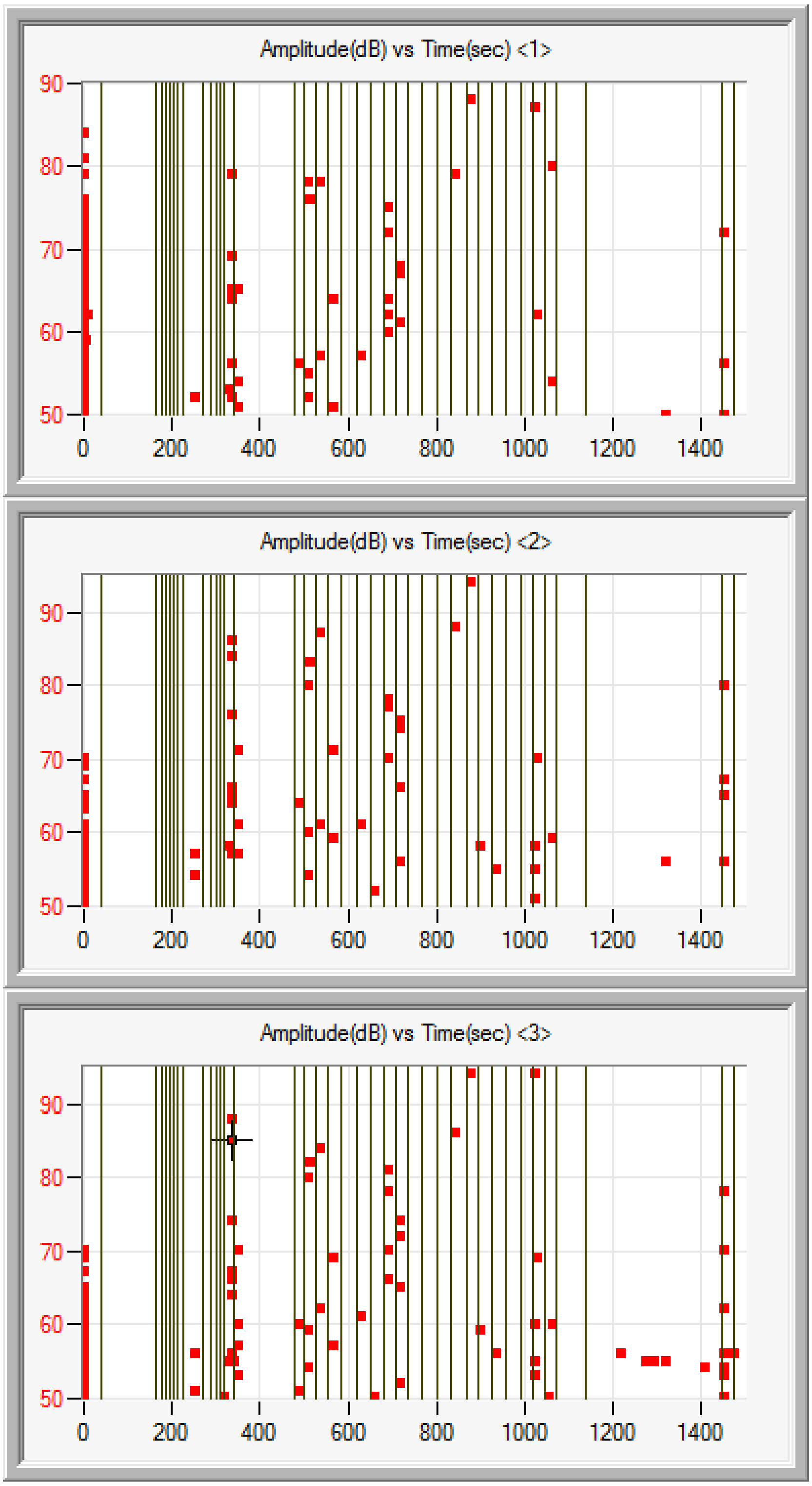

Figure 5-20 - Amplitude vs Time for Channels 1-3 - static test.

After 340 seconds the load reaches 500kN, the same load as applied during Run 1. A large number of hits occurred and the load was held for a period of 2 minutes to determine if any other events were taking place. It can be seen that after the initial burst of hits, there are no further hits when held under 500kN of radial load.

As the load increased further, hits were witnessed under nearly every load up to 1500kN. It can be seen that there is a clear gap between the time mark, as the load is increased, and any hits (Figure 5-21).

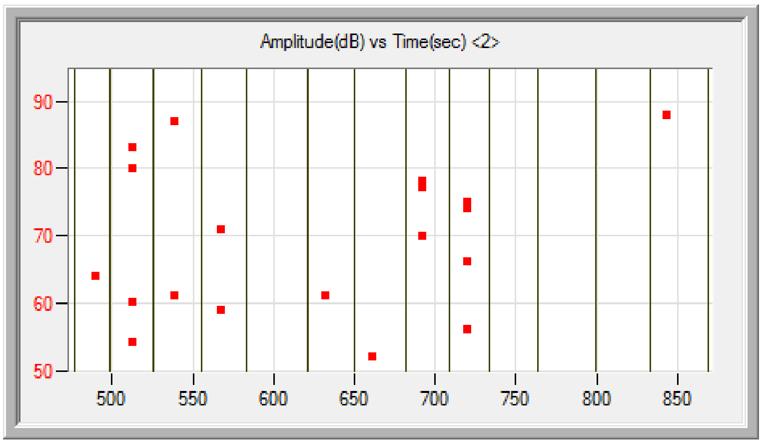

Figure 5-21 - Demonstration of hit location relative to load change

There are two potential explanations for this behaviour:

1) Due to the inherent sensitivity of applying load through displacement, when the load is increased, the load is first decreased by 50kN and then increased by 100kN. It is possible that the hit represents an example of the Kaiser effect, meaning that there is no AE until the previous load is surpassed. This would also explain why there were very few hits until the load reached 500kN.
2) 'False' AE hits are known to be produced when the hydraulic actuators go from the unloading phase to the loading phase. Yu *et al.* (2011) discusses that the opening and closing of the servo-valve is known to cause erroneous hit data. Also, because of the high loads that the bearing is subjected to, there may exist a micro-slip region between the shaft and inner raceway, plastic deformation of the shaft due to the high bending stresses of the shaft or even plastic deformation of the raceway/rollers all of which can produce AE hits.

Although not expanded on or analysed in detail by Fuentes *et al.* (2016), the results of a compression test involving a single roller and an inner raceway are presented. The maximum load applied to the single roller is 1000kN and far exceeds the individual roller loads of this experiment, however it can be seen that AE bursts occur at loads as low as 100-150kN. Although it is unknown whether the source of these AE bursts is due to plastic deformation within the contact zone or just the settling of the test rig, hits are produced continually as the load was increased.

Taking this information forward, it is thought that if the number of rollers in contact had been increased in the study by Fuentes *et al.* (2016), the number of transient bursts would have increased as plastic deformation occurs at two separate locations. For this static experiment, there are a maximum total of 26 rollers in contact with the inner and outer raceway way at any one time (13 per row). Therefore, rather than observing a single hit as the load is increased, multiple hits would be thought to be witnessed due to the Kaiser effect as each of the roller locations exceeded their previous maximum load.

AE hits were also observed during the unloading phase as the load became close to 400kN. It is thought that this may be due to the release of strain energy as the material is unloaded as well as the detection of slight axial slippage between the inner raceway and shaft as the amount of any bending or misalignment within the bearing is reduced. This is also shown by Fuentes *et al.* (2016), where the cumulative hits continue to rise as the load on a single roller is reduced from 750N to 0N.

5.5.3 Run 3

Following the static test, the signals produced during a dynamic test differed greatly from those produced during Run 1. Figure 5-22.a illustrates how the shape of the wavestream recorded on Channel 2 has changed from the form of previous wavestreams, as the shaft rotation speed and load have been increased to 450rpm and 1500kN respectively. Figure 5-22.b is extracted from Figure 5-22.a and demonstrates the typical wavestream for a single shaft revolution.

When previously studying the effects of speed and load on the generation of AE in roller bearings (Chapter 4), it was found that the amplitude, and hence the amount of energy contained within the signal, increased as the speed and load were increased. This was discussed at length within the literature review and Chapter 4 and it was found to be due to the change of the number of rollers in contact causing the load to fluctuate which changes the stiffness and hence produces vibration and AE.

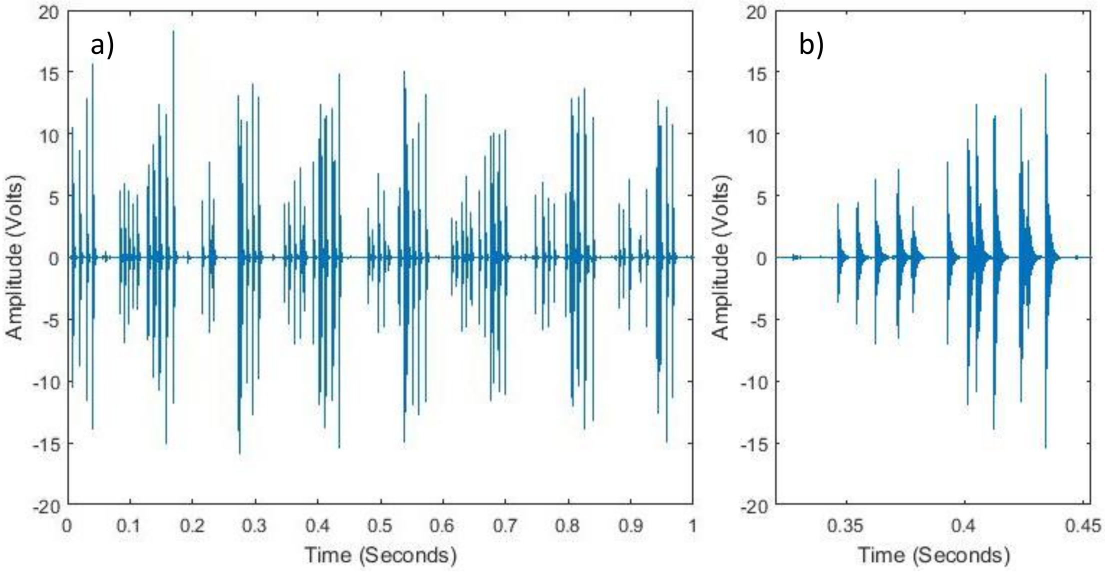

Figure 5-22 - PCI-2 Ch2 wavestream at 450rpm and 1500kN after 17314 revolutions for a) full recorded wavestream and b) wavestream over a single revolution.

Comparing wavestreams at 450rpm, Figure 5-22, with those collected at 100rpm, Figure 5-14, it can be seen that the number of transients per revolution has increased significantly. This is likely to be caused due to the increase in both speed and load however there is the possibility that, although the load was below the static load limit, some form of damage may have been introduced unintentionally during the static test, possibly due to misalignment causing concentrations of high contact stress for example. It is important to note that because the amplitude of the transients at 100rpm was fairly high, the decision was taken to decrease the amplifier gain from 40dB to 20dB, reducing the amplitude by a single order of magnitude. This is because the input of the analogue to digital converter can only handle voltages between +/- 10V, resulting in clipping of the signal if the voltage exceeds this. This decision was based on the analysis of the healthy signals in Chapter 4, where an increase in speed was followed by an increase in signal amplitude. For simplicity of analysis and continuity, the signals have been scaled to resemble the amplitudes as if they were amplified with a gain of 40dB.

It can be seen that for a single revolution of the shaft, Figure 5-22.b, there are two separate sets of transient bursts, each containing 3-5 bursts occurring periodically, with the first set of transients at a lower amplitude than the second.

Frequency analysis of both the raw and enveloped signal determines that the transient bursts witnessed in Figure 5-22.a are produced at a rate of 94Hz, corresponding closely to the BPFI of 102Hz (Figure 5-23). It can also be seen that the BPFI, including its harmonics, also have fringes either side of the central frequency, each spaced at the shaft frequency of 7.5Hz. Enveloping the signal with a Hilbert transform allows for the detection of the first two harmonics of the shaft frequency but the energy in the harmonics of the BPFI has reduced significantly.

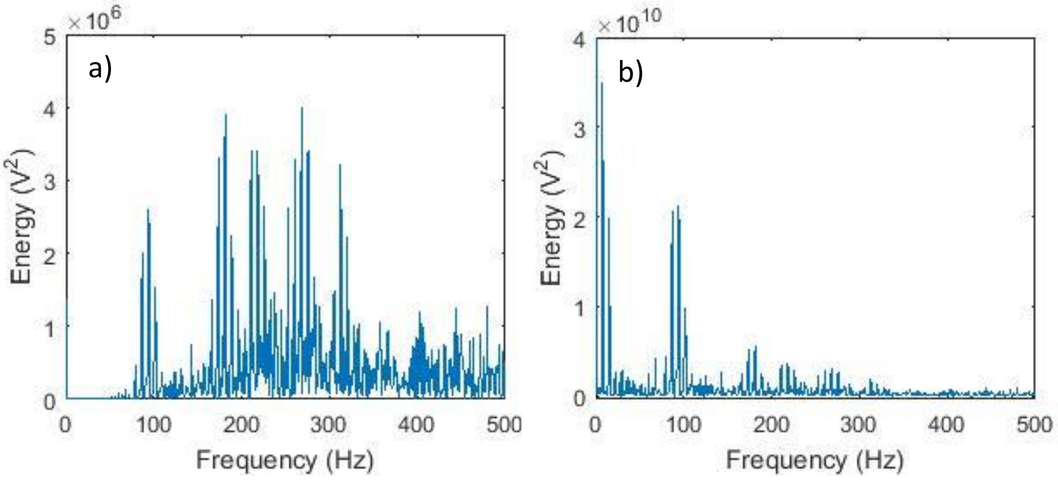

Figure 5-23 - Frequency analysis of a) Raw Wavestream and b) Enveloped Wavestream of signal in Figure 10.

As the surrounding literature is focussed on the early detection of defect frequencies, it would commonly conclude that this is clear evidence of the detection of an inner raceway failure. Inner race failure is also reportedly difficult to detect due to the number of interfaces through which the signal must pass (Mba & Rao, 2006; Shiroishi *et al,*. 1997; Tan & Mba, 2005).

This also negates the possibility that the BPFI detected here is due to the natural loading and unloading of a healthy raceway as the outer race defect frequency would appear more dominantly than the inner race. There are a number of hypotheses as to why there exist two sets of transient bursts per revolution;

1) If these transients are produced by a <u>*single*</u> defect on the inner raceway, then the lower amplitude would be where the ‘damage’ enters the loaded region and the higher amplitude as it passes through the area of maximum load (as commonly demonstrated in the vibrational frequency plots (Halme & Andersson, 2010)). Due to the Kaiser effect, there would be minimal AE as the roller exits the area of maximum load as the defect had been previously subjected to higher stresses (Miettinen & Pataniitty, 1999).

2) If there are *two* defects, occurring in two separate locations on the inner raceway then the first, the lower amplitude transients may represent a reduced severity of damage and vice versa with the larger amplitude transients as witnessed previously by Elforjani and Mba (2010). It is also important to note here that as there are two rows of rollers, if the damage was initiated during the application of load during the static test, Run 2, then it is viable that an area of damage may have initiated on each of the two rollers.

After a further 2795 revolutions the wavestream continues to evolve, demonstrating that the severity of the damage within the bearing is beginning to increase (Figure 5-24). There still exist two separate sets of bursts per shaft revolution, one at a lower amplitude and the other higher, however there are now a greater number of transients occurring over a full rotation, accompanied also by an increase in amplitude.

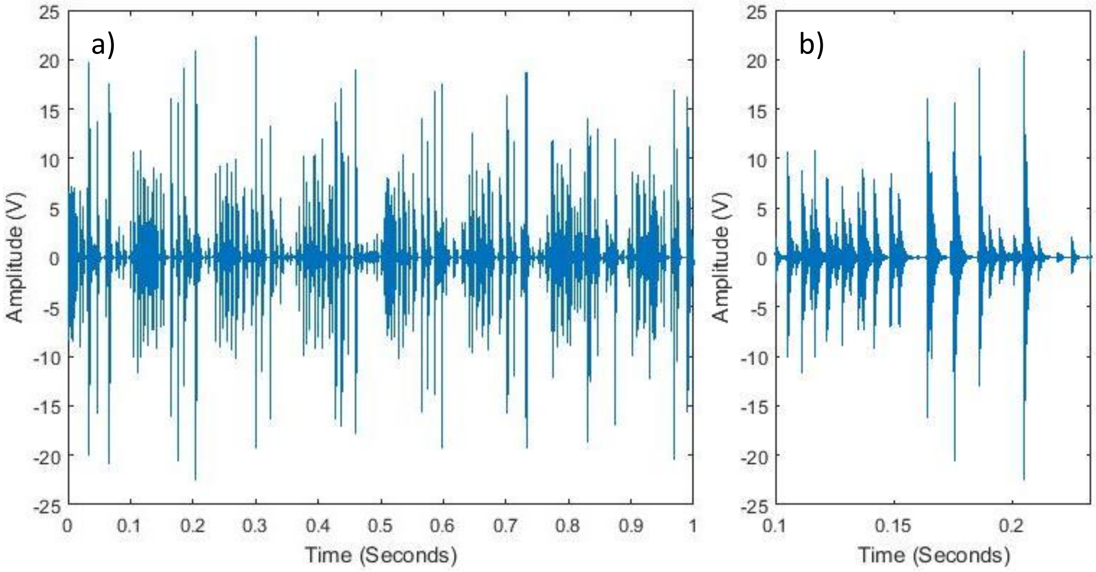

Figure 5-24 - PCI-2 Ch2 wavestream at 450rpm and 1500kN after 20109 revolutions for a) a full recorded wavestream and b) a wavestream over a single revolution.

The transients witnessed in Figure 5-22 occurred at a rate of 94Hz, corresponding to the BPFI. Although not immediately clear in the frequency plots, Figure 5-25, through visual analysis of Figure 5-24.a and Figure 5-24.b it is determined that, although not everywhere, in parts of the signal the burst rate has increased up to 302Hz, 3xBPFI, even though the operating conditions remained constant at 450rpm under a radial load of 1500kN.

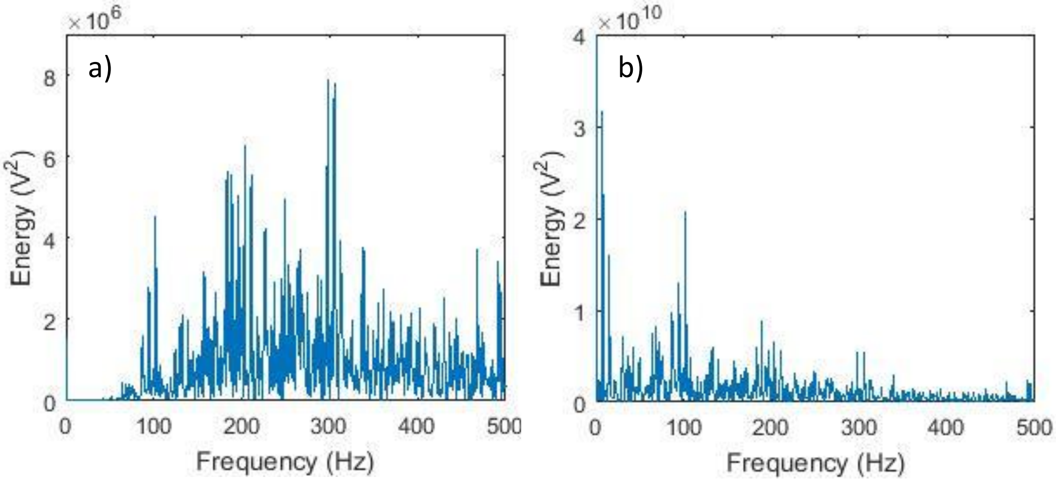

Figure 5-25 - Frequency plots of wavestream illustrated in Figure 5-24 a) and b) respectively

Typical signal analysis methods aim to enhance the detection of the BPFI within a raw signal but as the data used is usually artificial, either simulated signals or seeded defects, there has been little discussion of multiple bursts occurring so periodically between the standard defect frequencies. Elforjani and Mba (2010) and McFadden and Smith (1984) however, have both demonstrated that there existed two peaks of different amplitudes, when investigating a single scratch on a bearing race. By reversing the direction of the bearing it was found by McFadden and Smith (1984) that the second peak was due to a secondary scratch as the order of the peaks had reversed and upon inspection of the raceway, Elforjani and Mba (2010) identified two regions of bearing damage.

As this bearing has a maximum of 13 rollers per row in the loaded region of the bearing at any one time, it is conceivable that there will be transient activity from any number of these locations, especially if there is debris present as seen during Run 1. Also, the load present on the rollers produces contact pressures up to 2500MPa, exceeding the fatigue load limit of bearing steel, that is, the load required to exceed a contact pressure of 1500MPa. Therefore, it is possible that sub surface deformations are taking place within the inner and outer raceway.

5.5.4 Run 4 and 5

It has been shown that the form of the wavestream evolved throughout the observed period and the first evidence of the final evolution of the wavestream is recorded on the PCI-2 after 38747 revolutions (Figure 5-26). Due to overheating issues on the previous day, the speed was reduced from 450rpm to 250rpm whilst the load remained unchanged at 1500kN. The response of the DFS6000 sensors attached to the ACMS system display a similar wavestream.

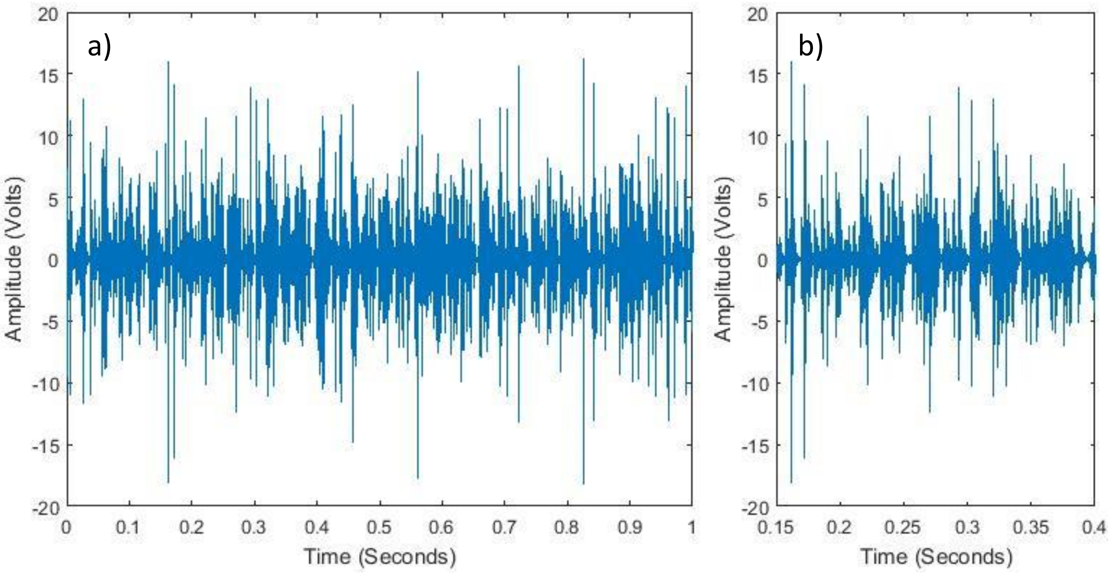

Figure 5-26 - PCI-2 Ch2 wavestream at 250rpm and 1500kN after 37847 revolutions for a) a full recorded wavestream and b) a wavestream over a single revolution.

The two individual sets of bursts previously seen in Figure 5-22 and Figure 5-24 have now disappeared and instead have amalgamated due to an increased number of transients across the full revolution. Despite running at a lower shaft speed, there is little change in the amplitude from when the system was run at 450rpm. Frequency analysis of the raw and enveloped signal determined that the peak frequency occurs at 214Hz for the raw signal and 37Hz for the enveloped signal (Figure 5-28). The peak at 37Hz in the FFT of the enveloped signal however is more likely to be a sideband of the 52Hz peak next to it. Also visible in the FFT of the enveloped signal is the peak at 214Hz, the same band identified in the raw signal FFT.

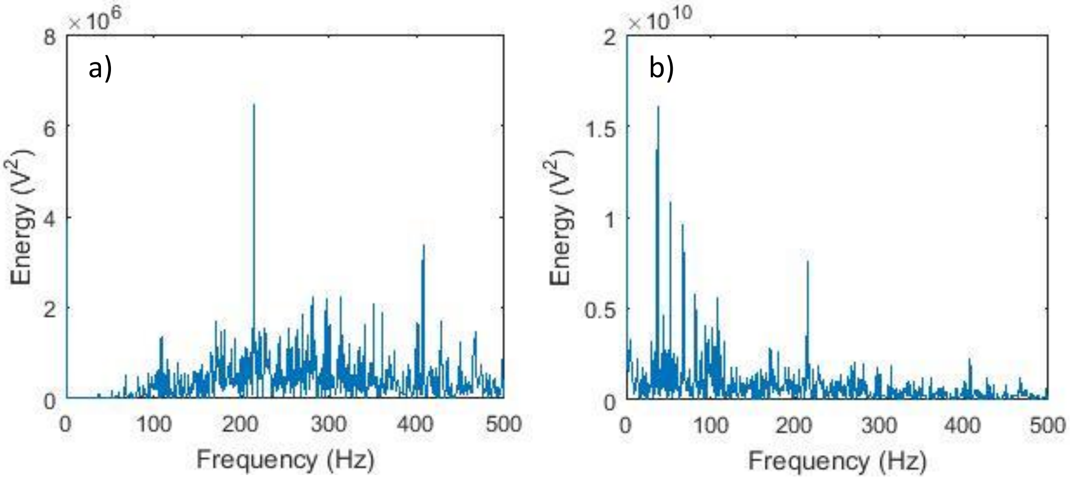

Figure 5-28 - Frequency plots of wavestream illustrated in Figure 5-26 using a) the raw wavestream and b) the enveloped wavestream.

The signals produced over the remainder of the testing period continued to share the same characteristic signal shape. After a total of nearly 120,000 revolutions, the test rig automatically shut down again due to increased oil temperature and ferrous debris in the oil return tray. Attempts were made to remedy the increased oil temperature but it was found that the heat exchanger had become blocked and was unable to cool the oil sufficiently. As there was also a significant amount of debris collected by the oil return magnets (Figure 5-27) the decision was made following Run 5 that the test rig would be stripped down to find the source of the debris and allow for the heat exchanger to be repaired.

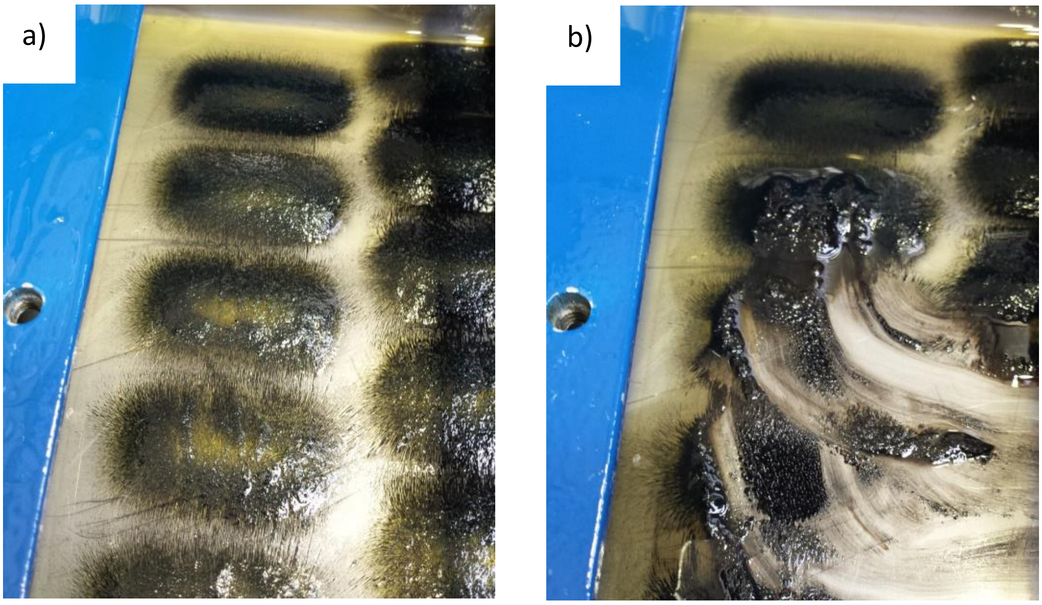

Figure 5-27 - Magnetic Pick Up a) demonstration of the ferrous particles aligning much like iron filings and b) demonstration of the fine particle nature which caused the ferrous material to smear.

The evolution of the signal throughout the time period monitored has demonstrated a number of characteristics that would commonly be classified as an acceptable detection of damage upon the inner raceway. As such, it was expected that once stripped down, the inner raceway would demonstrate large patches of surface fatigue.

Upon inspection of the races, it was found that there was a slight increase in the amount of surface damage on any of the raceways when compared with the race condition prior to their reinstallation (Figure 5-29). It can be seen in Figure 5-29.a that across the surface of the outer raceway there are a large number pits and scores occurring somewhat randomly. Figure 5-29.b and Figure 5-29.c shows the roller end effects scoring on the outer raceway, where Figure 5-29.c illustrates particularly deep scoring marks. Figure 5-29.d contains a large area where it is thought that the over-rolling of debris has produced a large defect on the outer race. Although the outer raceway defect was not detected at all in the frequency analysis of the wavestreams, it is possible that, due to the way that the damage is spread out across the raceway, the defect frequency is not excited and instead transients appear at a more random spacing.

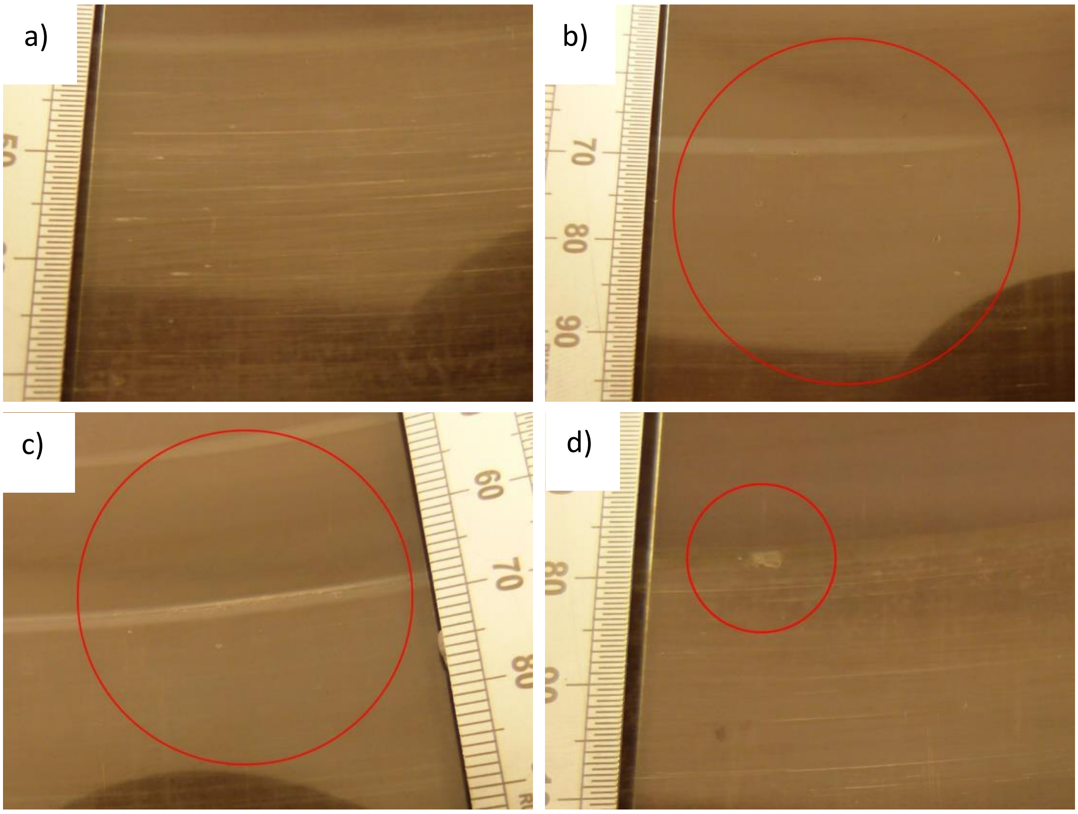

Figure 5-29 - Visual damage to the surface of the outer raceway - Set B

It was also noticed that both the inner and outer raceways of the test bearing had rotated away from their initial positions and, once the inner raceway was pressed off the shaft, what is thought to be the true source of the high energy transient bursts was discovered. Across the whole circumference of the shaft there exist a number of cracks and areas of fretting fatigue (Figure 5-30). Fretting occurs as minute amounts of relative motion, or ‘slip’, exist between two bodies in contact (Neale, 1995). Microscopic slippage between the inner raceway and shaft often occurs due to the bending of the shaft (SKF, 2012b). Due to the cyclic stressing fatigue cracks are commonly found with fretting damage and evidence of these cracks are clear to see in Figure 5-30. This fretting damage provides an explanation as to the origin of the ferrous debris and, more importantly, the severity of the damage may provide a better explanation as to the origin of the transient bursts witnessed throughout the analysis above.

Figure 5-30 - Fretting damage of drive shaft after 120,000 revolutions

The reason why the transients produced through fretting fatigue would appear at the inner raceway may be due to the high applied loads on the bearing. The inner raceway rotates with the shaft upon which it is pressed and, as they rotate together, the amount of stress at any one point on the inner race fluctuates continuously. When under high radial loads, it is thought that these stresses cause the inner race to flex slightly around the rollers. As such, there will exist a greater stress between the shaft and the inner race at each of the roller-race contact points, leading to crack growth and propagation.

In most circumstances, fretting is overlooked and Naumann (2016) classifies any fretting and rubbing within a bearing as being a 'secondary source' as the analysis methods used focus solely on the detection of the bearing defect frequencies.

However, if the transients are due to the crack growth within the shaft, then this test highlights the sensitivity of AE in its application to rotating machinery. It has been documented by Shiroishi *et al.* (1997) that inner raceway failures are difficult to detect via AE however, if shaft damage can be detected then it makes sense that defects within the inner raceway would be detectable.

This work has also shown the sensitivity of AE to detect multiple phenomena in what is a very large bearing, including the detection of what is thought to be the roller slap frequency as well as the over-rolling of debris, which produced sporadic evidence of the ball spin frequency and inner race frequencies.

This discovery strongly contradicts the standard methodology used to analyse the wavestreams which, without further information, strongly indicated the presence of damage on the inner raceway. This is an important discovery as if this was placed within an operational wind turbine, a maintenance schedule would have been put in place to replace the test bearing whereas, in fact, it was the shaft that would have required replacement. This may in itself increase the length of downtime, further increasing the cost associated with the repair.

5.6 Conclusions

The majority of the literature focusses on the enhancing the detection of transient bursts produced when a large defect already exists on the surface of a bearing component as there commonly exists a low signal to noise ratio. It has however been shown that under extreme bearing loads (1500kN) and relatively low speeds, the transient bursts produced by natural damage propagation have a significantly large signal to noise ratio. The high sensitivity of AE has been continually demonstrated and has been shown to successfully detect transient bursts produced from the over rolling of debris on the roller and inner raceway. The detection of roller slap has also been identified, showing that false positives are caused within the wavestreams, as well as the ability to detect plastic deformation and failure of the drive shaft surface. The detection of the shaft fretting was also a type of false positive due to the transient bursts occurring at the inner race defect frequency.

This is the first known case where the fretting fatigue of a drive shaft has been misdiagnosed as inner race bearing failure when using AE. If this was a bearing on an in-service wind turbine, current state of the art data analysis techniques would have deduced that the failure was of the inner raceway of the planet bearing. Although there may be some microscopic damage to the inner raceway, the damage to the shaft is far greater and with further running would warrant replacement before causing other components to fail due to loosening of fits for example. Only on visual inspection would the fretting have been detected and the associated downtime of sourcing and transporting components would have increased the cost of the maintenance significantly. Therefore not only is the sensitivity of AE monitoring clearly demonstrated, but also the need for careful analysis to prevent the mis-diagnosis of defects.

6 Application of AE to a Back to Back Gear Test Rig

6.1 Chapter Overview

6.1.1 Introduction

Chapters 4 and 5 both investigated the AE response of two simple test rigs that applied a radial load to a rolling element bearing mounted on a simply supported shaft. Although these tests managed to increase the knowledge base regarding the damage of bearings, the test rigs investigated were relatively simple in their design and it was possible to place the sensors close to the source of damage. This chapter investigates the AE response of helical gear pairs under test when the sensors are placed on the support bearing housing, hence increasing the complexity of the signal transmission path. The test rig used to conduct this investigation is based at Newcastle University Gear Design Unit and the experiments carried out by them are designed to investigate failure of helical gears by means of gear tooth surface pitting. However, during a routine experiment, whilst the test rig was instrumented with AE sensors, the test rig was stopped due to a tooth shearing off on one of the helical gears.

The first section, Section 6.2, provides an overview of the test rig and is followed by Section 6.3 which details the installation of the AE sensors as well as the experimental procedure followed. The results, Section 6.4, are split into two groups, Group 1 and Group 2. The data discussed in Group 1 was gathered at a lower torque and is classed as a healthy benchmark because inspection of the gears before and after the test period demonstrated no significant change in gear condition. Group 2 however analyses the data when the test rig is operated at a higher torque up to the point where the failure occurs. The key findings within the analysis of the data are discussed with respect to the literature throughout the chapter and the conclusions can be found in Section 6.5.

6.1.2 Aims and Objectives

Although AE sensors were applied by the author to the test rig in an attempt to determine the condition of the gears, vibration sensors were also attached to the rig as part of its normal operation, automatically shutting down the test rig if the levels exceed a predetermined threshold. When the gear tooth failed, the vibration data triggered the shutdown of the test rig so therefore it is known that the vibration data is capable of detecting a failure.

Therefore, this chapter aims to:

- Investigate the characteristics of AE signals emitted from a healthy gear when under fluctuations of speed and load when the signals are recorded following transmission through the bearing and bearing housing.
- Compare the healthy response of AE signals to the response of inherited vibration data to determine similarities and differences between the techniques.
- Determine whether the analysis of the AE data is able to, with confidence, detect the initiation of damage within the gear pair before any sign of change within the vibration data.
- Investigate the response of AE after the tooth has broken and, as this is a back to back test rig, investigate if the signals produced by the damage on one side of the test rig are able to propagate through the mechanical system so as to be detectable at the other end of the test rig.

6.2 Rig Overview

The back-to-back gear test rig, located within the Newcastle University Gear Design Unit, aims to test the surface fatigue of two pairs of spur/helical gears and is capable of operating with a maximum pinion speed of 6000rpm and a maximum wheel torque of 1400Nm. Figure 6-1 and Figure 6-2 provide an overview of the test rig with gear pair ‘A’ on the left-hand side, gear pair ‘B’ on the right hand side and a hydraulic, vane actuated torque unit located midway between them. A 30kW motor drives a belt attached to a pulley on the left side of the torque unit, close to gear pair ‘A’. With a gear pair at each end, the test rig operates with a closed torque loop, recirculating the energy supplied by the motor. As a result, the motor is only required to compensate for any power losses, frictional and otherwise, within the loop.

Figure 6-1 - Overview of the test rig

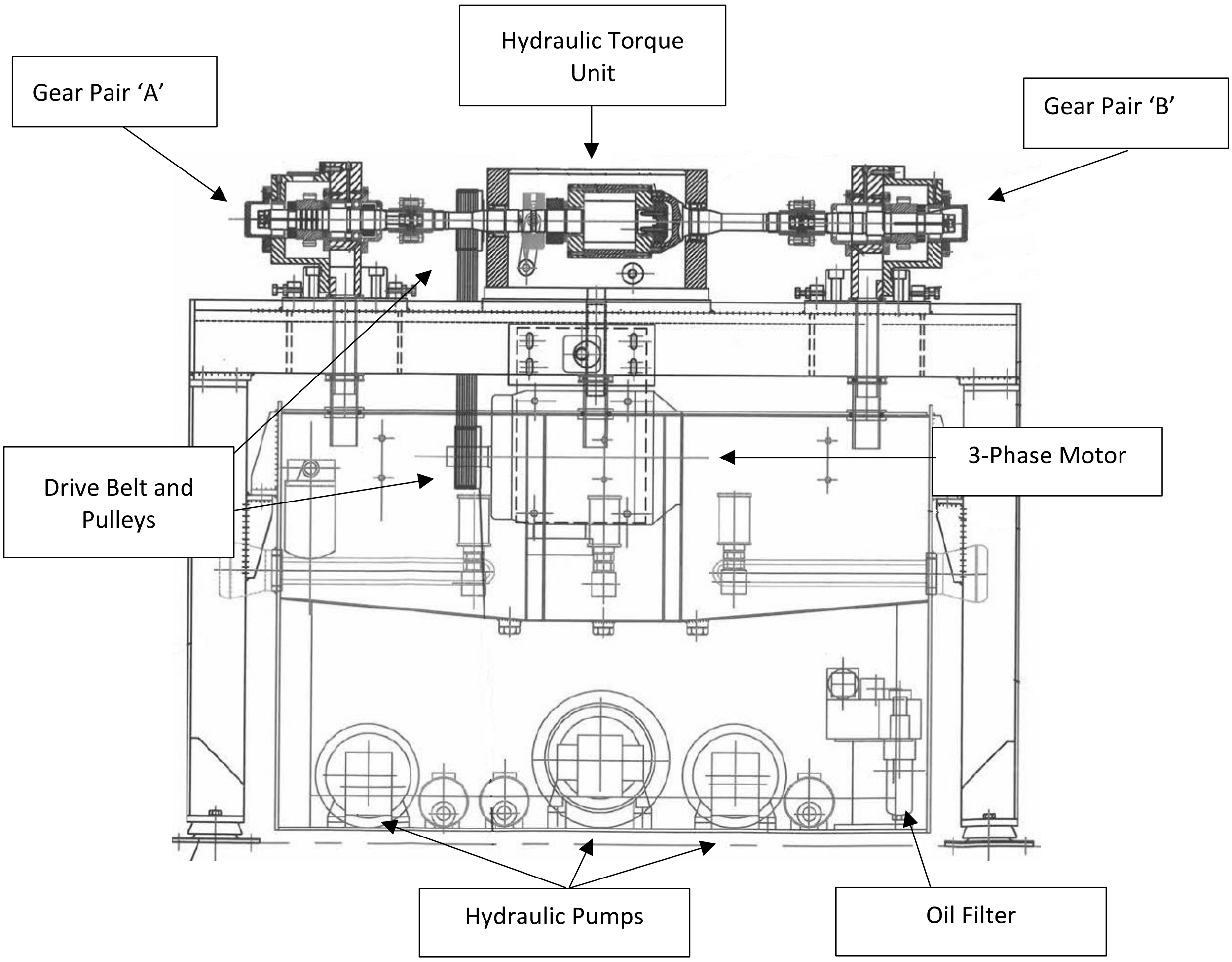

Figure 6-2 - Schematic of the test rig

Figure 6-3 shows the shaft upon which the gears are mounted, demonstrating the tapered section that the gears are pressed onto before being secured in position. A number of grooves can be seen in the tapered section, this allows for the gears to be hydraulically 'blown off' by applying hydraulic pressure through the centre of the shaft. Each of the shafts are supported by two single row, full complement, cylindrical roller bearings, type SKF NJG 2306VH, with one located in the door and the other behind the gear mounting block, as shown in Figure 6-4. The inner race of each of these support bearings has been removed causing the rolling elements make direct contact with a hardened and ground section of the shaft but also allowing for simplified access to/removal of the gears. The axial forces generated by the helical gears are reacted by a four-point contact bearing type, SKF QJ 208, the location of which is also shown in Figure 6-4. Where the shaft terminates in the access door, there exists between 5-10mm of clearance between the end of the shaft and the start of the bearing housing. Although heavily simplified, as in there is no ability to change the torque flow through different gear pairs during operation, the rig itself is overall representative of a typical transmission unit as the shafts terminate in a bearing housing and the geometry of the gears, coupled with the applied torque and speed, is common to those found in transmissions for automotive applications.

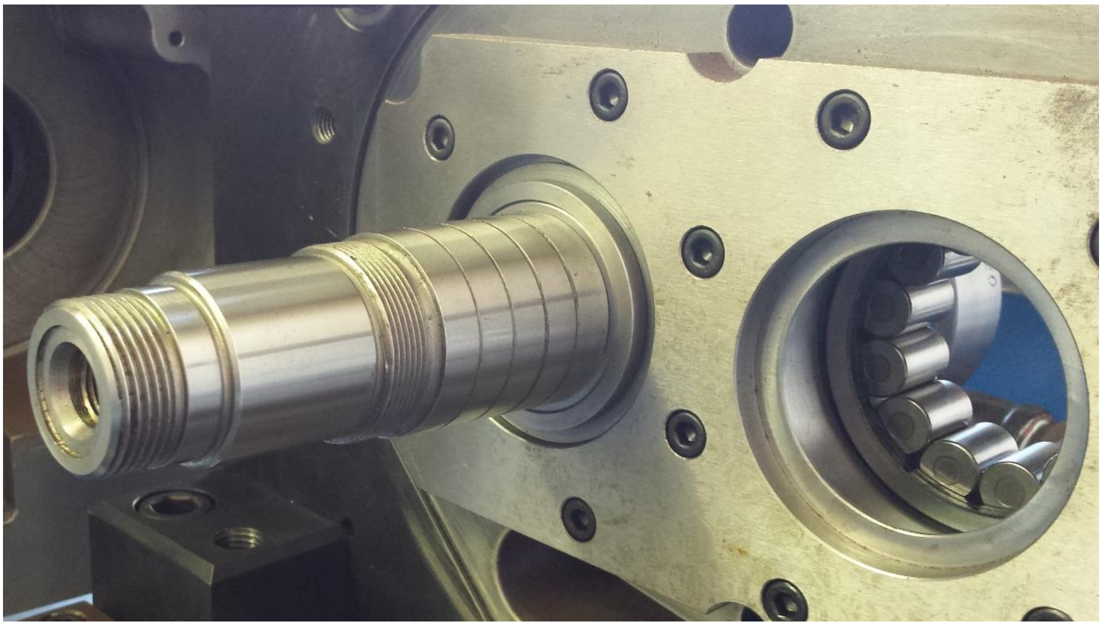

Figure 6-3 - Shaft upon which the gear is mounted

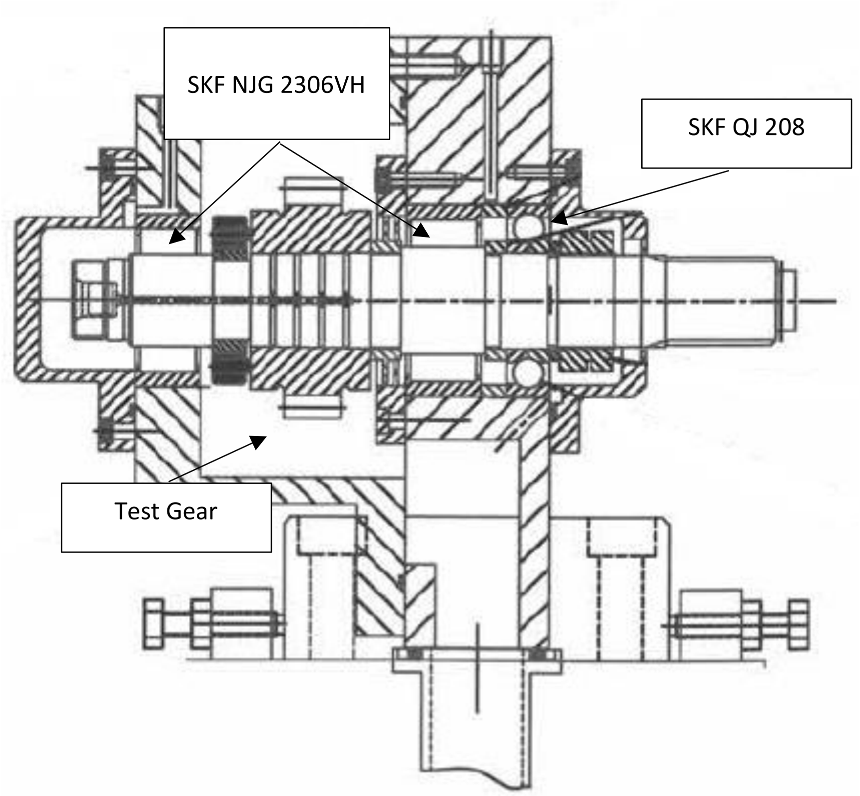

Figure 6-4 - Schematic of the shaft support and gear mounting

Housed under the rig is the 3-phase motor that is coupled to the drive shaft via a drive belt and pulley wheels. The hydraulic system, comprising of hydraulic pumps, in-line oil filters, a heater/stirrer unit and oil sump, are all housed below the test rig and are required to produce the hydraulically applied torque to the gears pairs as well as providing both cooling oil and adequate lubrication to the gears and bearings (Figure 6-5). The drive motors and hydraulic pumps that are required to operate the test rig are all bolted to the main chassis of the test rig and, hence, it is possible that these may produce a large amount of ambient noise in both the AE and vibration data when the test rig is running.

Figure 6-5 - Pumps and drive motors positioned below the test rig

To accurately control and monitor the test rig during operation, a variety of sensors are used. Such sensors include cycle counter, torque sensor, oil flow sensor, oil pressure sensors, motor power demand, pinion speed sensor, 3-axis vibration sensors and oil temperature sensors. The output of each of the sensors is connected to a NI cDAQ chassis (data acquisition hardware) which is processed and recorded using NI LabView at a frequency of 2Hz. The data collected not only allows for post-test analysis, but the real time analysis allows for thresholds to be determined which, if exceeded, trigger an automatic shut-down procedure designed to protect the test rig from any potential damage.

The primary function of the test rig, as previously mention, is to provide repeatable analysis of gear materials, and for this test schedule included the determination of the pitting characteristics of helical gears, Figure 6-6, when made from a novel steel alloy. The design specifications of the helical gears are summarised in Table 6-1. To increase the likelihood of pitting wear, the gears are designed to have a ratio of 1.5 as the gears have a common factor, causing the teeth to ‘hunt’ when running. Typical gear design aims for the gear ratio to be irrational as this decreases the occurrence of a tooth on one gear repeatedly meshing with only a few teeth on the other gear.

Figure 6-6 - Helical Gears under investigation

Table 6-1 - Gear Specifications

	Units	Pinion	Wheel
Number of teeth, z	-	16	24
Normal module, m_n	(mm)	3.9	3.9
Pressure angle, α_n	(°)	20	20
Profile shift coefficient, x_p	(mm)	0.29	0.00
Nominal tooth depth, h	(mm)	2.40	2.40
Facewidth, b_{face}	(mm)	25	25
Tip diameter, d_a	(mm)	82.12	115.88
Root diameter, d_f	(mm)	63.40	97.16
Reference diameter, d	(mm)	72.053	108.080
Base diameter, d_b	(mm)	66.4253	99.6380
Minimum root fillet radius, ρ_F	(mm)	1.7	1.9

There exist a large number of mechanical components in close proximity to the location of AE monitoring, and following on from observations in Chapter 4 and 5, it is now known that the characteristic frequencies of these components have the ability to influence the AE signal. Therefore, Table 6-2 determines the characteristic frequencies of the gears and bearings described in Figure 6-4.

Table 6-2 - Characteristic Frequencies

Component	Characteristic Frequency	Frequency (Shaft Orders)
Pinion Gear	Gear Mesh Frequency (GMF)	16 x F_P
Wheel Gear	Gear Mesh Frequency (GMF)	24 x F_W
SKF NJG 2306VH	Ball Pass Frequency Inner (BPFI)	8.05 x F_S
	Ball Pass Frequency Outer (BPFO)	4.95 x F_S
	Ball Spin Frequency (BSF)	1.98 x F_S
	Fundamental Train Frequency (FTF)	0.38 x F_S
SKF QJ 208	Ball Pass Frequency Inner (BPFI)	7.56 x F_S
	Ball Pass Frequency Outer (BPFO)	5.44 x F_S
	Ball Spin Frequency (BSF)	2.45 x F_S
	Fundamental Train Frequency (FTF)	0.42 x F_S

6.3 Experimental Set Up

6.3.1 AE Set Up

The literature surrounding the study of AE produced by gears often sees the sensors mounted on the gear face, allowing for the signals to be recorded directly from the source with an added benefit of the reduction in signal attenuation and interference from other noise sources (Toutountzakis *et al.* 2005; Toutountzakis & Mba 2003a; Eftekharnejad & Mba 2009; Pullin *et al.* 2012). Having sensors mounted on the gear face during a dynamic test requires the signal to be passed through a slip ring mounted on the shaft. However, as this investigation was part of a wider experiment, it was not possible to modify the test rig in any way and therefore it was decided that the sensors would be placed on the bearing housing block closest to each of the gear pairs due to their ease of access (Figure 6-7).

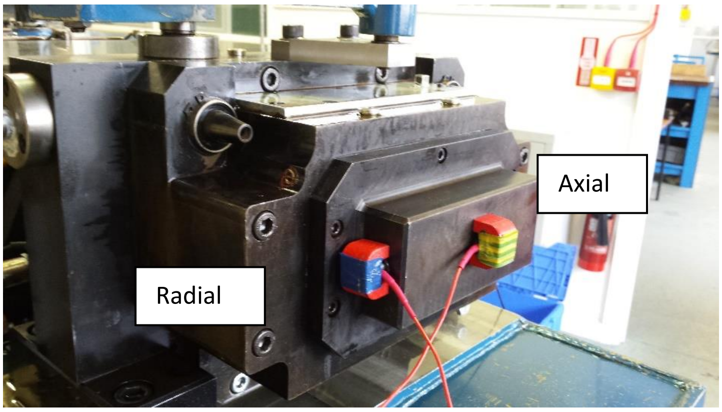

Figure 6-7 - Example of Sensor Mounting Locations

Whereas the previous chapters were able to gather AE directly from the source under investigation, placing the sensors away from the source increases potential of interference, signal modulation and aliasing. Unlike the simple rigs discussed in Chapter 4 and 5, where the sensors were mounted close to the primary AE source, the signals received here will have been generated by the gears and the bearings as well as extraneous noise emitted from pumps and motors. As a result, signals may become modulated as well as attenuating over the numerous interfaces. This is however much closer to the setup of condition monitoring equipment on commercial rotating machinery and may help provide insight into how AE signals behave in real world applications.

In total, four Nano30 sensors were coupled to the test rig using Loctite 5910 to secure the sensors while also acting as a coupling media. In addition to this, the sensors were secured in place with magnets that helped ensure that the sensors remained attached to the rig for an extensive period of time. Two sensors were placed on the bearing housing of each gear pair where, as shown in Figure 6-7, one sensor was placed axially to the bearings and the other radially. Each sensor was connected to an amplifier set at 40dB with a bandpass frequency of 20-1200kHz and H-N sources were used to determine the quality of the bond between the sensor and the housing. For clarification, Table 6-3 determines the location of each sensor upon the test rig for each of the gear pairs. The PCI-2 system was set up to record time-driven data including the Absolute Energy, Rise Time, counts and duration at a rate of 1Hz. Wavestreams were also recorded at a rate of 2MHz for a total of 0.25 seconds once every minute.

Table 6-3 - Sensor Locations

	Gear Pair	Location
Channel 1	A	Axial
Channel 2	A	Radial
Channel 3	B	Axial
Channel 4	B	Radial

6.3.2 Test Schedule

This investigation applied AE sensors to the test rig for only a short period of time, taking advantage of an extensive test programme that was being conducted by the Newcastle University Gear Design Unit on behalf of an external customer. The broad range of tests conducted by Newcastle University Gear Design Unit that make up the overall test programme ran a large number of helical gears at a pinion speed of 3000rpm under torque levels of 365, 573 and 855Nm, as measured on the larger gear. These torques were selected as they produced maximum tooth contact pressures of 1,400, 1,600 and 1,800MPa respectively. Empirical data collected by the Gear Design Unit over an extensive period of time has shown that contact pressures of 1,400MPa do not cause micro-pitting of the gear tooth surfaces over the test duration whereas a contact pressure of 1,800MPa is likely to cause micro-pitting failure after a total of 30-40 million cycles.

For the window of observation this chapter focusses on, two torque levels were investigated, 365Nm and 855Nm whilst running at a pinion drive speed of 3000rpm. The gears were brought up to the final operating speed/load incrementally so that any issues with the rig could be highlighted quickly as well as allowing for the temperatures to stabilise at each stage. This is reached by increasing the speed in stages to 500, 1000, 1500, 2000, 2500 and 3000rpm with each speed held constant for a total of 5 minutes before being increased further. Whilst the speed is being increased to 3000rpm the torque is held at a constant 50Nm to ensure that the gears are in contact. Once the final operating speed is reached, and has been sustained for a period of 5 minutes, the torque is then increased over 11 stages until the 'target torque' is achieved. When the target torque is 365Nm, the incremental values are 50, 80, 110, 145, 175, 210, 240, 270, 300, 335 and 365Nm with each increment held for a minute. When the target torque is 855Nm, the incremental values are 50, 130, 210, 290, 370, 450, 530, 610, 690, 770 and 855Nm. Figure 6-8 provides an illustration of the speed and torque increments for a target torque of both 365Nm and 855Nm.

Each test is run for a total of 10 million cycles upon one flank and then the direction is reversed to run the alternate flank for another 10 million cycles, with the 'Run' started again with an incremental application of speed and torque. Once each tooth flank has been subjected to 10 million cycles, the gears are removed and inspected for any pitting damage before being reinstalled and re-run under the same conditions. The test is then concluded once each flank has been subjected to a total of 50 million cycles.

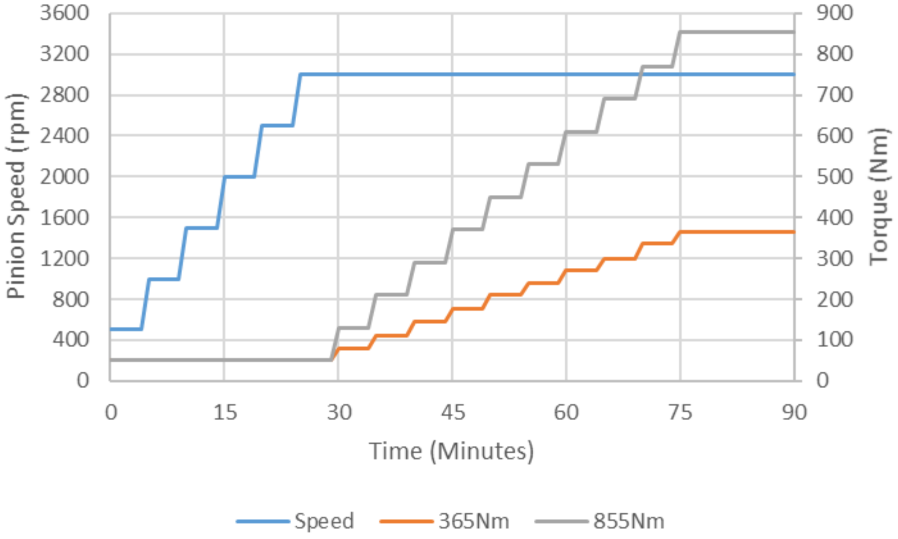

Figure 6-8 - Speed and Torque Increments

The data analysed in the next chapter is split into two distinct groups based on the torque under which the gears were operated, with each group testing two different gear pairs (Table 6-4). AE monitoring of Group 1 was initiated after flank A had already been subjected to 40 million cycles and flank B had been subjected to 30 million cycles. The gear surfaces were analysed each time each flank had been exposed to 10 million cycles and therefore the condition of the gear pair was known before testing commenced. Group 1 is assumed to be healthy as there was little/no evidence of micro-pitting on the gear tooth faces. The monitoring of Group 2 was started from the first 10 million cycles of each gear pair however, the test was aborted after flank B had been exposed to 1.7 million cycles due to a tooth failure.

Table 6-4 - Test Schedule

Group	Flank	Torque (Nm)	Cycles	Gear Pair A	Gear Pair B	Run Number
1	B	365	$10x10^6$	1093, 1110	1094, 1111	1
	A	365	$10x10^6$	1093, 1110	1094, 1111	2
	B	365	$10x10^6$	1093, 1110	1094, 1111	3
2	A	855	$10x10^6$	1097, 1114	1098, 1115	4
	B	855	$1.7x10^6$	1097, 1114	1098, 1115	5

The tooth failure occurred on the pinion gear, 1098, of gear pair 'B'. Analysis of the tooth break surface shows that the tooth failed through bending fatigue although the point of fracture initiation occurs well below the point of maximum stress as shown in Figure 6-9. The test itself is only designed to cause micro/macro pitting and the failure of a gear tooth in this fashion is rarely witnessed. This suggests that the failure was initiated due to a localised defect within the gear tooth itself, possibly caused by grinding burn or even an inclusion in the material. Although the localised defect area would have been in place before the gear pair were run on flank 'A', it is thought that if crack propagation began during this run, the tooth would have failed quickly, not lasting the full 10 million cycles. Also, if the crack location originated on Flank 'B', when the gear is run on flank 'A; then the defect would have been under compression. Only when placed in tension would the crack begin to grow and propagate through the tooth thickness.

Figure 6-9 - Tooth break of Pinion gear 1098 after 1.7million revolutions on Flank B - Run 5

6.4 Results

6.4.1 Results Overview

The results are divided into two main sections, each detailing the response of gear group 1 and 2 respectively. The gear pairs tested in Group 1 showed no evidence of micro-pitting on the surface of the gear teeth before or after the testing period. This was concluded with the use of gear tooth involute profile measurements. Therefore, this group will be used as a 'healthy' benchmark, allowing for characteristics to be determined when analysing both AE and vibration signals.

To determine the characteristics of a 'healthy' gear pair, Group 1, the time-driven AE data and the vibration RMS data are first compared to each other to demonstrate the effect of the speed and load increments during the start-up procedures of Runs 1-3. The AE wavestreams collected over the duration of the tests are then analysed and discussed, allowing for comparison later in the chapter when analysing the data recorded for the damaged gear, Group 2. As the tooth failure occurred during the running of the gear pair in Group 2, it is difficult to determine when the failure began to initiate. Therefore, all of the data in Group 2 is treated as 'damaged' data and hence the analysis of this section will focus on how the signal has changed from the 'healthy' benchmark set by Group 1. Trends will also be determined and analysed to determine if the point of damage initiation can be pin-pointed to a single point in time.

6.4.2 Signal Characteristics – Speed Response

AE wavestreams were recorded at 15 minute intervals and, as a result, the individual speed and load increments, each incremented at 5 minutes and 1 minute respectively, were not able to be captured. However, time-driven AE data collected at 1Hz was able to be used to effectively detail the changes in absolute energy with respect to speed and load change. Figure 6-10, Figure 6-11 and Figure 6-12 plot the AE absolute energy, and vibration RMS amplitude, for each gear pair, A and B, for the speed increment phase of Runs 1-3 respectively. It can be seen that the trends of both AE absolute energy and vibration RMS correlate directly to the increase in shaft speed agreeing with observations made by Toutountzakis and Mba (2003). For all three runs, the absolute energy of the AE data for gear pair 'A' increases quickly during the initial 'low level' speed increments but the difference in amplitude between each speed increment becomes smaller as the speed gets closer to 3000rpm. However, for the same gear pair the vibration RMS reacts in the opposite way, starting off low in amplitude for lower speed increments before demonstrating a larger difference in amplitude between increments as the pinion speed reaches 3000rpm. This is thought to be due to the difference in sensor characteristics as well as a difference in signal analysis techniques. AE detects higher frequency transients and as such, as the speed increases, the number of transients increase within a set period of time. Absolute energy is calculated using the area under the signal recorded and therefore, as the speed increases the signal becomes heavily saturated, causing the growth in absolute energy to reduce as the speed increases. That is unless the amplitude or frequency of the signal begins to increase. The RMS amplitude output of the vibration sensors however, will only increase with the amplitude of the raw vibrational signal.

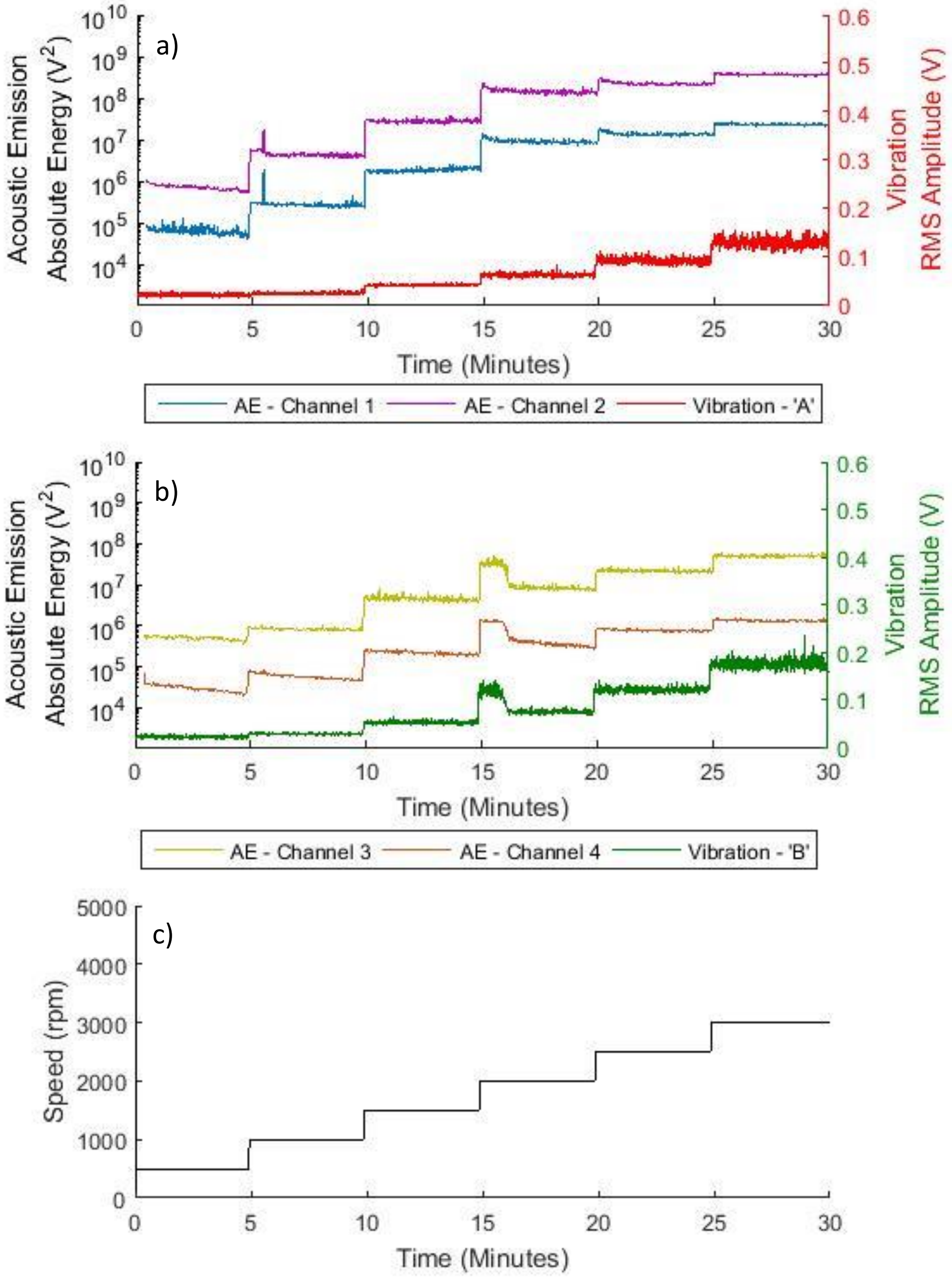

Figure 6-10 - Comparison between the Absolute Energy of AE Time-Driven Data and Vibration RMS Amplitude as speed (c) is changed for a) Gear Pair 'A' and b) Gear Pair 'B' – Run 1

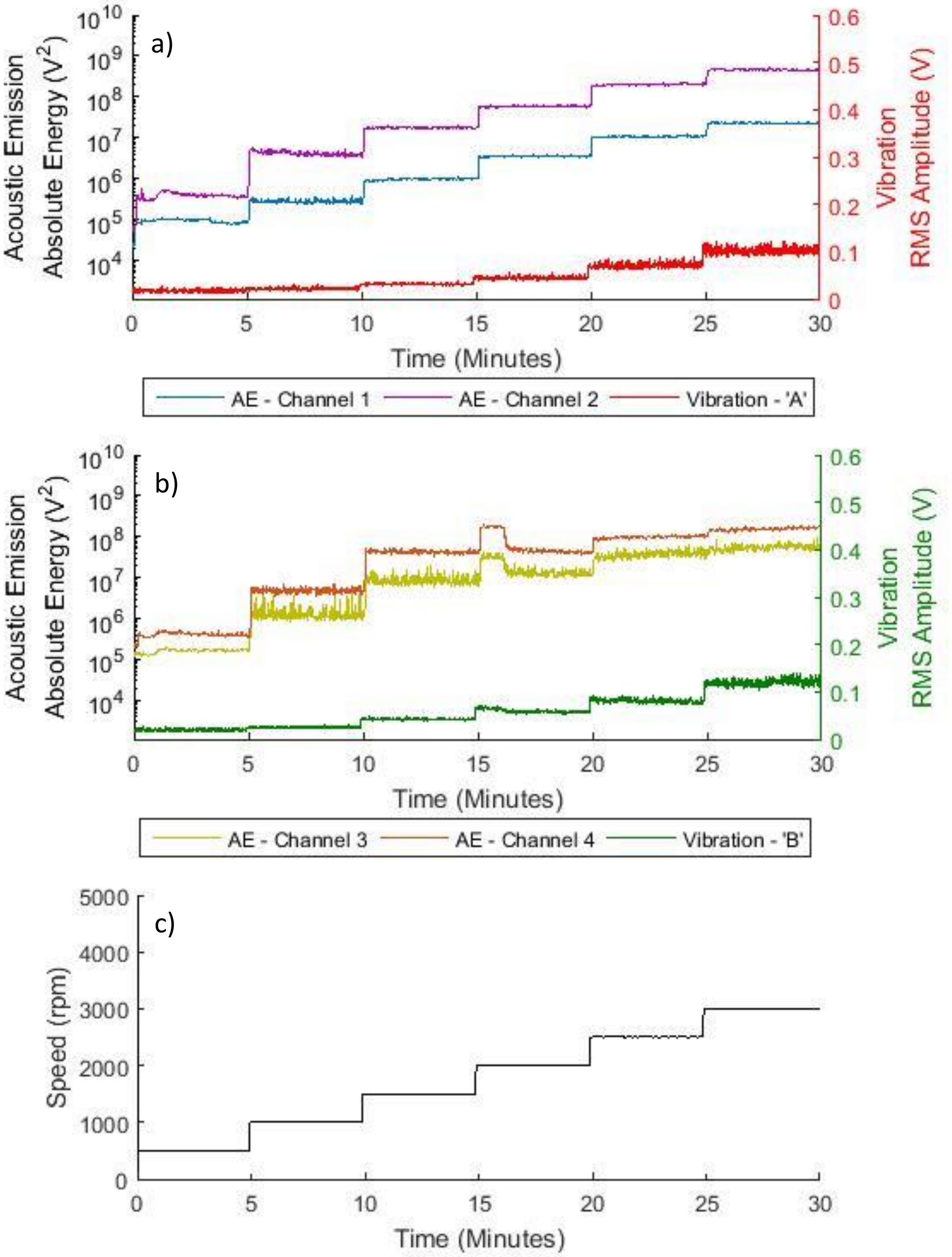

Figure 6-11 - Comparison between the Absolute Energy of AE Time-Driven Data and Vibration RMS Amplitude as speed (c) is changed for a) Gear Pair 'A' and b) Gear Pair 'B’ – Run 2

It can also be seen that for each of the three runs that, for Gear Pair ‘B’, there exists an increase in the absolute energy and vibration RMS when the speed is increased from 1500rpm to 2000rpm. This increase in then followed by a significant drop in both absolute energy and RMS amplitude after approximately 1 minute in runs 1 and 2 and 3.5 minutes in run 3.

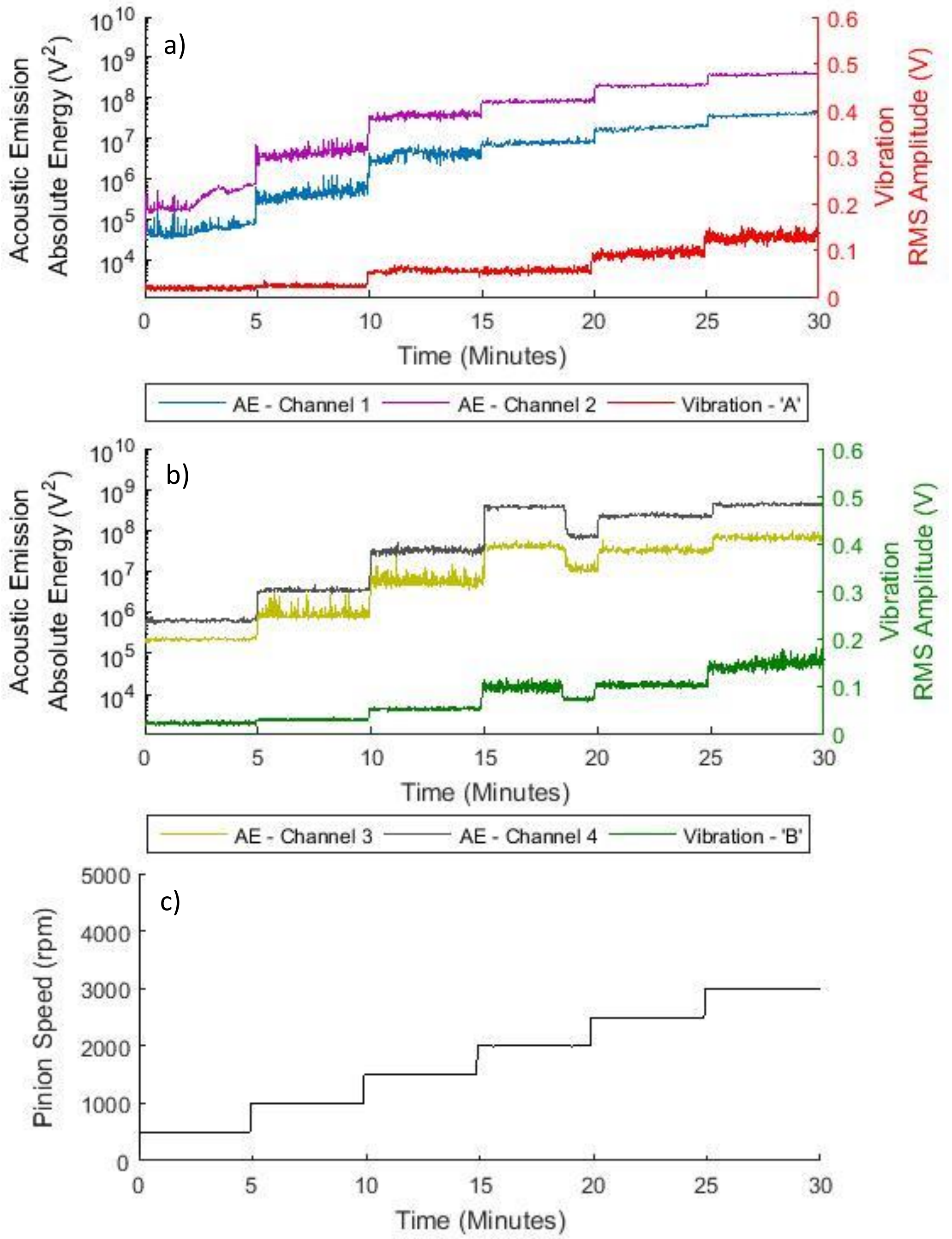

Figure 6-12 - Comparison between the Absolute Energy of AE Time-Driven Data and Vibration RMS Amplitude as speed (c) is changed for a) Gear Pair 'A' and b) Gear Pair 'B' – Run 3

The rise and drop occurs only on the AE and vibration sensors monitoring Gear Pair 'B' and, as this is a back-to-back study, rules out the possibility of this phenomena being produced by an increase in speed, load or the presence of electrical interference. All other recorded parameters, such as temperature, oil flow and motor power were investigated, but there was no evidence of change within these signals that may be deemed responsible.

The gears were removed after Run 1 and, following inspection, the same gears were reinstalled prior to Runs 2 and 3. If this change of amplitude was due to an installation error, then the possibility of the drop occurring at the same speed increment and for the same duration is highly unlikely.

Finally, although AE was only applied to the test rig towards the latter stages of the testing of gear pairs, 1093/1110 and 1094/1111, vibration RMS data was gathered from the beginning of the test. Analysis of these data shows that the gear pair 1094/1111 exhibited this phenomenon from the first run, and all subsequent runs, always occurring as the speed was increased from 1500-2000rpm. This suggests that this may be due to a harmonic excitation for this particular gear pair, and is further evident in the data collected during Run 4 where the gear pairs have been changed and the drop at 2000rpm no longer occurs. Instead, as the speed is increased from 2500rpm to 3000rpm there exists a very brief spike in absolute energy in Channels 3 and 4, followed by a decrease in absolute energy as demonstrated in later in Section 7.4.5, Figure 6-30. No such phenomenon is present in the run up procedure of Run 5.

However, if this is an excitation of the harmonics of a particular gear pair, it is not known why the level of AE absolute energy and vibration RMS would drop off after a short period of time. Instead, if this was a harmonic excitation, it would be thought to be excited throughout the whole 2000rpm speed increment. When running spur gears under a constant speed, Toutountzakis and Mba (2003) witnessed slight deviations away from the mean in the absolute energy of the AE signal. The deviations witnessed were thought by the authors to be due to the excitation of the resonant frequencies of individual gears as well as the system as a whole. The appearance of this deviation however is unlike what is witnessed at 2000rpm in gear pair 'B' and instead is more akin to the 'fuzziness' of the absolute energy of both gear pairs at speeds of 500, 1000 and 1500rpm. Also of note is the consistency in the amplitude of both the AE and vibration between runs 1-3. AE Channels 1-3 all have a similar level of absolute energy amplitude however Channel 4 demonstrates a lower level of absolute energy during run 1, which is opposed to higher the amplitudes witnessed in runs 2 and 3. This is due to the set-up of the experiment itself. When carrying out HN sources to determine the quality of the bond between sensor and specimen, it was found that the AE amplitude was much lower than expected with amplitudes of 80dB instead of the expected 95-100dB. Therefore, the sensor was removed and re-bonded to the surface. As a result of this and due to time constraints, the silicone was still wet during the first part of the test, causing a lower level of absolute energy, although the HN source was between 95-100dB.

6.4.3 Signal Characteristics – Torque Response

Figure 6-13, Figure 6-14 and Figure 6-15 plot the AE, absolute energy, and vibration, RMS amplitude, for each gear pair, A and B, for the tsorque increment phase of Runs 1-3 respectively. Unlike the increment of speed, the response of AE absolute energy and vibration RMS varies between gear pairs 'A' and 'B' as well as the direction in which the gears are rotating.

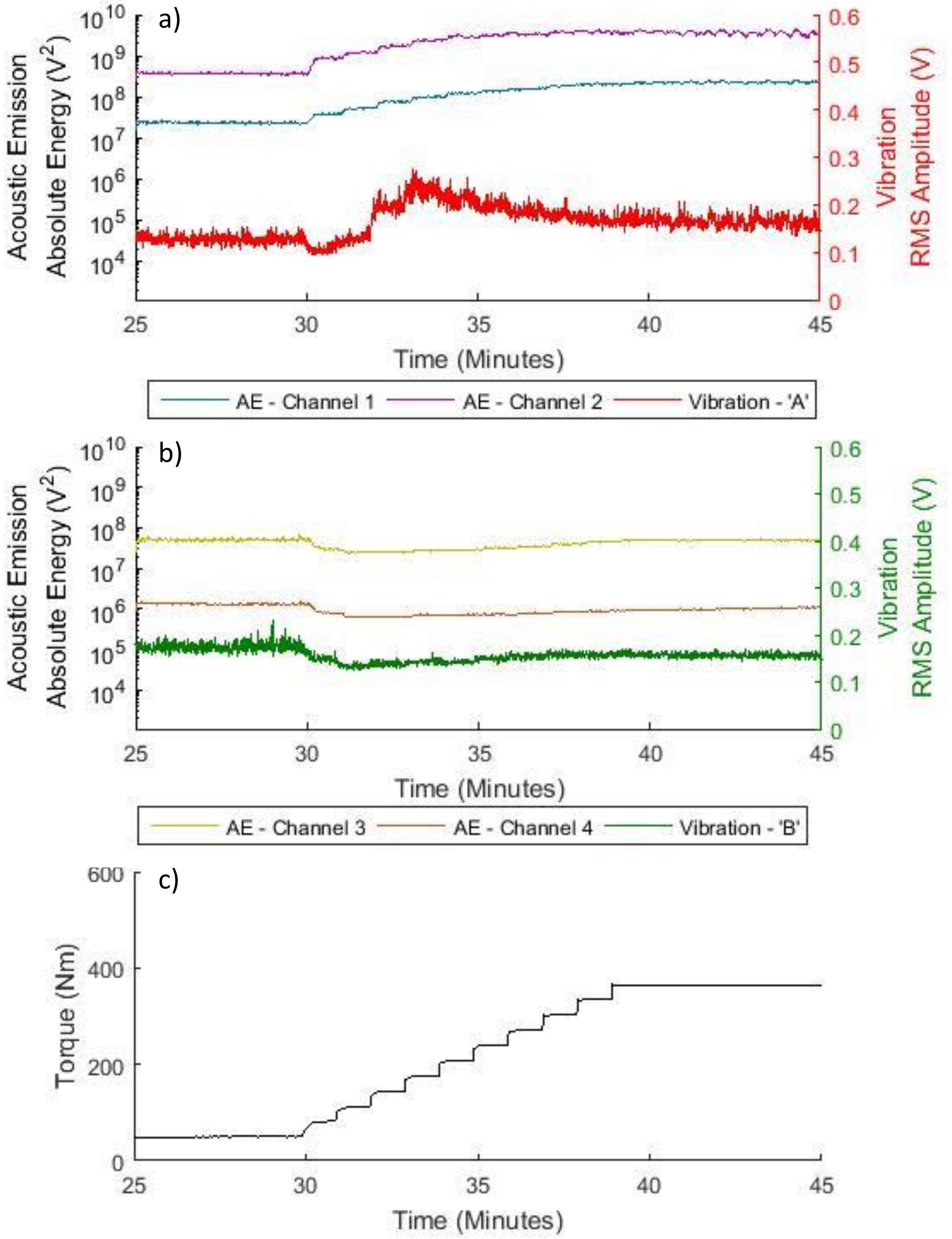

Figure 6-13 - Comparison between the Absolute Energy of AE Time-Driven Data and Vibration RMS Amplitude as torque (c) is changed for a) Gear Pair 'A' and b) Gear Pair 'B' – Run 1

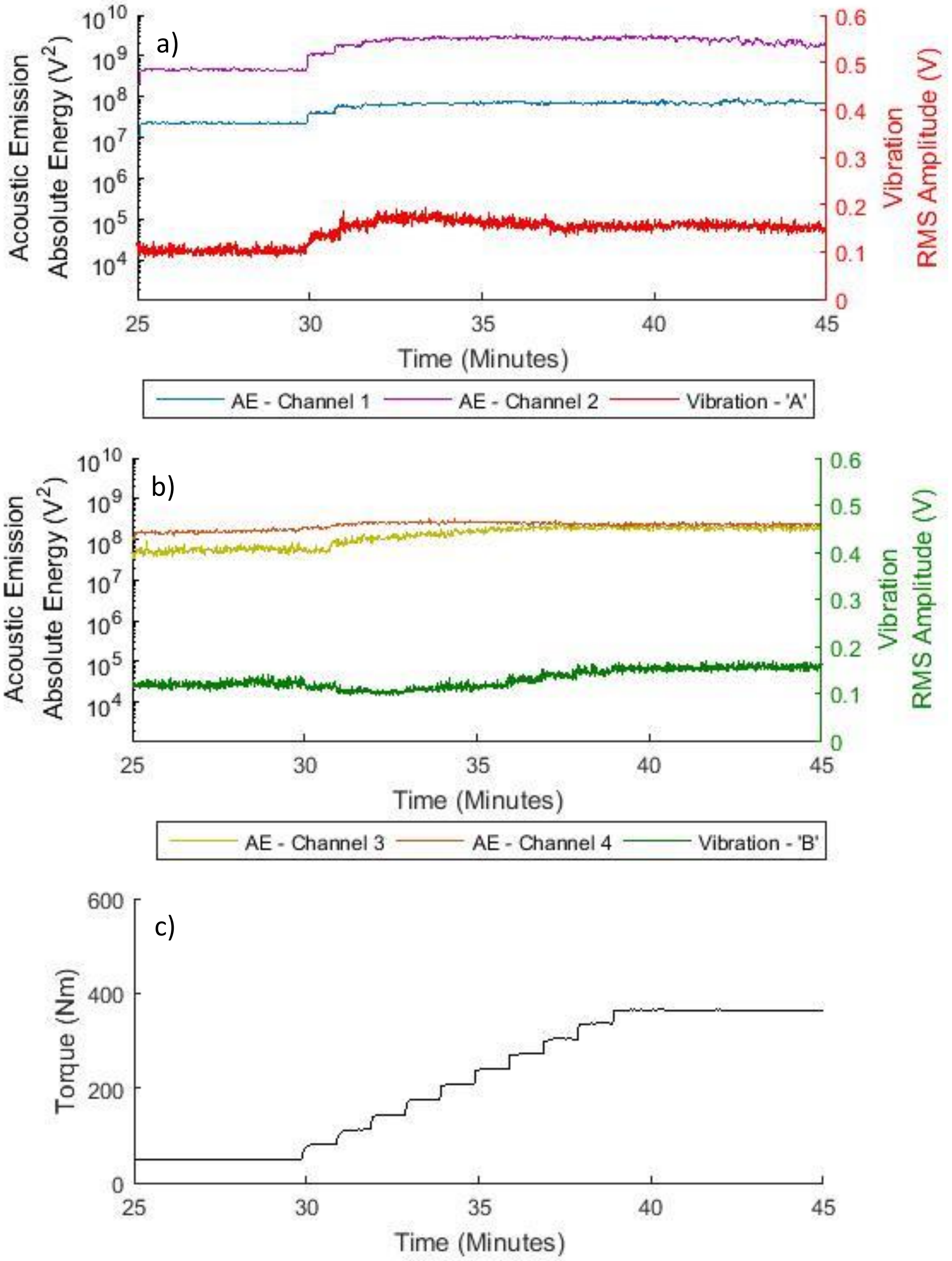

Figure 6-14 - Comparison between the Absolute Energy of AE Time-Driven Data and Vibration RMS Amplitude as torque (c) is changed for a) Gear Pair 'A' and b) Gear Pair 'B' – Run 2

Run 1 shows that the two AE sensors connected to gear pair ‘A’ increase in absolute energy as the torque is increased (Figure 6-13-a). The vibration ‘RMS’ initially reduces in value as the torque is increased from 50-80Nm, but then increases incrementally as the torque is increased to its maximum value of 365Nm.

The two AE sensors connected to gear pair ‘B’ on the other hand show little change when the torque is increased from 50 to 80Nm but both drop considerably when the torque is increased from 80Nm to 110Nm (Figure 6-13-b). This reduced level is maintained until the torque is increased to 240Nm and the energy slowly begins to increase again. A similar response is also witnessed in the amplitude response of the vibration RMS.

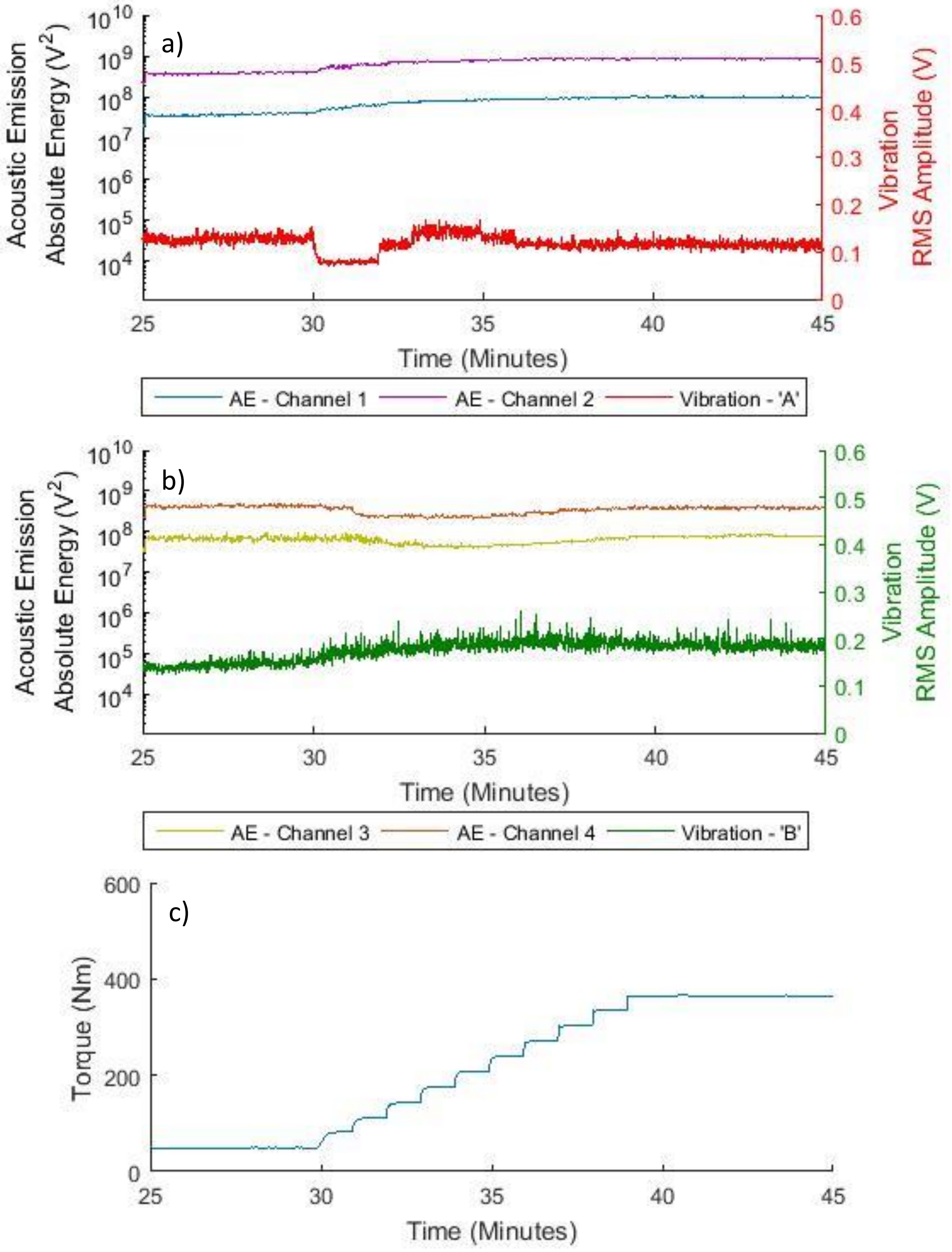

Figure 6-15 - Comparison between the Absolute Energy of AE Time-Driven Data and Vibration RMS Amplitude as torque (c) is changed for a) Gear Pair 'A' and b) Gear Pair 'B’ – Run 3

The AE response of gear pair 'A' is similar in Runs 2 and 3 when compared with Run 1, increasing in absolute energy as the load is increased. The vibration levels however differ depending on which flank is being run. When flank B is in contact during runs 1 and 3, the vibration RMS initially decreases in amplitude before increasing incrementally after the torque is increased from 110 to 145Nm (Figure 6-14-a and Figure 6-15-a). When run on flank 'A' however, the RMS amplitude increases as soon as the load is increased from 50 to 80Nm as seen in the response of the AE sensors (Figure 6-14-a). For gear pair 'B' however, it appears that the AE energy response is more sensitive to the running face of the gear as the absolute energy increases with load in Run 2 when the gear pair are run on flank 'A'. The energy however decreases in amplitude when ran on flank 'B' in both Run 1 and 3. Unlike gear pair 'A', there is no clear correlation between gear tooth face being run and the response of the vibrational RMS. The torque is applied through a vane actuator and therefore, in theory, the load is equally distributed between both of the gear pairs. The increased torque changes the load applied to the bearings in both the axial and radial directions. When testing the high speed bearings in Chapter 4, it was found that there was little increase in AE activity in the bearing as the radial load was increased. Therefore, it is thought that this increase in absolute energy with torque may be due to surface interactions of the gear teeth.

In the current literature survey, a reduction in AE has not been witnessed with increasing load, even when monitored directly on the gear face, and, to add more confusion it is seen that in some scenarios, the AE increases as vibration decreases. Toutountzakis *et al.* (2005) concludes that the AE detection of damage in gear tooth contacts is "fraught with difficulties" and this is echoed in the fact that for a back-to-back gear test rig, where each pair of gears are both subjected to the same environmental and experimental conditions, the response of each gear is opposite to the other.

6.4.4 Full Runs – Group 1

Figure 6-16 and Figure 6-17 separate the data into the two gear pairs, ‘A’ and ‘B’ respectively, where the designation of a-c in each figure refers to the plot of all data gathered in Runs 1-3 respectively. It is of note that, as mentioned in Section 6.4.2, the silicone used to bond Channel 4 to the test rig was still wet at the start of Run 1. It can be seen in Figure 6-17.a that as the silicone cures, the Absolute Energy increases as the transmission of the signal through the couplant improves.

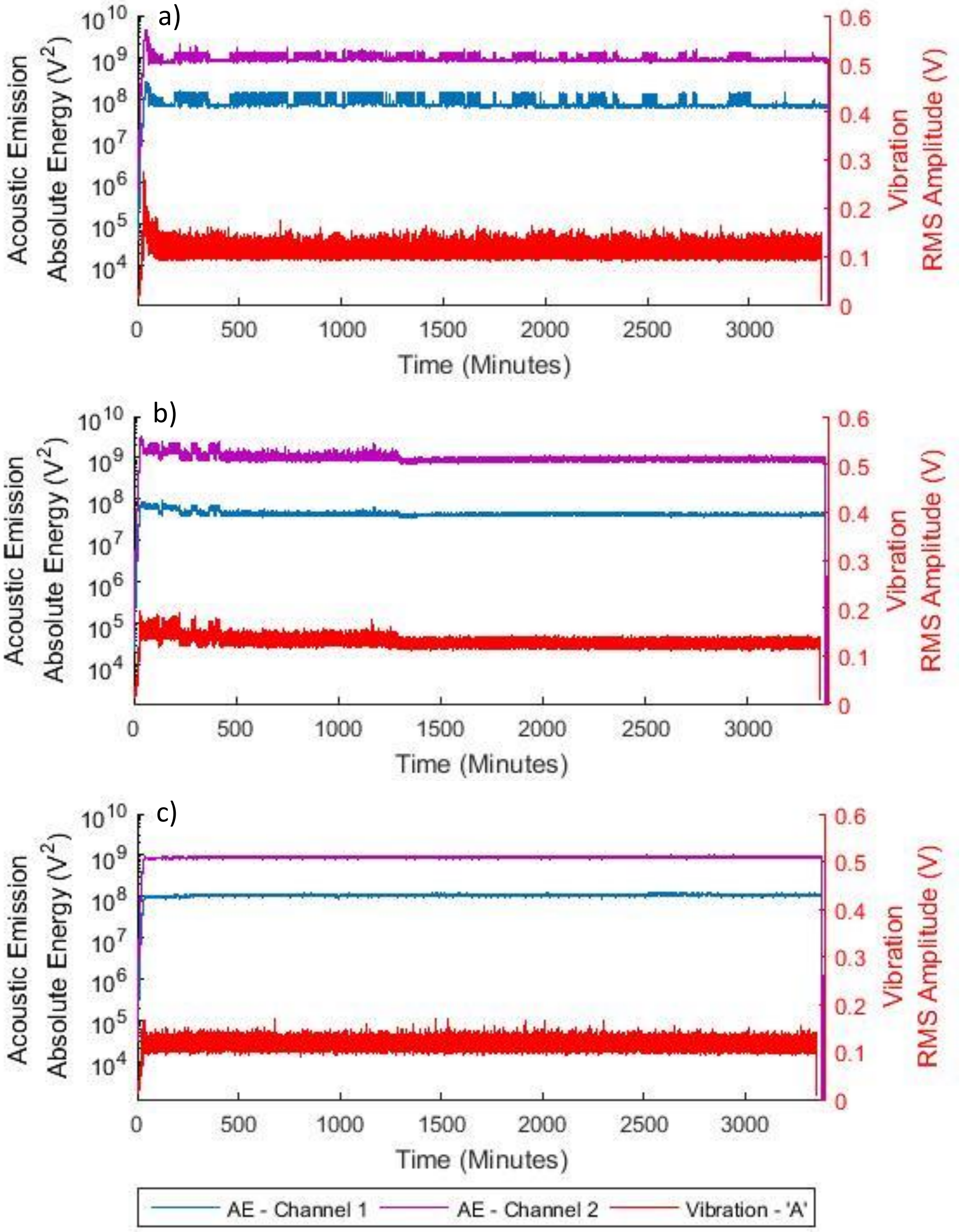

Figure 6-16 - Gear Pair 'A' - AE Absolute Energy and Vibration RMS data over the full test length of a) Run 1, b) Run 2 and c) Run 3

It can be seen that the signals produced by both the AE and vibration sensors monitoring gear pair 'A', have a distinctive amount of variation in signal levels for the duration of Run 1 and the start of Run 2.

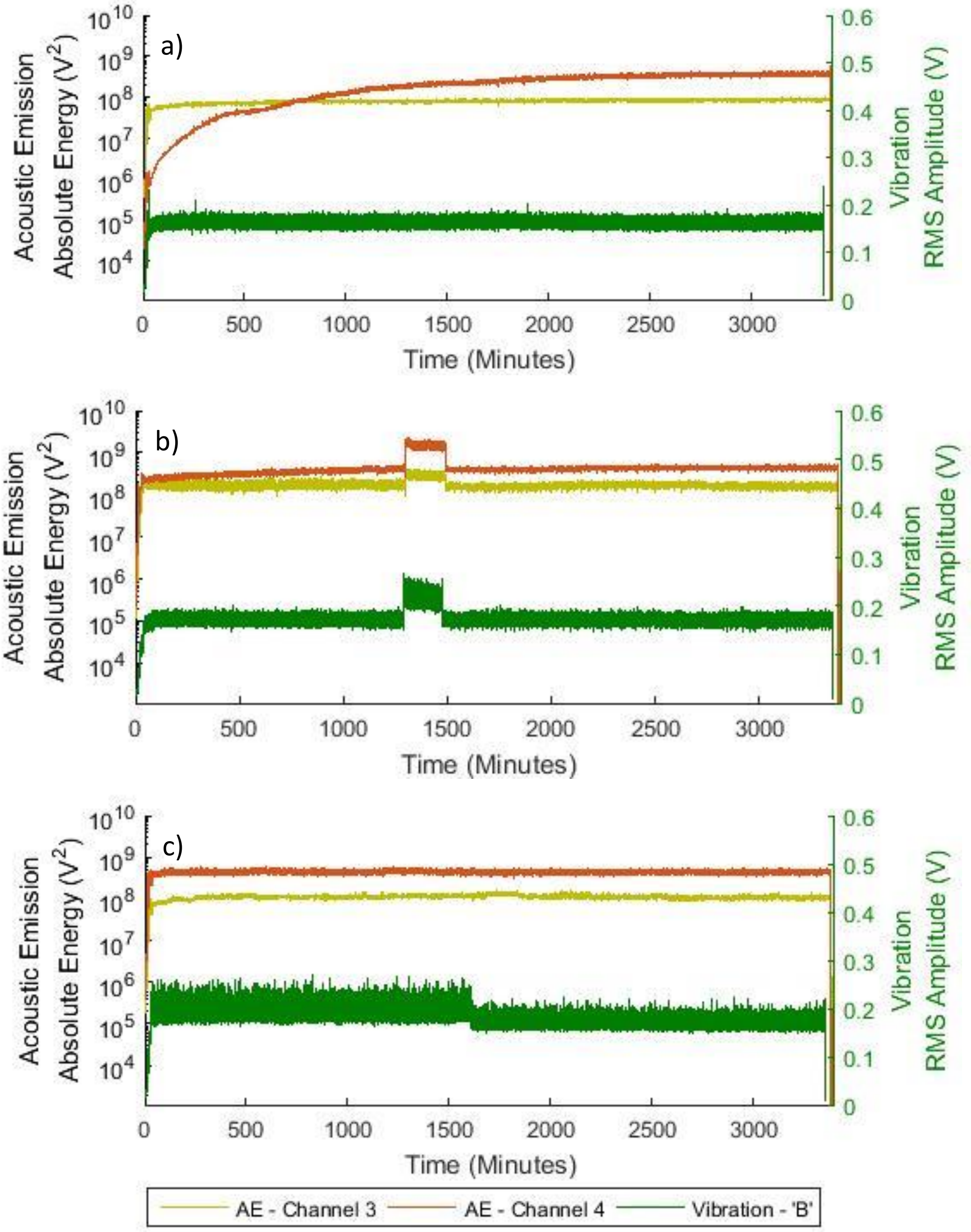

Figure 6-17 - Gear Pair 'B' - AE Absolute Energy and Vibration RMS data over the full test length of a) Run 1, b) Run 2 and c) Run 3

After approximately 1300 minutes into the test of Run 2, the AE and vibration response both drop together, to a level continued throughout the remainder of Run 2 and the duration of Run 3. The fluctuating amplitudes witnessed in Figure 6-16-a and Figure

6-16-b are not mirrored in Figure 6-17-a, indicating that the source of this is inherent to the system response and dynamics of Gear Pair ‘A’. On the other hand, when the fluctuating amplitude in Figure 6-16-b reduces to the ‘stable’ level after 1300 minutes, the AE and vibration levels of gear pair ‘B’ both increase significantly for a period of 190 minutes, as shown in Figure 7-16-b, before reducing back to their previous levels. Analysis of the other recorded parameters demonstrates fluctuating amplitude across a number of other channels including speed, torque, temperature and motor power. Curiously, it is only the sensors attached to Gear Pair ‘A’ which exhibit the fluctuations within the signal and hence it is thought that the noise is intrinsic to Gear Pair ‘A’.

Analysis of the other recorded system parameters, mainly speed and motor power, initially indicate the possibility that the ‘noise’ may be due to an environmental source, electrical or otherwise. Due to the way the increasing motor power correlates to the increase in AE energy, Figure 6-18, it was initially thought that the increased motor current was producing electromagnetic interference (EMI). If this was the case however, it is thought that with Gear Pair ‘B’ being in such close proximity to Gear Pair ‘A’, as well as being mechanically connected, that if there were any electrical interference from the motor then Gear Pair ‘B’ would also be affected.

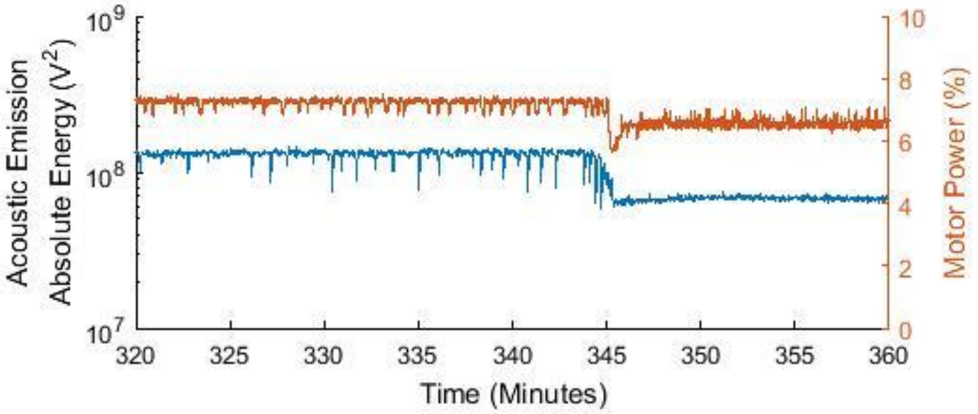

Figure 6-18 - Relationship between the AE absolute energy and Motor Power

Studying the relationship between speed and motor power it was found that, as indicated by the time-marks within Figure 6-19-a, the motor power decreases when the target speed is exceeded and vice versa. This is normal behaviour as the motor is controlled by an inverter through a feedback loop. However, when looking at the data recorded by the speed sensor and motor power at a later time within the same run, it can be seen that there is a step change in amplitude shortly after 345 minutes (Figure 6-19-b), with the speed increasing and motor power decreasing. Prior to the step change, the speed fluctuated between 2995-3000rpm, with the motor power reducing, and hence reducing speed, as soon as the speed reaches 3000rpm. Following the change however, the speed seems to be much higher, consistently hitting the target speed of 3000rpm and, as such, the motor power is much lower than previously seen.

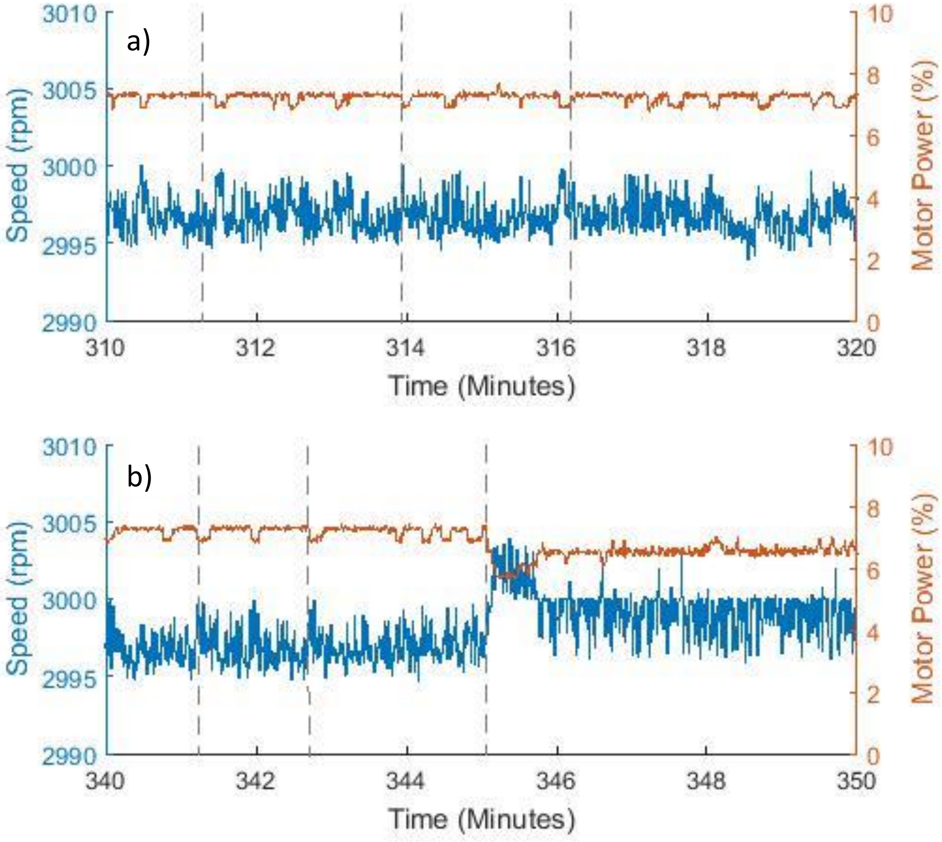

Figure 6-19 - Relationship between pinion speed and motor power demonstrating a) the normal response of the pinion speed and motor power and b) the response over a step-change induced by 'noise'

Another factor which helps rule out the possibility of the noise being electrically induced, is witnessed in Figure 6-16-b and Figure 6-17-b, where after approximately 1300 minutes, the ‘noise’ suddenly vanished from Gear Pair ‘A’, seemingly exciting Gear Pair ‘B’ for 190 minutes before disappearing completely. If the excitation was electrical, then it would be thought to be more consistent.

Based on this analysis of the speed and motor power signal it is thought that the source of the ‘noise’ is mechanical and, as it is produced, there is a direct effect on the shaft speed. The back-to-back gear rig circulates the power within the mechanical loop and, once at speed, the power required by the motor is only that to overcome the losses, frictional and otherwise, within the power loop. Therefore, if these losses were to be reduced quickly, then it is possible that the drive shaft would 'over-speed' due to the delay in the feedback loop. It is possible that this over-speed may cause the hydraulic pressure to the torque unit to decrease, potentially creating an AE source. To analyse the signals further, and hence deduce the cause of increased amplitude levels, Figure 6-20 plots the RMS trend of the wavestreams recorded during Run 1. Again, it is possible to demonstrate that as the silicone cures on Channel 4, the RMS of the wavestreams increases due to the improved transmission of energy through the couplant as it cures.

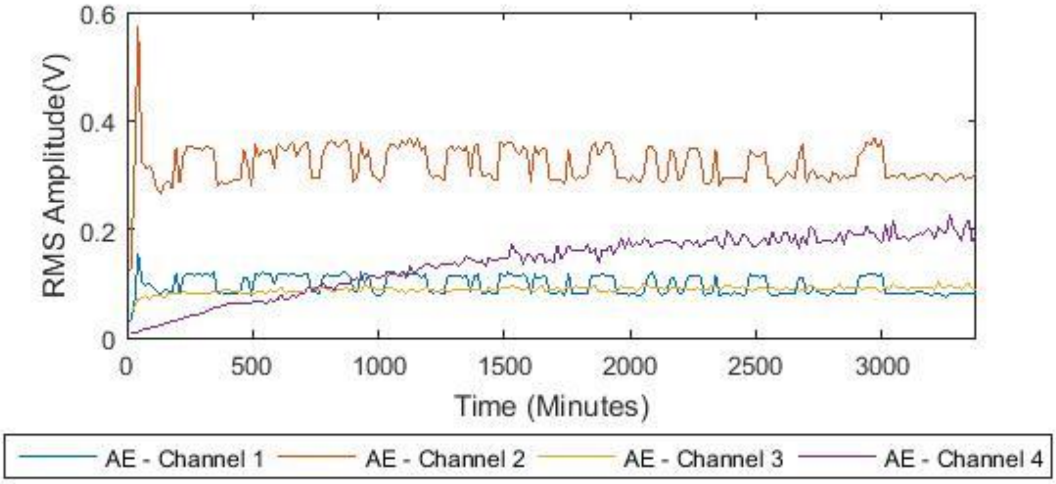

Figure 6-20 - RMS response of AE wavestreams recorded during Run 1

Analysing a wavestream which produces an RMS peak in Figure 6-20, Figure 6-21 plots 0.1 seconds of the wavestreams recorded after 1905 minutes of Run 1 had passed. As previously seen in the absolute energy levels, the radially mounted sensors of gear pair 'A' and 'B', Channels 2 and 4 respectively, exhibit higher transient amplitudes than the corresponding axially mounted sensors (Channels 1 and 3 respectively). This is due to the signal being stronger in the radial direction of the support bearings, corresponding with the wave propagation direction as discussed in more detail in previous chapters. When comparing the response of each gear pair, it can be seen that the two sensors connected to gear pair 'A'. channel 1 and 2, exhibit a large number of periodic transient bursts throughout the entire wavestream. As for the AE sensors connected to gear pair 'B' however, only Channel 3 demonstrates the same periodic bursts as witnessed in channel 1 and 2 albeit at a much lower amplitude. There is however no evidence of the same rate of transient bursts occurring on Channel 4, and instead 3 separate transient bursts are witnessed occurring at a much lower frequency than the transient bursts present of the other three channels.

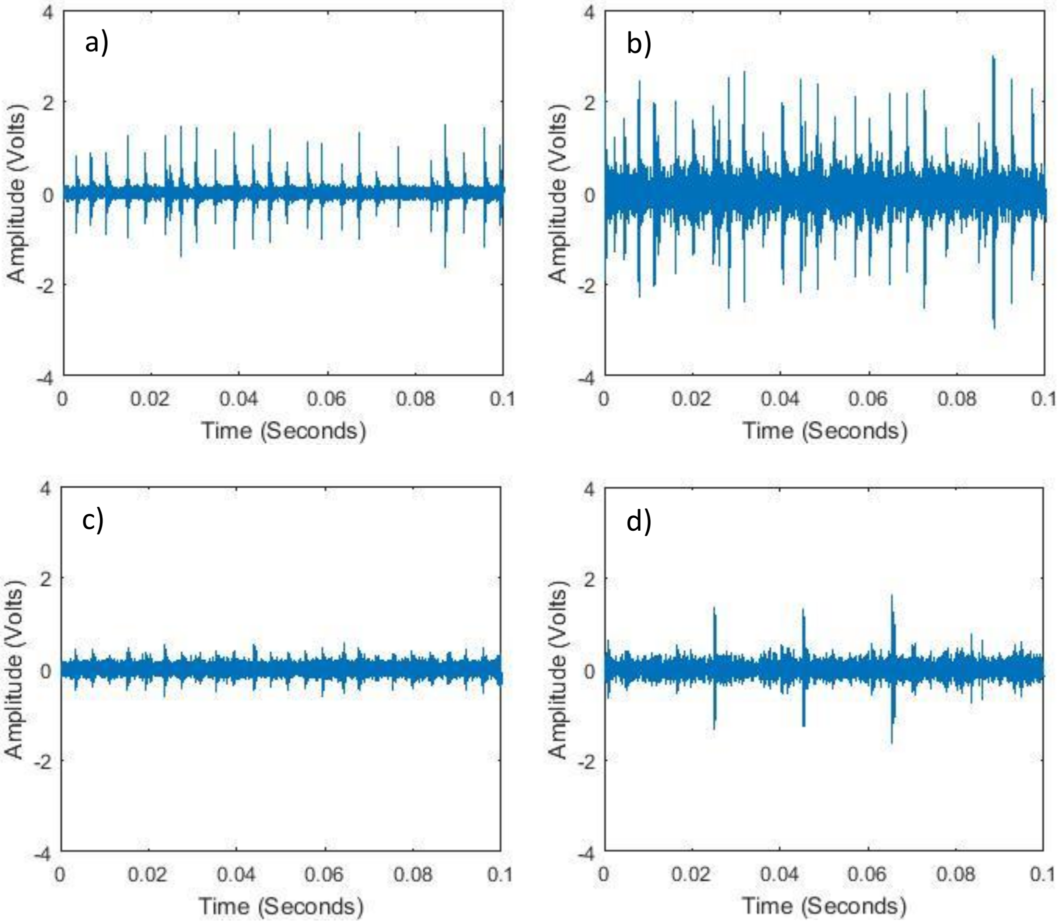

Figure 6-21 - Raw signal of Run 1 after 1905 minutes for a) Channel 1 b) Channel 2 c) Channel 3 and d) Channel 4

Frequency analysis of these signals determines that the periodic bursts in Channels 1-3 occur at a rate of 248Hz, relating directly to the BPFO of the NJG 2306 VH bearing when being run at 3000rpm (Figure 6-22). (Note: In Figure 6-22 and any other frequency spectrum between 0-1kHz within this section, the scale of the y-axis differs for each frequency spectrum to allow for the excitation frequencies to be represented visually). Also visible in the frequency spectrum of Channel 4 is the ball spin frequency, BSF excited at 198.4Hz. An increase if energy is also visible at 397Hz, and this is produced as a single point on a roller makes contact with each of the two races, i.e 2xBSF. For the support bearing attached to the slower shaft, rotating at 2000rpm, there is no clear evidence within the frequency spectrum of the BPFO, 165Hz, or its associated harmonics.

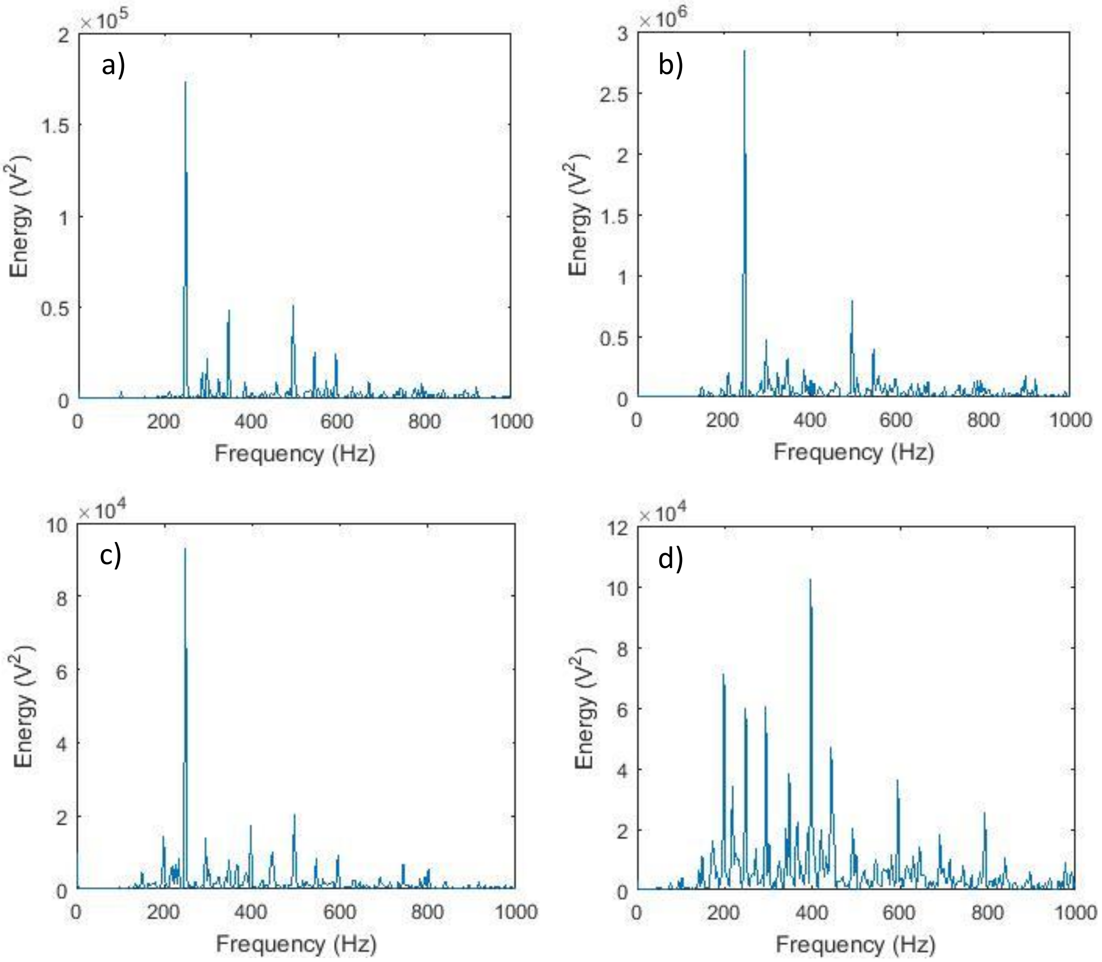

Figure 6-22- Frequency spectrum of Run 1 wavestreams after 1905 minutes for a) Channel 1 b) Channel 2 c) Channel 3 and d) Channel 4

Figure 6-23 plots the raw signals after approximately 2010 minutes (after approximately 6 million cycles of the pinion), when the RMS amplitude of Figure 6-20 is at its lower stage. Whereas there is little change between the wavestreams recorded on Channels 3 and 4, there is a noticeable difference in the periodicity and amplitude of the transient bursts produced at Channels 1 and 2. Although still exciting the BPFO, shown in the frequency spectrums plotted in Figure 6-24, there is a significant reduction in the energy at the 1st and 2nd harmonic of the BSF as well as the signal itself demonstrating fewer transient bursts than when the 'noise' is at a higher amplitude. This determines that whatever is causing the seemingly random increase in AE absolute energy and vibration RMS, is also exciting the natural bearing frequencies.

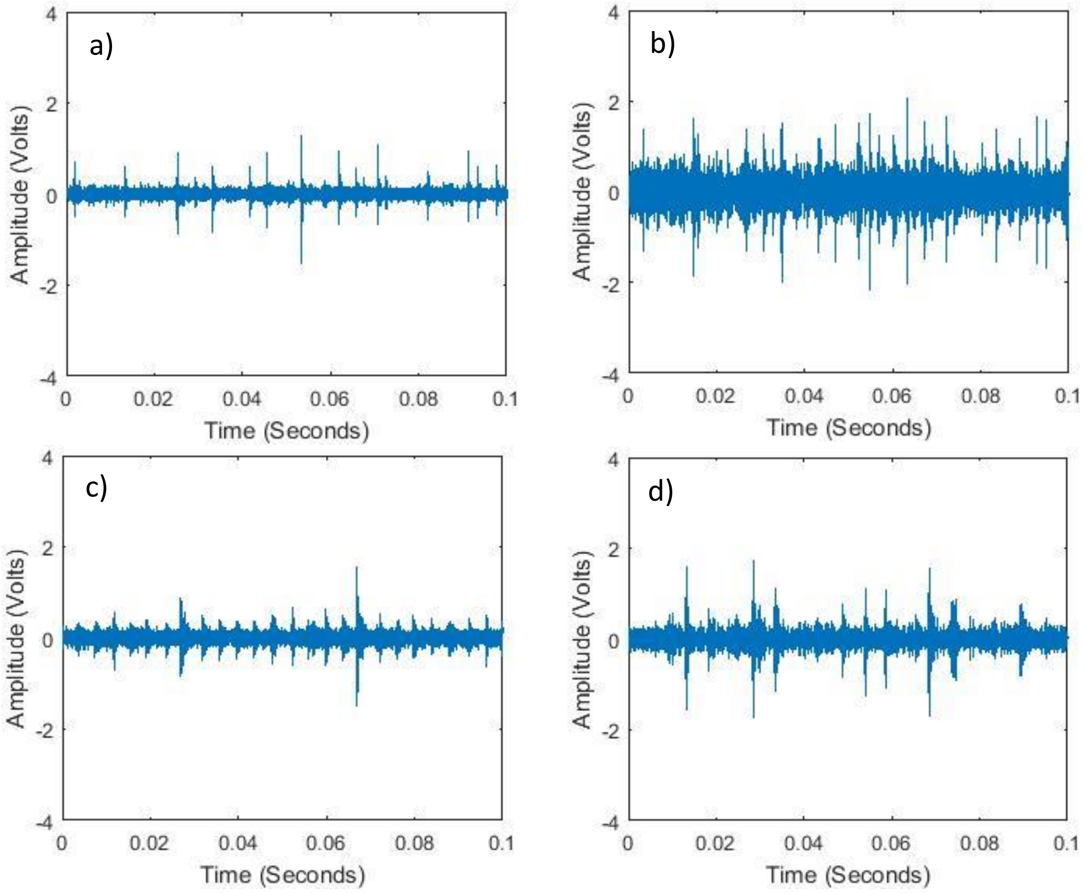

Figure 6-23 - Raw signal of Run 1 after 2010 minutes for a) Channel 1 b) Channel 2 c) Channel 3 and d) Channel 4

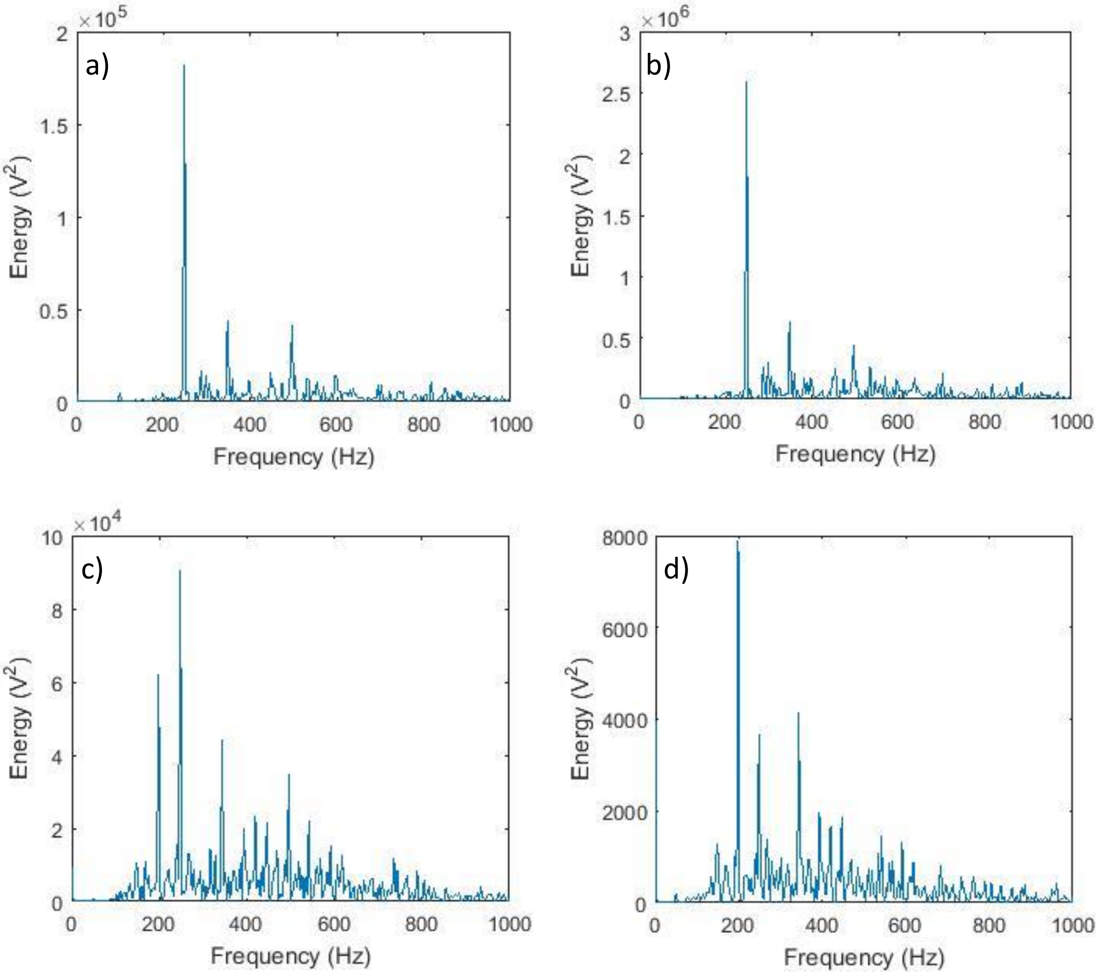

Figure 6-24 - Frequency spectrum of Run 1 wavestreams after 2010 minutes for a) Channel 1 b) Channel 2 c) Channel 3 and d) Channel 4

To help illustrate that the rate of transient bursts produced in Figure 6-21 and Figure 6-23 were representative of all signals produced, Figure 6-25 plots the order spectrum of Channels 1-4 for the duration of signals recorded during Run 3, with respect to the pinion shaft speed of 3000rpm or 50Hz. It is possible to see the 1st and 2nd harmonics BPFO of the cylindrical roller bearing (SKF NJG 2306VH) at 4.95 and 9.90 orders respectively as well as the BPFI of the SKF QJ 208 ball bearing at 7.5 orders. However, at the scales used, there is no clear excitation of the gear mesh frequency (GMF), 800Hz or 16 orders, within either of the frequency spectrums shown. The closest observation of a frequency occurring close to the GMF is witnessed in Figure 6-22, where there is an excitation of 796Hz. Although close to the theoretical GMF, this is instead thought to be the 4th harmonic of the BSF because the strongest spectral excitation exists at 2xBSF, 397Hz, due to the single point on the roller hitting the inner and outer raceway.

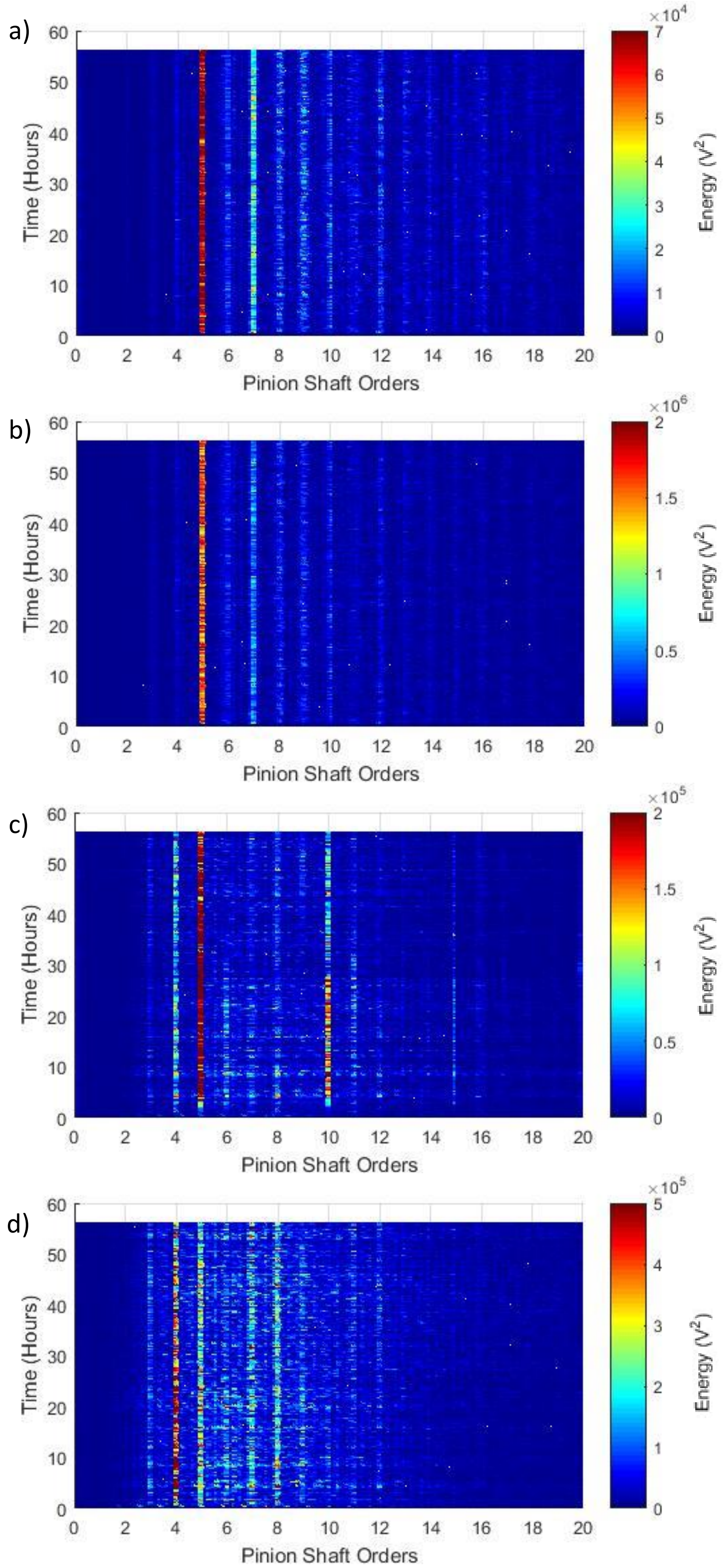

Figure 6-25 - Order analysis for the duration of Run 3, a) Channel 1, b) Channel 2, c) Channel 3 and d) Channel 4

Tan and Mba (2005) demonstrate that transient bursts spaced at the gear mesh frequency were clearly visible in an AE wavestream when running a spur gear under relatively low speed and load (745rpm and 73Nm). The sensor used to record these wavestreams was attached to gear itself and, through simultaneous recording of a sensor mounted to the gear face and another on the bearing housing, Toutountzakis *et al.* (2005) build on the work of Tan and Mba (2005) to demonstrate that the transient bursts produced by the gear mesh become severely attenuated. Whereas the peak amplitude of the transients was approximately 2V when monitored on the gear face, the peak amplitude drops to 0.04V when recorded through the bearing housing. Similar findings were discussed by Singh *et al.* (1999) when analysing the attenuation of static gears in contact under load. In addition to this, it was also noted that, depending on the position on the rolling elements within the bearing, some of the transient bursts suffered a larger amount of attenuation than others. When relating the work of Toutountzakis *et al.* (2005) to the data gathered through this experiment, it can be appreciated that if similar levels of attenuation occurred then the transient bursts relating to the gear mesh frequency would be readily absorbed by the noise floor of the wavestream.

The type of gear monitored also adds to the difficulty when trying to detect the gear mesh frequency. Spur gears, as monitored by Toutountzakis *et al.* (2005), have straight cut teeth and because of this, the teeth rapidly carry load when coming into mesh. This sharp engagement is the reason why spur gears are audibly louder than other gear types, and hence why the gear mesh frequency is more easily detected in the raw wavestreams of vibration and AE signals.

This test uses helical gears, which are designed to progressively introduce the teeth into mesh, slowly increasing the stress applied to the gear tooth, and hence increasing the gear life whilst reducing the mechanical noise. This makes helical gears favourable when designing gearboxes for automotive purposes but, as shown by Raja Hamzah and Mba (2009), because the gear teeth are gradually brought into mesh, there is a significant reduction in the detection of the gear mesh frequency even though the AE sensors were placed onto the gear itself.

Both Toutountzakis *et al.* (2005) and Raja Hamzah and Mba (2009) demonstrated a reduction in the detection of the gear mesh frequency when the speed is increased from 700-1450rpm. The gears under investigation in this study are rotating at 2000 and 3000rpm (gear and pinion) and therefore it is believed that this, combined with the sensors being located on the bearing housing, may be responsible for the difficulty in detecting the gear mesh frequency. These operating speeds may also explain the detection of the bearing frequencies in the wavestreams of Figure 6-21 and Figure 6-23. The wavestreams discussed by Toutountzakis *et al.* (2005), show no evidence of transients produced by the support bearing itself, but as demonstrated in Chapter 4, higher speeds and load increase the detection of the characteristic frequencies of a healthy bearing.

Figure 6-26 plots the binned frequency between 0-100kHz for each of the four channels monitored where designations (a) and (b) illustrate the axial and radial sensors mounted to Gear Pair ‘A’ respectively, and designations (c) and (d) illustrate the axial and radial sensors mounted to Gear Pair ‘B’ respectively. It can be seen that the axially mounted sensor connected to Gear Pair ‘A’, Channel 1, is excited at a number of frequencies including, 17, 33, 44 and 67kHz. The axially mounted sensor connected to Gear Pair ‘B’ however, Channel 3, instead demonstrates excitation at 37 and 64kHz. The scales of the two channels, 1 and 3, is maintained across both images in Figure 6-26 and it can be seen that there is more energy in the spectrum of Channel 1 when compared to Channel 3. This difference in energy is similar to the observations made when analysing the difference in the time driven AE absolute energy for gear pairs ‘A’ and ‘B’, Figure 6-16 and Figure 6-17 respectively. There are a number of sources of this error including the bond quality, location and sensitivity of the sensor as well as the small differences in the level of gain applied to the signal when passed through the amplifier.

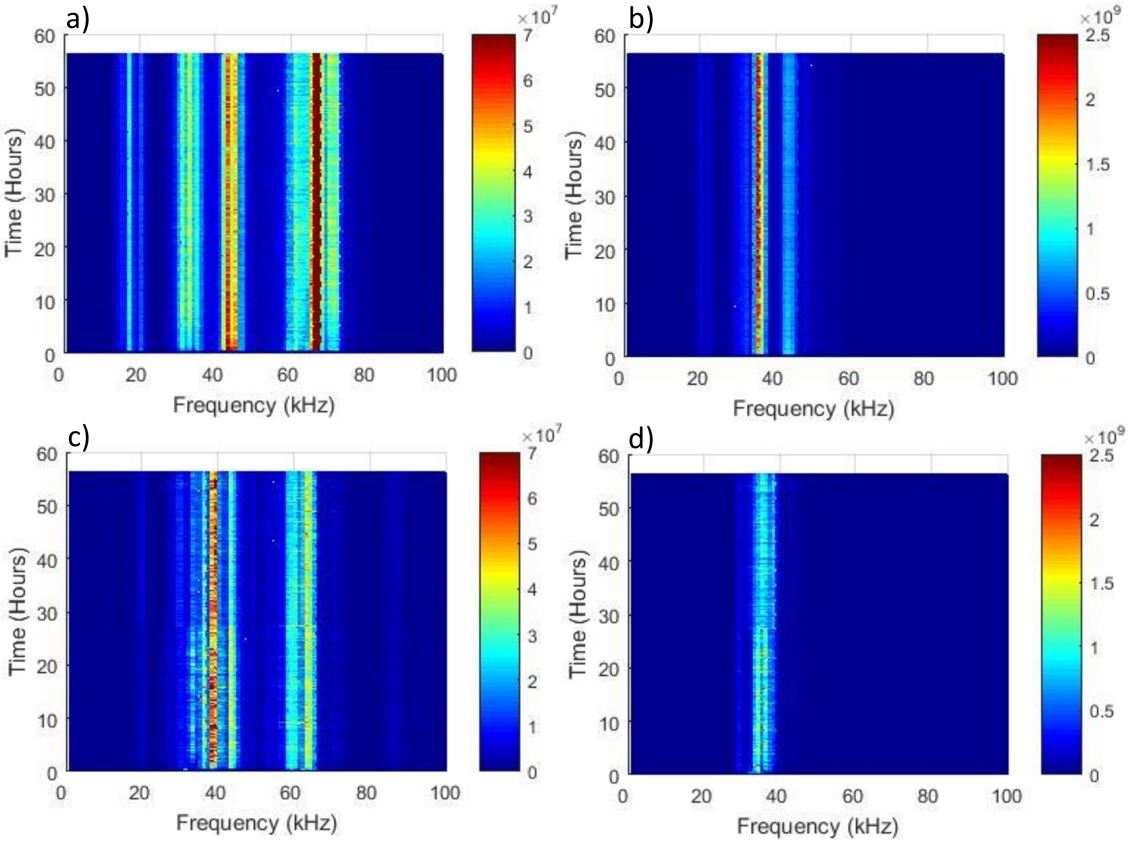

Figure 6-26 - Frequency plot between 0-100kHz for a) Channel 1, b) Channel 2, c) Channel 3 and d) Channel 4 for the duration of Run 3 – where the unit of the Z-axis scale is Energy (V^2)

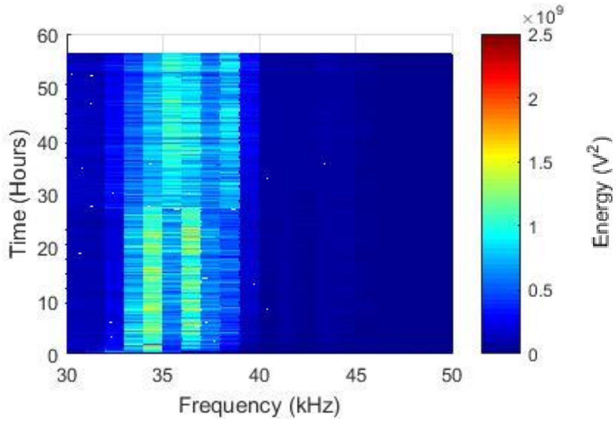

Figure 6-27 - Magnification of Figure 6-26.d

Although there is a difference in the frequency excitation for the axially mounted sensors, the frequency excitation of the radial sensors is relatively consistent between the two gear pairs. The radial sensor mounted on Gear Pair 'A', Channel 2, excited at 36 and 43kHz whereas the radial sensor mounted on Gear Pair 'B', Channel 4 demonstrates excitation at 36kHz. The amplitudes of each of the four channels remains relatively constant throughout the duration of Run 3 providing an indication that the condition of this gear pair also remained constant. In Figure 6-17.c, a step change was witnessed in the vibration RMS amplitude after approximately 1600 minutes that was not witnessed in the time driven AE data. There is however a small change in the frequency plot of Channel 4, Figure 6-26.d, after a similar amount of time. There is no change in the overall frequency of excitation or the amplitude at which it is excited however, the frequency band of excitation becomes more spread out between 34 and 40kHz.

Unlike the frequency response demonstrated in Figure 6-26, there is little similarity in the frequency spectrums of the axial and radial sensors of each gear pair when analysed between 100-200kHz and 200-500kHz, Figure 6-28 and Figure 6-29 respectively. Excitation of Channel 1 demonstrates a peak at 108kHz, a frequency also excited in Channel 2 and 4. Channel 3 however, has a greater concentration of energy at 140kHz and 150kHz, with the energy concentration again spreading after 1600 minutes (27 hours) as previously shown in Figure 6-27.

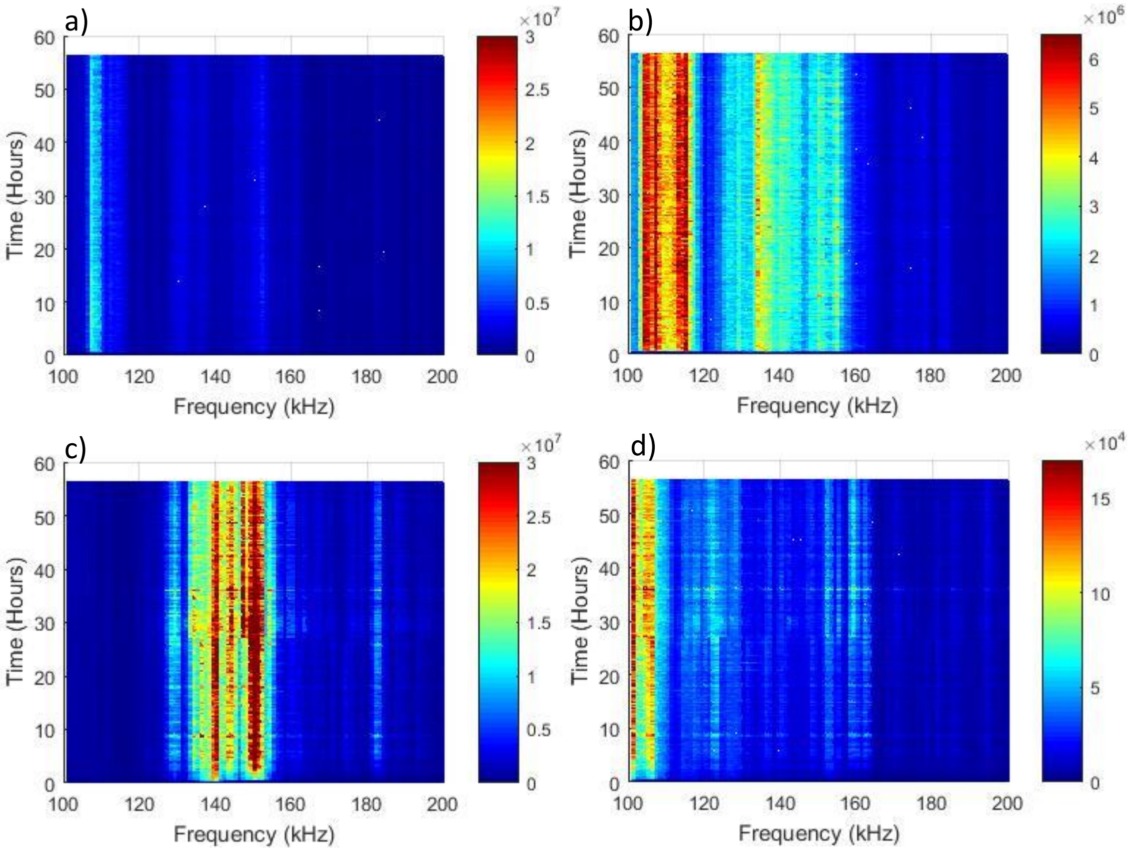

Figure 6-28 - Frequency plot between 100-200kHz for a) Channel 1, b) Channel 2, c) Channel 3 and d) Channel 4 for the duration of Run 3 – where the unit of the Z-axis scale is Energy (V^2)

The only similarity visible is demonstrated in the band of 200-500kHz, Figure 6-29, where, unlike in Figure 6-26 where similarities were drawn between the respective radial and axial sensors of each gear pair, similarity is now drawn between the two sensors mounted to each gear pair. It can be seen that the axial sensor attached to Gear Pair 'A', channel 1, demonstrates excitation between approximately 340 and 360kHz, an area of high sensor sensitivity due to excitation of its resonant frequency of 350kHz for a Nano30 sensor. This is mirrored in the radial sensor attached to the same gear pair, Channel 2 although there is a stronger amount of energy at 240kHz rather than between 340 and 360kHz although the energy amplitude is greater in Channel 1. The frequency bands excited for the sensors connected to Gear Pair 'B' differ significantly from those connected to Gear Pair 'A'. Rather than exciting discrete frequency bands, the binned frequency plot of Channel 3 demonstrates excitation at a multitude of frequency bands between 200 and 375kHz, with a separation of between 10 -15kHz between each band. The separation between the frequency bands for the radial sensor, Channel 4, is greater than that of the axial sensor with separation of approximately 25kHz. In the lower frequency bands, 0-100kHz and 100-200kHz, it was noted that after approximately 27 hours there existed a slight change in which frequency was excited, aligning with the reduction in the amplitude of the vibration RMS seen in Figure 6-17.c. A change is also visible in the spectrum between 200-500kHz, although rather than shifting the excited frequency slightly, the amplitude of the frequencies excited in Channel 3 and 4 increase around the frequencies close to the sensors resonant frequency 300-350kHz for Channel 3 and there is excitation at 250kHz and 300kHz for Channel 4.

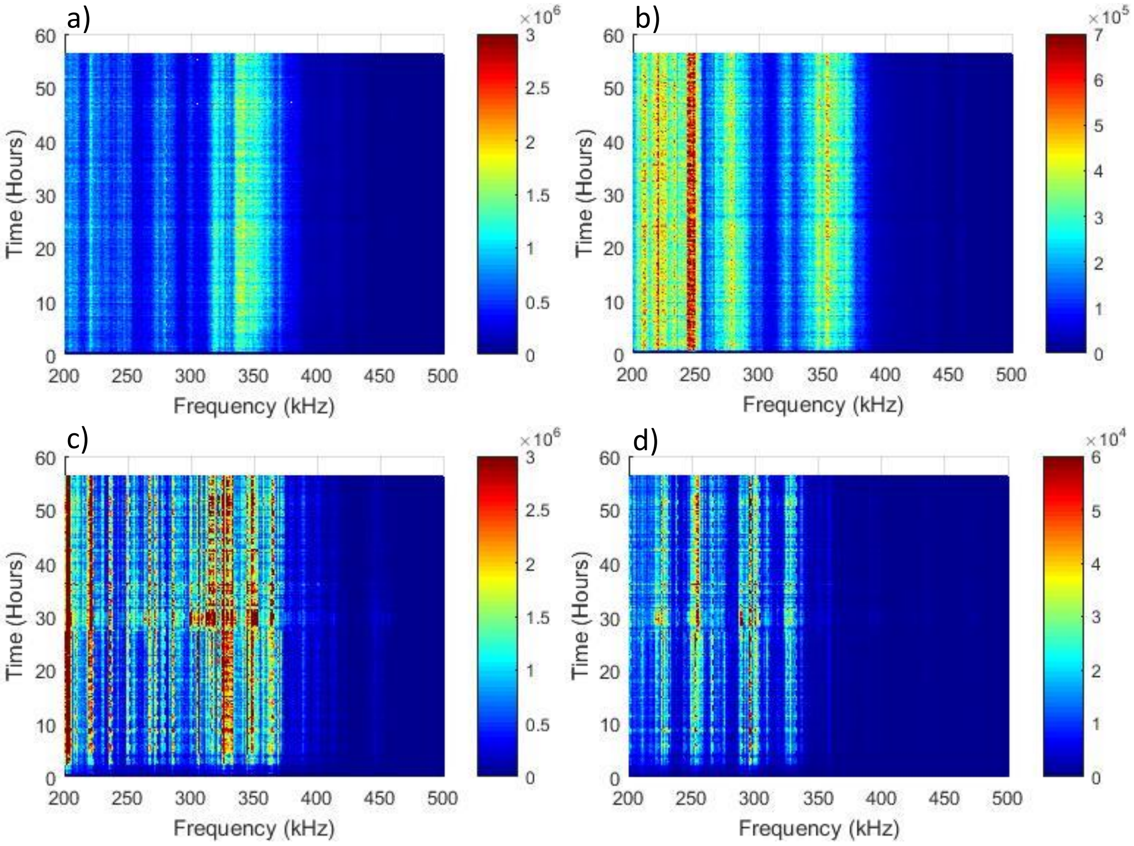

Figure 6-29 - Frequency between 200-500kHz for a) Channel 1, b) Channel 2, c) Channel 3 and d) Channel 4 for the duration of Run 3 – where the unit of the Z-axis scale is Energy (V^2)

6.4.5 Full Runs – Group 2

As previously stated, when running the gears in Group 2, the pinion of gear pair 'B' suffered a complete tooth fracture during Run 5, Figure 6-9, ending the experiment. Visual analysis of the damaged region of the gear indicated that the tooth failure originated in the root of the tooth and, as this is the highest stress point within a gear, it is considered that the damage propagation would have occurred quickly. The gear upon which the failure occurred, designated Gear 1098 in Table 6-1, was run at 855Nm on flank A for 10 million cycles before failing after 1.7 million cycles when being run on flank B. Visual analysis of the crack face indicates that the failure was ductile and hence the crack would have grown with an increased number of cycles. As there is no obvious trend within the AE or vibration data, the initiation point of damage is unknown. As such, the remainder of this section aims to determine if it possible to establish a point of damage initiation and if so, if it is possible to form trends within the AE data which illustrate the growth and propagation of the tooth crack or indeed the influence of the changing gear condition on the behaviour of the bearings.

Figure 6-30 and Figure 6-31 plot the time-driven AE and vibration data for the duration of Run 4 and 5 respectively, as previously carried out in Section 6.5.3 for ‘healthy’ runs 1-3. It can be seen that, similar to Runs 1-3, once the initial start up phase of the gear has been competed, both the AE and vibrations level remain relatively constant throughout the window of observation, even though it is known that failure occurred in the latter stages on Run 5. Observations of the insensitivity of AE to gear defects have been made previously by Toutountzakis *et al.* (2005) who witnessed that the RMS response to seeded gear defects saw no increase and, at times, even demonstrated a lower RMS value than that of the healthy counterpart when analysed during a dynamic test. Through both static and dynamic testing however, other authors have demonstrated that as damage propagates on the gear tooth, including both tooth root fillet cracking and surface pitting, there exists an increase in AE trend, including measures such as ring down counts, RMS and Absolute Energy (Pullin *et al.,* 2012; Toutountzakis *et al.,* 2005; Toutountzakis & Mba, 2003b; Tan *et al.,* 2005). This is generally in contrast to the vibration response and it is noted by Singh *et al.* (1999) that that there is little difference between the raw vibration signal and the signal created during the initial stages of tooth crack growth.

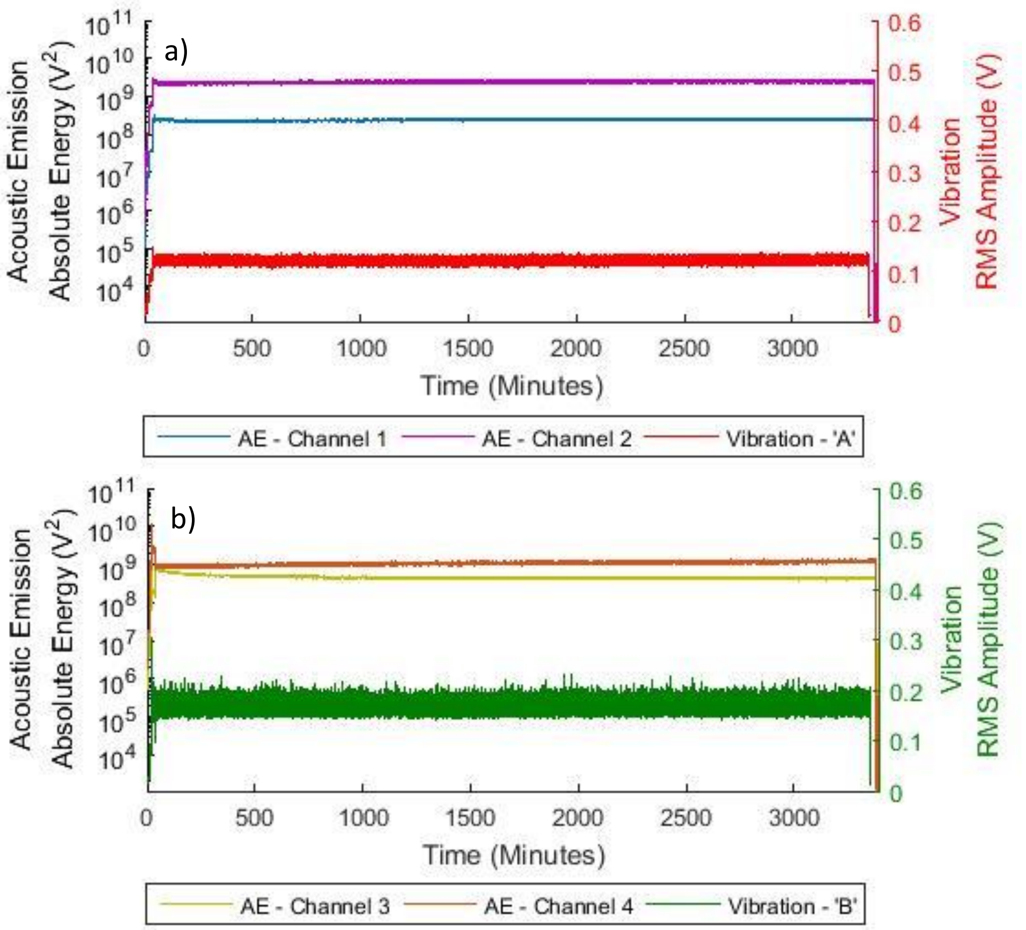

Figure 6-30 - Comparison between the Absolute Energy of AE Time-Driven Data and Vibration RMS Amplitude over the test duration for a) Gear Pair 'A' and b) Gear Pair 'B' – Run 4

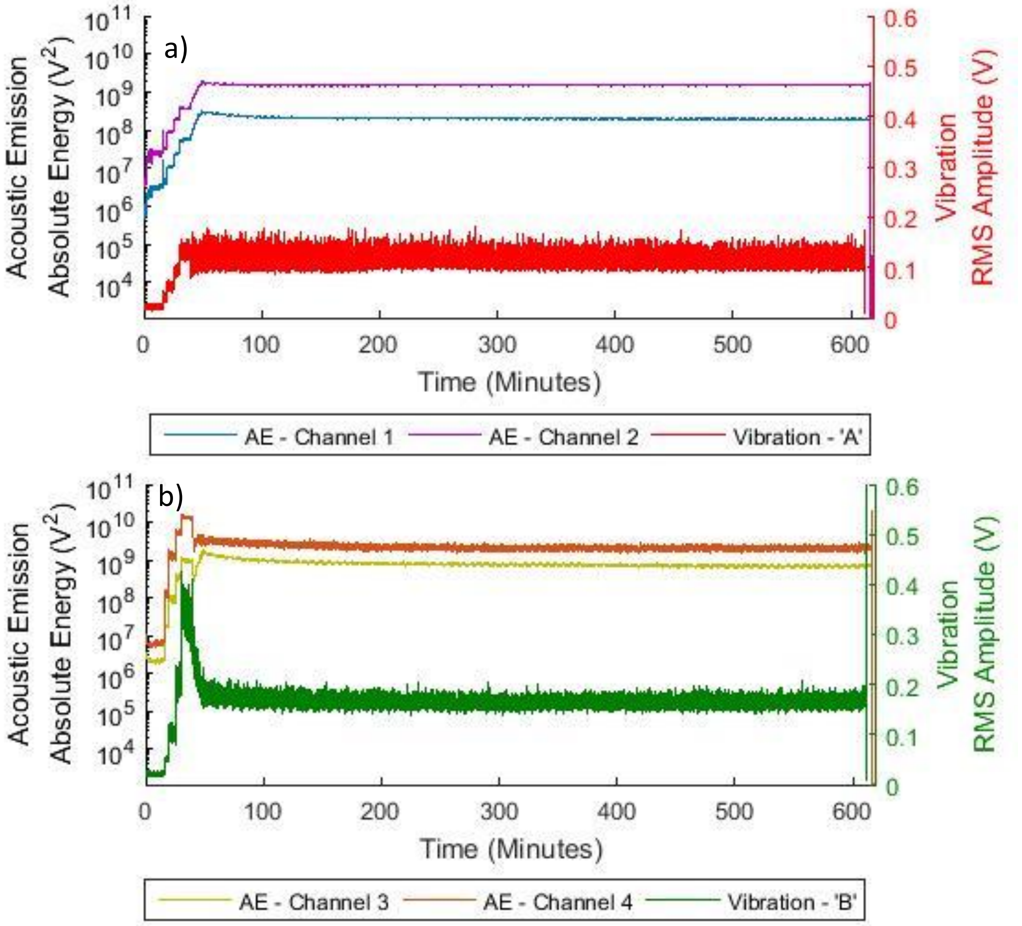

Figure 6-31 - Comparison between the Absolute Energy of AE Time-Driven Data and Vibration RMS Amplitude over the test duration for a) Gear Pair 'A' and b) Gear Pair 'B' – Run 5

This inherently has led a number of authors to agree that simple AE analysis methods are able to detect damage better than vibration though a majority of the test rigs used to come to such conclusions were simplified versions and non-representative of the complex gear systems used within industry.

Figure 6-32, a plot of the final 20 minutes of the observation window for Run 5, demonstrates that there is no growing trend in either the AE or vibration data leading up to the event where tooth failure occurs. Instead, the only evidence that damage exists at all is evident immediately before the automatic shutdown of Run 5 after 616 minutes as the vibration level exceeded 0.85V. This is the point of final failure of the gear tooth, the detection of which occurs concurrently on both the AE and vibration signals. Whereas there is a large spike in the AE and vibration sensors connected to Gear Pair ‘B’, there is only a small peak in vibration amplitude and AE absolute energy on the sensor connected to Gear Pair ‘A’. This demonstrates that there is slight influence between each of the two gear pairs due to fluctuations in the load application as the pinion tooth is now removed.

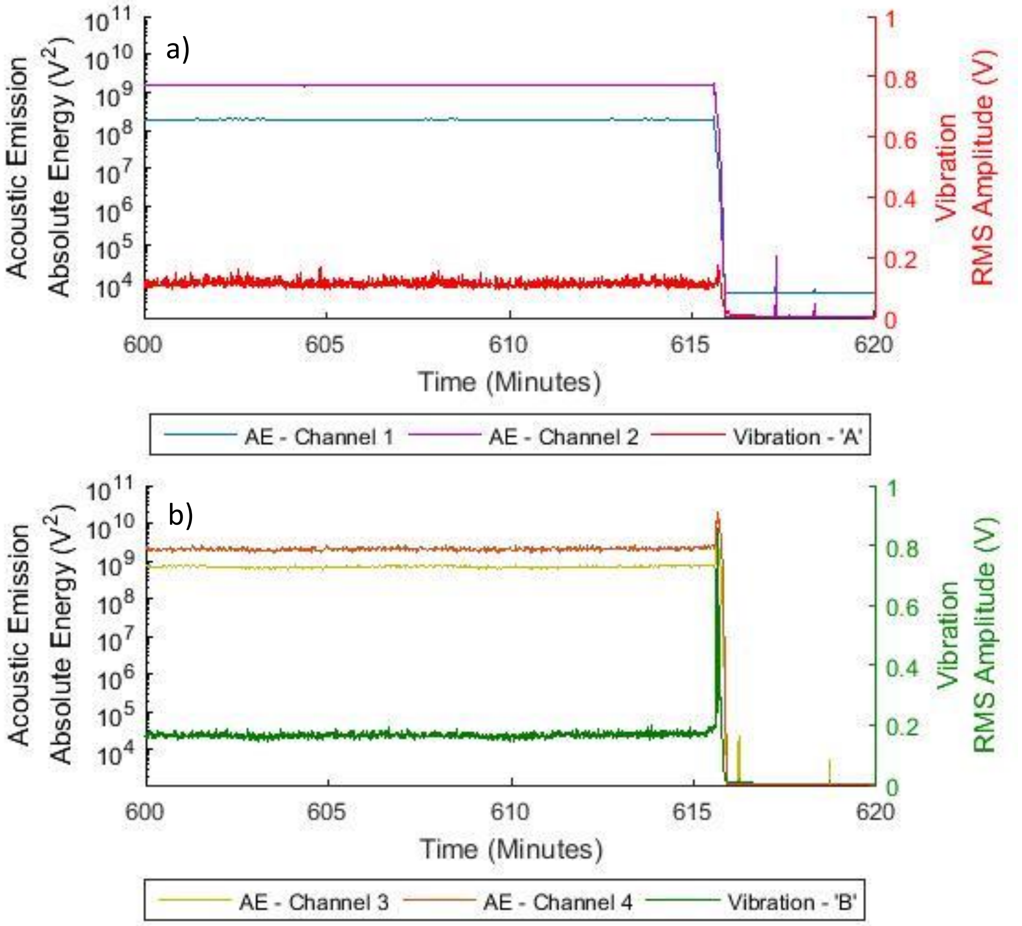

Figure 6-32 - Close up of the AE Absolute Energy and Vibration RMS prior to automatic shutdown of a) Gear Pair 'A' and b) Gear Pair 'B'

6.4.5.1 Start Up Phases – Run 4 & 5

Whereas Figure 6-30 and Figure 6-31 illustrate all of the data collected in each observation window, Figure 6-33 and Figure 6-34 plot the start-up phases of Run 4 and 5 respectively, as the speed is incremented under a constant torque of 50Nm, the same operating conditions used in Runs 1-3. The start-up response of gear pair ‘A’ in Runs 4 and 5, Figure 6-33.a and Figure 6-34.a respectively, is comparable to the AE and vibration levels witnessed in Runs 1-3. When comparing the response of Gear Pair ‘B’ however, there is a large difference not only between Run 4 and 5, Figure 6-33.b and Figure 6-34.b respectively, but also when comparing Run 4 to Runs 1-3. (Note: Due to being plotted on a log scale, the difference in the AE absolute energy is not as obvious visually as the difference in the vibration RMS amplitude).

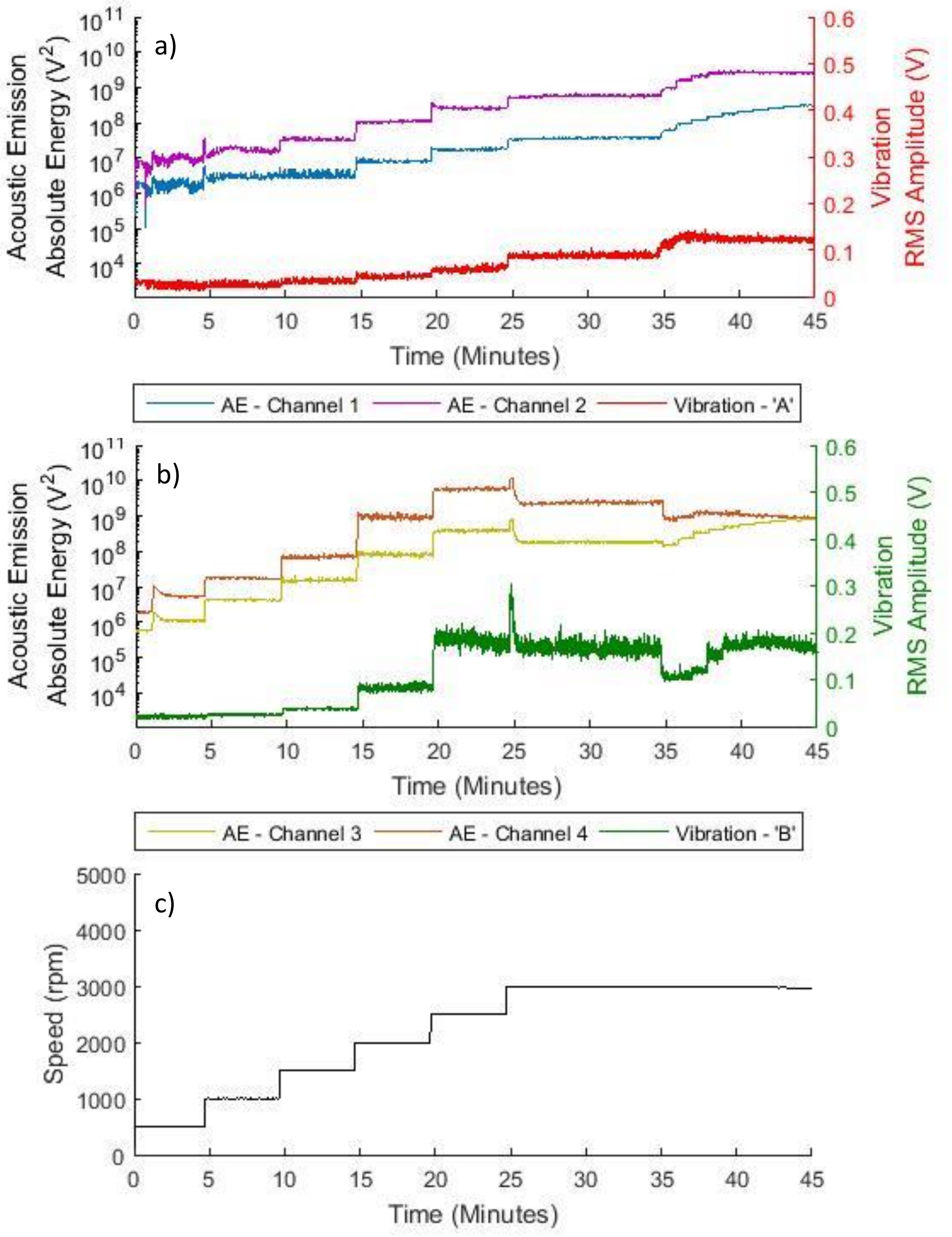

Figure 6-33 - Comparison between the Absolute Energy of AE Time-Driven Data and Vibration RMS Amplitude as speed is changed for a) Gear Pair 'A' and b) Gear Pair 'B' – Run 4

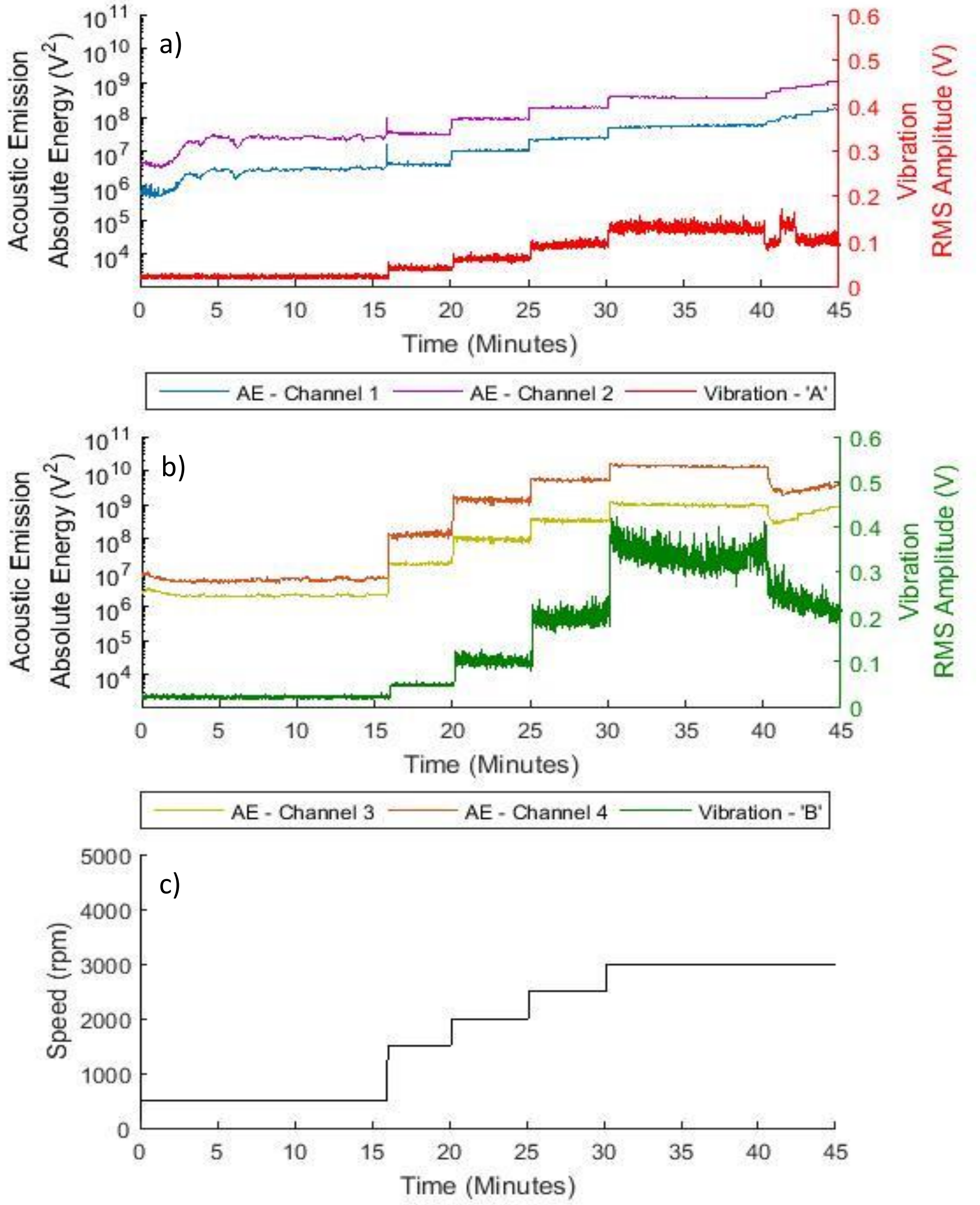

Figure 6-34 - Comparison between the Absolute Energy of AE Time-Driven Data and Vibration RMS Amplitude as speed is changed for a) Gear Pair 'A' and b) Gear Pair 'B' – Run 5

Such a stark difference in the response of Gear Pair ‘B’ in Runs 4 and 5, when compared with Runs 1-3, suggests that there was a flaw within the gears of Gear Pair ‘B’ from the start of the Run 4. It could be argued that this increase may be due to the gears going through a running in period at this point as the running in period of the gears in Group 1 was not observed. However, the two gears of Gear Pair ‘A’ were also being run for the first time yet their AE and vibration response is significantly lower than that of Gear Pair ‘B’.

The large difference between vibration and AE amplitude in Runs 4 and 5 highlights that there has either been a change in gear condition during Run 4 or that when running on flank ‘B’ there is a greater amount of energy released. A possible reason for flank ‘B’ being more sensitive than flank ‘A’ is the location of the defect. If it was located within the root of flank ‘B’, the defect would be subjected to a compressional load when being run on flank ‘A’. However, when run on flank ‘B’, the bending stresses would now cause the defect to be in tension, allowing for a crack to propagate through the root of the gear tooth.

Figure 6-35 and Figure 6-36 plot the torque increment phase of the start-up stage of Runs 4 and 5. Unlike Runs 1-3, the target torque was increased to 855Nm and therefore direct comparisons cannot be made between the two sets of data. However, when previously analysing the torque response of Runs 1-3 it was discussed that the response appeared to change with the direction the gears were operated in, i.e flank ‘A’ or ‘B’. For Runs 4 and 5 there is a less obvious response, with the sensors connected to Gear Pair ‘B’ initially reducing in value as the load is first increased before increasing further with increasing load. Gear pair ‘A’ however exhibits a step increase across all sensors with increased load.

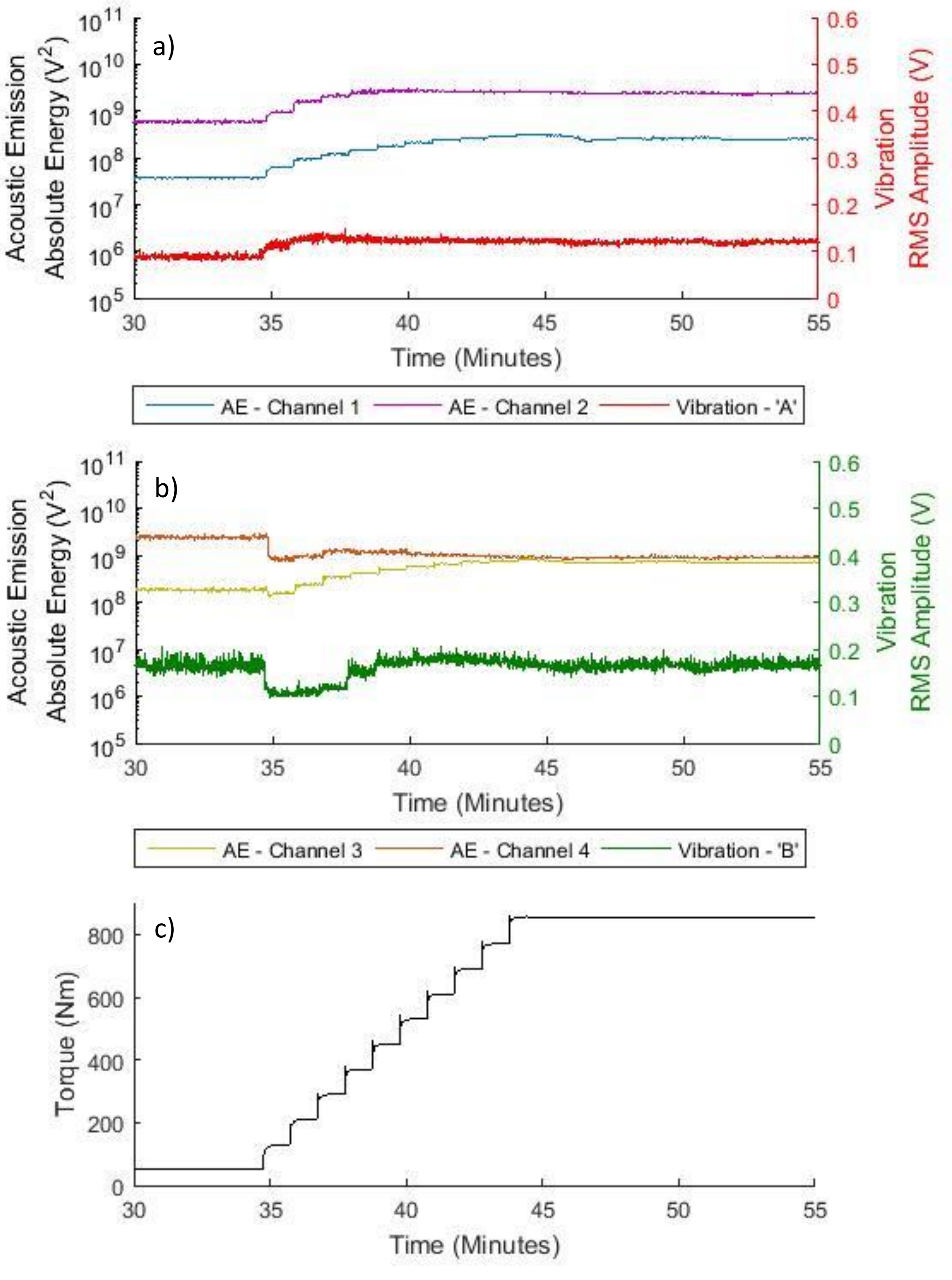

Figure 6-35 - Comparison between the Absolute Energy of AE Time-Driven Data and Vibration RMS Amplitude as torque (c) is changed for a) Gear Pair 'A' and b) Gear Pair 'B’ – Run 4

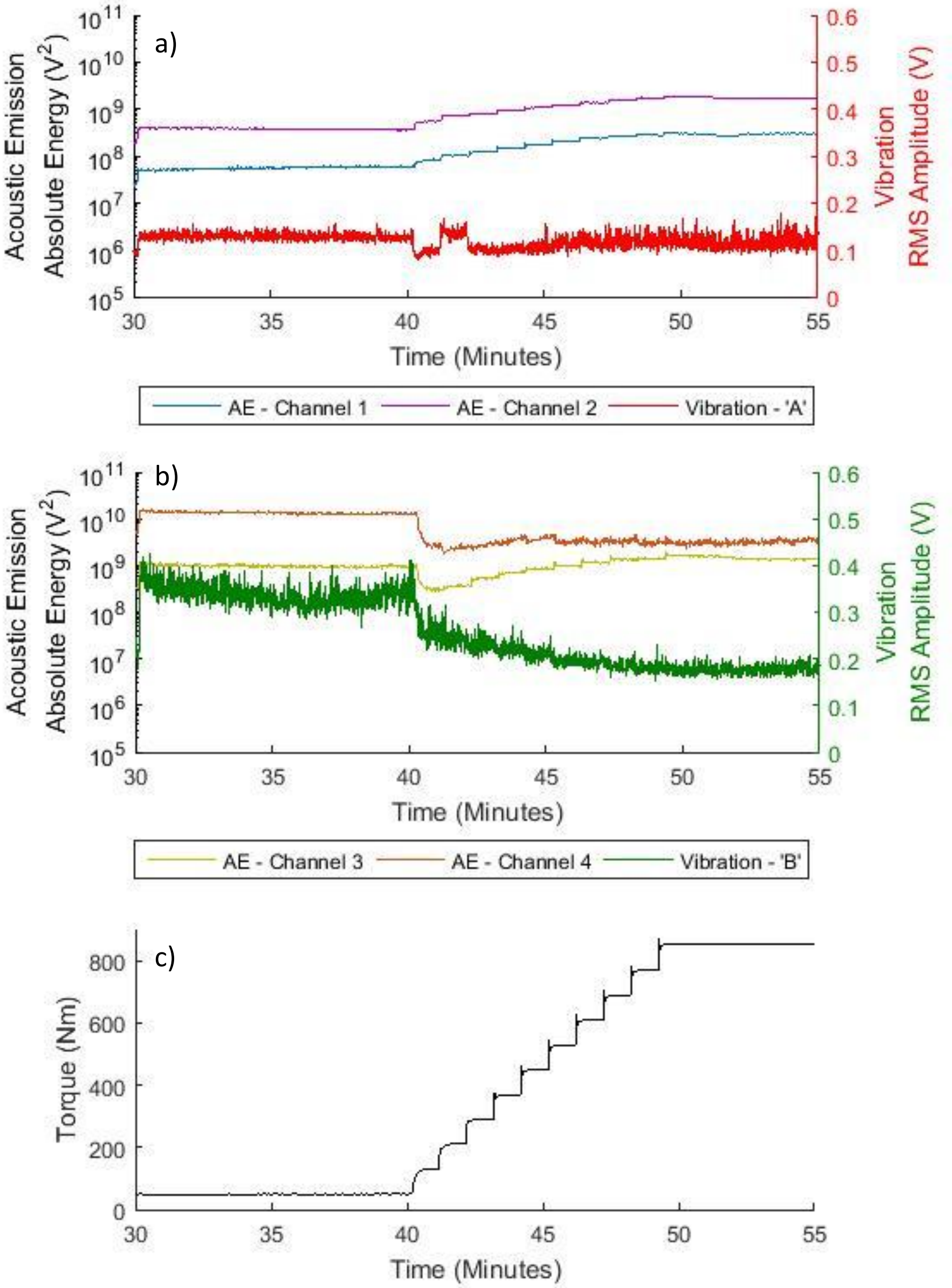

Figure 6-36 - Comparison between the Absolute Energy of AE Time-Driven Data and Vibration RMS Amplitude as torque (c) is changed for a) Gear Pair 'A' and b) Gear Pair 'B' – Run 5

6.4.5.2 Wavestream Analysis

Figure 6-37, a and b, plots the RMS trends calculated over the AE wavestreams collected throughout Runs 4 and 5 respectively whereas Figure 6-38, a and b, plots the peak to peak amplitude of each wavestream instead. For the duration of Run 4, Figure 6-37-a, it can be seen that all of the channels exhibit a consistent RMS amplitude with the wavestreams of the radially mounted sensors, Channels 2 and 4, having a larger RMS value than the axially mounted sensors, Channels 1 and 3. Similar trends are also seen when the gear pair were run on flank 'B', Figure 6-37-b, although there is a larger initial RMS amplitude on Channel 4, the sensor mounted radially on gear pair 'B', which goes on to reduce to a more consistent level as time passes. The RMS amplitude witnessed on Channel 4 in Figure 6-37.b also reaches a maximum of 1V before reducing back down to a level of 0.5V for the duration of the observation window. This is the first indication of any increased levels of amplitudes that may indicate an initiation of damage.

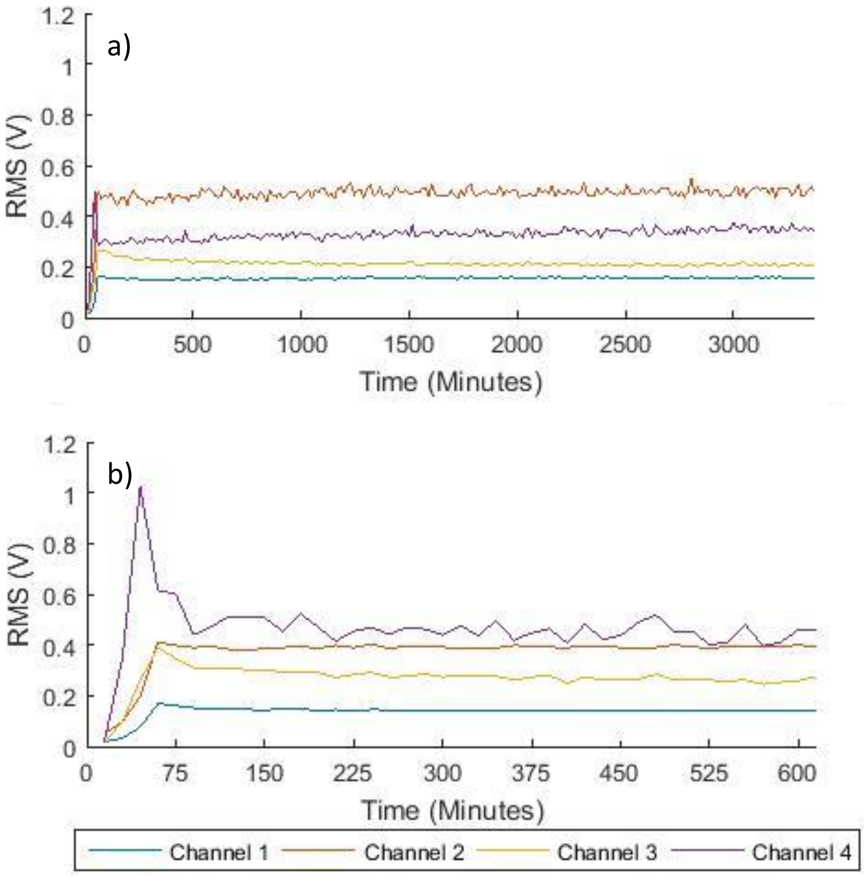

Figure 6-37 - RMS Amplitude for the wavestreams collected in a) Run 4 and b) Run 5

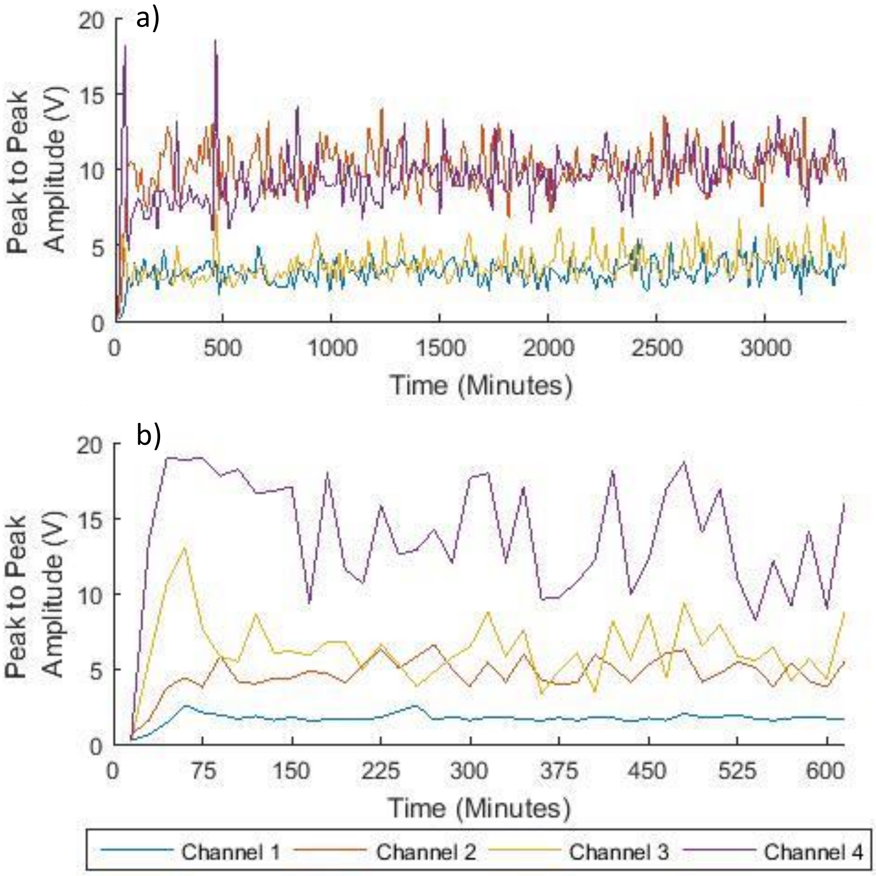

Figure 6-38 - Peak to Peak Amplitude for the wavestreams collected in a) Run 4 and b) Run 5

It can be seen in Figure 6-38.a that during Run 4 there exists similarity in the peak to peak amplitudes of the radially and axially mounted sensors for Gear Pairs 'A' and 'B' respectively with radial sensors exhibiting peak to peak amplitudes of 7-14V and axial sensors 3-5V. Similar observations however cannot be drawn for the peak to peak amplitudes in Run 5, Figure 6-38.b. Although the RMS amplitude of Figure 6-37.b quickly reduces down to a consistent level following the large initial spike, the peak to peak amplitude of the same data, Figure 6-38.b, does not reduce down in a similar fashion. Instead, the peak to peak amplitude reaches 19V after 50 minutes and then remains above 16V until 150 minutes have passed. The peak to peak amplitude of Channel 4 then fluctuates between 10-17V until final failure occurs after 615 minutes.

The reason that there is a stark difference between the trends of the two different signal analysis techniques, RMS and peak to peak amplitude, is due to the occurrence of high amplitude transients within the wavestream. Demonstrating this, Figure 6-39 plots the raw wavestreams as recorded on Channels 1-4, 90 minutes into Run 5. The RMS values of the four channels are 0.1464, 0.3824, 0.3055 and 0.5128 respectively whereas the peak to peak amplitudes are 1.8338, 3.9935, 8.5922 and 16.6455 volts respectively. The disparity between the RMS and peak to peak values highlights the insensitivity of RMS to transient bursts when compared with peak to peak measures as previously shown in Figure 6-38.

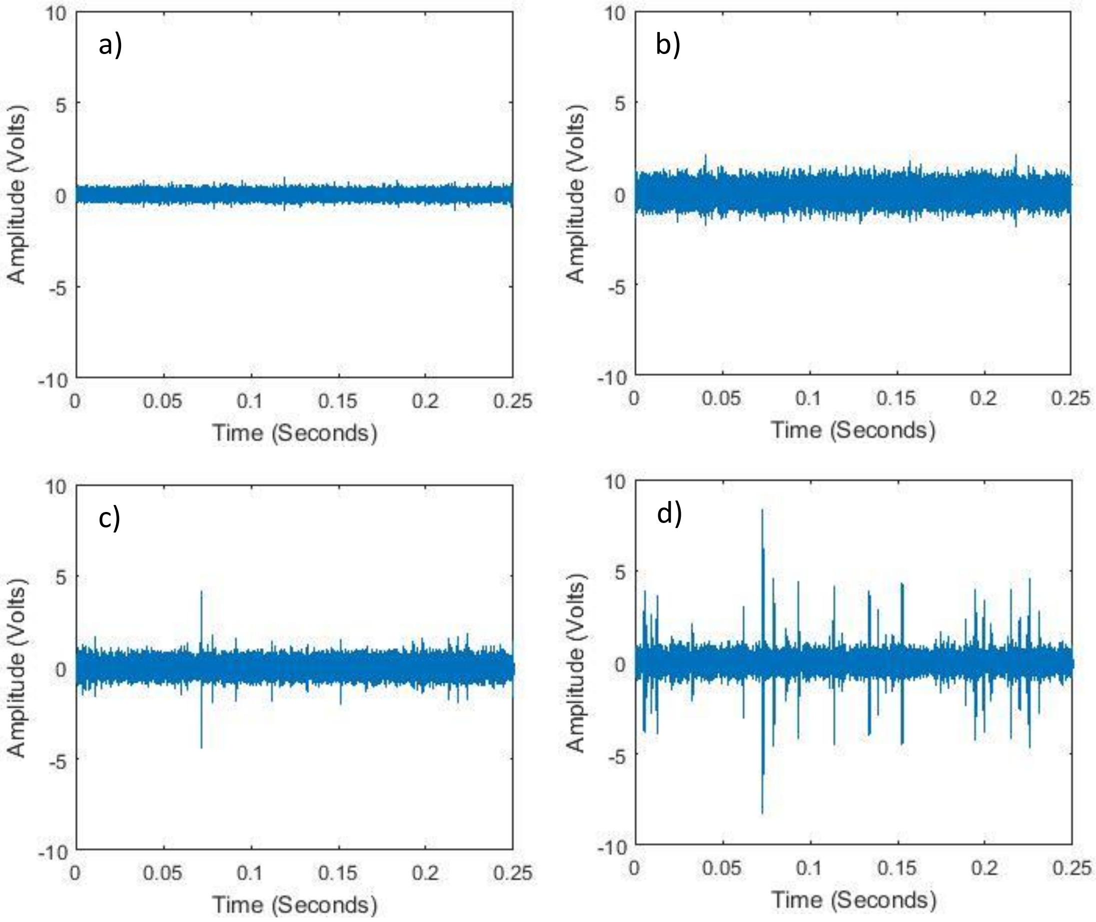

Figure 6-39 - Raw wavestreams 90 minutes into Run 5 as recorded on a) Channel 1, b) Channel 2, c) Channel 3 and d) Channel 4

The occurrence of the high amplitude transients which are present throughout the wavestreams recorded on Channel 3 and 4 during Run 5, indicates the possibility of crack growth within the gear tooth. Further evidence of this is demonstrated when investigating the rate at which the large transients occur. Unlike the ‘healthy’ data where transient bursts were produced at the characteristic bearing frequencies, visual analysis of Figure 6-39.d demonstrates that the majority of the transient bursts recorded at Channel 4, and in particular the higher amplitudes bursts, occur at the shaft frequency, 50Hz. This means that the transients are being produced as a single tooth is coming into contact and therefore it is deduced that this is likely to be when the 'damaged' tooth is coming into contact. Such a high amplitude transient burst is evidence of significant events occurring within the system. Without the prior knowledge of how the gear tooth failed however, it would be impossible to determine from the raw signal alone as AE can originate from a number of sources including friction, crack growth, pitting, rolling over of debris etc. (Kim *et al.,* 2009; Elforjani & Mba, 2009). The significance of these bursts however, is amplified further when taking into consideration the attenuation of 'healthy' signals through each of the support bearings as also commented on by Toutountzakis *et al.* (2005).

Figure 6-40.a-d plots the order spectrum of the wavestreams recorded through Run 5 for Channels 1-4 respectively. Unlike observations made previously in the order analysis of the healthy data, where the characteristic frequencies of the support bearings was clearly visible, it can be seen that the main excitation within Gear Pair 'A' and 'B' exists at 16 orders, the GMF of the two gears in contact. The amplitude of the GMF excitation for the sensors attached to Gear Pair 'A' remains relatively constant throughout the observation window however the amplitude of Gear Pair 'B' fluctuates throughout the experiment. The two channels connected to Gear Pair 'B' however do demonstrate excitation at the shaft frequency and its harmonics, i.e 1 order, 2 orders 3 orders etc., for the order analysis of the first wavestream recorded. Following this, the amplitude at these frequencies begins to reduce with a multitude of lower order frequencies also being excited. The variable manner in which low level orders are being excited may be an indication of sporadic transient bursts or a large number of reflections within the raw wavestreams, making it difficult to isolate frequencies at particular orders. The spread of frequencies excited within the order spectrum of wavestreams recorded on Channels 3 and 4 continues for the duration of Run 5. Although it is known that there was a catastrophic failure within this time period there exist no clear trends in the data collected from Gear Pair 'B'.

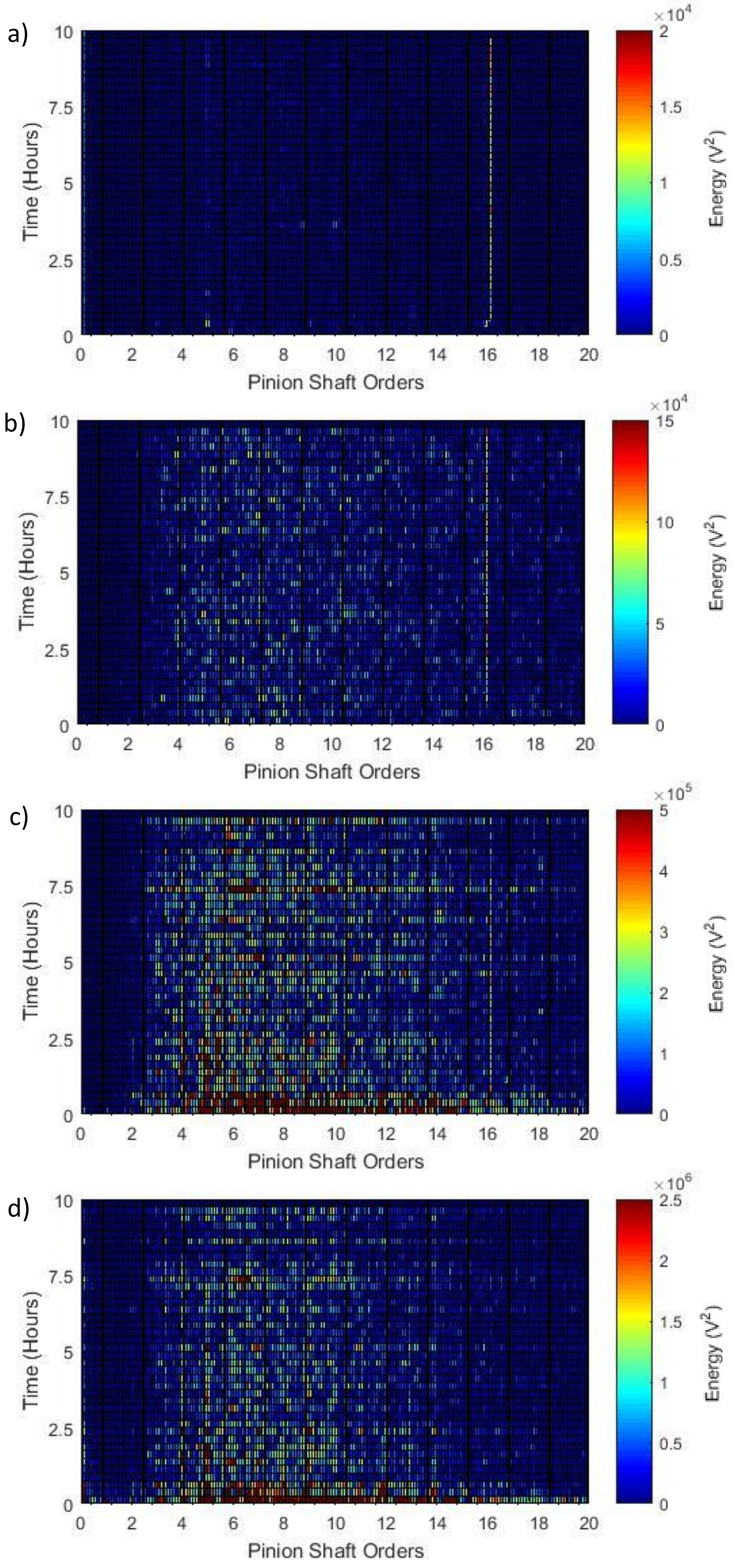

Figure 6-40 - Order Analysis of Run 5 a) Channel 1, b) Channel 2, c) Channel 3 and d) Channel 4

Figure 6-41 plots the binned frequency spectrum between 0-100kHz for the duration of Run 5 where designations (a) and (b) are the axially and radially mounted sensors of Gear Pair ‘A’, Channels 1 and 2 respectively, designations (c) and (d) refer to the axially and radially mounted sensors of Gear Pair ‘B’, Channels 3 and 4 respectively. Similar to the frequency spectrum of the ’healthy’ data recorded in Run 3 (Figure 6-26) the frequency bands excited by the axially and radially mounted sensors are similar for each gear pair, i.e. the response of Channel 1 is similar to Channel 3 and the response of Channel 2 is similar to Channel 4. For the two axially mounted sensors, Channels 1 and 3, there is clear excitation at 43kHz and 65kHz although the scale of the excitation energy in Channel 3 is an order of magnitude higher than that of Channel 1 and hence, there is a large disparity between the two gear pairs. For both Channel 1 and 3 there is an initial increase in energy amplitude and then the amplitude of Channel 1 reduces and remains constant throughout the remainder of the observation window. The energy amplitude of Channel 3 however reduces in over the duration of Run 5 even though it is known that the condition of the pinion gear was deteriorating.

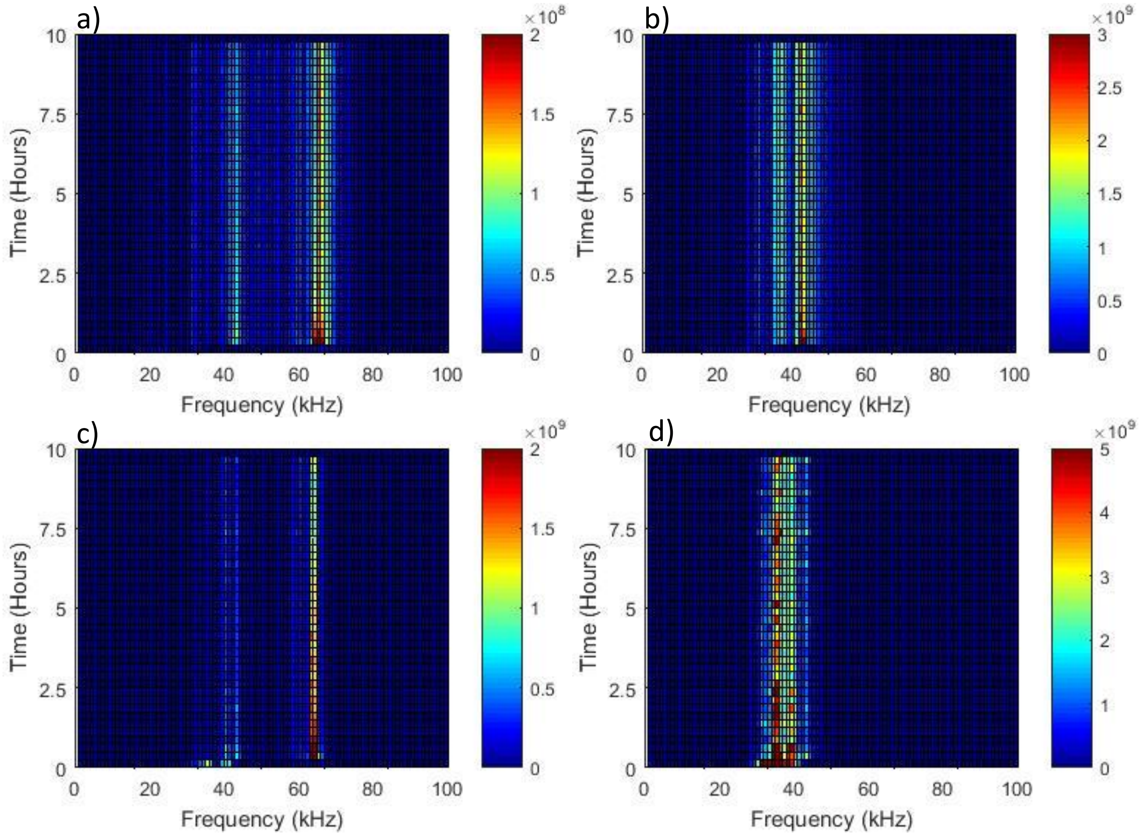

Figure 6-41 - Frequency between 0-100kHz for a) Channel 1, b) Channel 2, c) Channel 3 and d) Channel 4 for the duration of Run 5 –where the unit of the Z-axis scale is Energy (V^2)

This is similar to an observation made by Toutountzakis *et al.* (2005) who demonstrated that as the severity of a seeded defect on the tooth of a gear was increased, the RMS decreased in amplitude.

The radially mounted sensors, Channels 2 and 4, both show excitation at 36 and 43kHz, similar to the frequencies excited during Run 3. As with the axially mounted sensors, Channels 1 and 3, there is a large initial energy in both sensors which, for Channel 2 decreases in amplitude before maintaining a constant level throughout the remainder of the observation window. Channel 4 however, unlike the response of Channel 3, does not decrease over the duration of the test. There are instead frequent peaks of energy at 36kHz, occurring sporadically through the spectrum, coinciding with the fluctuations in amplitude of the peak to peak plot, Figure 6-38.

Figure 6-42 plots the frequency spectrum of the data recorded during Run 5 between 100-200kHz. As with the frequency spectrum plotted between 0-100kHz, there is similarity between the radial sensors as well as the axial sensors. All four channels demonstrate excitation at 150kHz and Channels 1, 2 and 4 also exhibit further excitation at 108kHz. Unlike when the spectral data was analysed between 0-100kHz, there are no further peaks of energy for the duration of Channel 4. Instead, the amplitude of the energy remains relatively constant throughout the plot. Pullin *et al.* (2012) demonstrated that as a crack propagated in the gear tooth root during a static gear test, there was an increase in spectral energy between 110-120kHz. Apart from the initial increase in spectral energy during the analysis of first wavestream, there are no further increases in spectral energy within the window. In the spectral analysis of the wavestreams recorded during the tooth root crack propagation by Pullin *et al.* (2012), it was shown that following the initiation of the crack the spectral energy decreases even though the tooth was still being cyclically loaded. It is considered that, as previously hypothesised, the initiation of damage in Run 5 may have occurred on the first few rotations of the gear on flank B, briefly increasing the spectral energy before reducing in amplitude. The sensors used in the test conducted by Pullin *et al.* (2012) were also mounted to the face of the gear. It has been shown in the previous chapters that AE undergoes severe attenuation when having to pass through multiple boundaries and, in this case, there is thought to be increased attenuation as the rolling elements of the bearing supporting the gear shaft are running directly on the shaft.

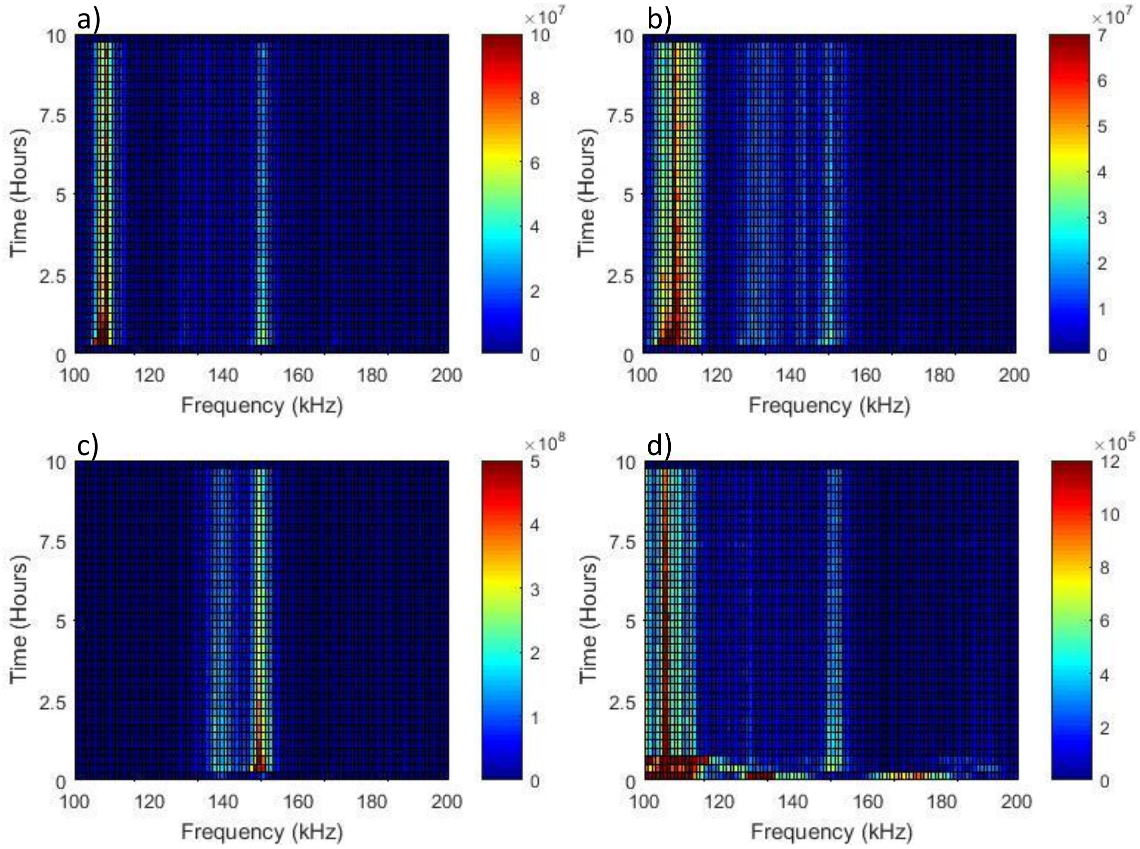

Figure 6-42 - Frequency between 100-200kHz for a) Channel 1, b) Channel 2, c) Channel 3 and d) Channel 4 for the duration of Run 5 – where the unit of the Z-axis scale is Energy (V^2)

Further evidence of the existence of a large amount of spectral energy in the initial stages of Run 5 can be seen when analysing the wavestreams between 200-500kHz (Figure 6-43). Whereas Channels 1 and 2, the axial and radial sensors connected to Gear Pair ‘A’, are excited at a relatively constant amplitude at 220, 245, 275 and 365kHz throughout the duration of Run 5, the amplitude of the energy excited in the spectral analysis of channels 3 and 4 is high initially before decreasing over the remainder of the observation window.

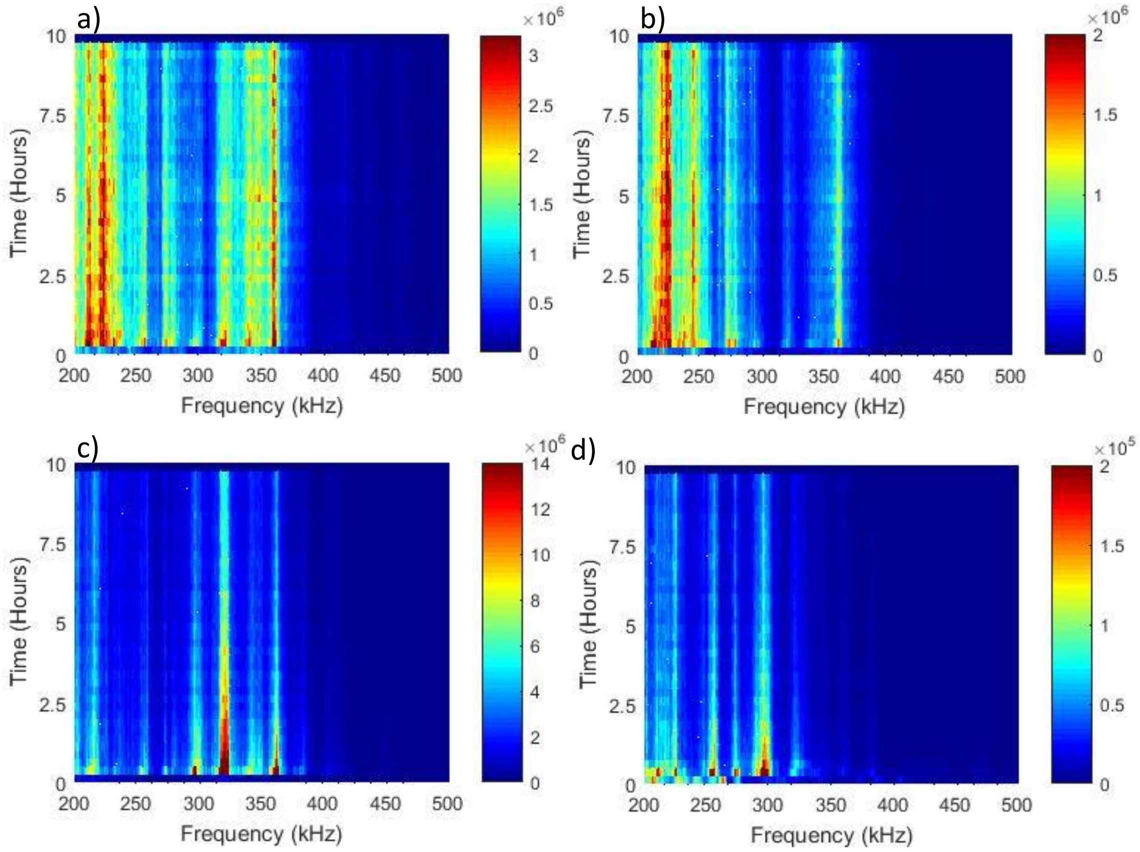

Figure 6-43 - Frequency between 200-500kHz for a) Channel 1, b) Channel 2, c) Channel 3 and d) Channel 4 for the duration of Run 5 – where the unit of the Z-axis scale is Energy (V^2)

6.5 Conclusion

Through the characterisation of the healthy AE wavestreams, it has been seen that AE energy in the wavestreams recorded in the running of helical gears increases in amplitude as the rotational velocity is increased. For a single gear pair however it has been shown that disproportionate increases in amplitudes occur, for short durations for a single speed increase, 1500rpm in this case. This phenomenon occurs only for this gear pair and it is not visible in the gear pair operated opposite or in subsequently tested gear pairs. It has also been shown that, for this test set-up, the direction of the gears seems to have an impact on the AE energy amplitude when the torque is increased. For two gear pairs operating back to back, it was seen that as the torque was increased, the amplitude of one gear pair would increase whereas the amplitude of the other gear pair would decrease. Again, the true origin/cause of this occurrence is also unknown.

This chapter has successfully demonstrated the difficulty in monitoring the condition of gears running dynamically on a test rig that has not been specifically designed for the acquisition of AE data. For the healthy analysis of gears, it was shown the GMF was difficult to detect through order analysis although previous authors have been able to successfully demonstrate that the GMF is readily available in the wavestreams recorded by them, even when monitored through a support bearing (Toutountzakis *et al.* 2005). It is thought that this is due to the gear design as well as the distance from the bearing to the outside of the bearing case. It was shown by Raja Hamzah and Mba (2009) that the amplitude of bursts at the GMF reduced significantly when comparing the response of spur gears and helical gears due to the gentler introduction of the gears to mesh in the helical pairs. Coupled with the signal having to travel down a long shaft and into a full complement roller support bearing, it is easy to see that the signals may become easily modulated and lost in the general noise floor of the signal recorded.

The detection of damage has been successful overall as both vibration and AE increased in amplitude once the tooth had sheared completely. The forensic diagnosis however has proven to be inconclusive as it was not possible to generate any growing trends within the data. Instead, it is shown that when transitioning from the ‘healthy’ gear pair used in Runs 1-3, to the ‘damaged’ gear pair, Runs 4 &5, there is an immediate difference in the amplitude of the signals produced. This is mirrored in the RMS amplitude of the vibration signal but it is shown that the AE analysis was highly sensitive to the increase, particularly when analysing the increase in peak to peak values of the raw wavestreams, essentially measuring where high amplitude transients occurred. Using the peak to peak measure also demonstrated the insensitivity of RMS to sporadic transient bursts. When analysing the bearings in previous chapters, the transients produced were continuous throughout the period at which they were being recorded, increasing the RMS respectively. With the gear failure, however, the transients occurred far more sporadically as it is thought that the crack was growing.

Also in contrast to the analysis of bearings in Chapter 4 is the trend witnessed in the frequency plots. Whereas in the frequency analysis of bearings the increase in damage was matched by an increase in frequency amplitude, for the gear tooth failure, the amplitude decreased as the gear tooth tended towards failure. This is in contrast to initial observations made by Pullin *et al.* (2012) but in agreeance with Toutountzakis *et al.* (2005). Although not discussed in the work by Pullin *et al.* (2012), following the initiation of the crack and an increase in spectral energy, the energy decreases although the gear tooth was still being cyclically loaded and hence this would agree with findings in this research as well as work by Toutountzakis *et al.* (2005). It is thought that this is due to the crack reaching a size where, under the loading conditions, the crack face can open without increasing the strain energy at the crack tip. Due to a second tooth coming into contact after a small displacement of the cracked tooth, the load witnessed by the 'damaged' tooth is reduced. Helical gears would be more sensitive to premature engagement of a successive tooth due to having both a transverse contact ratio as well as a helical contact ratio, increasing the number of teeth in contact at any one point. The complexity of the transmission path may also be responsible for the decreased sensitivity to damage as even though Toutountzakis *et al.* (2005) measured the response through a support bearing, the sensor was placed very close to the outer raceway of said bearing. This test placed the sensor on a bearing housing, relatively far away from the outer raceway of the bearing.

As well as the damage detection, this chapter has also highlighted the occurrence of noise in signals when monitoring rotating machinery. The origin of the extraneous noise is unknown and it seems to affect not only the AE recording but also the vibration and parametric data also being recorded. Data like this is often unreported and discarded as it contains information that is of little use to the operator although it is highly important in the development of condition monitoring systems and the damage detection algorithms employed to determine changes in the signals. Noise like this may produce false positives when in the field, potentially causing unnecessary shutdown and increased expenditure.

7 Discussion, Conclusion and Future Work

7.1 Discussion

The supporting chapters have demonstrated that the sensitivity of the AE technique for rotating machinery depends heavily on test set up and the complexity of the system over all. For a small, high speed bearing it was shown that there existed a large difference between the ability to detect seeded defects and damage that was allowed to propagate naturally. The sensors were for this test, although placed on the bearing housing, were in close proximity to the AE source in a similar set up to the work carried out by Al-Dossary *et al.* (2009), Choudhury and Tandon (2000) and Al-Ghamd and Mba (2006). For a similar set up, albeit on a much larger scale, it became apparent that the increased size meant that the sensors would have to be placed further from the source of damage although AE was still able to detect the flaking fatigue of the drive shaft surface. When transferring to a gear test of relatively high complexity, it was not possible to determine any trends within the data leading up to the final failure. Previous researchers have demonstrated the ability to detect gear tooth crack and the pitting wear of bearing surfaces, however much of these observations are made on simplified test rigs, where the sensors are generally placed in close proximity to the source, i.e. on the gear face (Pullin *et al.* 2012; Toutountzakis *et al.* 2005). In real world applications, it is rarely possible for the sensor to be placed so close to the source of damage as it is often unknown which component is likely to fail first.

For the tests where the overall objective was to degrade the component over an extended period of time, the experimental conditions remained relatively constant with little fluctuation in both the speed and load applied. In a practical application, however, the operating conditions fluctuate continuously. A wind turbine, for example, is a highly complex machine whose operating conditions are anything but constant. Powered by a natural, uncontrollable force, the system continually changes its rotational speed and generator torque, as well as experiencing fluctuations in the axial and radial loads applied to each of the components. Coupled with the environmental conditions that a wind turbine has to also endure, it is foreseen that it will be extremely difficult to determine relationships between the continuous AE produced and the multitude of variables contributing to the production of the AE signal.

The gear test rig was the most complex rig investigated in this investigation, with a number of rotating components influencing the signal produced as well as a number of electronic and hydraulic circuits required to operate and control the test rig. Although much less complex than a wind turbine, it was still difficult to determine, with confidence, the cause of noise in the wavestreams and parametric data even though the rig was operating under relatively controlled conditions. Therefore, to deploy AE as a technology to replace vibration within a turbine, a significant amount of data collection and analysis is required in order to be able to demonstrate further understanding as well as developing confidence in the reliability and accuracy of the technology as a whole.

It is also worthwhile to note that there commonly exist a large number of rotating components within a single piece of machinery and as advancements in technology are made, the number is unlikely to reduce. The gear test rig in Newcastle University was generally quite complex relative to much of the test rigs investigated in the literature and, although it was possible to detect that there was a change in the running condition, the damage had become relatively severe before it had become possible to be detected with confidence. Escalating the application of AE to a multi-geared transmission will be difficult and the reliance on the characteristic frequencies will be diminished if the transmission being monitored has a number of the same components, for example, the planet gears of a simple epicyclic are all of the same design and will have the same bearings. It is also common for bearings to be coupled together and used multiple times within a transmission and although it may be possible to detect damage globally, the actual location of the damage may not be so easy to determine.

The most significant findings within the thesis have relied on the increase in RMS trends as well as the periodicity of transient bursts within AE signals. Direct comparison between AE and vibration has been carried out, demonstrating that in general, they are on an equal level to each other with data analysis techniques used. Data analysis techniques more suited to the analysis of AE are available but they often require extensive knowledge of the signal properties as well as what information is to be extracted from the raw signal. Unlike vibration, AE can be used to determine high frequency emission from the damage and, although it may not be fully understood, this may prove useful in future work due to the burst content. The sampling frequency of the vibration sensors means that it can be difficult to determine characteristic frequencies of bearings as well as gears however, with the application of more advanced filtering and analysis techniques, it may be possible to extract the periodic high frequency bursts present within AE analysis.

Repeatability between individual tests has proven to be an issue within the work carried out within this thesis. Through the comparison of wavestreams recorded from healthy bearings it was demonstrated that the response can change due to the decoupling and recoupling of sensors combined with the disassembly and reassembly of the test rig. Future work should look to have dedicated sensors and sensor locations as well as a more robust technique of determining coupling quality. Where at all possible, the sensors should remain bonded to the system and a reference excitation should be used to track any degradation of coupling quality over time. Better still, if designers of condition critical systems were able to incorporate sensors or sensor locations into their designs, information of system condition would be readily available. Also, although the data rate and processing power is relatively high, it may even be possible to apply the AE technique to instrumented bearings such as those being developed by SKF in a project called SKF Insight^{TM} (SKF 2017b). SKF Insight^{TM} integrates sensors into the design of the bearing, able to wirelessly transmit information about bearing speed, temperature, vibration and load and, although the technology is still in it's infancy, it has already been implemented in rail systems to good effect (SKF 2017a). Although there will still be an issue of trying to determine if the damage was from a gear or bearing, the confidence in detection would be increased by reducing the number of other possible sources.

An area which needs more investigation when detecting incipient failure is the knowledge surrounding the determination of the damage location. With the analysis of vibration data, the periodic bursts produced by the over rolling of large defects are used to determine location with confidence. With incipient damage, however, it is not possible that transient bursts will always be produced when the defect is rolled over. Within this thesis, what was thought to be the detection of an inner race defect for the wind turbine bearing turned out to be flaking of the shaft and, although the gear tooth was cracking over a period of time, the rate of AE bursts did not suggest this with confidence.

7.2 Conclusions

7.2.1 AE Generation

The work presented in this thesis has demonstrated that the continuous wavestreams recorded when monitoring rotating machinery using AE, are highly sensitive to an increase in speed with all analysis techniques used showing an increase in amplitude as the speed is increased. The effect of load is less conclusive and it has been shown that for the same test set up, statistical AE analysis parameters have been shown to increase and decrease with an increase in load applied. Frequency analysis was used to demonstrate that the continuous AE wavestreams were formed of frequencies unique to the system under investigation, thought to be the resonant frequencies of the system. Frequency analysis indicated also indicated that the frequency of excitation changed with increase in load and not speed, demonstrating that the frequency of the signal changed as the stiffness of the system was altered.

Order analysis was also used to demonstrate that the signals within the wavestreams were producing bursts of transients at periodic intervals equal to that of the characteristic frequencies of rotating bodies interacting with each other, i.e. Characteristic Bearing frequencies and gear mesh frequencies. These characteristics frequencies are widely used in the application of vibrational monitoring and it was shown that AE is able to determine the same frequencies despite having higher operating frequency ranges.

A large, full complement bearing was investigated and it was found that for parts of the signals observed, that an event referred to as roller slap is responsible for the generation of transient bursts, as two rollers ‘fall’ into each other as they rotate across the highest part of the arc.

There was a brief investigation into the mechanics of AE generation and the effect of the lubrication regime, or Lambda ratio, was found to have little effect on the generation of AE with no discernible differences visible between a bearing operating with boundary lubrication and EHL.

Healthy bearing characterisation was beneficial in determining a benchmark for comparison however the sensitivity of AE was highlighted as different characteristics were determined for two experiments set up at different times but using the same sensors and locations.

7.2.2 Damage Detection

The response of three different systems was investigated and it was shown that AE was able to successfully detect damage in each of them. The sensitivity of AE to the severity of the damage however differed from test to test.

Seeded defects placed on the outer raceway of a cylindrical roller highly exaggerated the sensitivity of AE, demonstrating an increase in RMS of a wavestream in the presence of an engraved defect of 0.4 x 0.6mm. It was discussed that it was possible that the heightened sensitivity was due to the sensitivity of AE to test set up and, through the disassembly and assembly, it is possible that the RMS was artificially increased.

Life tests on bearings, with the same specification to that used in the seeded defect analysis, demonstrated that although RMS increased with increased damage, the level of damage witnessed was far greater than the damage detected in the seeded defect test. The first life test, the more aggressive of the two, demonstrated a step change between two signals recorded 15 minutes apart and on inspection following the test, both the inner and outer race had degraded significantly. The second life test degraded the bearing in a far more controlled manner and the test rig was stopped soon after an increase in signal level was witnessed. The damage was confined to that of a single roller however the defect spread across the entire length of the roller.

During the application of AE to a large bearing operating under high radial loads, it was though that due to the detection of the BPFI, including growth at this frequency over time, that the bearing had failed on the inner raceway. On further inspection, however, it was found that the inner raceway itself was relatively undamaged and instead the presence of AE bursts was due to the surface fatigue of the main shaft. This observation highlighted that although AE is sensitive enough to detect damage far away from a sensor, where the signal has to travel through multiple components boundaries, it is not possible with the data analysis techniques used to identify with confidence the true source of AE.

It was also shown through the study of a back to back gear test rig, although the initial condition of a component may be known, it is not possible to determine with accuracy if that particular component is healthy or damaged without producing an extensive catalogue of information regarding a particular product. Although AE was able to successfully detect the point where a gear tooth failed and became detached from the gear body, there was little indication during the run up procedure that failure was imminent.

7.2.3 Closing Comment

The critical analysis of the surrounding literature coupled with experimental works carried out within this thesis has increased the confidence of the author that AE is capable of successfully detecting damage with rotating machinery. Although it is clear that further research is required within this field, an AE wavestream contains far more information within it than when compared to the information content within a vibrational signal. Tapping into and developing further understanding of this information will help to improve the condition monitoring of rotating machinery as a whole. This thesis has contributed to the community responsible for developing this understanding through healthy bearing characterisation, seeded and natural defect detection as well as applying AE to further test rigs that are more akin to real world scenarios.

7.3 Future Work

An extensive database of wavestreams has been generated and further work is required to develop techniques that will further the understanding and knowledge of the information contained within the signals. Advanced data analysis techniques such as Empirical Mode Decomposition, Wavelet Transforms, and Chebychev analysis have already been investigated by other authors in the analysis of seeded bearing defects, demonstrating potential when trying to moving away from vibration analysis techniques in order to apply AE data analysis techniques (Qiu *et al.* 2003; Qiu *et al.* 2006; Hao *et al.* 2009; Abbasion *et al.* 2007; Dybała & Zimroz 2014; Huang *et al.* 1998; Tsolis & Xenos

2011; Rai & Mohanty 2007). This data analysis should not only focus on the test bearing but also the data recorded at each of the support bearings during the high-speed testing. The analysis of this data was out of the scope of this thesis however, when expanding the technology, it is not always going to be possible to monitor so close to the test bearing and indications were shown in the vibration spectrum of the aggressive life test that as the system deteriorates, it is possible to detect damage through other bearings. Although there exists a broad data set to begin with, further testing needs to be conducted with a greater focus aimed at being able to run long life tests but also being able to check the condition of the bearing periodically to determine when the damage initiation truly starts. To do this, it is suggested that larger bearings are investigated, allowing for an endoscope to be used to check the condition of the rollers and raceways without the need to disassemble and reassemble the test rig each time. A large number of life tests should be carried out using the same specification of bearing as well as changing the size and type of bearing, ball bearing or journal bearing for example. If it is not possible to increase the size of the test bearing to allow for the use of an endoscope, the test rig should be modified to allow for the test bearing to become over-slung to allow for the test bearing and its housing to be removed without disturbing the support bearings. If this is possible, it is vital that the support bearing signals are monitored and analysed alongside the analysis of the test bearing data. This is because by moving the test bearing from in between two support bearings, the load on the support bearing in the centre increase significantly, and combined with an increased level of misalignment, the likelihood of damage initiation increases.

As well as changing the size of the bearing and the ability to inspect the raceways without disassembly, it is a worthwhile investment to apply AE sensors to in service rotating machinery, of varying complexity, in order to further the understanding of how varied operating conditions affect the generation of AE overall. In a laboratory environment, AE and vibration techniques have both demonstrated that it is possible to detect damage but, without the application of AE to real equipment, such as wind turbines, drill bearings, wheel bearings, transmission units etc. it is not possible to determine concrete links between research and the commercial world.

It is also recommended that further investigation into the effect of lubrication as well as the AE generated by friction, sliding/rolling is carried out. One way to continue to test the effect of Lambda ratio is, for a healthy bearing, run the test rig for a predetermined number of hours with a speed, load, oil viscosity and oil temperature that in combination produce EHL. Continue then, for the same bearing to change only the oil viscosity and temperature, hence changing the Lambda ratio to change the lubrication regime from EHL to boundary /mixed lubrication regimes.

8 References

Abbasion, S. et al., 2007. Rolling element bearings multi-fault classification based on the wavelet denoising and support vector machine. *Mechanical Systems and Signal Processing*, 21(7), pp.2933–2945.

Al-Dossary, S., Hamzah, R.I.R. & Mba, D., 2009. Observations of changes in acoustic emission waveform for varying seeded defect sizes in a rolling element bearing. *Applied Acoustics*, 70(1), pp.58–81.

Al-Ghamd, A.M. & Mba, D., 2006. A comparative experimental study on the use of acoustic emission and vibration analysis for bearing defect identification and estimation of defect size. *Mechanical Systems and Signal Processing*, 20(7), pp.1537–1571.

ASTM, 2010. *A standard guide for determining the reproducibility of acoustic emission sensor response*,

ASTM E1313-17, 2017. ASTM E1313-1: Standard Terminology for Nondestructive Examinations.

Badgujar, M. & Patil, A., 2014. Fault Diagnosis of Roller Bearing Using Acoustic Emission Technique and Fuzzy Logic. *ijltet.org*, 3(4), pp.170–175.

Bashir, I., Bannister, R. & Probert, D., 1999. Release of acoustic energy during the fatiguing of a rolling-element bearing. *Applied Energy*, 62(3), pp.97–111.

Boness, R.J. & McBride, S.L., 1991. Adhesive and abrasive wear studies using acoustic emission techniques. *Wear*, 149(1–2), pp.41–53.

Boness, R.J., McBride, S.L. & Sobczyk, M., 1990. Wear studies using acoustic emission techniques. *Tribology International*, 23(5), pp.291–295.

Bruce, T. et al., 2015. Characterisation of white etching crack damage in wind turbine gearbox bearings. *Wear*, 338–339, pp.164–177.

Chang, H. et al., 2009. Acoustic emission study of fatigue crack closure of physical short and long cracks for aluminum alloy LY12CZ. *International Journal of Fatigue*, 31(3), pp.403–407.

Choudhury, A. & Tandon, N., 2000. Application of Acoustic Emission Technique for the Detection of Defects in Rolling Element Bearings. *Tribology International*.

Colombo, S. et al., 2005. Frequency response of different couplant materials for mounting transducers. *NDT and E International*, 38(3), pp.187–193.

Couturier, J. & Mba, D., 2008. Operational Bearing Parameters and Acoustic Emission Generation. *Journal of Vibration and Acoustics*, 130(2), p.24502.

Doll, G.L. & Kotzalas, M.N., 2010. *Wear-Resistant Bearings*,

Dybała, J. & Zimroz, R., 2014. Rolling bearing diagnosing method based on Empirical Mode Decomposition of machine vibration signal. *Applied Acoustics*, 77, pp.195–203.

Eftekharnejad, B. & Mba, D., 2009. Seeded fault detection on helical gears with acoustic emission. *Applied Acoustics*, 70(4), pp.547–555.

Elasha, F. et al., 2015. Application of Acoustic Emission in Diagnostic of Bearing Faults within a Helicopter Gearbox. *Procedia CIRP*, 38, pp.30–36.

Elforjani, M. & Mba, D., 2010. Accelerated natural fault diagnosis in slow speed bearings with Acoustic Emission. *Engineering Fracture Mechanics*, 77(1), pp.112–127.

Elforjani, M. & Mba, D., 2009. Detecting natural crack initiation and growth in slow speed shafts with the Acoustic Emission technology. *Engineering Failure Analysis*, 16(7), pp.2121–2129.

Elforjani, M. & Mba, D., 2008. Monitoring the Onset and Propagation of Natural Degradation Process in a Slow Speed Rolling Element Bearing With Acoustic Emission. *Journal of Vibration and Acoustics*, 130(4), p.41013.

Feng, Z., Liang, M. & Chu, F., 2013. Recent advances in time–frequency analysis methods for machinery fault diagnosis: A review with application examples. *Mechanical Systems and Signal Processing*, 38(1), pp.165–205.

Ferrer, C. et al., 2010. Discrete acoustic emission waves during stick–slip friction between steel samples. *Tribology International*, 43(1–2), pp.1–6.

Finlayson, R., Friesel, M. & Carlos, M., 2001. Health monitoring of aerospace structures with acoustic emission and acousto-ultrasonics. *INSIGHT-WIGSTON …*, 43(3), pp.1–4.

Fitch, J., 2003. Silent Assumptions of Bearing Reliability. *Practicing Oil Analysis*. Available at: http://machinerylubrication.com/Read/495/bearing-reliability.

Fuentes, R. et al., 2016. Observations on Acoustic Emissions from a Line Contact Compressed into the Plastic Region. *Proceedings of the Institution of Mechanical Engineers, Part J: Journal of Engineering Tribology*.

García Márquez, F.P. et al., 2012. Condition monitoring of wind turbines: Techniques and methods. *Renewable Energy*, 46, pp.169–178.

Graney, B. & Starry, K., 2012. Rolling Element Bearing Analysis. *Materials Evaluation*, 70(1), pp.78–85.

Halme, J. & Andersson, P., 2010. Rolling contact fatigue and wear fundamentals for rolling bearing diagnostics – state of the art. *Proceedings of the Institution of Mechanical Engineers, Part J: Journal of Engineering Tribology*, 224(4), pp.377–393.

Hao, R., Feng, Z. & Chu, F., 2009. Defects diagnosis of bearing by means of acoustic emission and continuous wavelet transform. *Key Engineering Materials*, 414, pp.651–657.

Harris, T.A. & Kotzalas, M.N., 2006. *Essential Concepts of Bearing Technology, Fifth Edition*, CRC Press.

Hase, A., Mishina, H. & Wada, M., 2012. Correlation between features of acoustic emission signals and mechanical wear mechanisms. *Wear*, 292–293, pp.144–150.

Hawman, M.W. & Galinaitis, W.S., 1988. Acoustic emission monitoring of rolling element bearings. In *IEEE 1988 Ultrasonics Symposium Proceedings.* IEEE, pp. 885–889.

He, Y., Zhang, X. & Friswell, M.I., 2009. Defect Diagnosis for Rolling Element Bearings Using Acoustic Emission. *Journal of Vibration and Acoustics*, 131(6), p.61012.

Hellier, C.J., 2012. *Handbook of Nondestructive Evaluation*, McGraw-Hill.

Ho, D. & Randall, R.B., 2000. OPTIMISATION OF BEARING DIAGNOSTIC TECHNIQUES USING SIMULATED AND ACTUAL BEARING FAULT SIGNALS. *Mechanical Systems and Signal Processing*, 14(5), pp.763–788.

Howard, I., 1994. A Review of Rolling Element Bearing Vibration "Detection, Diagnosis and Prognosis." *DEFENCE SCIENCE AND TECHNOLOGY ORGANIZATION CANBERRA (AUSTRALIA)*, No. DSTO-R.

Hsu, N. & Breckenridge, F., 1981. Characterization and Calibration of Acoustic Emission Sensors. *Material Evaluation*, 39(1), pp.60–68.

Huang, N.E. et al., 1998. The empirical mode decomposition and the Hilbert spectrum for nonlinear and non-stationary time series analysis. *Proceedings of the Royal Society A: Mathematical, Physical and Engineering Sciences*, 454(1971), pp.903–995.

ISO 281, 1990. Rolling bearings -- Dynamic load ratings and rating life. Available at: https://www.iso.org/standard/4193.html.

ISO 281, 2007. Rolling bearings -- Dynamic load ratings and rating life. Available at: https://www.iso.org/standard/38102.html

ISO 683-17, 2014. Heat-treated steels, alloy steels and free-cutting steels -- Part 17: Ball and roller bearing steels. Available at: https://www.iso.org/standard/57231.html

Jeevagan, N. et al., 2014. Project Stay Alert. In *IEEE Global Humanitarian Technology Conference (GHTC 2014)*. IEEE, pp. 711–715.

Johnson, K.L., 1987. *Contact Mechanics*,

Kim, E.Y. et al., 2009. DEVELOPMENT OF AN ONLINE CONDITION MONITORING SYSTEM FOR SLOW SPEED MACHINERY.

Kuboyama, K., 1986. Development of low speed bearing diagnosis technique. *Detection, Diagnosis and Prognosis of Rotating Machinery to Improve Reliability, Maintainability, and Readiness Through the Application of New and Innovative Techniques*, pp.178–185.

Lees, a W. et al., 2011. The use of acoustic emission for bearing condition monitoring. *Journal of Physics: Conference Series*, 305, p.12074.

Li, C.J. & Li, S., 1995. Acoustic emission analysis for bearing condition monitoring. *Wear*, 185, pp.67–74.

Liu, X., Wu, X. & Liu, C., 2011. A comparison of acoustic emission and vibration on bearing fault detection. *Proceedings 2011 International Conference on Transportation, Mechanical, and Electrical Engineering (TMEE)*, pp.922–926.

Lundberg, G. & Palmgren, A., 1947. Dynamic Capacity of Rolling Bearings. *Ada Polytechnica, Mechanical Engineering Series 2, Royal Swedish Academy of Engineering Sciences*, 3(7).

Mba, D. & Rao, R., 2006. Development of Acoustic Emission Technology for Condition Monitoring and Diagnosis of Rotating Machines; Bearings, Pumps, Gearboxes, Engines and Rotating. *The Shock and Vibration Digest*, 38(1), pp.3–16.

McFadden, P.D. & Smith, J.D., 1984. Acoustic emission transducers for the vibration monitoring of bearings at low speeds. *ARCHIVE: Proceedings of the Institution of Mechanical Engineers, Part C: Mechanical Engineering Science 1983-1988 (vols 197-202)*, 198(8), pp.127–130.

Miettinen, J. & Pataniitty, P., 1999. Acoustic emission in monitoring extremely slowly rotating rolling bearing. *… congress on condition monitoring and …*, pp.289–297.

Monavar, H., Ahmadi, H. & Mohtasebi, S., 2008. Prediction of defects in roller bearings using vibration signal analysis. *World Applied Sciences Journal*, 4(336), pp.150–154.

Morhain, A. & Mba, D., 2003. Bearing defect diagnosis and acoustic emission. *Proceedings of the Institution of Mechanical Engineers, Part J: Journal of Engineering Tribology*, 217(4), pp.257–272.

National Instruments, 2015. Function Libraries - DIAdem 2015 Help - National Instruments. Available at: http://zone.ni.com/reference/en-XX/help/370858M-01/concepts/diadem_4_10/

Naumann, J.R., 2016. *Acoustic emission monitoring of wind turbine blades*. University of Sheffield.

Neale, M.J., 1995. *Component Failures, Maintenance and Repair: Tribology Handbook*, Butterworth-Heinemann Ltd.

Nienhaus, K. et al., 2012. Development of Acoustic Emission (AE) based defect parameters for slow rotating roller bearings. *Journal of Physics: Conference Series*, 364, p.12034.

Nilsson, J. & Bertling, L., 2007. Maintenance Management of Wind Power Systems Using Condition Monitoring Systems—Life Cycle Cost Analysis for Two Case Studies. *IEEE TRANSACTIONS ON ENERGY CONVERSION*, 22(1).

Novoa, A.B. & Vicuna, C.M., 2013. New Aspects Concerning the Generation of Acoustic Emissions (AE) in Spur Gears and the Influence of Operating Conditions. In *Surveillance 7 International Conference*.

NSK, 2009. New Bearing Doctor - Maintenance of Bearings. Available at: http://www.nskamericas.com/cps/rde/dtr/na_en/EN-New_Bearing_Doctor.pdf

NSK, 2017. Protect your bearing investment. *A PUBLICATION OF NSK AMERICAS*. Available at: http://www.nskamericas.com/cps/rde/dtr/na_es/na_literature_bearing/06_TechTalk__Protect_bearing_investment.pdf

Orhan, S., Aktürk, N. & Çelik, V., 2006. Vibration monitoring for defect diagnosis of rolling element bearings as a predictive maintenance tool: Comprehensive case studies. *NDT & E International*, 39(4), pp.293–298.

Physical Acoustics, 2017a. ACMwt^{TM} – Asset Condition Monitoring for Wind Turbines - Acoustic Emission Systems and NDT Products by PHYSICAL ACOUSTICS. Available at: http://www.physicalacoustics.com/by-product/acmwt

Physical Acoustics, 2017b. PCI-2 – PCI-Based Two-Channel AE Board & System, by Physical Acoustics. Available at: http://www.physicalacoustics.com/by-product/pci-2/

Price, E.D., Lees, A.W. & Friswell, M.I., 2005. Detection of severe sliding and pitting fatigue wear regimes through the use of broadband acoustic emission. *Journal of Engineering Tribology*, 219(Part J), pp.85–98.

Pullin, R. et al., 2012. Identification of the Onset of Cracking in Gear Teeth Using Acoustic Emission. *Journal of Physics: Conference Series*, 382(1), p.12050.

Qiu, H. et al., 2003. Robust performance degradation assessment methods for enhanced rolling element bearing prognostics. *Advanced Engineering Informatics*, 17(3–4), pp.127–140.

Qiu, H. et al., 2006. Wavelet filter-based weak signature detection method and its application on rolling element bearing prognostics. *Journal of Sound and Vibration*, 289(4–5), pp.1066–1090.

Raharjo, P. et al., 2011. An Investigation of Acoustic Emission Responses of a Self Aligning Spherical Journal Bearing. *University of Huddersfield Repository*.

Rai, V.K. & Mohanty, a. R., 2007. Bearing fault diagnosis using FFT of intrinsic mode functions in Hilbert–Huang transform. *Mechanical Systems and Signal Processing*, 21(6), pp.2607–2615.

Raja Hamzah, R.I. & Mba, D., 2009. The influence of operating condition on acoustic emission (AE) generation during meshing of helical and spur gear. *Tribology International*, 42(1), pp.3–14.

Ramadan, S. et al., 2008. Detection of stress corrosion cracking of high-strength steel used in prestressed concrete structures by acoustic emission technique. *Applied Surface Science*, 254(8), pp.2255–2261.

Rao, V. et al., 2013. Study of fault in outer race of Roller Bearings using Acoustic emission and Vibration analysis. In *Advances In Modelling And Analysis Of Aerodynamic Systems*. pp. 62–66.

Rindorf, H., 1981. *Acoustic Emission Source Location In Theory and In Practice*,

Rogers, L.M., 1979. The application of vibration signature analysis and acoustic emission source location to on-line condition monitoring of anti-friction bearings. *Tribology International*, 12(2), pp.51–58.

Sandoval, H., Pedraza Ramirez, C.A. & Quiroga Mendez, J.E., 2013. Acoustic emission-based early fault detection in tapered roller bearings. *Revista Ingeniería e …*, 33(3), pp.5–10.

Serrato, R., Maru, M.M. & Padovese, L.R., 2007. Effect of lubricant viscosity grade on mechanical vibration of roller bearings. *Tribology International*, 40(8), pp.1270–1275.

Shiroishi, J. et al., 1997. Bearing condition diagnostics via vibration and acoustic emission measurements. *Mechanical systems and …*, 11, pp.693–705.

Singh, A., Houser, D.R. & Vijayakar, S., 1999. Detecting Gear Tooth Breakage Using Acoustic Emission: a Feasibility and Sensor Placement Study. *Journal of Mechanical Design*, 121(4), p.587.

SKF, 2016. Basic design bearings. Available at: http://www.skf.com/uk/products/bearings-units-housings/roller-bearings/cylindrical-roller-bearings/single-row-cylindrical-roller-bearings/basic-design-bearings/index.html.

SKF, 2012a. *Bearing calculation*, Available at: http://www.skf.com/binary/49-62749/RTB-1-05-Bearing-calculation.pdf

SKF, 1994. *Bearing Failures and Their Causes*, Available at: http://www.mana-omerzu.si/files/Bearing_Failures_and_Their_Causes.pdf

SKF, 2012b. *Bearing investigation - Extract from the Railway Technical Handbook, Volume 1,. Chapter 6, Page 122 to 135*, Available at: http://www.skf.com/binary/86-62751/RTB-1-06-Bearing-investigation.pdf

SKF, 2015. Radial bearings. Available at: http://www.skf.com/group/products/bearings-units-housings/roller-bearings/principles/bearing-basics/bearing-types-and-designs/radial-bearings/index.html.

SKF, 2017a. SKF Insight - Railway testimonial. Available at: http://www.skf.com/group/products/condition-monitoring/skf-insight-railway-testimonial.html

SKF, 2017b. SKF Insight^{TM}. Available at: http://www.skf.com/group/industry-solutions/railways/condition-monitoring-products/skf_insight.html?WT.oss=insight&WT.z_oss_boost=0&tabname=All&WT.z_oss_rank=4

SKF, 2017c. White Etching Cracks are a Symptom of Bearing Failure | SKF Group. Available at: http://www.skf.com/group/knowledge-centre/aptitude-exchange/white-papers/what-are-white-etching-cracks/index.html

Tan, C.K., Irving, P. & Mba, D., 2005. Diagnostics and prognostics with acoustic emission, vibration and spectrometric oil analysis for spur gears: A comparative study. *Insight - Non-Destructive Testing and Condition Monitoring*, 47(8), pp.478–480.

Tan, C.K. & Mba, D., 2005. Limitation of Acoustic Emission for Identifying Seeded Defects in Gearboxes. *Journal of Nondestructive Evaluation*, 24(1).

Tavner, P., 2011. SUPERGEN Wind 2011 General Assembly. *SUPERGEN Wind 2011 General Assembly*, (March).

Torkamani, S. et al., 2014. A novel damage index for damage identification using guided waves with application in laminated composites. *Smart Materials and Structures*, 23(9), p.95015.

Toutountzakis, T. & Mba, D., 2003a. Observations of acoustic emission activity during gear defect diagnosis. *NDT & E International*, 36(7), pp.471–477.

Toutountzakis, T. & Mba, D., 2003b. Observations of acoustic emission activity during gear defect diagnosis. *NDT & E International*, 36(7), pp.471–477.

Toutountzakis, T., Tan, C.K. & Mba, D., 2005. Application of acoustic emission to seeded gear fault detection. *NDT & E International*, 38(1), pp.27–36.

Tsolis, G. & Xenos, T., 2011. Signal denoising using empirical mode decomposition and higher order statistics. *Int J Signal Proc Image Proc Pattern Recog*, 4(2), pp.91–106.

Vicuña, C.M., 2014. Effects of operating conditions on the Acoustic Emissions (AE) from planetary gearboxes. *Applied Acoustics*, 77, pp.150–158.

Wada, M. & Mizuno, M., 1989. Study on friction and wear utilizing acoustic emission. Relation between friction and wear mode and acoustic emission signals. *Journal of the Japan Society for Precision Engineering*, 55(4), pp.673–678.

Weeks, I., 2015. Cardiff School of Engineering An Experimental Investigation into the Mixed Lubrication of Steel Surfaces Presented for the candidature of Doctor of Philosophy.

Wiggelinkhuizen, E. et al., 2008. Assessment of condition monitoring techniques for offshore wind farms. *Journal of Solar Energy Engineering, Transactions of the ASME*, 130(3), pp.310041–310049.

Williams, T. et al., 2001. Rolling Element Bearing Diagnostics in Run-To-Failure Lifetime Testing. *Mechanical Systems and Signal Processing*, 15(5), pp.979–993.

Wu, J.-D. & Chen, J.-C., 2006. Continuous wavelet transform technique for fault signal diagnosis of internal combustion engines. *NDT & E International*, 39(4), pp.304–311.

Yu, J. et al., 2011. Prediction of fatigue crack growth in steel bridge components using acoustic emission. *Journal of Constructional Steel Research*, 67, pp.1254–1260.

Zaretsky, E. V, Poplawski, J. V & Peters, S.M., 1996. Comparison of life theories for rolling element bearings. *Tribology Transactions(USA)*, 39(2), pp.237–248.

9 Appendix

```
function project()
    % program bearingload
    % integer::i,j,npoints,Z,balls
    %
real::n,JRe,eps,pd2dr,phi1,phi1low,phi1high,dphi,philoc,JReloc,pi,D,l,di,Pd,Fr
    %
real::Kl,Kn,n1,n2,deltar,conv,epsold,Qmax,gamma,sigmarho,b,sigmamax,spacing
    % real::angle,angledeg,Qi
    % character*9::brgdes


    % Code to calculate the load distribution in a rolling element bearing
    % Also calculates max Hertz contact stresses etc
    % Code initially written for roller bearings to calculate JRe integral
    % open(21,file='out.txt');
    % open(11,file='input.dat',status='old',action='read');
    A = readtable('input.dat');
    B = table2cell(A);
    bearing_data = B(:,1);
    pi = 3.1415926535897932;
    n = 10.0/9.0;
    n1 = 8.0/9.0;
    n2 = 0.9;
    npoints = 1000000;
    conv = 1;

    brgdes = cell2mat(bearing_data(1,1));
    Z = str2double(cell2mat(bearing_data(2,1)));
    D = str2double(cell2mat(bearing_data(3,1)));
    l = str2double(cell2mat(bearing_data(4,1)));
    di = str2double(cell2mat(bearing_data(5,1)));
    Pd = str2double(cell2mat(bearing_data(6,1)));
    Fr = str2double(cell2mat(bearing_data(7,1)));

    % ! Z = 19;
    % ! D = 30;
    % ! l = 30;
    % ! di = 182;
    % ! Pd = 95;
    % ! Fr = 60542;

    fid = fopen('out.txt', 'w');
    fprintf(fid, 'Bearing Load Analysis
\n__________________________________________________ \nBearing Designation =
%s \nNo of rollers = %d \nRoller diameter = %d mm \nRoller length = %d mm
\nInner race diameter = %d mm \nDiametral clearance = %d microns \nRadial load
= %d N', brgdes, Z, D, l, di, Pd, Fr);

    spacing = (2*pi)/Z;
    Pd = Pd/1000;
```

```
    Kl = 78600*(l^n1);
    Kn = (1/(2*((1.0/Kl)^n2)))^n;

    % ! write(21,*)Kl
    % ! write(21,*)Kn
    % ! initial guess value of epsilon

    eps = 0.4;
    fprintf(fid, '\n_____________________________________________________
\n\nConvergence of Epsilon \n');
    while (conv > 0.0000001)
        epsold = eps;
        pd2dr = 1-(2*eps);
        if (pd2dr < -1.0)
            pd2dr = -1.0;
        end
        phi1 = acos(pd2dr);
        phi1low = (-1.0)*phi1;
        phi1high = phi1;
        % ! write(21,*)phi1low,phi1high
        dphi = (2*phi1)/npoints;
        JRe = 0.0;
        for i = 0:(npoints-1)
            philoc = phi1low + ((i+0.5)*dphi);
            JReloc = cos(philoc)*dphi*((1-((1/(2*eps))*(1-(cos(philoc)))))^n);
            JRe = JRe+JReloc;
        % ! write(21,*)philoc,JREloc
        end
        JRe = JRe/(2*pi);
        fprintf(fid, '%d \t%d \n', eps, JRe);
        deltar = ((Fr/(Z*Kn*JRe))^n2)+(0.5*Pd);
        eps = 0.5*(1-(Pd/(2*deltar)));
        conv = abs(epsold-eps);
        disp_str = sprintf('Running %d', conv);
        disp(disp_str);
    end
    % ! converged eps has now been achieved
    % ! calculate max element load, contact semiwidth, contact stress
    Qmax = Fr/(Z*JRe);
    fprintf(fid, '\n_____________________________________________________
\nMaximum element load = %d N',Qmax);

    % ! Calcualate load distribution on loaded elements
    fprintf(fid, '\n_____________________________________________________
\nLoad Distribution on elements \nBalls, Angle, Load');
    balls = 1;
    angle = 0;
    while (balls<=Z)
        Qi = 1-((1/(2*eps))*(1-cos(angle)));
        if (Qi >= 0)
            Qi=(Qi^n)*Qmax;
        else
            Qi = 0;
        end
        % ! Qi=((1-(1-cos(angle))*(1/(2*eps)))**n)*Qmax
```

```
        angledeg = (angle/pi)*180;
        fprintf(fid, '\n%5d \t%6.2d \t%12.5d', balls, angledeg, Qi);
        balls = balls+2;
        angle = angle+spacing;
    end

    gamma = (2*D)/((2*D)+(2*di)+Pd);
    sigmarho = (1/D)*(2/(1-gamma));
    b = 0.00335*((Qmax/(l*sigmarho))^0.5);
    sigmamax = (2*Qmax)/(pi*l*b);
    fprintf(fid, '\n_____________________________________________________
\nHertzian Contact Calculations \nMaximum contact dimension = %d mm \nMaximum
Hertzian stress = %d MPa\n', b, sigmamax);
end
```

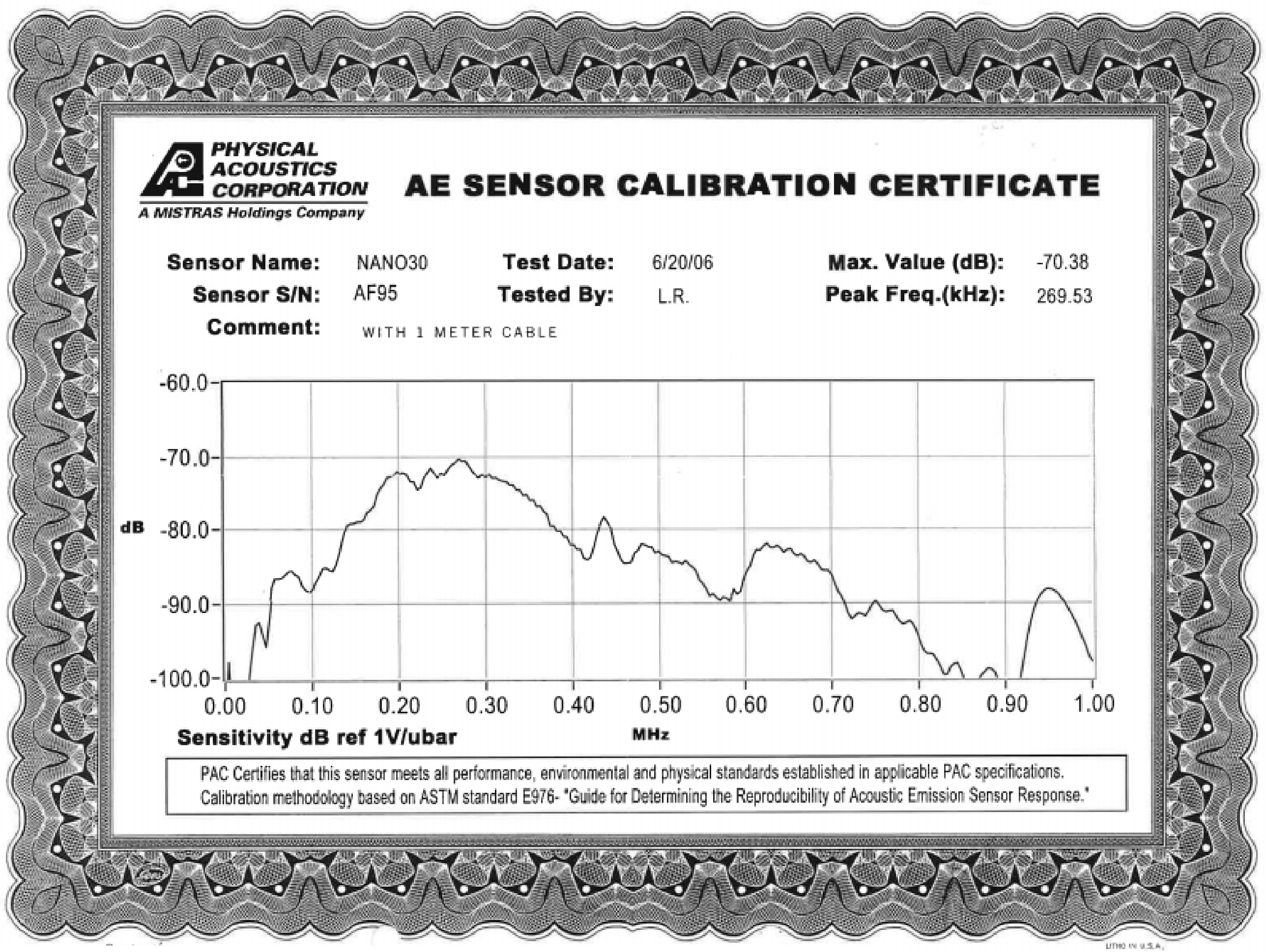

PHYSICAL ACOUSTICS CORPORATION
A MISTRAS Holdings Company

AE SENSOR CALIBRATION CERTIFICATE

Sensor Name: NANO30
Sensor S/N: AF95
Comment: WITH 1 METER CABLE
Test Date: 6/20/06
Tested By: L.R.
Max. Value (dB): -70.38
Peak Freq.(kHz): 269.53

PAC Certifies that this sensor meets all performance, environmental and physical standards established in applicable PAC specifications.
Calibration methodology based on ASTM standard E976- "Guide for Determining the Reproducibility of Acoustic Emission Sensor Response."

LITHO IN U.S.A.

Figure 9-1 - Example of a PAC Nano30 AE sensor calibration chart

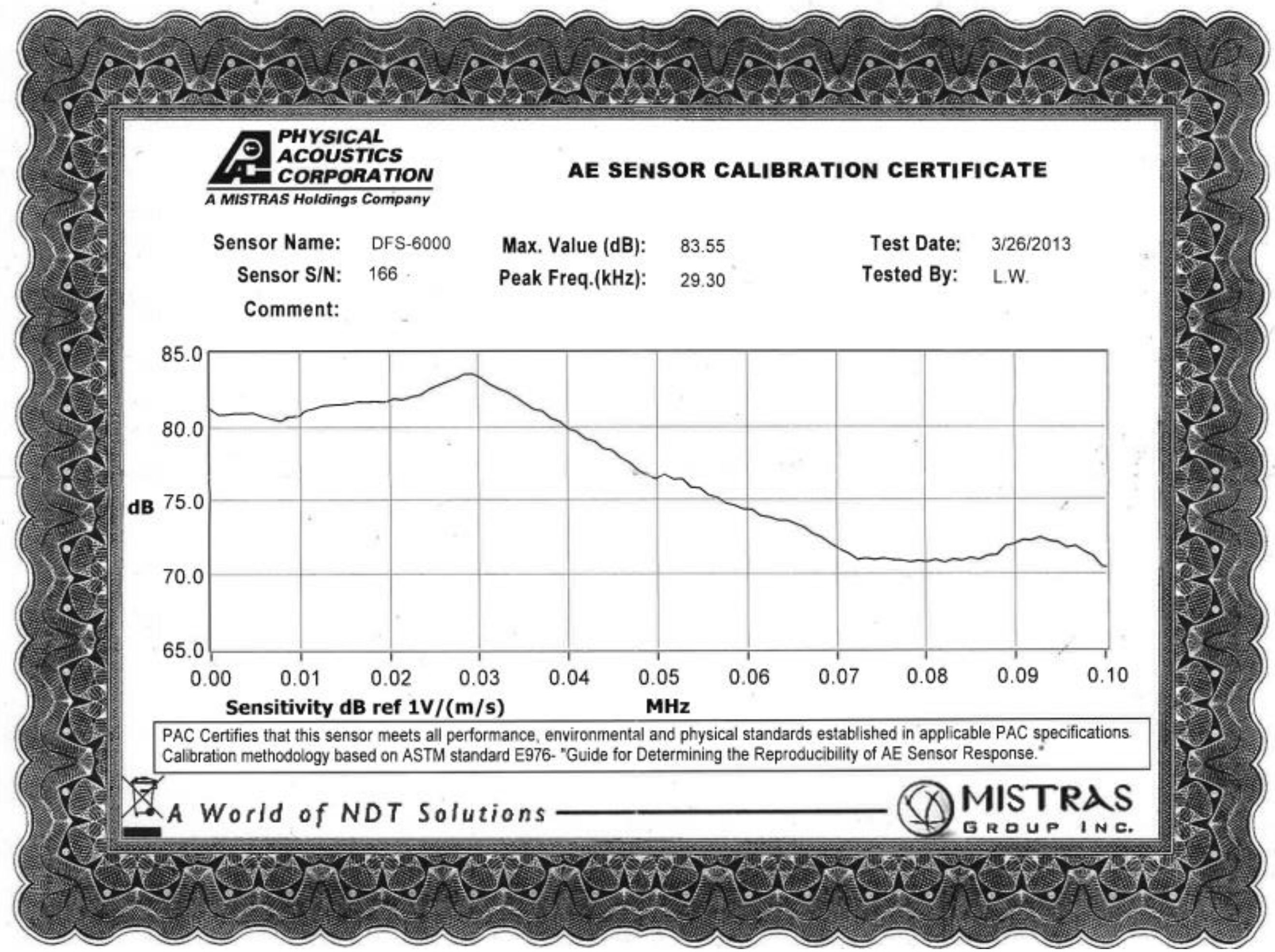

PHYSICAL ACOUSTICS CORPORATION
A MISTRAS Holdings Company

AE SENSOR CALIBRATION CERTIFICATE

Sensor Name:	DFS-6000	**Max. Value (dB):**	83.55	**Test Date:**	3/26/2013
Sensor S/N:	166	**Peak Freq.(kHz):**	29.30	**Tested By:**	L.W.
Comment:					

PAC Certifies that this sensor meets all performance, environmental and physical standards established in applicable PAC specifications.
Calibration methodology based on ASTM standard E976- "Guide for Determining the Reproducibility of AE Sensor Response."

A World of NDT Solutions — MISTRAS GROUP INC.

Figure 9-2 - Example of a DFS600 sensor calibration chart - AE

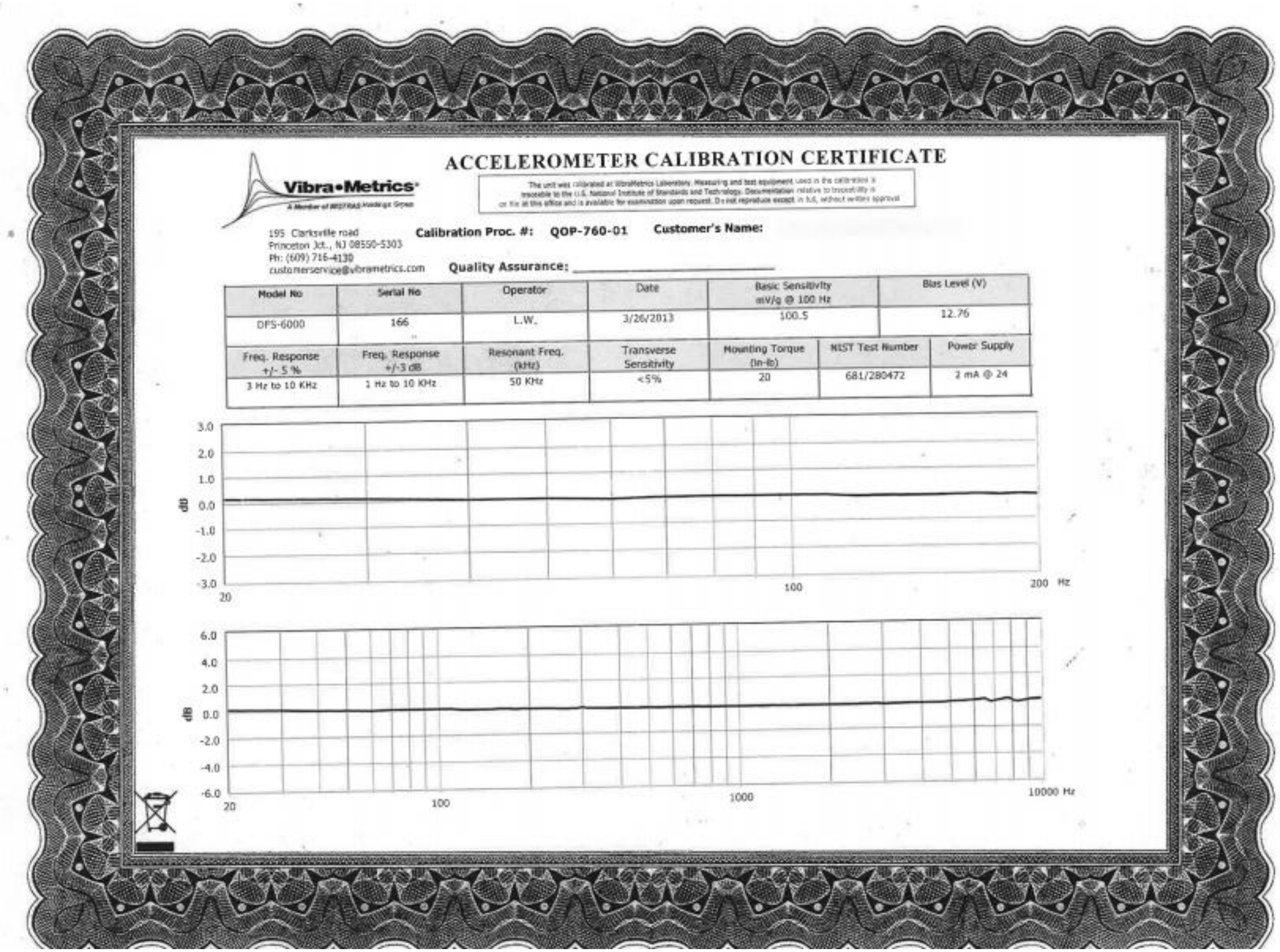

ACCELEROMETER CALIBRATION CERTIFICATE

Vibra•Metrics
A Member of MISTRAS Holdings Group

The unit was calibrated at VibraMetrics Laboratory. Measuring and test equipment used in the calibration is traceable to the U.S. National Institute of Standards and Technology. Documentation relative to traceability is on file at this office and is available for examination upon request. Do not reproduce except in full, without written approval

195 Clarksville road
Princeton Jct., NJ 08550-5303
Ph: (609) 716-4130
customerservice@vibrametrics.com

Calibration Proc. #: QOP-760-01 **Customer's Name:** [redacted]

Quality Assurance: ____________________

Model No	Serial No	Operator	Date	Basic Sensitivity mV/g @ 100 Hz	Bias Level (V)
DFS-6000	166	L.W.	3/26/2013	100.5	12.76

Freq. Response +/- 5 %	Freq. Response +/-3 dB	Resonant Freq. (kHz)	Transverse Sensitivity	Mounting Torque (in-lb)	NIST Test Number	Power Supply
3 Hz to 10 KHz	1 Hz to 10 KHz	50 KHz	<5%	20	681/280472	2 mA @ 24

Figure 9-3 - Example of a Vibrametrics DFS6000 calibration chart - Vibration

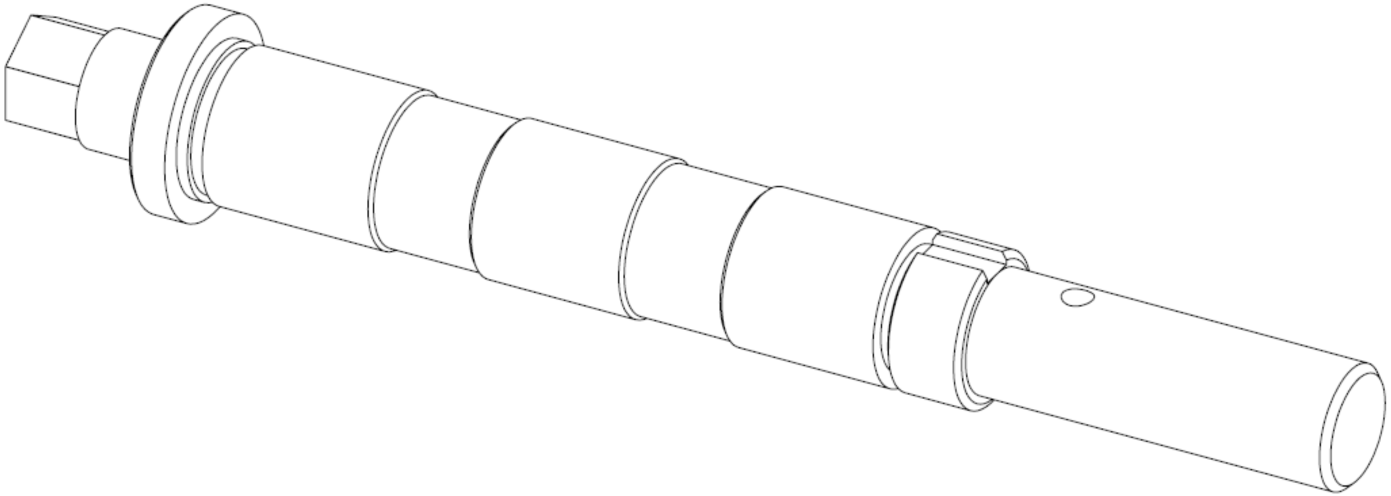

NOTE:

Material to be EN40B or equivalent.
Nitride hardened 0.25mm deep to
600-750 Vickers Minimum.
All dimensions to +/- 0.1mm unless otherwise stated.
Centres may be drilled in shaft ends for grinding

Grind bearing faces to Tolerance after hardening

Contact A. Cockerill on 07934845186 or cockerilla@cardiff.ac.uk if any queries

UNLESS OTHERWISE SPECIFIED:
DIMENSIONS ARE IN MILLIMETERS
SURFACE FINISH:
TOLERANCES:
LINEAR:
ANGULAR:

FINISH:

DEBUR AND BREAK SHARP EDGES

DO NOT SCALE DRAWING

REVISION

	NAME	SIGNATURE	DATE
DRAWN	Aaron Cockerill	AJC	30 OCT 14
CHK'D	Alastiar Clarke	AC	6 NOV 14
APPV'D			
MFG			
Q.A			

TITLE:

FAST SHAFT

MATERIAL:
EN40B

WEIGHT:

DWG NO.

A3

SCALE:1:1

SHEET 1 OF 2

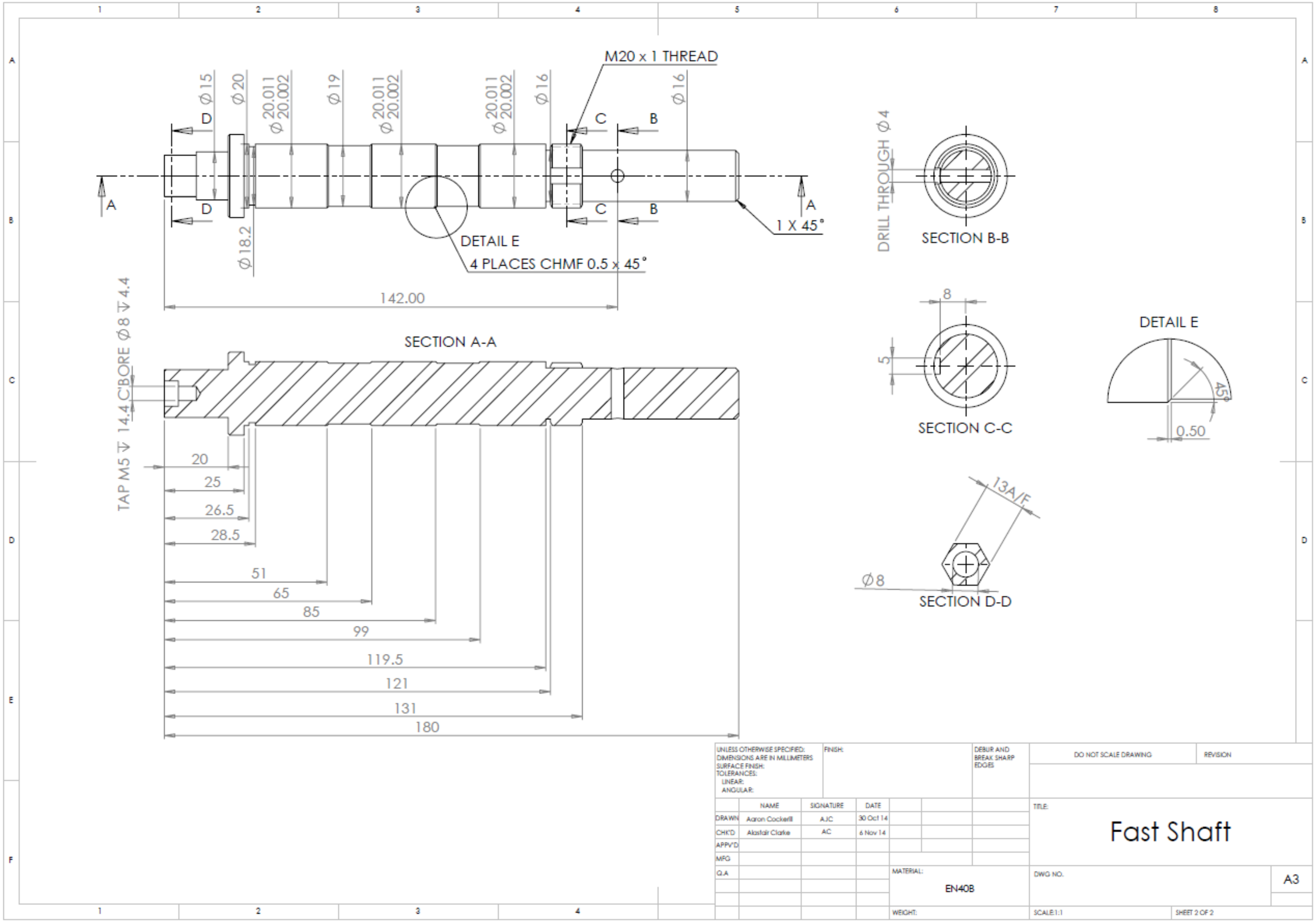
M20 x 1 THREAD
Ø15
Ø20
Ø20.011
Ø20.002
Ø19
Ø20.011
Ø20.002
Ø20.011
Ø20.002
Ø16
Ø16
D
D
C
C
B
B
A
A
1 X 45°
Ø18.2
DETAIL E
4 PLACES CHMF 0.5 x 45°
142.00
SECTION A-A
TAP M5 ↧ 14.4 C'BORE Ø8 ↧ 4.4
20
25
26.5
28.5
51
65
85
99
119.5
121
131
180
DRILL THROUGH Ø4
SECTION B-B
8
5
SECTION C-C
DETAIL E
45°
0.50
13A/F
Ø8
SECTION D-D
UNLESS OTHERWISE SPECIFIED:
DIMENSIONS ARE IN MILLIMETERS
SURFACE FINISH:
TOLERANCES:
LINEAR:
ANGULAR:
FINISH:
DEBUR AND BREAK SHARP EDGES
DO NOT SCALE DRAWING
REVISION
NAME
SIGNATURE
DATE
DRAWN
Aaron Cockerill
AJC
30 Oct 14
CHK'D
Alastair Clarke
AC
6 Nov 14
APPV'D
MFG
Q.A
MATERIAL:
EN40B
WEIGHT:
TITLE:
Fast Shaft
DWG NO.
A3
SCALE:1:1
SHEET 2 OF 2